UNIVERSIDAD AUTÓNOMA DE NUEVO LEÓN

FACULTAD DE CIENCIAS QUÍMICAS

TESIS

"INVESTIGATION ON THE APPLICATION OF MOLYBDENUM-BASED ONE DIMENSIONAL AND TWO-DIMENSIONAL NANOSTRUCTURES IN GAS-SENSING AND HYDROGEN EVOLUTION REACTIONS"

PRESENTADA POR:

TIJIN THOMAS

COMO REQUISITO PARCIAL PARA OBTENER EL GRADO DE:

DOCTORADO EN CIENCIAS

CON ORIENTACIÓN EN PROCESOS SUSTENTABLES

AGOSTO 2022

UNIVERSIDAD AUTÓNOMA DE NUEVO LEÓN

FACULTAD DE CIENCIAS QUÍMICAS

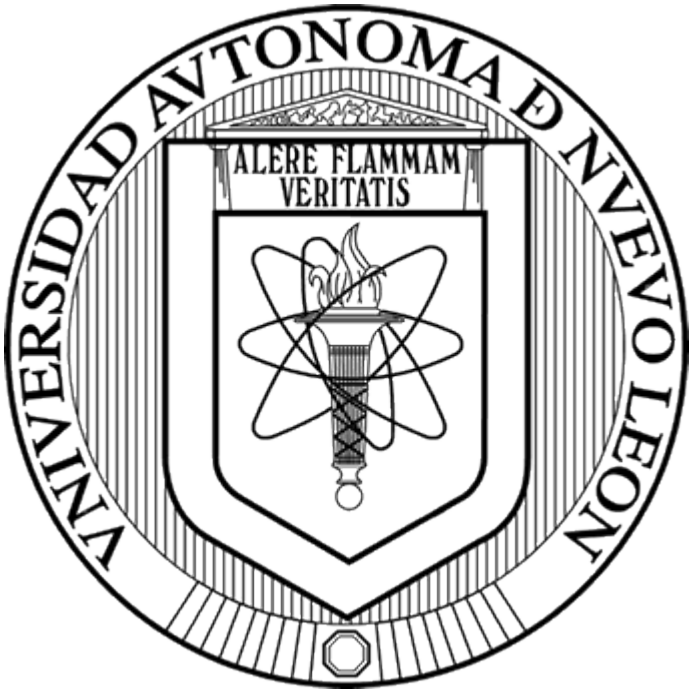

INVESTIGATION ON THE APPLICATION OF MOLYBDENUM-BASED ONE DIMENSIONAL AND TWO-DIMENSIONAL NANOSTRUCTURES IN GAS-SENSING AND HYDROGEN EVOLUTION REACTIONS

by,

TIJIN THOMAS

The thesis submitted in partial fulfilment of the requirements for the
DEGREE OF DOCTOR OF PHILOSOPHY IN SCIENCE
with orientation in sustainable processes

AUGUST 2022

INVESTIGATION ON THE APPLICATION OF MOLYBDENUM-BASED ONE DIMENSIONAL AND TWO-DIMENSIONAL NANOSTRUCTURES IN GAS-SENSING AND HYDROGEN EVOLUTION REACTIONS

THESIS AUTHORIZATION

DR. SANAL KOZHIPARAMBIL CHANDRAN

PRESIDENT

DRA. ANDREA CERDÁN-PASARÁN

SECRETARY

DRA. SHADAI LUGO LOREDO

FIRST VOCAL

DRA. BINDHU KRISHNAN

SECOND VOCAL

DRA. SELENE SEPÚLVEDA GUZMÁN

THIRD VOCAL

DRA. MARIA ELENA CANTU

SUBDIRECTOR OF STUDIES OF POSTGRADUATE

INVESTIGATION ON THE APPLICATION OF MOLYBDENUM-BASED ONE DIMENSIONAL AND TWO-DIMENSIONAL NANOSTRUCTURES IN GAS-SENSING AND HYDROGEN EVOLUTION REACTIONS

DR. SANAL KOZHIPARAMBIL CHANDRAN

THESIS DIRECTOR

DR. EDUARDO MAXIMINO SANCHEZ CERVANTES

CO-DIRECTOR

DRA. SHADAI LUGO LOREDO

MEMBER OF TUTORIAL COMMITTEE

DR. JUAN MANUEL HERNANDEZ LOPEZ

MEMBER OF TUTORIAL COMMITTEE

DRA. ANDREA CERDÁN-PASARÁN

MEMBER OF TUTORIAL COMMITEE

DEDICATION

To my loving parents Mr. Thomas K T and Dr. Jain Thomas,

To my beloved Shilpa Paul,

To my loving Aiga Mariya, Teena, and Ebin.

Acknowledgment

Thank you, Almighty, for guiding me in the proper direction and for my quick thinking, which allowed me to complete my thesis within the allotted time. I thank CONACYT and PAICYT for all the financial support during my 3 years of Ph.D. work. A big thanks to EGAII FCQ, CIIDIT, and FIME, Universidad Autonoma de Nuevo Leon for providing the research facilities during the synthesis and characterization. I am grateful to Dr. Sanal Kozhiparambil Chandran for all his guidance, support, and assistance as supervising guide throughout the research and stay in Monterrey. I owe special gratitude to my co-advisor, Dr. Eduardo Maximiano Sanchez, for all his support in the laboratory, advice, and useful tips. I express my sincere gratitude towards my doctoral committee members, Dr. Juan Manuel, Dra. Andrea Cerdan and Dra. Shadai Loredo for all their support and guidance. I am thankful to Dra. Selena Sepulveda Guzman and Dra. Anabel Alvaro Mendez for providing the laboratory facilities and their constant support throughout the research. One part of my thesis was done at CIICAp, Universidad Autonoma del Estado de Morelos, Cuernavaca. I am thankful to Dra. Vivechana Agarwal, Dr. Yogesh Kumar Saluja, Dr. Jesus Alberto Ramos Ramon, Dr. Naveen, and all other faculty and friends of CIICAp for hosting and supporting me with all their resources and guidance. A special mention to Simei Torres, Myriam, and their Baby Miguel for their hearty welcome, love, and care throughout the stay in Cuernavaca. I thank Mrs. Soorya Pushpan for all her help during the experimental characterization. Special thanks to Dr. Reshmi R for all her support and guidance during my initial stages of research. I am grateful to my dearest friend Dr. Priyesh for introducing me to Dr. Sanal. I extend my gratitude to Dr. Nagabandi Jayababu, Dr. Julakanti Shruthy, and everyone else who has worked on this project with me throughout the years. Special mention to Sr. Victor, Sra. Elsa, Sr. Carlos, Sr. Fransisco, and Ruby for hosting me in Mexico during different periods. I owe Lizzie Garza Cantu a debt of gratitude for her efforts to teach me the basics of Spanish during my time in Mexico. Sincere thanks to Alan Rico, Clovis Nchikou, Jawer Acuna, Samuel Quintero, Dr. Vineetha Vinaya Kumar, Albert Paul, Paulosutty Abraham, Aiswarya Nadukkandy, Akshana P.S, Sebin Devasia, Dr. Jacob Johny, Karan Singh, Muhammed Faisal, Ramsha Ali, Dr. Akhila Mohan, Saranya Sasi, Hilal Rahman, Benazeera Bheegum, Shinto Babu, Dr. Bindhu G Nair, Dr.Aijo, Charly, all my friends, and colleagues who encouraged and helped me throughout this journey.

Abstract

Tijin Thomas, August 2022
Universidad Autónoma de Nuevo León,
Facultad de Ciencias Químicas.

Title of the thesis: INVESTIGATION ON THE APPLICATION OF MOLYBDENUM-BASED ONE DIMENSIONAL AND TWO-DIMENSIONAL NANOSTRUCTURES IN GAS-SENSING AND HYDROGEN EVOLUTION REACTIONS

Number of Pages: 155
The thesis submitted in partial fulfillment of the requirements for the **DEGREE OF DOCTOR OF PHILOSOPHY IN SCIENCE** with orientation in sustainable processes.

Area of study: Sustainable Processes

Purpose and method of the study: One of the primary goals of the researchers is to develop sustainable and clean energy to replace traditional fossil fuels, as environmental difficulties are becoming more prevalent owing to the release of hazardous gases from the burning of such fuels. Proper monitoring of the emission of those gases is also critical for which gas sensors with higher sensing response, long term stability, fast response, and recovery times are needed. Hydrogen is considered as the fuel for the near future as a replacement for non-renewable fossil fuels and the cleanest way of its production is by the means of electrocatalytic/photocatalytic water splitting. Molybdenum based one dimensional and two-dimensional nanostructured materials have been proven for their applications in gas sensing as the sensing element and in the clean production of hydrogen by the means of electrochemical water splitting as the catalyst, but the research is still inadequate for meeting the real application. In this work, we attempt the synthesis, characterization, and applications of one-dimensional molybdenum trioxide, two-dimensional molybdenum carbide MXenes, and their composites for their applications in gas sensing and electrochemical hydrogen evolution reaction for a real device with less environmental impact.

Contributions and Conclusions: In this study, we carried out the gas sensing and hydrogen evolution application of molybdenum-based 1D and 2D nanostructures with the help of a systematic study of the synthesis and characterization strategies involved. To detect the presence of ammonia gas, gas sensors were produced in this work using vacuum thermal evaporation of α-MoO_3 nanorods on glass substrates, followed by an annealing technique in ambient air. The gas sensing assessment of the produced sensors demonstrated that the specimen annealed at 400 ^oC had exceptional sensitivity towards ammonia gas at room temperature (28 ^oC). In the process of the testing, it was determined that the sensors remained

responding to ammonia levels as low as 1ppm, highly repeatable, and remarkably stable after one year of working, with just a 1% decline in the sensing response. Additionally, a porous silicon/molybdenum trioxide hybrid structure, that was produced via simple thermal evaporation of the MoO_3 over an electrochemically produced silicon substrate, proved effective in sensing CO_2 gas at a low concentration level (50 ppm) and working temperature (150 ^oC). We compared the effect of the substrate in the sensing performance, and it was found that at 250 ^oC, the sensor fabricated on porous silicon demonstrated approximately fourfold the sensitivity (15 % at 150 ppm) of the sensor fabricated on crystalline silicon (3.9 % at 200 ^oC and 150 ppm) and a much faster response time (8s at 100 ppm). Meanwhile, Mo_2CT_x MXene was prepared from Mo-In-C non-MAX phase using a solid-state process followed by UV aided phosphoric acid etch and ultrasonic exfoliation for the first time. We developed Mo_2CT_x MXene sensors that were supported on a different substrate (glass, crystalline, and porous silicon) and used them to detect CO_2 at room temperature. The gas sensing experiments were carried out at temperatures ranging from 30 to 250 ^oC and CO_2 concentrations ranging from 50 to 150 ppm. When compared to crystalline silicon sensors, sensors built of porous silicon and glass demonstrate superior room temperature sensing response as well as rapid reaction and recovery time of 30 and 45 s, respectively, when operated at 30 °C and 50 ppm of CO_2, which are the fastest recorded values at ambient temperature to the date. Finally, electrochemical hydrogen evolution reaction (HER) application of the produced Mo_2CT_x MXenes as working electrodes was carried out and the MXene synthesized from the non-MAX phase at 850 ^oC exhibited the lowest overpotential, with a value of -138 mV at 10 mA/cm^2 current density and a Tafel slope of 41 mV/dec.

Signature of the Advisor: _____

DR. SANAL KOZHIPARAMBIL CHANDRAN

Resumen

Tijin Thomas, Agosto 2022
Universidad Autónoma de Nuevo León,
Facultad de Ciencias Químicas.

Título de la tesis: INVESTIGATION ON THE APPLICATION OF MOLYBDENUM-BASED ONE DIMENSIONAL AND TWO-DIMENSIONAL NANOSTRUCTURES IN GAS-SENSING AND HYDROGEN EVOLUTION REACTIONS

Número de páginas: 155
La tesis presentada en cumplimiento parcial de los requisitos para el **GRADO DE DOCTORADO EN CIENCIAS** con orientación en procesos sustentables.

Área de estudio: Procesos Sustentables

Propósito y método del estudio: Uno de los objetivos principales de los investigadores es desarrollar energía sostenible y limpia para reemplazar los combustibles fósiles tradicionales, ya que las dificultades ambientales son cada vez más frecuentes debido a la liberación de gases peligrosos de la quema de dichos combustibles. El monitoreo adecuado de la emisión de esos gases también es crítico para lo cual se necesitan sensores de gas con mayor respuesta de detección, estabilidad a largo plazo, respuesta rápida y tiempos de recuperación. El hidrógeno se considera como el combustible para el futuro cercano como un reemplazo de los combustibles fósiles no renovables y la forma más limpia de su producción es mediante la división electrocatalítica / foto catalítica del agua. Los materiales nanoestructurados unidimensionales y bidimensionales basados en molibdeno han sido probados por sus aplicaciones en la detección de gases como elemento de detección y en la producción limpia de hidrógeno por medio de la división electroquímica del agua como catalizador, pero la investigación sigue siendo inadecuada para cumplir con la aplicación real. En este trabajo, intentamos la síntesis, caracterización y aplicaciones de trióxido de molibdeno unidimensional, carburo de molibdeno bidimensional MXenes, y sus compuestos para sus aplicaciones en la detección de gases y la reacción de evolución electroquímica del hidrógeno para un dispositivo real con menor impacto ambiental.

Contribuciones y conclusiones: En este estudio, llevamos a cabo la aplicación de detección de gases y evolución de hidrógeno de nanoestructuras 1D y 2D basadas en molibdeno con la ayuda de un estudio sistemático de las estrategias de síntesis y caracterización involucradas. Para detectar la presencia de gas amoníaco, se produjeron sensores de gas en este trabajo utilizando la evaporación térmica al vacío de nano varillas α-MoO_3 sobre sustratos de vidrio, seguida de una técnica de recocido en aire ambiente. La evaluación de detección de gas de los

sensores producidos demostró que la muestra recocida a 400 ºC tenía una sensibilidad excepcional hacia el gas amoníaco a temperatura ambiente (28 ºC). En el proceso de la prueba, se determinó que los sensores seguían respondiendo a niveles de amoníaco tan bajos como 1ppm, altamente repetibles y notablemente estables después de un año de trabajo, con solo una disminución del 1% en la respuesta de detección. Además, una estructura híbrida porosa de silicio / trióxido de molibdeno, que se produjo a través de la evaporación térmica simple del MoO_3 sobre un sustrato de silicio producido electroquímicamente, demostró ser efectiva para detectar gas CO_2 a un bajo nivel de concentración (50 ppm) y temperatura de trabajo (150 ºC). Comparamos el efecto del sustrato en el rendimiento de detección, y se encontró que a 250 ºC, el sensor fabricado en silicio poroso demostró aproximadamente cuatro veces la sensibilidad (15 % a 150 ppm) del sensor fabricado en silicio cristalino (3,9 % a 200 ºC y 150 ppm) y un tiempo de respuesta mucho más rápido (8s a 100 ppm). Mientras tanto, Mo_2CT_x MXene se preparó a partir de la fase Mo-In-C no MAX utilizando un proceso de estado sólido seguido de grabado de ácido fosfórico asistido por UV y exfoliación ultrasónica por primera vez. Desarrollamos sensores Mo $_2CT_x$ MXene que se apoyaban en un sustrato diferente (vidrio, silicio cristalino y poroso) y los utilizamos para detectar CO_2 a temperatura ambiente. Los experimentos de detección de gases se llevaron a cabo a temperaturas que oscilaron entre 30 y 250 ºC y concentraciones de CO 2 que oscilaron entre 50 y 150 ppm. En comparación con los sensores de silicio cristalino, los sensores construidos con silicio poroso y vidrio demuestran una respuesta de detección de temperatura ambiente superior, así como un tiempo de reacción y recuperación rápido de 30 y 45 s, respectivamente, cuando se operan a 30 ° C y 50 ppm de CO_2, que son los valores registrados más rápidos a temperatura ambiente hasta la fecha. Finalmente, se llevó a cabo la aplicación de la reacción electroquímica de evolución del hidrógeno (HER) de los Mo_2CT_x MXenes producidos como electrodos de trabajo y el MXene sintetizado a partir de la fase no MAX a 850 ºC exhibió el sobrepotencial más bajo, con un valor de -138 mV a 10 mA / cm^2 densidad de corriente y una pendiente de Tafel de 41 mV/dec.

Firma del Asesor:

DR. SANAL KOZHIPARAMBIL CHANDRAN

TABLE OF CONTENTS

LIST OF TABLES

LIST OF FIGURES

1. INTRODUCTION

This chapter is intended to provide a brief overview of the research investigation history and properties of one and two-dimensional transition metal oxide, and MXenes particularly focused on orthorhombic MoO_3, and Mo_2CT_x. The structure, morphology, electrical properties, and their applications in various fields especially gas sensing, and electrochemical hydrogen evolution are discussed in chronological order reviewing the previous works of literature.

1.1 Introduction to nanomaterials.

Nanotechnology is concerned with the study of nanoscale structures or tiny materials. Nanoparticles are particles that range in size from one to one hundred nanometers and are composed of metals, carbon, metal oxides, or organic matter [1]. Nanostructured materials are characterized by their adaptability, functionality, and self-assembly[2]. The physical, chemical, and biological properties of nanoparticles are distinct from those of their bulk counterpart. This is due to increased surface area per volume, increased chemical reactivity or stability, increased mechanical strength, etc [3]. Also, when a material's size is reduced to a scale, which is in the order of the radius of exciton, i.e., to a few nanometers, quantum confinement takes place, and the exciton properties are modified [4]. Quantum confinement refers to the confinement of space associated with electron–hole pairs (excitons) in one or many dimensions within one material, and also refers to the discrete nature of electronic energy levels. Whenever the dimension of the potential reaches near to the de Broglie wavelength of electrons, such types of effects occur, resulting in shifts or discrete levels of energy. As a result, nanocrystals are sometimes referred to as "quantum dots" (QDs) because of the phenomenon known as quantum confinement. Aspects of nanomaterial characteristics such as electrical, optical, and mechanical behavior are all affected by the quantum dot effect, as well as their interactions with one another. Nanomaterials have higher electron energies than bulk materials, which is the reason behind their distinct properties. Confined electrons have a higher energy than electrons in bulk materials, and this is dependent on the size of the QD. When the dimensionality of semiconductor nanomaterials is reduced from 2D to 1D or from 1D to 0D, they exhibit a variety of fascinating characteristics. Possibly, the quantum confinement effect takes place when nanomaterials are made smaller to size less than 10-100 nm or even smaller. Size confinement is caused by the set of discrete electron energy levels [5,6].

Nanomaterials are categorized into zero-dimensional (0D), one-dimensional (1D), two-dimensional (2D), as well as three-dimensional (3D) based on their dimensions (Fig:1.1)

[7]. Zero-dimensional nanomaterials (0D) have all their outer dimensions at the nano size, which is between 1 and 100 nm. A quantum dot is a 10 nm-sized semiconductor nanocrystal (0D) that acts as a potential well and is used in electronic devices to entrap charge carriers [8]. One-dimensional (1D) nanostructures have two outer dimensions at the nanometer length scale, and the third one usually at the microscale. Nanofibers, nanowires, nanotubes, and nanorods are examples of these materials [9]. The atoms in nanotubes are arranged in pentagons, hexagons, and heptagons in a unique cylindrical crystalline shape. Whereas the length-to-width ratio of nanowires is one of the highest among 1D nanomaterials, >1000. With an aspect ratio of between 3 and 20 [10], nanorods fall somewhere in between 0D and 1D nanomaterials. Thin films, nanoplates, and nanocoating are examples of 2D nanomaterials, which only have one outer dimension at the nanoscale. Coatings on ceramic or metal substrates that are only a few atomic layers thick are referred to as thin films [11]. There are no external dimensions to 3D nanomaterials, which have nanoscale features on the inside. Nanostructured materials and nanocomposites belong to this category. Nanocomposites are multiphase crystalline solids in which at least one phase has an external dimension in the nanoscale. Nanofillers diffused in a bulk structure are commonly referred to as nanocomposite. It is possible to choose between 0D, 1D, and 2D nanofillers for these applications (Fig 1.1) [12].

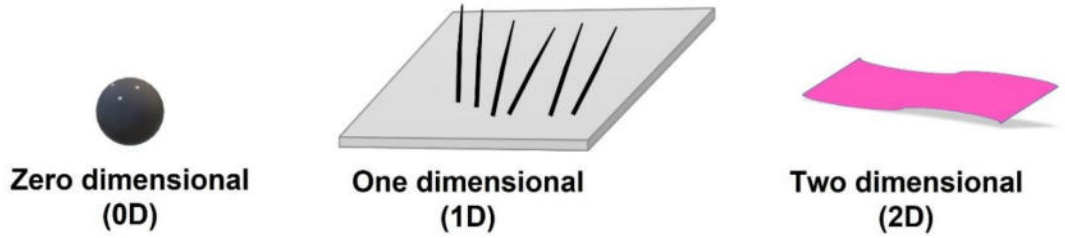

Figure 1.1 Schematic representation of zero, one- and two-dimensional nanomaterials.

1.1.1 One dimensional nanomaterial

- A variety of terms have been used to refer to one-dimensional nanostructures, including whiskers, fibrils, or fibers nanowires, and nanorods. The definition of whiskers and nanorods is somewhat arbitrary, although they are generally considered shorter than nanowires and fibers. Whiskers and fibers were used to describe 1D structures of diameters ranging from a few hundred nanometers up to several hundred microns. However, in the recent literature the term "nanowire" or "nanorod" is used more frequently. One-dimensional nanostructured materials can be synthesized and formed using a variety of techniques, some of which have been extensively studied while others have received little attention. These approaches fall into four categories (Figure: 1.2):

1.1.2 **Ultra-thin two-dimensional nanomaterials**

Two-dimensional (2D) ultrathin nanomaterials have sheet-like structures with lateral sizes greater than 100 nm or going all the way to some micrometers in diameter and even larger, but their thickness is only one or a few atoms thick (usually <5 nm) [13]. The distinctive properties of ultrathin 2D nanomaterials, as compared to their equivalents of other dimensions, are numerous. One advantage 2D nanomaterials is that they exhibit significantly superior electrical characteristics when compared to other types of nanomaterials. This makes them attractive choices for basic condensed matter research as well as electronic device applications. Another advantage is the remarkable mechanical and optical transparency provided by their atomic thickness, which bodes well for the development of new electrical and optoelectronic devices that are both flexible and transparent in nature. As a final benefit, their vast lateral surface area and ultra-thin thickness make them ideal for surface-active applications. The family of ultra-thin 2D nano materials includes graphene, phosphorene, transition metal dichalcogenides like MoS_2, MXene, etc. Ultra-thin 2D nanostructures have become an important nanomaterial in, materials science, condensed matter physics and chemistry due to their distinctive structural characteristics and outstanding properties. Due to their exceptional properties, a wide range of synthesis techniques, such as liquid exfoliation, mechanical cleavage, ion intercalation, anion exfoliation and exchange , chemical vapor deposition, wet-chemical synthesis, solid-state reaction, etc., have now been designed for the preparation of ultrathin 2D nanomaterials [14].

1.2 Synthesis of nanomaterials

Nanomaterials and nanostructures can be synthesized using either the top-down or bottom-up approaches. A common top-down method for producing nanoparticles is attrition or milling. With a top-down approach, the major issue is that the surface structure is not perfectly smooth and uniform. Whereas the term "bottom-up" refers to constructing a material atom by atom, molecule by molecule, or cluster by cluster. The bottom-up approach, on the other hand, guarantees a better chance of producing nanostructures with fewer defects, a rather more uniform chemical makeup, and improved short and long-range ordering. To put it another way, the bottom-up approach is primarily driven by the lowering of Gibbs free energy, resulting in the formation of more stable nanostructures and nanomaterials. To create nanoparticles using the bottom-up approach, either homogeneous nucleation from a liquid or vapor, or heterogeneous nucleation on a substrate, are used. Nucleation and growth can be used to produce nanofibers and other 1D nanomaterials [15]. Various approaches to synthesis of 1D and 2D nanomaterials include hydrothermal method, chemical vapor deposition, sol-gel method, physical vapor deposition, solid-state reaction techniques etc. were used [12].

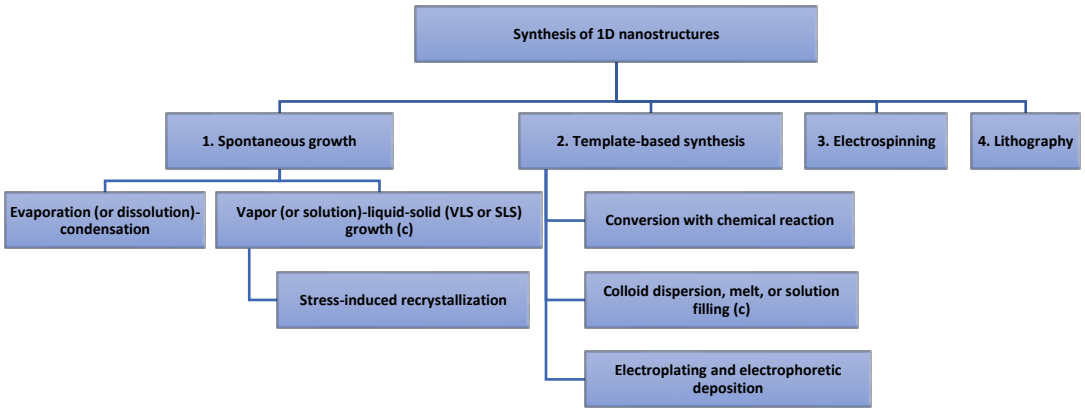

Figure 1.2 Various approaches to synthesis of 1D nanostructures.

Bottom-up approaches, such as spontaneous growth, template-based synthesis, and electrospinning, are preferred over top-down approaches, such as lithography (Fig 1.2). Depending on the crystal structures and surface qualities of the nanowire materials, spontaneous growth frequently leads in the creation of single - crystalline nanowires or nanorods along a preferred crystal growth direction. This method creates polycrystalline or amorphous materials.

The decrease in Gibbs free energy, or chemical potential, is the driving force behind spontaneous growth. It is usually achieved by phase transformation, chemical reaction, or stress release. Because nanowires and nanorods require anisotropic growth, the crystal must grow more rapidly in one direction than in the others. It is possible to obtain nanowires with a uniform diameter along their longitudinal axis if crystal growth proceeds in one direction, while no growth occurs in other directions. Even for given materials and growing conditions, the growth surfaces' defects and impurities can influence the final product's morphology in spontaneous growth. Hydrothermal method is one example of dissolution-condensation method which comes under the spontaneous growth.

Among these, hydrothermal synthesis is a popular method for the synthesis of nano materials. Solution-reaction-based methodology underpins this strategy. The synthesis of nanomaterials by hydrothermal means can take place at temperatures ranging from ambient to

extremely high[16]. In addition that vacuum thermal evaporation is also a proven technique to deposit 1D and 2D nanomaterials on suitable substrate materials for various applications such as gas sensing, field effect transistors (FET) etc. [17–19]. Solid state reaction method is employed during the synthesis of MAX phase for 2D MXene synthesis because of the advantages like reduced cost, less pollution and high yield [20].

1.3 Transition metal oxides.

As a broad term, transition metal oxides refer to any substance in which oxygen atoms are bonded to a transition metal. A variety of transition metal oxides, including those with the general formulas, MO, M_2O_3, MO_2, M_2O_5, MO_3, M_nO_{2n-1}, and M_nO_{2n+1} is known to exist. Bonding in these oxides ranges from fully ionic (NiO, CoO) to entirely covalent (OsO_4,RuO_4) whereas metallic bonding is observed in oxides such as TiO_2, NbO, and ReO_3. Transition metal oxide crystal structures range from cubic to triclinic. Rock-salt structures are seen in simple binary oxides of MO composition, whereas the MO and M_2O_3 have fluorite, rutile, distorted rutile, or more complicated structures. Also, many sesquioxides have the corundum structure. Transition metals contribute significantly to the formation of ternary oxides such as perovskites, spinels, bronzes, and garnets. The physical properties such as magnetic, electrical, and other characteristics of many of these oxides vary substantially when they shift from one crystalline phase to another [21,22].

1.4 One dimensional orthorhombic molybdenum trioxide (α-MoO_3)

Among transition metal oxides, molybdenum oxides are highly customizable oxide compounds with well-established device applications, catalysis, sensors, energy-storage systems, field emission instruments, lubricants, superconductivity, thermoelectric materials, biosystems, chromogenics, and electrochromic systems, among other fields of science. Because of their unique properties, molybdenum oxides are among the most economical and reliable optical and electronic oxides. Different stoichiometries exist, ranging from fully stoichiometric MoO_3, which has a large bandgap (>2.77 eV), to highly conducting reduced oxides, such as MoO_{3-x} ($2 < x < 3$), and finally semi-metallic MoO_2 with a substantially smaller bandgap. Because of the peculiar chemistry caused by the varied valence states, molybdenum oxides are attracting attention among transition-metal oxides. It is possible to decrease Mo^{6+} ions to Mo^{5+} ions, then to Mo^{4+} ions by introducing oxygen defects (MoO_2) [23]. In reality, the oxygen defects in the MoO_x crystal cause a fluctuation in electrical properties as well as a tuneable bandgap in the 2.8-3.6 eV range [24]. Additionally, due to the existence of multiple structural variations for the MoO_x, it can be used in a variety of energy converting and storage applications, such as lithium-ion batteries and catalysts for the hydrogen evolution

reaction (HER)[25–27]. Likewise, surface reactions caused by the localized resonance of plasmons of MoO_x make it suitable for application in gas sensing and photodevices[28–30]. MoO_3 is a transition metal oxide with exceptional stability when compared to other oxide compounds. There are three polymorphous phases for a crystalline MoO_3: a thermodynamically stable orthorhombic (α-MoO_3) phase and a meta-stable phase, monoclinic (β-MoO_3) and a hexagonal (h-MoO_3). The location of MoO_6 octahedra, known as the fundamental building block of MoO_3, in which molybdenum atoms pair with six oxygen atoms to produce MoO_6 octahedra, has been used to determine the phase stability and crystal structure of MoO_3. As stated earlier, the orthorhombic (α-MoO_3) phase is the one that is thermodynamically stable compared to the other two polymorphs. With its layered crystallographic structure, α-MoO_3 has particularly attracted the interest of researchers since its layers exist aligned to the (010) lattice planes [31,32]. α-MoO_3 is made up of corner-sharing chains of zig-zag MoO_6 octahedra linked together via covalent forces on the a-(1 0 0) and c-(0 0 1) axes (0 0 1) and weak van der Waals forces on the b-axis (0 1 0) (Fig:1.3) [33–35]. The pentavalent Mo^{5+} ions, which have a strong affinity for oxygen, are more abundant in α-MoO_3 because of their distinctive layered structure [36,37]. As a result, significant efforts have been undertaken to develop α-MoO_3 materials with attractive features for use in gas sensors, fuel cells, electrocatalysts, and optoelectronic devices by tailoring their dimensions, microstructures, morphologies, and even the components [38]. α-MoO_3-based gas sensors have recently been extensively researched for measuring the trace concentrations of harmful gases such as nitrogen dioxide, hydrogen, ethanol, carbon monoxide, ammonia, triethylamine, etc.[19,39–42]. Consequently, significant efforts are being made to enhance α-MoO_3's gas-sensing capability by integrating engineered nanostructures with tunable shapes, dimensions, and morphological characteristics. This has resulted in the development of nanostructured α-MoO_3 with zero-dimensional (0-D), one-dimensional (1-D), two-dimensional (2-D), and three-dimensional (3-D) morphologies, which have been synthesized using a variety of synthesis techniques such as thermal evaporation, hydrothermal, RF sputtering, sol-gel, Chemical vapor deposition, etc. [43–49]. Furthermore, due to its inherent structural anisotropy, α-MoO_3 has displayed numerous nanostructured morphologies; hence, in recent years, attempts have been made to improve the sensing responses and enable the sensor to work at low concentration by creating nanostructures that not only contain a high crystallinity along with high surface to volumes (S/V) ratio, such as nanobelts, nanorods, nanowires, nanoplates, nanosheets, nanotubes, and nanoflowers[50–52]. High S/V ratios allow analyte gas molecules to easily navigate into the sensor's surface, leading to faster response, improved detection limits, better sensitivity, and reduced power consumption. However, selectivity and operating temperature are still major issues for MoO_3-based sensing applications [53].

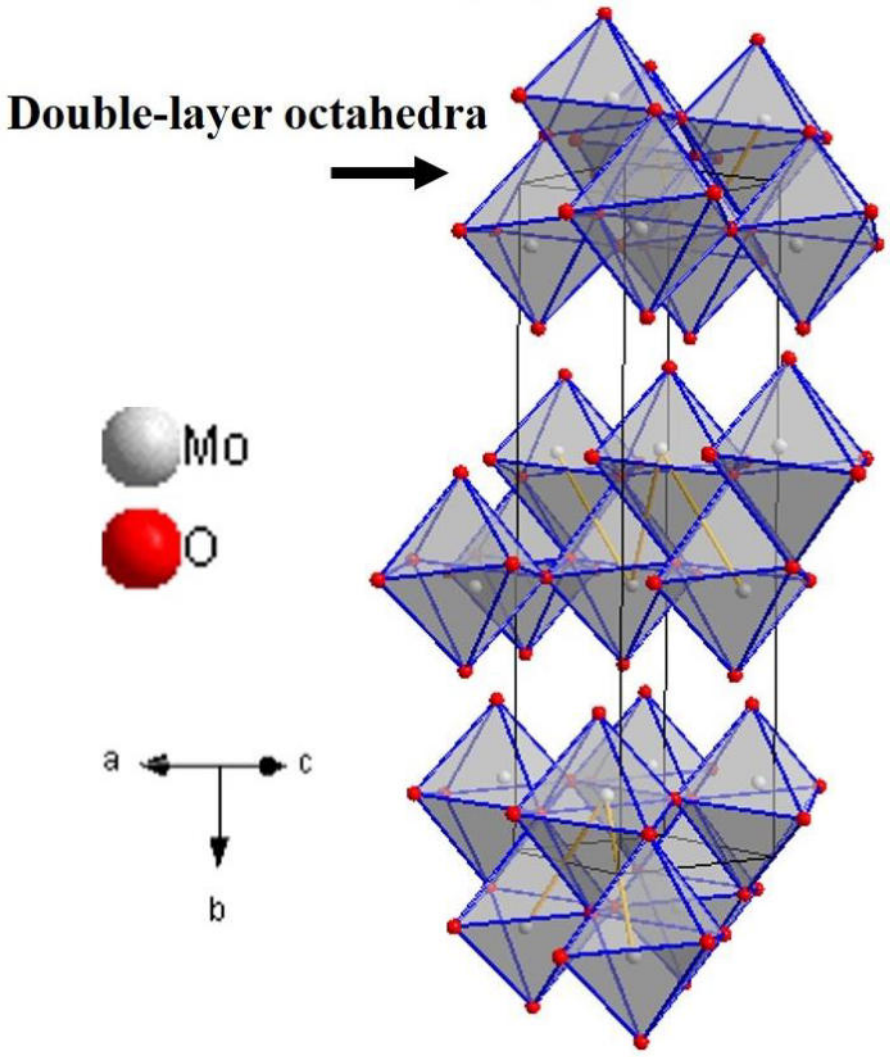

Figure 1.3 Schematic representation of orthorhombic molybdenum trioxide octahedra

The high S/V ratio of 1-D MoO_3 nanostructures has attracted considerable interest because of their rapid charge transfer along a single spatial dimension which ranges between1–100 nm [54–57]. The networked topology of 1-D nanostructure materials decreases agglomeration while allowing the passage of target gas molecules to the surface of the material [58]. The ability of ultralong 1-D structures to provide a straight transport channel for electrons propagating down the axis is well recognized, and this considerably improves gas sensing capability. Gas sensors developed from these 1-D nanostructures, on the other hand, have excellent sensitivity and rapid response times, as well as higher stability, lower operating temperatures, and lower power consumption [59,60]. Numerous one-dimensional nanostructures of MoO_3 have been used in gas sensors, including nanobelts, nanoribbons, nanorods, nanofibers, nanowires, and micro rods [29–31,42,48,53,59–62]. So, in this study we are studying the gas sensing characteristics of α-MoO_3 nanorods/composites towards various gases synthesized by physical vacuum thermal evaporation techniques and thereby fabricating highly efficient gas sensors with fast response/recovery along with low detections limits.

1.5 MXenes

Two-dimensional (2D) nanomaterials have become a hot topic ever since graphene was discovered in 2004 [63,64]. The reduction in dimension and size has resulted in many intriguing properties in 2D materials, which were not observed in their bulk counterparts. As a result, 2D materials hold tremendous hope for a wide range of applications from electronic/optoelectronic devices to electrochemical catalysis[65]. In the last few years, with great progress in models and simulations, more and more two-dimensional materials similar to graphene have been made[66]. Recently, a novel and a possibly substantial group of early transition metal carbides and/or carbonitrides called MXenes have been added to the universe of 2D materials [67,68]. Most MXenes are synthesized by etching the A layers out from MAX phases, which are ternary carbides or nitrides with the chemical formula $M_{n+1}AX_n$, where M is an early transition metal, A is a group IIIA or IVA element, X is C or N, and n= 1, 2, and 3. $M_{n+1}X_n$ layers are piled on top of each other to form hexagonal structures in MAX phases [69]. MAX phases have multilayer hexagonal structures with alternate $M_{n+1}X_n$ and A layers [70]. Since the M–X bonds are significantly more robust than the M–A bonds, the A layers may be chemically etched selectively without damaging the M–X bonds, leading to weakly bound $M_{n+1}X_n$ layers that are easily separated using sonication (Fig 1.4) [67]. MXene is the name given to the generated 2D materials to emphasize the absence of A layers from its parent MAX phase and its 2D character analogous with that of graphene. It should be noted that the surface of the $M_{n+1}X_n$ is always functionalized with chemical groups which include oxygen (-O), hydroxyl (–OH), or/and fluorine (–F) during the etching process[71]. As a result, the chemical formula for MXenes is $M_{n+1}X_nT_x$, where T_x denotes the functional groups on the surface [72]. On MXene surfaces, the proportions of various functional groups are unpredictable and vary depending on the etching method used.

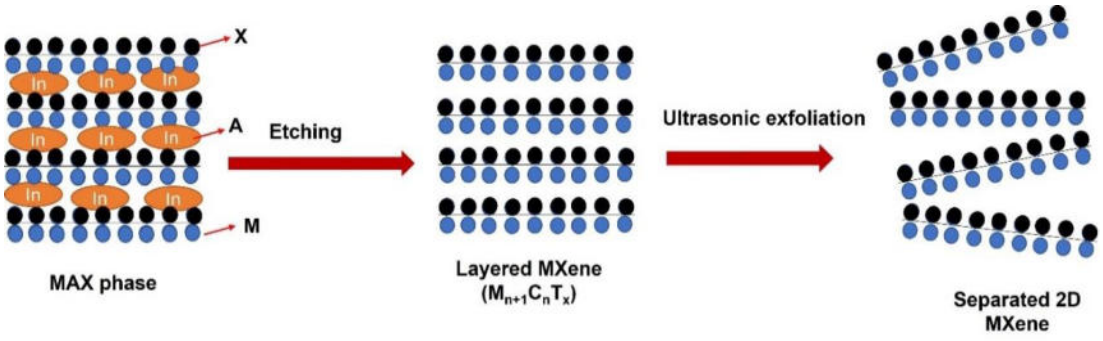

Figure 1.4 Schematic representation of synthesis of MXene form MAX phase.

MXenes have a wide range of interesting mechanical, electrical, magnetic, and electrochemical characteristics due to their tunable chemical properties. With their two-dimensional morphologies and layered structures, MXenes may easily form nanocomposite with other materials, allowing for the integration of the exceptional features of multiple

materials in a complementary approach. Since MXenes and composites based on them have gained substantial research attention, they hold tremendous potential for a wide range of applications. MXenes and MXene-based composites are primarily used in energy storage as high-efficiency electrodes for lithium–sulfur batteries, sodium–ion batteries, and supercapacitors, owing to their high conductivity and outstanding electrochemical activity[73–77]. Recently, they have risen to even greater prominence in disciplines that are connected to the environment, which is noteworthy. Particularly speaking, they have been utilized as effective catalysts or co-catalysts in electrocatalytic or photocatalytic water splitting and as photocatalyst in reduction of carbon dioxide (CO_2) [78–80]. Along with that , they have been used to remove pollutants from water, such as heavy metals, toxic organic dyes, eutrophic chemicals, and nuclear waste [81,82]. Furthermore, they have been employed in biosensors and gas sensors, where they have demonstrated outstanding performance[83–85]. Currently, worldwide emphasis is focused on energy and environmental challenges, which are both interdependent. Green, renewable energy sources, like the solar and wind, are increasingly being investigated in light of growing concerns about energy use and the environment [86,87]. The outputs of such renewable energy, on the other hand, are highly dependent on weather and climate conditions [88,89]. To ensure an effective supply of electricity, efficient and cheap energy conversion and storage systems like the water splitting as well as powerful light-weight batteries like metal-air batteries are required. With its higher energy density, easy manufacturing, and little environmental impact, hydrogen can be seen as a suitable replacement to limited fossil fuels. The electrocatalytic hydrogen evolution process (HER) from water splitting is among the most effective ways to generate hydrogen [90–93]. Hence utilization of efficient electrocatalysts is vital to the development of these technologies [94,95]. In general, noble metals with high catalytic activity, example platinum and ruthenium, are used in catalysis. However, due to a lack of reserves and high costs, the application on a broad scale has been severely constrained. As a result, the creation of highly efficient non-noble metal catalysts is critical for electrocatalysis applications [96,97]. The unique features of two-dimensional MXenes and MXene-based nanomaterials have recently caught the attention of researchers, who have begun to investigate these materials[92,93,98]. During electronic structure modification, the versatile chemical properties of MXenes is advantageous, and the distinct 2D layered structure gives a higher surface area thereby exposing the active sites to the greatest degree [99,100]. Furthermore, the high resistance to corrosion and hydrophilicity broaden the spectrum of applications as compared to carbon-based electrodes [101,102]. Because of their strong interactions with other materials and their ability to prevent nanomaterial aggregation, the functional groups in MXene nanosheets make it easier to assemble the hybrids and so improve their electronic properties [103–105]. In a

nutshell, MXenes have considerable potential as electrocatalysts and active materials in energy conversion processes.

1.6 Mo_2CT_x MXene

Since the electrochemical hydrogen evolution reaction (HER) and oxygen evolution reaction (OER) activities of Mo_2CT_x and $Ti_3C_2T_x$ were first reported in 2016, the number of reports of MXene-related water splitting and metal-air batteries has been increasing rapidly[106,107]. Among all MXenes, $Mo_{n+1}C_nT_x$, with n = 1,2 and 3, have received considerable attention as prospective HER electrocatalytic materials as they are stable in both acidic and alkaline electrolytes, an electronic structure similar to Pt, and excellent hydrogen adsorption capacity[108–111]. In general, electrochemical stability and hydrogen Gibbs free energy (ΔG_{H^*}) are two important criteria for the HER performance of the various catalysts, and the ideal value of ΔG_{H^*} is zero, which is directly connected to the complexities on the surface and strain from the outside [112]. Mo_2CO_2 has a better ΔG_{H^*} (-0.69 eV), resulting in good HER activity for an O-terminated MXene [113]. With the help of the theoretical and practical results of several metal elements, it was confirmed that Mo_2CT_x is one of the best HER catalysts [107]. When it comes to the synthesis of MXenes, HF etching is perhaps the most common way to do it. For this reason, it is essential to find eco-friendly and less harmful alternatives. Even though various groups reported proposed several alternatives like hydrothermal method, alkali treatment, and electrochemical methods[114–116] for an HF-free MXene synthesis, the research is still not adequate to address the problem. Furthermore, according to first-principles calculations, Mo_2InC is most likely to exfoliate into 2D Mo_2CT_x MXenes, which are not unexplored yet [117]. So, we propose an HF-free UV-assisted phosphoric acid etching for the synthesis of Mo_2CT_x MXene from Mo-In-C MAX phase.

MXene is viewed as a potential sensing element with a large number of active sites of gas adsorption due to its many functional groups on the surface, relatively high surface area, high porosity, and high conductivity [118]. Hydrophilicity at the surface of MXenes also beneficial for the sensing, which is caused by terminal groups like hydroxyl (-OH) ions, oxygen (-O) ions, fluorine (-F) ions, and chlorine (-Cl) ions that are present on their surfaces (referred to as "T") [119]. Because of its superior metallic conductivity as well as carrier mobility, MXene can achieve quick charge transport under low temperature circumstances, resulting in an improved gas response at room temperature [120]. The most interesting thing about the investigated MXenes as well as respective nanocomposite sensors is that they exhibited the greatest performance towards during the detection of various gases/volatile organic compounds/humidity at room temperature, which makes them ideal for real-time sensing [118]. Among the MXenes, $Ti_3C_2T_x$ is perhaps the most studied for various applications such as gas detection [121]. However, only a few research have been done on other MXenes like

$V_4C_3T_x$, Mo_2CT_x, Mo_2C, V_2CT_x, Ti_2CT_x, and Sc_2CO_2 for the detection of various gases, VOC's or humidity [122–126].

Detecting carbon dioxide (CO_2) is essential in a multitude of sectors, including renewable energy, agriculture, food, health care, and the chemical sector. Carbon dioxide (CO_2) makes up most the world's greenhouse gas emissions. The greenhouse gases in the atmosphere have impacted negatively on the ecosphere because of the massive amount of CO_2 emissions. A variety of CO_2 sensors with diverse structural configurations have been employed for this purpose [127–130]. Due to several constraints such as higher operating temperatures, inadequate detection limits, and longer response and recovery times, the present CO_2 sensors cannot achieve the desired performance for practical applications [131–134]. So, in this study we are investigating the gas sensing properties of Mo_2CT_x MXene for the fabrication of improved CO_2 sensors for the real-life applications as well.

1.7 Gas sensors

Sensor is an electronic device that turn physical quantities into signals that may be analyzed in response to specified measurements. These include gas sensors, which detect gases in a specific region and are frequently employed as part of safety systems to detect signals from physical conditions and chemical substances. Air around us contains a variety of gases that could be harmful to human health, pollute the air or be important to or medical process or industry. As a result, the ability to detect these gases is critical. A gas sensor has two parts: a transducer as well as an active layer that converts data into another electronic signal, such as frequency change, current change, or voltage change, so that the sensor can show something is happening. Many types of gas sensors, such as semiconducting, electrochemical, optical, catalytic, and acoustic gas sensors, are being utilized to detect various types of gases.

All sensors have a set of characteristics that determine how they perform, and these include things like selectivity, sensitivity, limit of detection, response, and recovery times. The small size, low power consumption, and wireless capabilities of the sensor also prove to be very beneficial to users [135]. A resistive-type gas sensor's sensing elements are often made of composite/hybrid materials grouped as base and catalyst, with each playing a role in improving sensing performance. In most cases, the high surface area and conductivity provided by base materials are what allow gas molecules to be adsorb and travel between electrodes. Graphene reduced graphene oxide, graphene 3D as well as two-dimensional transition metal dichalcogenides (TMDCs) are all in this category. On the other hand, nanostructured metal/metal oxide catalysts (NSs) are employed to increase the rate of the reaction on the sensor surface for the target gas. [136].

Because of the benefits such as ease of fabrication, low cost, high sensor response, and fast response/recovery times, nanostructured metal oxide gas sensors have received a great

deal of attention in recent decades. MOS chemical sensors have improved the commercial viability of gas sensors for toxic gas detection and air quality management applications due to their inherent and outstanding material features. A MOS sensor operates on the idea of chemiresistance, which is the variation in electrical properties (conductivity or resistivity) of nanostructures because of interaction with a target gas. In other words, when gas molecules interact with metal oxides, they either function as donors or acceptors of electrons or holes (Receptor function), and the resistance of the metal oxide changes because of the interaction (Transduction function). The resistance change is mostly attributed to presence of oxygen ions in the bulk or superficial area of the material.

MOs gas sensors detect oxidizing or reducing gases through the variation in resistivity of the sensing material due to the interactions of electrons in the conduction band with these targeted gas molecules. The metal oxide sensors' resistance increases or decreases depending on which majority carriers in the semiconducting layer and the type of gas molecules (oxidizing or reducing) in the surrounding atmosphere. In the case of n-type sensor materials, exposure to an oxidizing gas (acceptor) increases the resistance of sensor, whilst a reducing gas (donor) decrease the resistance, and the opposite is happening for p-type materials. The chemiresistive behavior of metal oxide gas sensors is described by the principle of receptor function (REDOX), which is combined with the transduction performance of the sensor [137].

The chemiresistance feature of metal oxides can be correlated to the width of the space charge area generated on the crystallites as a result of the transfer of electrons during the adsorption and desorption of gas molecules. It is the width of the space charge region that functions as a potential barrier in the conduction process between the grains, causing variations in the Fermi level. Because of the process of electron production and annihilation in the conduction band, band bending is observed and thereby the modulations in the Fermi level. During the interaction of an oxidizing gas with an n-type material, the band bends upward due to the depletion of electrons, while the band bends downward due to the accumulation of electrons occurs during the interaction of a reducing gas with an n-type material. The direct relationship between space charge region and band bending may be deduced as follows: the carrier concentrations in the grain, which in turn depend on the size and shape of the grain, determine the band bending in the space charge area [137].

Oxygen ionic species that have been chemisorbed onto oxide materials are influenced greatly by the operating temperature (T) as shown in the equations (1.1-1.4).

$$O_{2(gas)} \leftrightarrow O_{2(ads)} \quad (1.1)$$

$$O_{2(ads)} + e^- \leftrightarrow {O_2}^-_{(ads)} \ (< 100\ ℃) \quad (1.2)$$

$${O_2}^-_{(ads)} + e^- \leftrightarrow 2{O}^-_{(ads)} \ (100 - 300\ ℃) \quad (1.3)$$

$${O}^-_{(ads)} + e^- \leftrightarrow {O^{2-}}_{(ads)} \ (> 300\ ℃) \quad (1.4)$$

Since the discovery of gas sensors using ZnO thin films by Seiyama et al. in1960s, many metal oxides were effectively studied for the development of gas sensors. Metal oxide sensors can be classified into two main categories based on their sensing behaviors: n-type and p-type metal oxides gas sensors. The resistance of n-type metal oxides typically decreases in the presence of reducing gases like H_2, H_2S, CO, CH_4, NH_3, as well as volatile organic compounds (VOCs). And in case of oxidizing gases (such as O_3, SO_2, NO_2, NO, etc.), resistance decreases. P-type metal oxides, on the other hand, behave in the opposite way[138,139]. WO_3, MoO_3, SnO_2, TiO_2, Nb_2O_5, ZnO, and other n- and p-type metal oxides have been extensively researched for potential gas sensing applications towards reducing as well as oxidizing gases [140–144]. Nanomaterials have experienced a resurgence in recent years, credit goes to the development of technology and methods. There were various accomplishments in the preparation of nanostructured metal oxides, such as nanoparticles, nanorods, nanosheets, nanowires, nanofibers, nanoflowers, and nanocages, through the techniques such as hydrothermal method, thermal evaporation, sol-gel method, etc. The large specific areas and higher active surface states of nanostructured metal oxides are said to stem in potential gas sensing abilities. To be more specific, the crystalline ZnO nanowires demonstrated a sensor response of 15 toward 0.5 ppm NO_2 at an operating temperature of 225 °C [145]. The sensors based on WO_3 nanoparticles, SnO_2 nanowires, TiO_2 nanotubes, and In_2O_3, have been discovered to react positively to nitrogen dioxide, formaldehyde, hydrogen sulfide, and carbon monoxide [146–148].

Using a heterojunction created by combining a metal oxide with some other (similar) metal oxide, it is possible to improve the gas detecting performance of the sensors discussed above. The bridging between the major phase of one metal oxide and to the second phase of some other semiconductor was described as the heterojunction within that sensing material when this occurred [149]. The reports demonstrate that the surface area of the hybrid nanostructure is greater, and the alteration of potential barrier or accumulating layer in composite effectively improves gas sensing performance. These high-performance metal oxide heterojunction sensors are becoming more and more renowned among researchers [150–152]. It is easier for the gas molecules to get through the activation barrier when heat or light is applied. This improves the sensor's ability to detect gas. The requirement of a high operating temperature is the primary obstacle in the development of MOs sensors [153–155].

1.8 Hydrogen evolution reaction

For renewable energies to be more widely used in the energy market and in the chemical industry, it is necessary to store electricity as chemical fuel. Hydrogen (H_2), that is essential for the manufacture of ammonia (NH_3) by the Haber–Bosch process, the manufacture of steel and aluminum, and for CO_2 conversion, appears to be the appropriate fuel and has attracted a lot of attention in recent years. However, the reforming of fossil fuels, which currently accounts for over 95% of current hydrogen generation, produces CO_2. Water electrolysis, a cleaner alternative to chloro-alkali process, now accounts for only 4% of total H_2 generation, but this understanding is driving us to improve the production from the electrolysis quickly. With the dropping cost of renewable energy (using wind turbines or photovoltaics), water electrolysis could be used to produce economical and sustainable H_2. One of the most significant obstacles to increasing the utilization of electrolysis of water in the H_2 production percentage is the poor efficiency of this process, as well as the scarcity of cheap and reliable catalysts for said hydrogen evolution reaction (HER) and the oxygen evolution reaction (OER) [156]. Electrocatalysis has been dominated by the HER since its invention in 1789, and its simplicity and lack of side reactions have made it the most studied reaction. For a long time, researchers focused their efforts on figuring out how the physical features of metallic surfaces affect HER dynamics from a material standpoint. This extensive research has helped scientists better grasp the molecular composition of the catalyst surface and their connection to HER activity. After discovering that a shift from acid to alkaline pH substantially alters the kinetics of the HER, researchers have recently rekindled their interest for studying the underlying mechanisms of HER activity in an effort to better understand how its catalytic site interacts with the electrolyte. Recent studies have raised questions about the role of dynamics and solvent structure and at the electrode–electrolyte interface, the potential of reactants, and how spectator-additives are used in the HER kinetics. These questions are at the rim of the research field [152,157–159].

Hydrogen evolution reaction (HER) is now the most extensively studied and discussed cathodic reaction in terms of kinetics. Even if water electrolysis isn't the most cost-effective technique of producing hydrogen, it yields hydrogen that is extremely pure and does not pollute the environment. The reaction involved can be summarized as follows,

$$2H_2O_{(l)} \rightleftharpoons 2H_{2(g)} + O_{2(g)} \quad (1.5)$$

Which includes a cathodic hydrogen evolution,

$$2H_2O + 2e^- \rightleftharpoons 2OH^- + H_2 \quad \text{(Alkaline)} \quad (1.6)$$

or

$$H^+ + 2e^- \rightleftharpoons \frac{1}{2}H_2 \quad \text{(Acidic)} \quad (1.7)$$

along with an anodic oxygen evolution reaction,

$$4OH^- - 4e^- \rightleftharpoons 2H_2O + O_2 \quad \text{(Alkaline)} \quad (1.8)$$

or

$$H_2O - 2e^- \rightleftharpoons \frac{1}{2}O_2 + 2H^+ \quad \text{(Acidic)} \quad (1.9)$$

For water electrolysis in acidic solution equilibrium potential can be represented as in the equations 1.10 and 1.11:

$$E_c = E^0_{H_2} + \frac{RT}{F}\ln\frac{a_{H^+}}{a^{1/2}_{H_2}} \quad (10)$$

$$E_a = E^0_{H_2} + \frac{RT}{F}\ln\frac{a_{H^+}}{a^{1/2}_{H_2}} \quad (11)$$

When tested in acidic solutions, the standard potentials for reactions (1.8) and (1.9) are $\boldsymbol{E^0_{H_2}} = -0.828\ V\ and\ \boldsymbol{E^0_{O_2}} = 0.401\ V$ versus normal hydrogen electrode (NHE) at 25 °C. The reversible voltage for equation (1.10) therefore becomes, $\boldsymbol{E^0_{H_2}}$ = 1.229 V, at 25 °C which is equal to the energy ΔG^0 = -2F (-$\boldsymbol{E^0_{H_2}}$) = 237.2 kJmol^{-1} [91,160,161].

The most widely accepted pathway for hydrogen evolution involves the Volmer reaction, as shown in Equation (1.12), accompanied by either the Heyrovsky or Tafel reactions, as shown in Equations (13) and (14).

$$\boldsymbol{H^+ + e^- + M \leftrightarrows MH_{ads}} \quad \textbf{(1.12)}$$

$$\boldsymbol{MH_{ads} + H^+ + e^- \leftrightarrows M + H_2} \quad \textbf{(1.13)}$$

$$\boldsymbol{2MH_{ads} \leftrightarrows 2M + H_2} \quad \textbf{(1.14)}$$

Hydroxide ions (OH^-) and adsorbed hydrogen atoms (H_{ads}.) are formed when molecules of water get reduced in alkaline environment.

H_{ads} denotes the hydrogen atoms that have been adsorbed on the surface of the electrode, H^+ denotes the hydrated proton, H_2 is the hydrogen molecule, e denotes the electron and M is the active sites in this equation. In the very first scenario, hydrogen atoms generated from molecular hydrogen by the Tafel reaction get anodically oxidized by the Volmer reaction. The Heyrovsky reaction is involved in the synthesis of H_{ads} in the Volmer–Heyrovsky pathway, and H_{ads} gets oxidized first by the Volmer and then by Heyrovsky reactions. The anodic oxidation of molecular hydrogen will only be possible if the electrode that is being stirred by molecular hydrogen has the same electrode/solution difference as the hydrogen electrode in the very same electrolyte. In acid electrolytes, only a few ranges of electrode materials, namely the platinum metals, gold, and their alloys, can meet this criterion of performance. Electrocatalysts for low-temperature hydrogen/oxygen fuel cells can be made

from them. For the cathodic evolution of H_2, on the other hand, there is no such restriction. If the potential difference between the electrodes is sufficiently negative compared to the hydrogen electrode, the reaction will occur on either electrode. Because of this, more research has been done on the kinetics of hydrogen evolution than on the kinetics of hydrogen dissolution [161].

It is important to note that electrode material has a significant impact on HER kinetics. For example, a mercury (Hg) electrode has relatively slow reaction rates, whereas a HER on platinum is among the quickest electrocatalytic processes currently known. Notably, the kinetics is subject to parameter variables such as the electrolyte's composition or the crystallinity or orientations of the electrodes [156]. Conway and Tilak provided a model to determine the surface coverage related with hydrogen underpotential deposition and defined the variation in the Tafel slope associated with various mechanisms [162]. It should be noted that the related model has been created under standard conditions, in which hydrogen adsorption follows a straightforward isothermal behavior. However, in the complicated circumstances of materials that are electroactive where there are some active sites which are localized, and the mechanism of HER is not straightforward, such models perhaps cannot be utilized in a direct way. It is also crucial to measure the turnover frequency (TOF) in order to determine the electrocatalytic activity, however, it is difficult to obtain a reliable value for a sophisticated system like the HER electrocatalysis[163].

The pseudocapacitive nature of the electrode materials (electrocatalyst) is a critical feature of the HER activity since hydrogen should normally get adsorbed on to the electrocatalytic surface well before HER. In a sense, nearly all viable HER electrocatalysts are excellent pseudo capacitors in the region of hydrogen adsorption. An excellent pseudo capacitor ought to have the highest possible efficiency, which means that all the hydrogen adsorbed should be desorbed during the reverse scan. Hydrogen adsorbed should then returned to the electrolyte in the energy storage unit of pseudo capacitors, but the hydrogen evolution reaction (HER) is continuation of the irreversible reaction in which the overaccumulation of adsorbed hydrogen leads in the hydrogen evolution [164].

Since the high price of noble metal electrode materials like Pt is the major barrier to HER activity, the principal interest is on the prospect of discovering cheap electrocatalysts. The inefficiency of the method (rather than the high cost) is the primary reason why just 4 % of the H_2 generated by water electrolysis gets used. The electricity costs associated with an industrial electrolysis of water are significantly higher than the costs associated with using noble metal electrocatalysts [165]. The electrocatalyst morphology is important because HER is entirely based on a continuum of surface processes. Even though Pt is a very well-defined and simple electrocatalyst, surface morphology still plays a big role in how well HER works. Along with the physical structure, the chemical structure is critical and as conventional method

certain Pt atoms are replaced with the less expensive transition metal having similar chemical properties**,** to minimize the cost.

The catalytic performance is governed by the free energy of H adsorption for HER, as per the volcano plot. As a result, according to this theory, no pure metal (apart from a few noble metals) can effectively **e**lectrocatalyst the HER. As a result, the only way to use inexpensive metals in the HER electrocatalysis process is to alloy various metals to include distinct metals having weak and strong hydrogen bonding. In this scenario, two kinds of metal hydride bonds can develop, one strong to support H adsorption and one weak to support H_2 formation. Most scientists believe that H adsorption begins on the metal that has formed an intense M-H bond and that the H adsorbed can migrate through the metal's surface through surface diffusion. The weak M-H connection can be disrupted, resulting in the creation of a hydrogen molecule (H_2), which escapes from the electrode surface and enters the surrounding environment. Also accomplished through the application of noble metals, the addition of some other metal with a different size modifies the lattice structure, which can result in the formation of active sites for electrocatalysis when combined with noble metals. Although corrosion is less probable in the HER potential zone when compared to anodic potentials, where metal oxides assist in the electrolysis of metals, electrochemical instabilities can be a severe concern for active electrocatalysts in the potential region of HER**.** Studies on active metal alloys for HER are primarily concerned with increasing the active sites and improving the electrochemical stability [165]. In addition, the investigation of metallic alloy electrocatalysts may be of relevance in the creation of other forms of electrocatalysts focused on transition metal complexes, which are now being investigated. Anions like P are now being included into the composite structure as a result of the alloying techniques employed. Anion-containing alloys and their equivalent transition metal compounds have several characteristics in common [164]. Metal carbides are noteworthy because the carbon atoms occupy the interstitial lattice positions of the metal matrix (transition metals of the groups IVB-VIB). Consequently, the electronic properties of this family of materials renders them equivalent in electro-catalytic activity of the platinum like noble metals [166].

1.9 Antecedents

1.9.1 *α-MoO_3 nanorods for gas sensing application*

Chemical and physical techniques, as well as a combination of both, are used to make MoO_3 nanorods. Chemical vapor deposition[167], hydrothermal technique[168], solgel method [169], sputtering [9], electro deposition[170], and other methods were used in the bulk synthesis. Most of the literature focuses on the hydrothermal synthesis of MoO_3 nanorods [171–173]. The magnetic characteristics of MoO_3 nanorods generated by hydrothermal technique employing molybdic acid were investigated by Zhakharova *et al.* [174]. In current

electronics, however, a high degree of purity, homogeneity, and reproducibility of MoO_3 is required for mass industrial production, which chemical processes such as hydrothermal procedures cannot achieve. To solve this challenge, physical deposition techniques alone or a mix of physical and chemical procedures can be used. J. Zhou *et al.* employed a vacuum deposition approach to make MoO_3 nanorods on a silicon substrate, reporting the synthesis of aligned rods on a MoO_3 nanorods on silicon substrate by vacuum deposition by heating the Mo boat itself [175] . Whereas Rahmani *et al*. employed vacuum thermal evaporation to deposit and describe the gas sensing characteristics of lamellar MoO_3 films produced on quartz substrates and evaluated the gas sensing properties substrate [176] . Navas *et al.* reported on the synthesis of MoO_3 nanorods based on RF sputtering and investigated the fluctuation of characteristics as a function of annealing temperature [9]. There were just a few studies on the synthesis of aligned MoO_3 nanorods by physical thermal evaporation techniques for use in gas sensing[177].

To sense gases, 1-D α-MoO_3 nanostructures have been used by many research groups [178,179]. L. Chen *et al.* reported NO_2 sensor using α-MoO_3 nanorods utilizing ultrasonic synthesis, and studied the effect of chlorination on the response [180]. Yang *et al.* used hydrothermal synthesis of α-MoO_3 nanoribbons at ambient temperature for hydrogen detection at greater concentrations (1000 ppm) and the response time was 14 s [181]. When Yang and his team used a hydrothermal method to make α-MoO_3 nanobelts, they could detect Tri-methyl Amine (TMA) at a concentration of 1 ppm with a quick response time[182]. Research study by Wang *et al.* designed a MoO_3 sensor with an amorphous-crystalline core at operating at 180 °C was able to detect the presence of 500 ppm ethanol [183]. Nanobelts made of α-MoO_3 have been synthesized and used in sensing by L. Cai *et al.* [184]. Rahmani *et al.* investigated the gas detection properties of MoO_3 at 250 ^oC towards the sensing of NO_2 and H_2 [176]. Utilizing infrared irradiation method, nanorods made of molybdenum trioxide were made by E. Comini *et al.* and studied the detection of ethanol and CO at 500 °C [39]. Kumar *et al.* demonstrated that h-MoO_3 is capable of detecting ammonia at 200 ° C [185]. Ammonia can be detected at room temperature with a range of materials, but they all had lower detection responses. For example, binary nanocomposites of polyaniline/copper ferrite and graphene nanoribbons (GNR) were used, as well as cellulose/TiO_2/PANI and cellulose/TiO_2/PANI/$SnTiO_2$@rGO/CNT [36–38]

The recent surge in CO_2 emissions has concerned the scientists due to the environmental damage they are causing, such as global warming [190]. The largest CO_2 emissions are caused by the combustion of fossil fuels in commercial vehicles and electric motors [191]. CO_2 is detected using a range of sensors that incorporate catalytic, electrochemical, infrared, and semiconductor materials [192–195]. Nanostructured metal oxide-based (MOS) sensors are widely known among these devices for their improved gas

sensing behavior in terms of gas selectivity, as well as their improved detection abilities due to their chemical sensitivity and thermal stability [7-9]. MOS work by sensing the resistance change of an electric current or current when the target gas enters its surface[196]. Various MOS, such as ZnO, $LaFeO_3$, CuO, $FeYO_3$, $NiCo_2O_4$/r-GO, WO_3/SnO_2, , SnO_2, CdO, La_2O_3, TiO_2, $BaZrO_3$, and others, were studied for CO_2 detection by various groups [8-27]. Because of its huge bandgap (3.2 eV) and unusual electrical characteristics, nanocrystalline molybdenum trioxide (MoO_3), an n-type MOS, possesses remarkable sensing capabilities in this context [214]. For example, Yu *et al.* [215] investigated nanocomposite α-MoO_3/ZnO sensors operating at 270 ° C along with the monitoring of H_2S gas for concentrations ranging from 500 ppm to 100 ppm. Yang *et al.* [216] investigated the gas sensing effect of ethanol on MoO_3 nanobelts as well as the effects of Zn doping on the material. At a concentration of 1000 ppm of ethanol and a temperature of 240 °C, the best response, 326, was found. The development of a trimethylamine gas sensor based on flower-like α-MoO_3 reported by Sui *et al.* [217]. They tested sensitivities ranging between 5 ppm and 100 ppm at a temperature from 250 °C to 370 °C. The detection of CO_2 with a MoO_3-based gas sensor, on the other hand, has received little attention. The construction of potentiometric CO_2 sensors with increased operating temperatures (500 °C) and faster response/recovery times (16 s/22 s) using Li_2CO_3 and MoO_3 electrodes were reported by Wang *et al.* [210]. According to the existing literature [32], the use of porous silicon (pSi) in gas detection has enhanced gas sensor performance by widening the operating range (concentration and working temperatures) and sensing response. This improved performance is attributed to the increased surface area and high surface-to-volume ratio caused by the porosity of the silicon [218,219]. Several studies on porous silicon-based gas sensors for the detection of hydrogen, oxygen, water molecules, propanol, and so on [220] have previously been reported, utilizing the above-mentioned properties of porous silicon. However, in comparison to other gases, investigations on carbon dioxide sensing using porous silicon-based sensors were sparse, and there were very few published studies on hybrid porous-silicon/MoO_3 (pSi/MoO_3) gas sensors, as per the literature review [211].

1.9.2 Mo_2CT_x MXene for electrochemical hydrogen evolution reaction (HER) and gas sensing applications.

1.9.2.1 Mo_2CT_x for HER application:

Molybdenum carbide exhibits catalytic activity like that of platinum. Li *et al.* developed a Nitrogen and phosphorous co-doped carbon/RGO shell to be placed above a core of Mo_2C with such a fine architecture to protect the core from corrosion. The electrocatalyst produced because of this research was able to give enhanced performance, which was nearly

as good as that of the conventional Pt/C electrocatalyst. This synthesis technique is difficult to scale up, even though the manufacturing procedure was straightforward (a $H_2PMo_{12}O_{40}$-polypyrrole/RGO nanocomposite was utilized, and both polymerization and reduction were induced by the $H_3PMo_{12}O_{40}$), and the results were promising. But that was one of the first findings to demonstrate that the optimal HER electrocatalytic activity of Pt/C can be achieved with affordable materials, which is a significant step forward [221,222].

MXenes are emerging as a promising substitute for other 2D materials in several fields, including production of energy, energy storage, biomedical applications, and many others [71,223]. 2D Mo_2CT_x is a member of the family of MXene, that is presently being extensively researched due to its ability to be used in a wide range of applications, ranging from fuel cells to biosensors[224,225]. MXenes are being synthesized using non-MAX parent phases to use them in a variety of applications, including electrochemistry [226]. Mo_2CT_x MXenes are typically synthesized by etching the A layer of the parent MAX phase with highly toxic hydrogen fluoride (HF) [227]. Mei *et al.* proposed an HF-free UV-assisted, less toxic phosphoric acid etching of Mo_2GaC for the development of 2D-Mo_2C MXene for electrochemical applications [228]. Even after modelling of Khazaei *et al.* [10] predicting indium based Mo_2InC as the simplest MAX phase for the fabrication of Mo_2CT_x, majority of results published were centered on Al, Ga, Sn or Si as the "A" layer, with no publications on MAX phases with indium as the A layer.

The availability of a large number of active sites as a consequence of increased surface area and ability to accelerate the charging kinetics due to high conductivity makes MXenes appropriate for HER applications as an electrocatalyst [229]. Until now there are more than 30 types of MXenes are synthesized experimentally and even more proposed theoretically such as $Ti_4N_3T_x$, Lu_2CT_x, V_2CT_x, $Ti_3C_2T_x$, $Nb_4C_3T_x$, Zr_3C_2, Mo_2CT_x, $Nb_4C_3T_x$, $Mo_2TiC_2T_x$, $Ti_2(CN)$-T_x, etc.,[81,82,121,230–234]. Among these, molybdenum-based MXenes are now getting rapid attention and extensively studied as an electrocatalyst for HER applications because of their exhibition of long-term stability, electronic properties equivalent to Pt electrode, and enhanced hydrogen absorption capability[235–238].

Various reports on the HER incorporating Mo_2CT_x MXene electrodes are coming from around the globe with improved performance. For instance, Tan *et al.* reported the fabrication of $MoSe_2$-Mo_2CT_x composite electrode for the hydrogen evolution in acid 0.5M H_2SO_4 electrolyte with an overpotential of -108.3 mV at 10 $mA.cm^{-2}$ of current density [239]. While Wang et al. demonstrated the assembly of cobalt decorated Mo_2C spheres for HER with an overpotential of -139 mV at 10 $mA.cm^{-2}$ in the acidic 0.5 $mol.L^{-1}$ H_2SO_4 electrolyte [240]. The study of hydrogen evolution, oxygen evolution, and overall water splitting was reported by Liu et al. with an overpotential of -78 mV at 10 $mA.cm^{-2}$ for HER in basic 1M KOH electrolyte using CoP/Mo_2C electrode [241]. Tang *et al.* studied the HER performance of the

phosphorous doped Mo_2C MXene in both 0.5 M H_2SO_4 acidic and 1M KOH basic electrolytes with overpotentials 172 and 219 mV at 10 $mA.cm^{-2}$ current density [242]. All these reports were using Mo_2C MXene prepared via conventional HF etched method, which is highly toxic and causes a huge impact on the environment during the preparation. Therefore, we report the fabrication of Mo_2CT_x MXene via simple HF free ultraviolet light assisted phosphoric acid etching for HER application in the acidic electrolyte with lower overpotential and Tafel slopes. Along with that, we studied the effect of synthesis temperature of the non-MAX phase in the electrocatalytic performance of Mo_2C MXene electrodes.

1.9.2.2 Mo_2CT_x for gas sensing application:

Existing CO_2 gas sensors mainly use infrared-based detection, comprised of sophisticated electronics and detectors, which are bulky and high-power consuming, making them unreliable in real life. In contrast, there are some reports on chemical resistive type sensors, which work on the principle of measuring the change in resistance on the exposure of target gas which is simple in design and consumes less power[243]. Generally, semiconducting metal oxide such as ZnO, SnO_2, MoO_3, V_2O_5, CdO, WO_3, etc., and perovskite nanomaterials are considered as potential gas sensing materials [11–18]. However, they possess some disadvantages such as low-limit detection, high power consumption for high working temperatures, etc., which limits their efficiency and reliability. Besides, 2D nanomaterials such as graphene, transition metal dichalcogenides, phosphorene, black phosphorous, and MXenes are considered for gas detection because of their large surface-to-volume ratio, the abundance of reaction sites for gas adsorption, and exhibition of layer dependent electrical properties [83,120,247–249]. Among these materials, MXenes are a new class of 2D materials that are more suitable candidates for this application owing to their metallic electronic conductivity and hydrophilic nature[250]. They have a general formula $M_{n+1}X_nT_x$, where M can be any early transition metal, X = carbon or nitrogen or the both, and T_x = -F, -O or -OH functional group attached during the etching from a parent MAX phase, where A= group III or IV elements[67,71]. The gas sensing properties of MXene are one of the least explored areas as they are only in their emerging stages. Lee *et al.* reported the ammonia sensing using hybrid fibres of $Ti_3C_2T_x$ MXene/graphene with a response of 6.6% at a concentration of 50 ppm at room temperature with the longer response and recovery times in the order of several minutes [251]. Naqvi *et al.* reported the theoretical interpretation of the absorption mechanism of M_2NT_x (M=Ti, V) MXenes for various air pollutant gases with the help of first-principle calculations using DFT [125], whereas Yuvan *et al.* demonstrate the sensing of flexible sensors using the 3D MXene framework for detecting volatile organic compounds at lower concentrations[252]. The majority of the sensors were using titanium-based $Ti_3C_2T_x$ MXenes as the sensing materials[253–256]. Additionally, various other MXenes such as Sc_2CO_2 and

V_2CT_x were also attempted for the gas sensing application of various VOCs and pollutant gases[123,126]. Although Ti-based MXenes have been widely utilized, Mo-based Mo_2CT_x MXenes exhibit superior conductivity along with higher chemical activity compared to Ti-based MXenes, which can expediate gas adsorption and thereby improve the sensing performance[83,107]. For instance, the selective detection of toluene from various volatile organic compounds (VOCs) such as benzene, acetone, ethanol, etc., using Mo_2CT_x was reported by Guo *et al*.[124]. Nevertheless, to the best of our knowledge, only one report was there with CO_2 gas detection by Zhou *et al.* using a sophisticated nitrogen-doped $Ti_3C_2T_x$ MXene/polyethyleneimine composite with longer response and recovery (8.8-9 mins), which may result inadequate for real-time monitoring [257]. For the commercial application, there is a need for compact, low power consuming highly sensitive CO_2 gas sensors with fast response recovery.

The gas sensing detection limit can be enhanced by the introduction of porous silicon as substrates with high surface-to-volume ratios[258]. Several groups reported the fabrication of porous silicon-based sensors for the detection of various organic solvents, H_2, O_2, NH_3, humidity, etc. [259,260]. Even though there exist a few reports on porous silicon-based sensors for the detection of CO_2[211], no reports are there on porous silicon/MXene sensors to the best of our knowledge.

2. SCIENTIFIC OUTCOME

"Synthesis of 2D Mo_2CT_x MXene from Mo-In-C non-MAX phase via HF free etching route make it useful for its application in electrochemical hydrogen evolution and gas sensing. In addition to this study, the fabrication of gas sensors using 1D molybdenum trioxide exhibit better stability, repeatability, and sensitivity along with low limits of detection even at room temperature for real-life applications."

3. HYPOTHESIS

The deposition of one-dimensional nanostructures of Molybdenum trioxide by the means of physical deposition techniques on suitable substrate material enhances gas sensing mechanism. The intercalated two-dimensional Molybdenum based MXenes derived from suitable MAX phases expedite the synthesis for their application in electrochemical hydrogen evolution and gas sensing.

4. GENERAL OBJECTIVE

To synthesize one dimensional Molybdenum trioxides nanorods and two dimensional MXene nanostructures via chemical as well as physical methods with less environmental impact for their application in electrochemical hydrogen evolution and gas sensing.

5. SPECIFIC OBJECTIVE

- To prepare 1D Molybdenum oxide (MoO_3) using hydrothermal method.
- To deposit as synthesized 1D and 2D nanostructures on various substrate materials via thermal evaporation by varying different synthesis parameters like temperature of the substrate, annealing temperature etc.
- To do structural, morphological, compositional, and electrochemical characterizations using XRD, SEM/FESEM, TEM, Raman spectroscopy, EDX, LSV, and EIS.
- To prepare Mo_2InC MAX phase through solid state reaction.
- To prepare the Mo_2CTx MXene by exfoliating and etching the MAX (Mo_2InC) phases.
- To prepare electrodes to study hydrogen evolution using electrochemical workstation.
- To do gas sensing studies of synthesized 1D and 2D nano structures.

6. EXPERIMENTAL TECHNIQUES AND THEORETICAL ASPECTS.

This chapter explains the synthesis and characterization techniques used for the synthesis of one-dimensional molybdenum trioxide nanorods (α-MoO_3) and two-dimensional molybdenum carbide (Mo_2CT_x) MXene nanostructures. In the synthesis part, we explain the basics of the techniques and conditions used for the preparation of the samples. Whereas the characterization part discusses the theory behind each instrument and the parameters used for obtaining the results.

6.1 Synthesis of 1D α-MoO_3 nanorods and 2D Mo_2CT_x MXene.

6.1.1 Hydrothermal method for the synthesis of nanostructures.

A hydrothermal method is a type of reaction that utilizes water as the primary reaction medium in a special closed container (Parr bomb) to produce a high-pressure reaction environment (Fig 6.1). Under these circumstances, a material that is normally insoluble or only slightly soluble is dissolved and re-crystallized. Fig 6.2 depicts the basic hydrothermal method preparation steps.

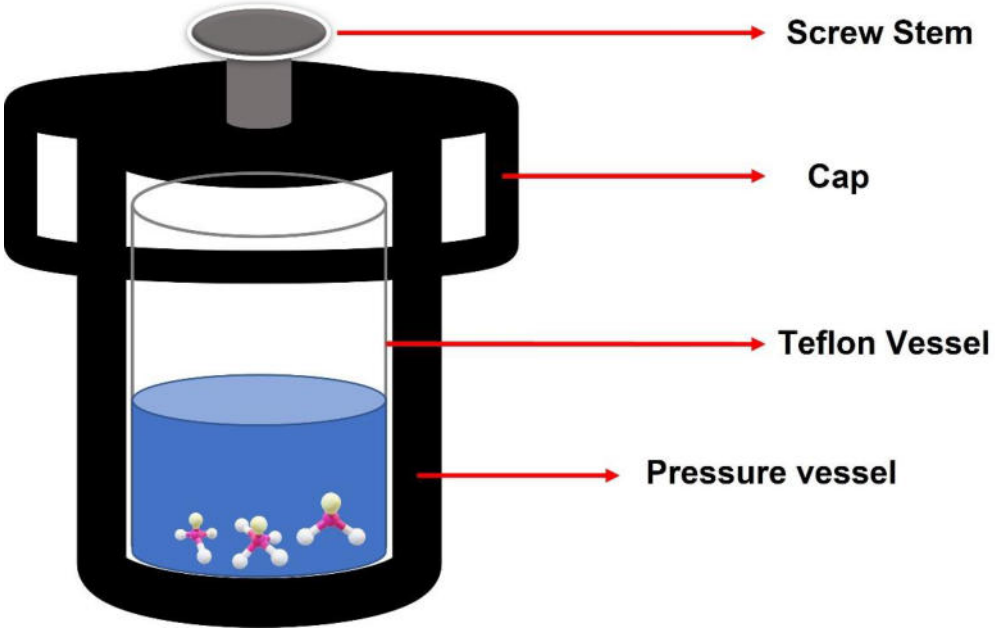

Figure 6.1 Schematic representation of parr bomb for hydrothermal synthesis

The following are the major stages in the growth of crystals in hydrothermal treatment: The reactants are first dispersed in one hydrothermal medium and then pass the solution as ionic species or molecular groups. Second, the difference in temperature between both the upper

and lower parts of the kettle separate the ions or molecules. Then, ions/ molecular groups are relocated to the region of low temperature, where the seed crystal grows to produce a supersaturated solution. Besides that, at the growth interface, ionic entities/ molecular groups are adsorbed, disintegrated, and desorbed. As a fourth step, the adsorbed material starts to move at the interface between the two materials. Crystallization of the dissolved matter is the final step. Crystal growth conditions have a significant impact on the morphology of hydrothermal crystals [14].

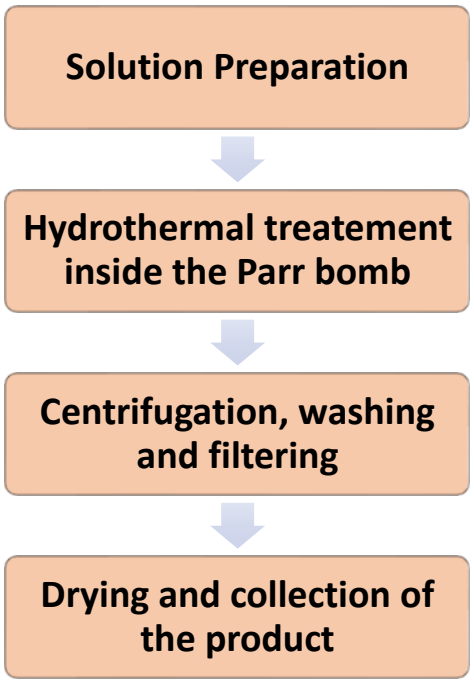

Figure 6.2 Steps involved in a hydrothermal method of synthesis.

6.1.2 Hydrothermal synthesis of α-MoO_3 nanorods.

For the synthesis of α-MoO_3 nanorods, we followed the hydrothermal route using sodium molybdate ($Na_2MoO_4.2H_2O$; Sigma Aldrich, >99%), hydrochloric acid (HCl; Merk, 37 %), and distilled water as the precursors. $Na_2MoO_4.2H_2O$ and HCl were used in a 1:5 molar ratio to synthesize MoO_3. For that, 2.129 g of sodium molybdate was added to 40 ml of distilled water and stirred using a magnetic stirrer for 40 minutes. The dropwise addition of 4 ml of HCl to the solution was done during this period. A light bluish solution was obtained after 40 minutes of stirring. This solution was immediately transferred to a Teflon beaker and then to a steel Parr Bomb reactor for the hydrothermal reaction inside a hot air oven. The reaction time for the hydrothermal synthesis was varied from 160 to 200 °C for 2 hours. After the reaction inside the hot air oven, the dark bluish solution was collected and washed several times in ethanol and distilled water to remove the unreacted HCl via centrifugation at 4000 rpm for 15-20 min. The thick slurry was collected after washing which was dried at 60 °C overnight to get

the powdered MoO_3. To improve the crystallinity and oxidation of the obtained MoO_3 powder, thermal annealing at 350 ^oC was performed. The schematic representation of the hydrothermal synthesis of MoO_3 is as shown in Fig 6.3. After annealing light bluish powder was collected and stored in a vacuum desiccator for further characterizations.

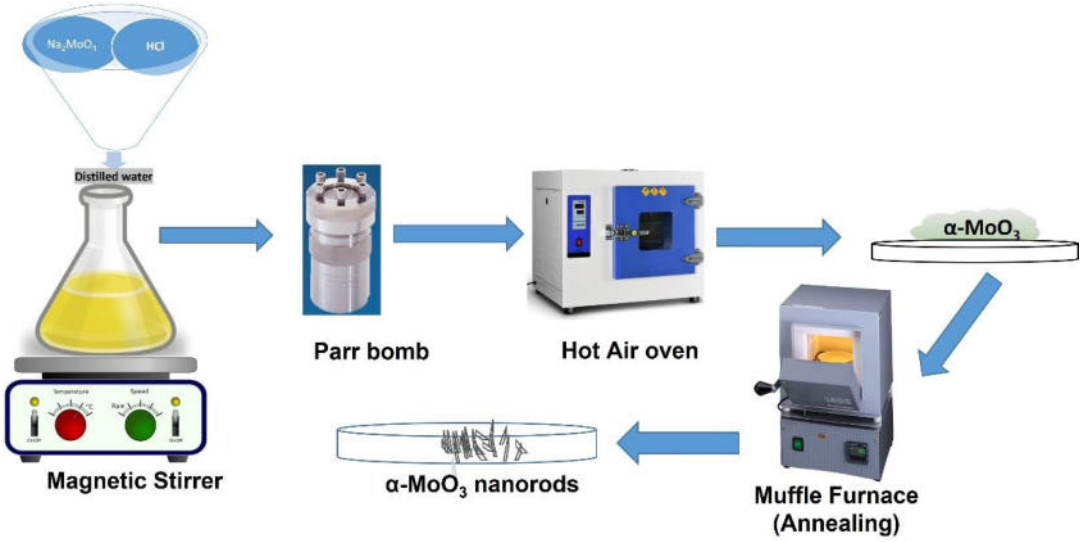

Figure 6.3 The hydrothermal production of MoO_3 nanorods is depicted in this schematic diagram.

6.1.3 Vacuum thermal evaporation technique for the synthesis of 1D nanostructures

When it comes to depositing elemental films, nothing beats evaporation, which is one of the simple and reliable deposition methods available today. System components include an evaporation source that causes the precursor material to evaporate and a substrate that is placed at a proper distance from the source used for the evaporation. Typically, the source as well as substrate are both contained within a vacuum chamber. The substrate platform can be heated, biased electrically, or rotated during deposition. To generate the preferred vapor pressure of precursor, it is only necessary to heat it to high temperatures, and it is simple to control the concentration of depositing material in the gaseous phase by varying both source temperature and gas flux from the carrier gas source. Figure:6.4 depicts a schematic representation of a typical evaporation system.

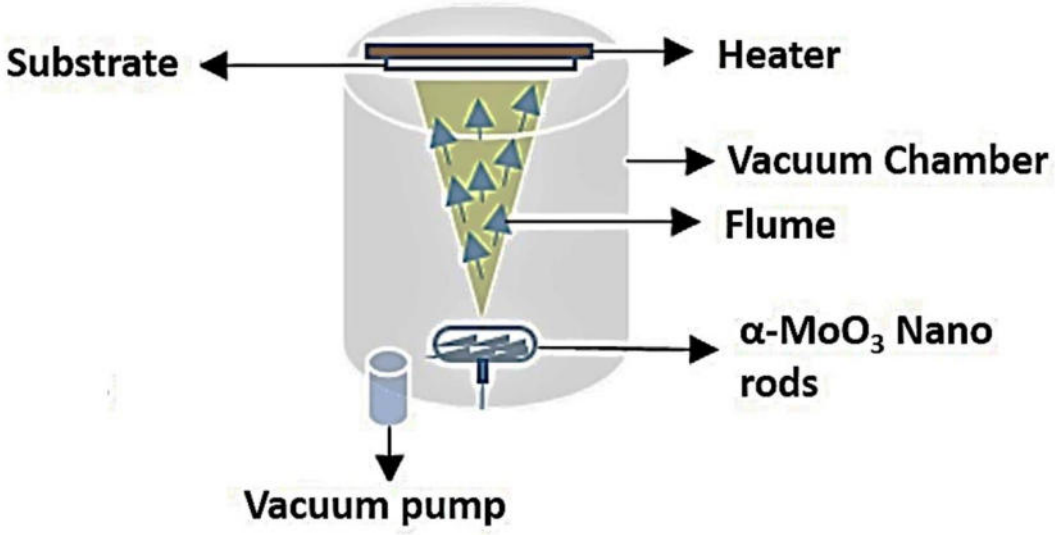

Figure 6.4 Schematic representation of vacuum thermal evaporation chamber.

The evaporation of thin films is typically carried out at relatively low pressure (10^{-3} to 10^{-10} torr) so that atoms, as well as molecules in the gaseous form, do not collide with one another before reaching the growing surface because the mean free path is indeed very long relative to the distance between the source and the substrate. Since atoms or molecules can easily move from the source to the substrate, the conformal coverage is weak and an even film across a vast region is difficult to create. For this reason, some alternative arrangements were developed, including (I) use of multiple point sources other than a single source, (II) putting both sources and substrates on the surface of a sphere, (III) substrates under rotation, and (IV) or a combination of all the above techniques.

6.1.4 Deposition of aligned α-MoO_3 nanorods on various substrates using vacuum thermal evaporation.

For the deposition of the α-MoO_3 nanorods on various substrate materials, we adopted a physical deposition route using thermal evaporation was used with α-MoO_3 nanorod powder as the precursor. For that ~100 mg of α-MoO_3 nanorods in powder form obtained after hydrothermal synthesis was evaporated from a molybdenum boat inside a box-type vacuum chamber as shown in Figure 6.5 The distance between the source and the substrate was kept at 17 cm inside the chamber. The pressure inside the chamber was kept at a base pressure of 1 x 10^{-3} Pa with help of turbomolecular pumps through at the deposition. The evaporation rate was fixed at 10 kÅ/s during the deposition which was continuously monitored using a crystal thickness monitor. The thickness of the obtained nanorod film deposited on the glass substrate was measured in the range of 150-200 nm using the thickness monitor. The temperature of the substrate was kept at a temperature of 250 ^{o}C using a substrate heater After deposition, the as-deposited films were annealed in a muffle furnace for 1-hour varying temperatures from (100

to 400 °C). The schematic representation of the deposition of the nanorods is as shown in figure 6.6.

Figure 6.5: Vacuum thermal evaporation unit used for the deposition of the nanorods.

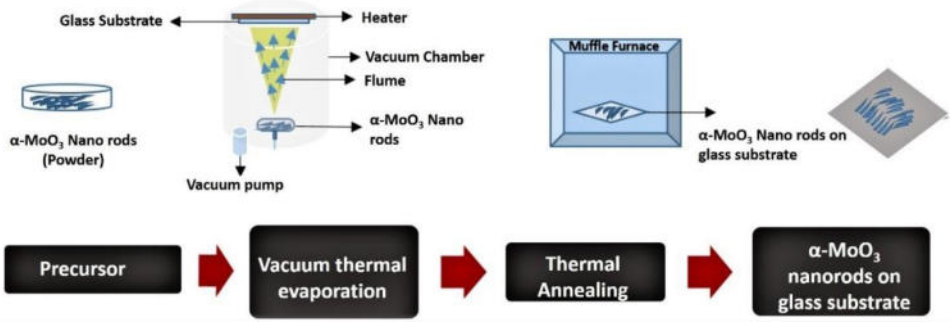

Figure 6.6 Schematic representation of the deposition of MoO_3 nanorods on the substrate.

6.1.5 Solid-state reaction method for the synthesis of MAX phase.

Solid-state synthesis, also known as the ceramic method, is a common technique for inducing a chemical reaction in solid starting materials that results in the formation of a new solid with a clearly defined structure. Finished products usually involve single crystals, polycrystalline

materials, glasses, and thin-film materials, all of which are widely used in energy and electronic applications, as well as other fields. It is necessary to combine fine-grain metal compounds and pelletize them before heating them at controlled conditions of temperature for a specific period. Several metal substances, including metal oxides or salts, involve extreme conditions to activate reactions in a super-heated flux or quickly condensing vapor phase. These conditions include high temperatures and pressures, among other things. This method of chemistry is referred to as "shake and bake" or "heat and beat" chemistry in some circles. In solid-state synthesis, it's crucial to know how fast the reaction is going. Solid-state reactions should be carried out to completion due to the lack of effective methods for purifying the solids that are formed. Reaction conditions affect how quickly the solid-state reaction happens. These include things like how the reactants are made, how they move, and what kind of reaction they're having. In the final materials, the chemical pathways and preparation techniques have a significant impact on their chemical and physical properties.

6.1.6 Synthesis of Mo-In-C non-MAX phase and Mo_2CT_x MXene

Mo_2CT_x was synthesized using Mo-In-C non-MAX phase synthesized via HF-free etching method. Mo_2C bulk powder (99.5 %; Sigma Aldrich) and indium powder (In, 99.9 %; Sigma Aldrich) are blended in a mortar and pestle at a molecular weight ratio of 1:5 for 40 minutes until a homogenous mixture is achieved for the preparation of Mo-In-C non-MAX phase. A tube furnace with constant Argon flow was used to calcinate the combination, which was done in an inert environment at different synthesis temperatures ranging from 850 to 1100 °C for a total reaction time of 2 hours. To eliminate the unreacted In particles, the solid material was submerged in concentrated hydrochloric acid (37%; Sigma Aldrich) for 24 hours. After removing excess HCl and unreacted In from the obtained slurry by washing it several times in distilled water, the obtained powder was etched under ultraviolet light in phosphoric acid for 24 hours to etch out the In from the Mo-In-C MAX phase. The solution was then washed multiple times with distilled water until the pH reached 6 to eliminate the phosphoric acid from it using centrifugation at 4000 rpm for 15 mins. Followed by the above process, the obtained slurry was exfoliated using an ultrasonic bath for 6 hours to obtain layered Mo_2CT_x MXene with -O terminated groups in deionized water which is as shown in the figure. The reaction time was also varied to study the changes in the structure and morphology from 2 hours to 10 hours in steps of 2 hours. The schematic representation of the synthesis process is as shown in Figure 6.7.

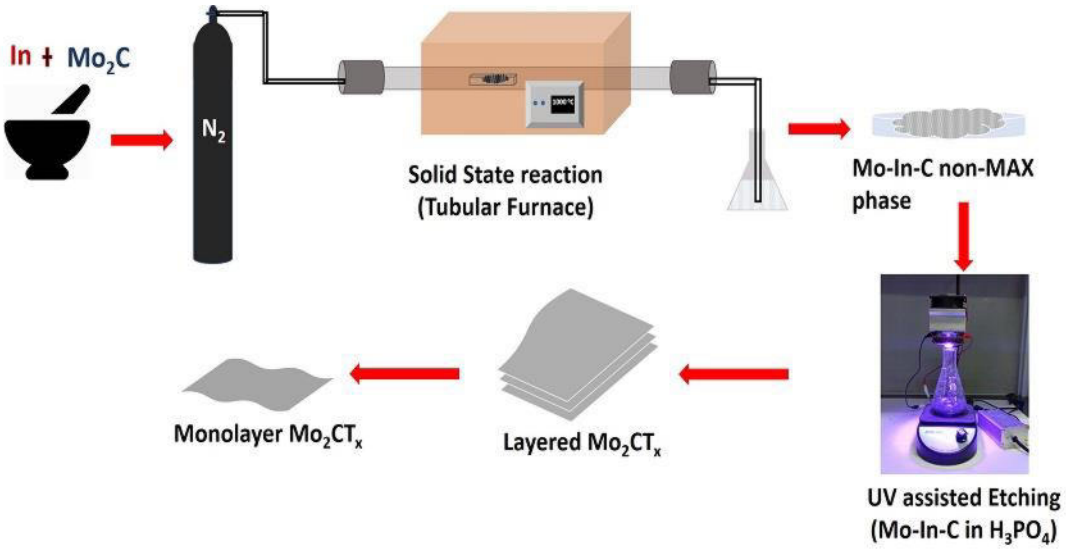

Figure 6.7 Schematic representation of the Mo_2CT_x MXene from Mo-In-C non-MAX phase.

6.2 Characterization of 1D α-MoO_3 nanorods and 2D Mo_2CT_x MXene

6.2.1 X-ray diffraction used to characterize the structure.

For the study of crystalline structure and atomic spacing, X-ray diffraction has been a widely used technique over the years. X-ray diffraction is a technique that relies on the constructive interference of monochromatic X-rays with a crystalline material to produce a pattern. To generate monochromatic radiation, cathode ray tubes are used, which must then be paralleled to concentrate the radiation and point toward the sample. When the incident rays interact with the specimen, constructive interference (as well as a ray of diffraction) is produced, according to Bragg's law:

$$n\lambda = 2d \sin\theta \qquad (6.1)$$

where n is an integer, λ is the wavelength of X-ray, d is the interplanar spacing that creates the diffraction, and θ is the diffraction angle.

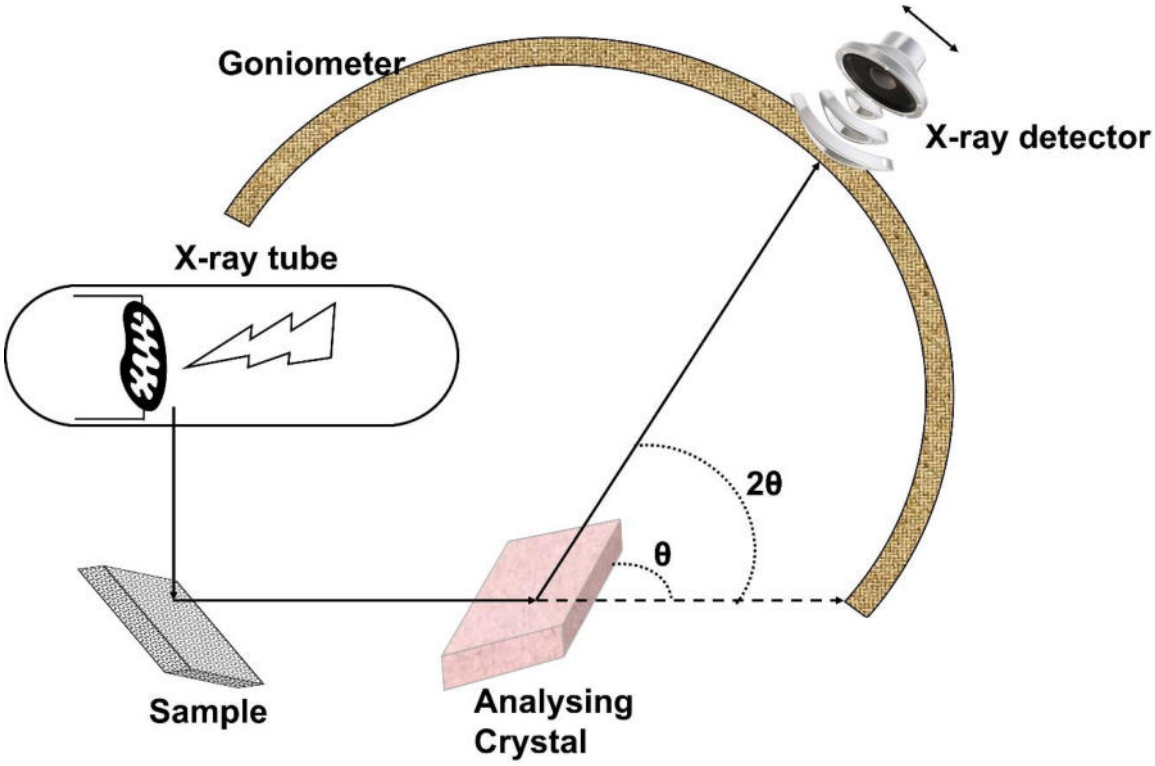

Figure 6.8 Schematic representation of X-ray diffraction equipment.

This law describes the relationship between electromagnetic wavelength and the angle of diffraction as well as lattice spacing inside a crystalline sample. The detected, processed, and counted X-rays are then used to determine the distance between the two points. Due to the different orientations of the powdered material, all probable diffraction peaks should be determined by scanning at different 2θ angles (Figure 6.8). To identify the compound, the diffraction peaks can be converted to d-spacings, wherein every compound has its unique d-spaces. Most of the time, this is accomplished through the comparison of the d-spacings with conventional reference patterns.

Experiments with X-ray diffractometers are conducted using three fundamental components: an excitation tube, a sample holding device, as well as an X-ray detector (Connolly, 2007). With the use of an X-ray tube, the electrons are produced by irradiating a heating element and pushed towards the direction of target by providing a voltage, causing a bombardment with electrons. As soon as electrons achieve enough energy to expel inner shell electrons within a target material, intrinsic X-ray spectra are formed. These spectra are made up of many components, with K_α and K_β the most prominent ones. K_α is formed by two components: $K_{\alpha1}$ and $K_{\alpha2}$. $K_{\alpha1}$ has a shorter wavelength and double the intensity of $K_{\alpha2}$, whereas $K_{\alpha2}$ has a comparatively longer wavelength and half the intensity of K_α. The wavelengths are characterized depending upon the target material (Cu, Fe, Mo, Cr). Diffraction demands monochromatic X-rays, which can only be produced using filters such as foils or crystal monochromators. Because $K_{\alpha1}$ and $K_{\alpha2}$ have sufficiently similar wavelengths, a

calculated average of the two is employed instead of a single value. Cu- K_α radiation D 1.5418 Å is used commonly as the target material for single-crystal diffraction. A collimator directs these X-rays to the sample. The intensity of reflected X-rays is measured as the specimen and detector rotate. When the incident X-rays impinging on the sample satisfy Bragg's law, constructive interference occurs, resulting in the appearance of a peak in intensity. In this case, the X-ray signal is recorded and processed by a detector, which further converts the signals to count rates, which is then transmitted to a device like a desktop computer. Two things make an X-ray diffractometer work. The sample moves in the path of collimated X-ray beams at an angle θ, and the detector moves on an axis to capture the diffracted X-rays. A goniometer is an instrument that is used to manage the angle and spin the sample [261].

The use of X-ray diffraction to determine the average size of nano nanocrystals within nano crystalline bulk counterparts is a simple method. Paul Scherrer [262] was the first scientist to publish his findings in a publication in 1918 which became renowned as the Scherrer formula. The average crystallite size, L, is calculated using the well-known Scherrer formula:

$$L = \frac{K\lambda}{\beta cos\theta} \qquad (6.2)$$

where, λ is the wavelength (nm) of the X-ray used, β is the full width at half maximum in radians obtained from the XRD peaks (highest peak) and K is a constant which takes the values 0.9 normally is related to the shape of the crystallite. The limitation of Scherrer formula is that, when the d value is small and 2θ value is big, the crystallite size calculated are generally higher than the actual value. This is because β cos θ value cannot be fixed as a constant. To overcome this, modified Scherrer formula is formulated by Monshi et al. [263], which is a logarithmic approach of equation. 6.2 as shown in the Equation.6.4. When ln β is plotted against ln (1/cos θ), the intercept gives ln K/λ L, from which a specific value of L can be found using the least squares approach.

Scherrer formula (Equation.6.2) can be written as,

$$\beta = \frac{K\lambda}{L\,cos\theta} = \frac{K\lambda}{L} \times \frac{1}{cos\theta} \qquad (6.3)$$

Taking logarithm on both sides, Eqn. 2.3 becomes,

$$\ln\beta = \ln\frac{K\lambda}{L} + \ln\frac{1}{cos\theta} \qquad (6.4)$$

The XRD characterization of the *1D* α-MoO_3 nanorods was done using PANlytical X'pert PRO High-resolution X-ray diffractometer equipped with Cu-Kα (λ=1.584 nm). The measurements were done by collecting the data for the 2θ values between 10° to 90° at a scan rate of 5°/minute. For the 2D Mo_2CT_x MXene, it was done between 5° to 100° at a scan rate of 5°/minute.

6.2.2 Vibrational study using Raman Spectroscopy

Raman scattering is a type of spectroscopy that works well with infrared absorption spectroscopy. The method involves flashing a monochromatic source of light (like a laser) onto a specimen and detecting the light that is being scattered Figure:6.9a. Because of the clear pattern of bands in a Raman spectrum, the technique can be used for a wide range of analyses without requiring a comprehensive understanding of the effect. The pattern of bands, for example, can be used to identify a specific molecule in situ, and it may even be feasible to estimate the quantity of the component present. It is expected that most of the dispersed light will go through the specimen without interfering with the sample. The detector will get the energy that is of the frequency equal to the source. This is called elastic scattering or Rayleigh scattering. A very small percentage of the scattered light (less than one in 107 of the total) has its energy shifted away from the laser frequency. This is referred to as the Raman or Stokes shift. It is common practice to disregard and filter out the weaker anti-Stokes-shifted Raman energies because they are weaker at ambient temperature. This occurs because of interactions between both the vibrational energy levels of the sample molecules and the incident electromagnetic waves. Therefore, the molecule's electric field is perturbed because of the interaction. When shown at the molecular level of energy (Figure 6.9b), the Rayleigh scattering and the Stokes shift are depicted by arrows of varying lengths, indicating the difference in energy between the incident as well as scattered photons [264,265].

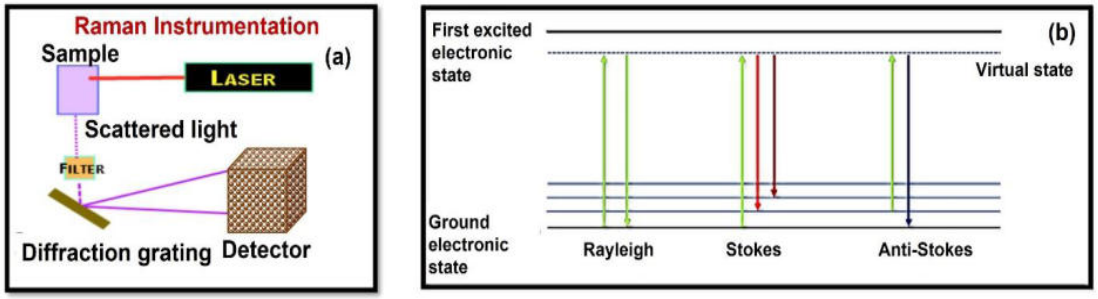

Figure 6.9 Schematic representation of (a)Raman spectroscopy instrument and (b) the Raman lines.

Using a 780 nm laser excitation source mounted on a Thermo Scientific Raman Spectrometer, we measured the vibrational characteristics of the fabricated 1D α-MoO_3 nanorod films.

6.2.3 Field emission Scanning microscopy and Transmission electron microscopy for morphology analysis.

The scanning electron microscope (SEM) scans the surfaces of a sample with a focused electron beam. Because the primary electrons, or the electrons in the beam, interact

with the material, they generate many signals that can be utilized to create images of the sample's topography and composition, which are then analyzed. When a primary electron penetrates a material, it usually travels a predetermined distance before coming into touch with a secondary electron. Upon colliding with this particle, the main electron takes on a different route, which is referred to as scattering in physics terms. The penetration of the beam of an electron into the specimen, as well as the subsequent scattering events, result in the creation of a reaction vessel in the shape of a teardrop (Figure 6.10). Secondary electrons (SE) are being produced whenever the primary electrons extract the specimen electrons from their bonds with the specimen electrons. They can't escape from the reaction vessel because they have insufficient energy. So, the Secondary electrons detected in SEM come entirely from the surface or area near-surface of the material, and not from any other location. In the deeper regions of the reaction vessel, the SE produced is absorbed by the samples. Because of the minimal depth of origin of the observed SE, they are particularly well suited for delivering high-resolution topographical data [266].

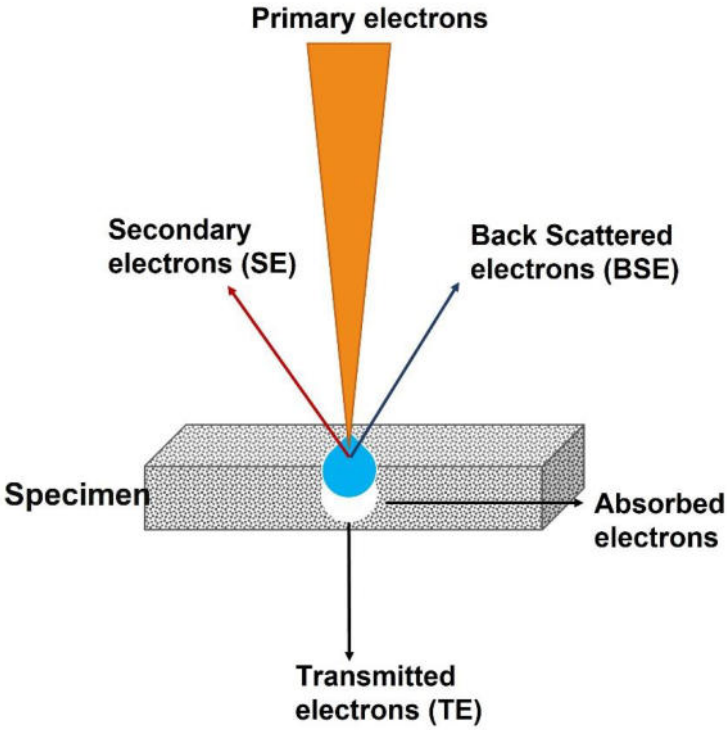

Figure 6.10 Schematic representation of the basic principles of electron microscopic imaging.

i. Field emission scanning electron microscope (FESEM)

A field emission gun (FEG) is used in place of the more common tungsten hairpin or LaB_6 filaments to accomplish high-resolution field emission scanning electron microscopy (FESEM) (Figure:6.11a). Under ideal conditions, a resolution of 0.5 nm was already obtained, and at 30 kV using conducting materials, a resolution of 5 nm is frequently achieved with conducting materials. By applying a powerful electric field to single-crystalline tungsten with a needle-shaped tip, a beam of electrons with an exceptionally high current density is produced. Field emission guns are used to produce this electron beam. When compared to the traditional thermal emission cannon, this one requires an extremely high vacuum (10^{-10} Torr). As a result of the extremely small size of the electron emission source and the large electron density is obtained in comparison to the other types of electron guns. The FEG is popularly known as the "high brightness gun." When combined with the significantly narrow range of generated electron energies better than the thermal emission guns, high resolution at lower kilovolts can be achieved without sacrificing performance [267].

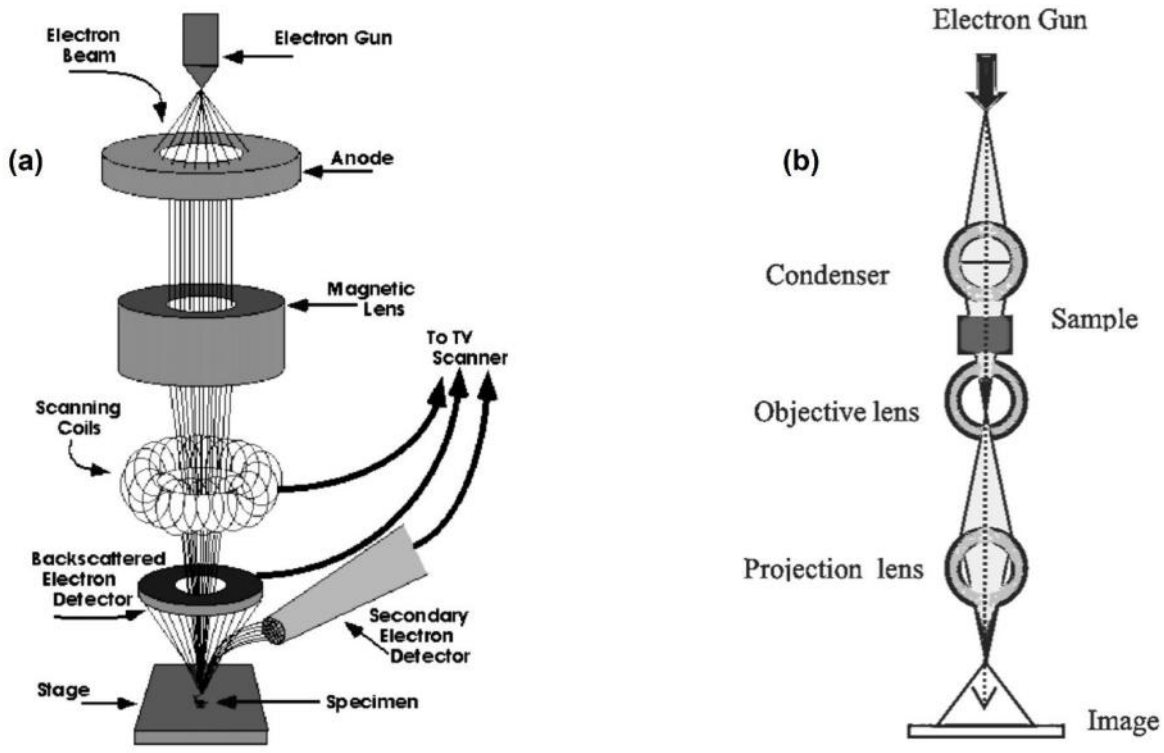

Figure 6.11 Schematic representation of (a) FESEM and (b) TEM instrumentation.

ii. Transmission electron microscopy (TEM)

The transmission electron microscope (TEM) is considered as a tool, artifact, or instrument designed specifically for the analysis and imaging of samples or samples given within the dimensions provided from micro-size (1 mm) and nano-size (1 nanometer). TEM consists

of an electron source called a gun or electron cannon that usually has a V-shaped filament made of tungsten or LaB6 (lanthanum hexaboride). An electric potential that is positive to the anode is then applied to the filament (cathode), which heats up until an electron current with a wavelength determined by the De Broglie equation (Equation 6.5) is generated (Figure6.11b).

$$\lambda = \frac{h}{\left[2m_0V\left(1+\frac{eV}{2m_0c^2}\right)\right]^{1/2}} \quad (6.5)$$

where, h= Planck's constant; m_0 = residual mass of the electron; e = electric charge; V = potential difference and c= speed of light.

Coherence of light is improved by an aperture and the condenser lenses before it reaches a sample, so the waves remain along the same path with a fixed phase difference. Following that, the electron beam strikes the sample, causing several processes to occur, some of which include dispersing the electrons that are affecting the sample to minimize energy loss (elastic) and others in which electrons transfer a part of the energy to inner electrons of the specimen (inelastic). The objective lens is next, and its job is to focus the beams scattered to create the first image through a diffraction process carried out by the projection lens, which extends the beam of electrons and reflects it on the phosphor display [268,269].

The approach for the preparation of self-supported samples begins with the slenderization of the sample; for this process, sheets of 100 and 200 nm thickness are obtained, and from these sheets, a disc of 3 mm in diameter is cut; this disc is polished using various methods such as chemical, electrochemical, ion bombardment, or ultramicrotomy to achieve a thickness in the range of a few microns. A copper grid is commonly used to hold the supported samples. This procedure is carried out by fragmenting the sample in an agate mortar, disintegrating it in a solvent such as ethanol solvent or acetone, depositing the solution on a grid, allowing the solvent to evaporate, and then introducing the sample under a microscope [270].

Selected Area Electron Diffraction (SAED) is a technique that can be used with S/TEM to look at the electron diffraction pattern that the electron beam makes when it interacts with the sample atoms. This pattern can reveal the crystallinity, crystal structure, lattice parameters as well as orientation of the specimen. When the size and location of the selected area aperture are chosen correctly, diffraction information from a certain area of the specimen can be gathered. Each set of originally parallel beams intersects in the rear focus plane of the microscope after being bent by the magnetic lens of the instrument, resulting in the diffraction pattern. The transmitted beams come together exactly at the optical axis. The diffracted beams interfere at a specific distance from the optical axis (equivalent to the interplanar spacing between the planes diffracting the beam) and at a certain angle (in accordance with the crystal

plane orientation diffracting the beams). This enables for the formation of bright spot patterns that is characteristic of SAED[271].

The way the diffraction image looks varies depending on how the beam is diffracted either by single crystal or by several different crystallites, like in a polycrystalline material. The single-crystalline diffractogram shows a pattern of bright spots in a regular way. This pattern is a two-dimensional representation of the reciprocal crystal lattice. If there are more crystallites, the diffraction pattern looks like a mix of the diffraction patterns of each one. Diffraction spots from all possible crystalline planes can be found in this superposition. A diffraction patterns of concentric rings is what happens because of two things:

1. A beam that meets the diffraction criterion can only make diffraction spots at certain distances from the beam that was sent through it.
2. Crystallographic planes can be in any orientation, so diffraction spots are constructed around the beam as it moves through it.

High-resolution transmission electron microscopy (HRTEM) is a type of imaging that can be done with specialized transmission electron microscopes. It lets you see the atomic structure of samples right away. It is a very good way to look at the properties of materials at the atomic level, like semiconductors, metals, nanoparticles, and sp2-bonded carbon, and how they behave. In the HRTEM, image formation occurs in two steps. Electrons that are incoming or incident interact with the specimen's atoms via both elastic as well as inelastic scattering processes. The electron wavefunction exiting the specimen's surface is then passed through the electron microscope's objective lens and successive magnifying lenses to generate the final magnified image [272]. HRTEM imaging is like transmission electron microscopy (TEM) imaging, with the exception that the magnifications utilized are high enough to easily observe the lattice spacing of inorganic materials (usually on the order of several angstroms).

6.2.4 Elemental characterization using X-ray Photoelectron Spectroscopy (XPS)

X-ray photoelectron spectroscopy (XPS) is a surface-sensitive analysis tool wherein X-rays bombard on the surface of a sample and the kinetic energy of the electrons released is recorded. The surface sensitivity of this approach, as well as its capacity to unveil information about the chemical state from the elements present in the sample, are two of the most important properties that distinguish it as an analytical tool. With the use of soft X-rays (with energies lower than 6 keV), the sample surface is irradiated, and the corresponding kinetic energies of the released electrons are measured. XPS is a technique for studying the structure of materials. For the emitted photoelectron to be produced, the x-ray energy must be transferred completely to a core level electron. This is theoretically stated in the equation (6.6):

$$h\nu = BE + KE + \phi_{spec.} \quad (6.6)$$

where $h\nu$= energy of x-ray photon; h=Planck's constant; ν= frequency of photon; BE= binding energy of the electron (a measure of how tightly it is bound to the atom.); KE= Kinetic energy of the emitted electron; $\phi_{spec.}$ = work function (energy needed to expel an electron from the fermi level to the vacuum level.

XPS core electron loss causes a "hole" in its core. This excited ionization state will relax because of the filling of the hole with the use of an electron from one valence orbital. This process of relaxation releases energy in one of two possible mechanisms: X-ray fluorescence or just the generation of an Auger electron. X-ray fluorescence is the more energetic of the two processes [273].

The potential to determine atomic quantities without the need of standards is a significant aspect of XPS technology. There are two types of approaches that are commonly found when performing quantitative studies in analysis. Using synthetic samples with known compositions that are sufficiently "near" to the sample to be dosed. The calibration curve obtained with standards of known composition is used to determine the unknown composition of the sample. X-ray fluorescence, atomic absorption, and elementary analysis are all examples of techniques that apply this approach. The elemental composition of a sample at an element A can be calculated using the formula,

$$C_A = \frac{(I_A/F_A)}{\sum_i (I_i/F_i)} \qquad (6.7)$$

C_A = composition in atomic % of element A;

I_A = surface of the photo-peak associated with A;

F_A = response factor of the photoelectron associated with element A;

I_i = surface of the photo-peak associated with element i;

Fi = response factor of the photoelectron associated with element i.

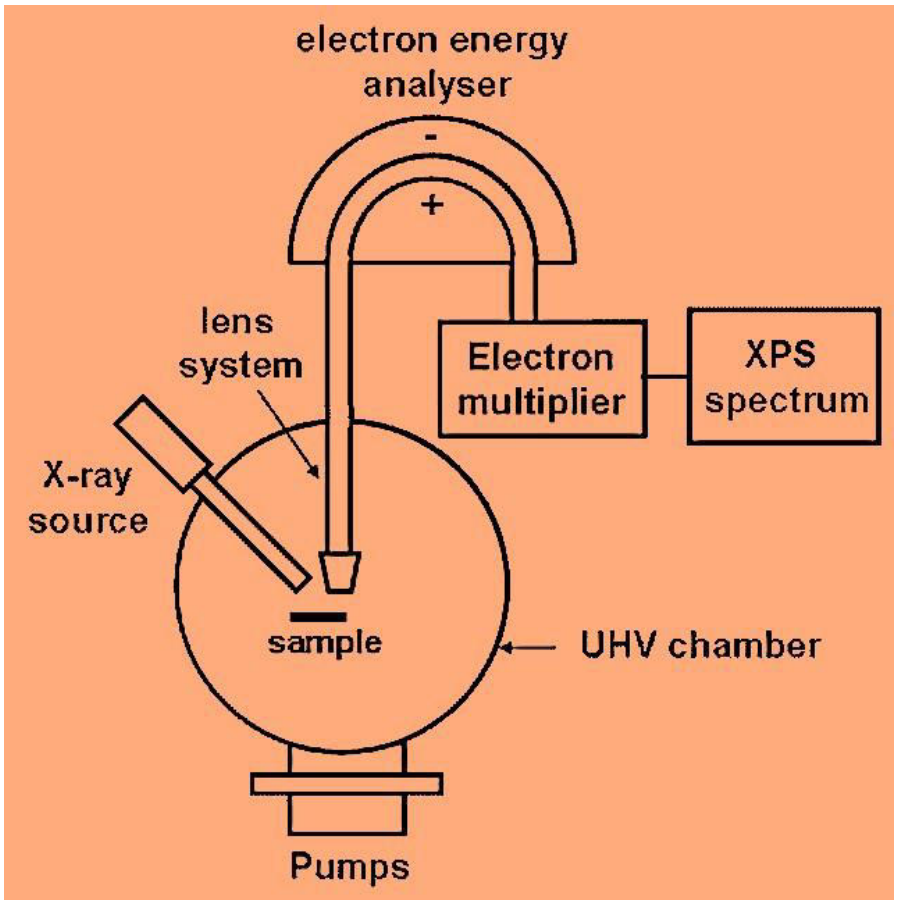

Figure 6.12: Schematic representation of XPS instrumentation.

Instrumentation for XPS analysis was the K-α Thermo Scientific X-ray Photoelectron spectrometer [Illumination source Al Kα: 1486.68 eV]. An internal chamber vacuum of 10^{-6} Pa was fixed during the XPS spectrum collection. The samples studied were 1x1 cm^2 in size and were maintained at ambient temperature (25 ^oC and 35% relative humidity) within the desiccators for 25 days before being loaded into the spectrometer. The calibration of the binding energy scale was carried out by measuring the standard Ag $3d_{5/2}$ core-level peak location from standard Ag foils. The sample surface was etched using argon at a velocity of 1.19 nm/s and a depth of 5 nm utilizing an ion gun placed at a 30^o angle. The charge reference using adventitious carbon peak (C 1s) was not employed in the investigation. Peak fit analysis was performed using the program Avantege. By analyzing XPS data from several materials, the core level binding energy correction factor was estimated as $\pm$0.04 eV.

6.2.5 Compositional characterization using Energy-dispersive X-ray Spectroscopy (EDS)

X-rays are extremely intense photons produced by transitions of electrons in the atoms of the target solid when an accelerated electron beam impinges on them. Typically, when an incident electron strikes at an atom of the specimen, it threw an electron out from the K-shell (n 14 1 shell) of the material, leaving a vacancy or hole in the shell where the incident

electron hit. X-rays are emitted when an electron from a different shell fills up the vacancy (electron transitions). The transitions of the electrons to the K-shell (n=1) are referred to as $K_{X\text{-}rays}$, transitions to the L-shell (n = 2) are referred to as $L_{X\text{-}rays}$, and transitions to the M-shell (n= 1 4 3) are referred to as $M_{X\text{-}rays}$. This type of transition is found in every chemical element, which is why EDS detection systems for electron microscopy have been developed and are now widely used in materials microstructural characterization. As we discussed earlier, the size of the interaction area and the size of the area from which X-rays are emitted are important factors in the accuracy of the EDS spectrum. X-ray energy and sample atomic weight both play an important role in the amount of signal created [274].

6.2.6 Electrochemical characterization of 2D Mo_2CT_x MXene using Linear Sweep Voltammetry and electrochemical impedance spectroscopy.

An electrochemical system measures the total conversion rate of reactant materials to products at the surface of an electrode by measuring the current (I) that flows through the metal/solution interface. At the electrode surface the following reaction takes place:

$$O + n \times e^{-} = R \tag{6.8}$$

To avoiding possible differences, depend upon the dimension of the interfaces, current is commonly normalized by surface area of the electrode (A) and represented as current density (j). As a result, response rate (v) can be written as follows:

$$v = \frac{I}{n.F.A} = \frac{j}{n.A} \tag{6.9}$$

where n is the number of electrons transferred in an electrochemical process, and F is the Faraday constant (96485 C mol^{-1}). By rearranging eq. (6.9), the total current flowing through an electrochemical system can be enhanced in one of two ways: either by enhancing surface area or by speeding up the reaction rate.

In addition to those above, temperature, pressure, and reactant concentration all influence the rate of electrochemical reaction. For the control of electrochemical reaction rate, electrode potential (E) also serves as an additional variable parameter. Since its absolute value cannot be determined through measurements, the minimum of the electrode potential scaling is established by the introduction the hydrogen electrode potentials. When the electrode rests at its equilibrium with no current flowing via the metal/solution interface, reversible potential (Er) is defined by Nernst equation (Equation 6.10) which is as follow

$$E_r = E^o + \frac{RT}{nF} \ln \frac{a_o}{a_R} \tag{6.10}$$

where E^o is the oxidation/reduction couple's standard electrode potential. If current is flowing via the electrode, the potential of the electrode will be different from E_r, therefore we refer to

it as being polarized. Assuming the electrode potential (E) is equal to the current density (j), the term overvoltage or overpotential (η) can be defined as:

$$\eta = E - E_r \tag{6.11}$$

The Tafel equation, which relates overvoltage and current density is

$$\eta = a + b.\log j \tag{6.12}$$

in which a and b are two constants. The parameter 'a' is the overpotential at unit current density (1 m.A/cm^2) with the value $\frac{RT}{\alpha nF}\log i_0$ and parameter b is the Tafel slope with the value $-\frac{RT}{\alpha nF}$, which is roughly 100 mV per decade of current density for most electrochemical reactions, so increasing the overvoltage by 100 mV enhances the rate of redox process by an order of magnitude. This is what distinguishes chemical systems from electrochemical systems: by regulating the electrode potential (or overvoltage), the rate of the reaction can be precisely controlled or enhanced dramatically, depending on the situation. Furthermore, using Eq. (6.11), one could determine the electrocatalytic effect of a specific electrode reaction on the ground of the influence of a and b on the type of the electrode material.

Although the Tafel equation is an empirical equation, the development of electrode kinetics has allowed for a better comprehension of charge transfer mechanisms at electrified interfaces. The following generic expression holds if the reaction (6.8) is a one-step n-electron charge transfer:

$$j = j_0\left(\frac{C_R}{C_R^*}exp\left(\frac{\beta nF\eta}{RT}\right) - \frac{C_O}{C_O^*}exp\left(-\frac{(1-\beta F\eta)}{RT}\right)\right) \tag{6.13}$$

where C_i and C_i* signify the concentrations of electroactive species on the surface of the electrode and in the volume of the electrolyte, respectively, denotes the symmetry factor (rather than the transfer coefficient), and j_o denotes the density of exchange current. Eq. (6.13) is predicated on the assumption of anodic current is positive while cathodic current is negative. The parameters β and j_0 are associated with charge transfer kinetics. In addition to electrode kinetics, mass transfer rate is a factor that is related to the C_i/C_i* ratio. When the anodic (positive) / cathodic (negative) overpotential is very high, Eq. (6.9) simplifies to the form of the Tafel equation; however, extra attention must be made to compensate j the mass transfer limits, so that only the charge transfer impact is taken into consideration (as mass transfer rate is independent of the electrode material). Tafel parameter and is correlated to j_0 in this situation, whereas Tafel slope b becomes:

$$b = \frac{2.303RT}{\beta nF\eta} \qquad \text{(Anodic polarization)} \tag{6.14}$$

$$b = -\frac{2.303RT}{(1-\beta)nF\eta} \qquad \text{(Cathodic polarization)} \tag{6.15}$$

In the event of a sophisticated electrode reaction (e.g., electrocatalytic reactions), the j–E relationship is not as straightforward, but the j–E or j-η curve contains all the information about the electrode process. As a result, obtaining reliable data on the j–E relationship is critical for the determination of electrocatalytic performance as well as the assessment of the parameters related to the of an electrode reaction. To fully comprehend the electrocatalytic process and also to develop novel electrocatalytic materials with improved properties, it is required to collect and analyze fundamental data.

i. Electrochemical cell

Electrochemical cells are the vessels used in voltammetry experiments which is as shown in the Fig 6.13. It consists of a working electrode, counter electrode, reference electrode and an electrolyte.

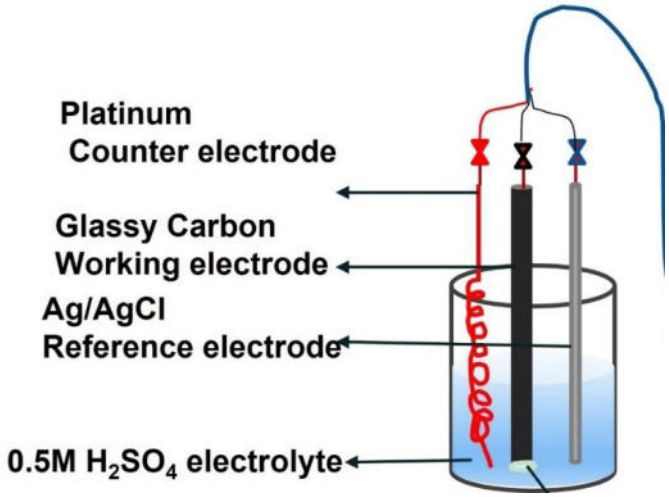

Figure 6.13 Schematic representation of a three-electrode electrochemical cell.

Electrolyte:

Electrical neutrality is ensured during a voltammetry experiment by the movement of ions in solution, which occurs as electron transfer takes place. In the process of transfer of electrons from the electrodes to the analyte, flow of ions takes place through the solution to compensate for the charge transfer and complete the electrical circuit, supporting electrolytes are salts that are dispersed in water that used to help overcome the resistance of the solution. The term "electrolyte solution" refers to the mixture of solvent and supporting electrolyte.

Working Electrode:

The working electrode is responsible for carrying out the electrochemical action. A potentiostat is used to adjust the applied potential on the working electrode proportional to the potential of the reference electrode. The working electrode is formed of redox-inert material in the desired potential range. To provide alternative potential windows or to decrease or enhance adsorption sites of the specimen of interest, the kind of working electrode could be

changed for each experiment. Examples of working electrode: glassy carbon, nickel foam, platinum etc.

Reference electrode

The equilibrium potential of a reference electrode is well-defined and steady. This electrode is used as a reference point in an electrochemical cell, against which the potential of all other electrodes can be measured. As a result, the applied potential is commonly expressed as "versus" a specified reference. There are a few regularly utilized (and usually commercially accessible) electrode systems, which have an electrode potential that is irrespective of the electrolyte that is used in cell. These electrode assemblies are described in detail below. There are several reference electrodes that are commonly used in aquatic media, including the stabilized calomel electrode (SCE), standard hydrogen electrode (SHE), and Ag/AgCl electrode, among others. A porous frit is used to keep the reference electrodes isolated from the solution. It is preferable to keep junction potentials as low as possible by integrating the solvent as well as electrolyte within reference segment to those in the experimental compartment.

Counter electrode

If you apply enough voltage to the working electrode to allow for the reduction (oxidation) of the analyte to take place, current will begin to flow through the circuit. With the counter electrode, the electrical circuit is completed. As the electrons move between, WE and the CE, current is measured as a result. The surface area of the counter electrode must be larger than the surface area of a working electrode in order to guarantee that the dynamics of the reaction that occurs at the counter electrode do not hinder the kinetics of the reaction happening at the working electrode. As a counter electrode, a platinum wire or disk is commonly employed, although carbon-based counter electrodes also are available on the market [275,276].

ii. Linear sweep voltammetry

In linear sweep voltammetry (LSV), the current flow through the working electrode is measured while the voltage between both the working electrode as well as the reference electrode is swept linearly over time, between two predefined values. Several factors influence the properties of the linear sweep voltammogram, including electron transfer reaction (s) rate, (ii) the chemical reactivity of the electroactive species, and (iii) the rate at which potential sweeps are applied to the electrode.

Measurements of LSV use voltage instead of time to plot the current response. The scan begins at the present potential E1, where only a small number of current flows (Fig 6.14). When a voltage is swept a little further down to more reductive values, a current start flowing and eventually reaches its maximum before dropping back down. Initially, as the voltage is

swept from E1, the equilibrium at the surface starts changing, and the current begins to flow as well. Due to decreased concentrations of reactants and increased concentrations of products on the electrode surface, current increases as the potential are swept away from its initial value. The occurrence of a peak arises happens at some point because the diffusion layer gets expanded so significant above the electrode that the flow of reactant towards the electrode is no longer fast enough to fulfil the Nernst equation. Thus the current starts to decrease at this point [277].

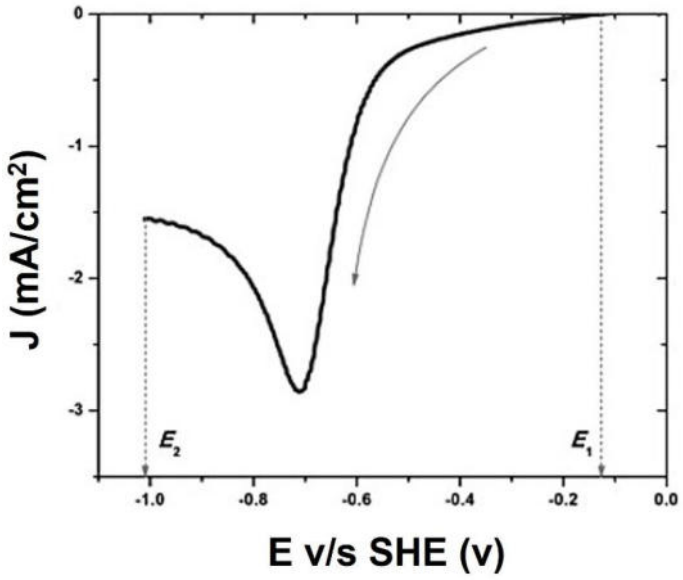

Figure 6.14 Example of Linear sweep voltammogram.

The electrochemical hydrogen evolution reaction was carried out using a three-electrode electrochemical cell, with platinum as the counter electrode, Ag/AgCl as the reference electrode, and prepared MXene deposited on nickel foam as the working electrode in 0.5 M H_2SO_4 electrolyte. Before the initialization of the experiments, cyclic voltammetry (CV) was done for 20 cycles at a scan rate of 50 mV/s to stabilize the system. The linear sweep voltammetry (LSV) measurements were obtained in the range 0 to -0.8 V with a scan rate of 5 mV/s.

iii. Electrochemical Impedance Spectroscopy

Electrochemical Impedance Spectroscopy (EIS) is a technique that uses electrochemical reactions to measure the impedance of a system in terms of the frequency of an alternating current. EIS is used to characterize transfer performances that is often employed in the linear time invariant system analysis. The fundamental problem in measuring an electrochemical system is that it must exist in a steady state during the data acquisition process. EIS is a technique that utilizes a low amplitude periodic potential or disturbance in current for exciting the electrochemical environment at various frequencies. The electrochemical impedance of an electrochemical cell can be estimated by monitoring the sensitivity of the

system (current or potential) to the perturbation. The impedance, denoted by the letter Z, can be stated as:

$$Z(\omega) = \frac{\tilde{V}(\omega)}{\tilde{I}(\omega)} = \left|\frac{\tilde{V}(\omega)}{\tilde{I}(\omega)}\right| \left(\cos \phi(\omega) + jsin\phi(\omega)\right) = Z_r + jZ_i \qquad (6.16)$$

where is the angular frequency, which is associated to the frequency of AC (f;Hz) by the relationship $\omega = 2\pi f$, is the phase angle between both the input and output signals, and j=-1 is the imaginary number. Variables $\tilde{V}$ and $\tilde{I}$ are phasers, which are complex time-invariant numbers explain the amplitude as well as phase of a sine wave. A frequency dependent complex number with real and imaginary parts, Z_r and Z_j, defining the electrochemical impedance according to Eq. (6.16). The real part, Z_r, of the electrochemical impedance is a resistance that is dependent on frequency of the signal, while the impendence's imaginary part, Z_j, is a reactance that depends on the frequency. According to International Union of Pure and Applied Chemistry (IUPAC) rules state that the real and imaginary parts of impedance should be represented as Z' and Z'', respectively.

Kramers–Kronig relations (Eq. 6.17 and 6.18) should be followed in the design of EIS measurements, which are obtained on the considerations that the electrochemical environment under examination is casual, linear, and stable in nature. Zj, can be computed from Z_r using the following formula:

$$Z_j(\omega) = \frac{2\omega}{\pi} \int_0^\infty \frac{Z_r(x) - Z_r(\omega)}{x^2 - \omega^2} dx \qquad (6.17)$$

If the impedance's high-frequency limit is established ($Z_r(\infty)$), then Z_r can be calculated from the Z_j as follows:

$$Z_r(\omega) = Z_r(\infty) + \frac{2}{\pi} \int_0^\infty \frac{xZ_j(x) - \omega Z_j(\omega)}{x^2 - \omega^2} dx \qquad (6.18)$$

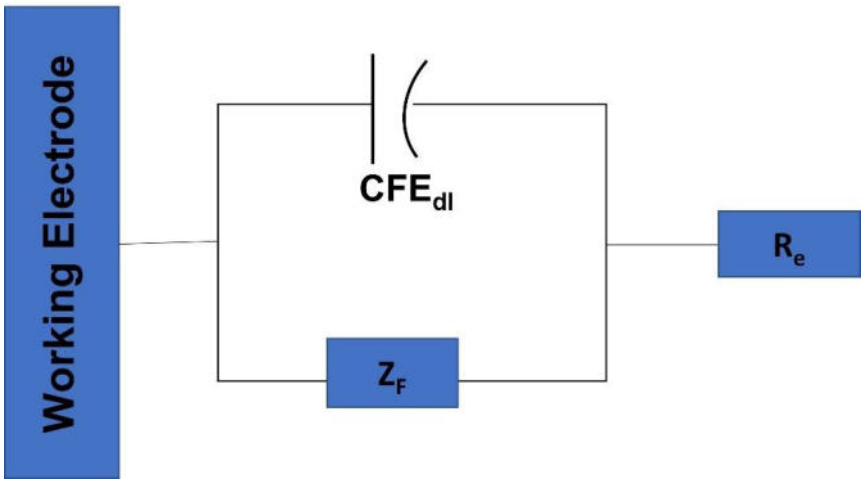

Figure 6.15 Equivalent circuit used in EIS

An electrochemical system consisting of a working electrode (WE), a counter electrode (CE), and a reference electrode (RE) is used for obtaining the data. It is necessary to

apply the voltage E(t) in between the WE and RE, and the associated current is determined. Impedance data are frequently presented as Nyquist (Z_r v/s Z_j) or Bode plots (f vs $|Z|$), and they're often portrayed with an equivalent circuit (Fig:6.15), in which a scientific explanation of the studied electrochemical environment is utilized to deduce the value for the faradaic impedance, Z_F using the relation,

$$Z_{total}(\omega) = R_e + \frac{Z_F}{1+Z_F(j\omega)^{\alpha}Q} \quad (6.19)$$

where α is parameter linked with the constant-phase element (CPE), ω is the angular frequency, CPE_{dl} is the double-layer constant-phase element, Q is the factor related with the CPE and R_e is the ohmic resistance.

For the electrochemical impedance spectroscopy in the present study the experiments were done in the 3-electrode electrochemical cell (Fig 6.14) in the frequency range 0.1 to 100 kHz.

6.2.7 Gas sensing characterization of the *1D α-MoO_3 nanorods and 2D Mo_2CT_x MXene*

The gas sensing measurements were done using two different set up due to the limitations in detection of different gases in a single set up. For measuring ammonia, we followed the procedure as described below.

Figure 6.16 depicts a schematic representation of the gas detection and measuring circuit for the purpose of illustration. The input voltage for the gas sensing test was set to 5 V, and the working temperature used for the gas sensors can be adjusted by altering the heater voltage (V_H) during the procedure of gas sensing verification. The test gas was generated by evaporation of the liquid that has been injected onto the bottom surface of the gas chamber (bottom includes heater plate) using a micro syringe. A virtual resistance, which changes in response to the sensor resistance, has been used to measure the output voltage. The resistance of the sensor is dependent on the test gas and its concentration [278]. The resistance is calculated using the formula,

$$R_a or R_g = \left(\frac{V_{in}}{V_{out}} - 1\right) \times R_{virtual} \quad (6.20)$$

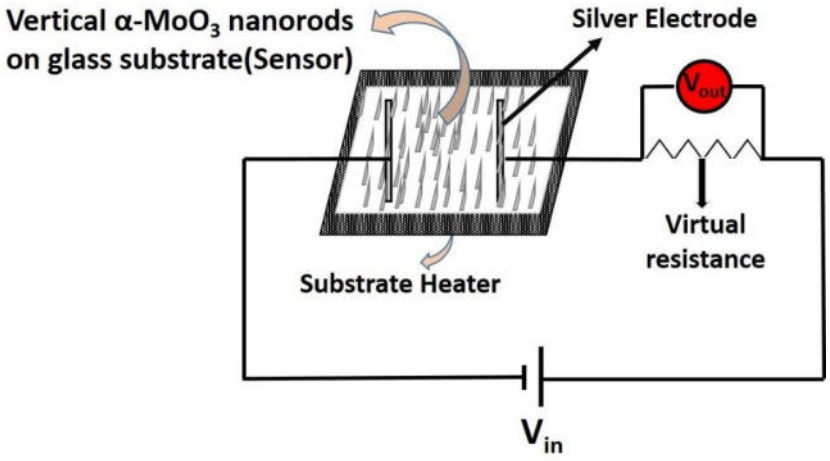

Figure 6.16: Schematic representation of gas sensing set up used for measuring ammonia gas.

For the CO_2 gas sensing we used a slightly different set up, which is shown in the figure 6.17. The gas sensing characterization setup consists of a portable glass test chamber. The electrical measurements were carried out using a Keithley 2450 source measuring unit. The working temperature of the fabricated sensors was controlled with a thermo-resistance attached to the sensing setup and monitored with a commercial type-J thermocouple connected to a computer.

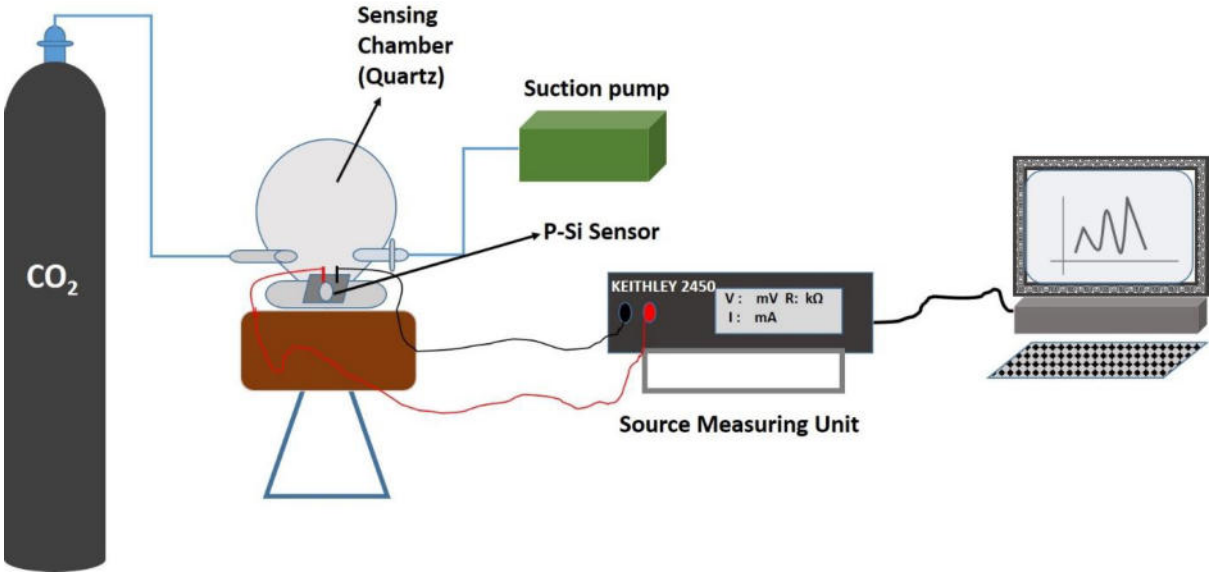

Figure 6.17 Schematic representation of gas sensing set up used for CO_2 sensing.

The sensor's sensitivity (S) is calculated as $\Delta R/(R_a \text{ or } R_g)$, where ΔR represents the change in resistance (R_a-R_g or R_g-R_a) (Equations 6.21-6.22) with target gas concentration and type (oxidizing or reducing) and R_g and R_a are the resistance measured in the presence and absence of the gas respectively. As the name suggests, selectivity is the property of a sensor that determines how well it responds to a certain class or kind of analyte. The lowest target gas concentration which could be detected by a sensor under specific conditions is known as detection limit (DL) or limit of detection (LOD) [279]. Responding time is defined as the time

required for the sensors to react to a change in concentration. The recovery time is thus the time required for the sensor to return to its pre-concentration value.

$$S = \frac{\Delta R}{R_x} = \frac{R_a - R_g}{R_g} \tag{6.21}$$

(Reducing gas for n-type/ Oxidizing gas on p-type MOS sensor)

or

$$S = \frac{\Delta R}{R_x} = \frac{R_g - R_a}{R_a} \tag{6.22}$$

(Oxidizing gas on n-type /Reducing gas on p-type MOS sensor)

7. ONE-DIMENSIONAL ORTHORHOMBIC MOLYBDENUM TRIOXIDE NANORODS: SYNTHESIS AND GAS SENSING APPLICATIONS

7.1 Introduction

Compared to current gas sensors for the detection of various gases, one-dimensional (1-D) transition metal oxide sensors are more stable, rapid responding, and recoverable. As suitable candidates for the sensing application, MoO_3 [41], WO_3 [280] , SnO_2 [281] , In_2O_3 [282], TiO_2 [283] , CuO [284]], ZnO [285] , and ZnO-NiO [286] were studied. Molybdenum trioxide (MoO_3) is one of the most studied transition metal oxides because of its large bandgap, layered structure, and exhibition of multiple valence states.[287]. Various MoO_3 morphologies, such as nanobelts [287], nanoflakes [288], films[186], and nanorods[172], are being studied for applications such as energy storage devices, solar cells, memory devices, gas sensors, light detectors, and so on [181,289–291]. Among them, one-dimensional nanorods are being extensively researched for use as gas sensors due to the existence of multiple surface atoms that are easily accessible because of their high ratio of surface to volume. When it comes to Debye length, MoO_3 has lateral dimensions that are comparable to each other, which is crucial since charge separation happens at this length [9]. 1-D orthorhombic molybdenum trioxide (α-MoO_3) is renowned for its unique capacity to detect gases due of its outstanding layered structure, the changeable valence state of molybdenum, and availability of adsorption sites that may trap analytes during the gas sensing process [182]. The sensing performance can be enhanced by making the composite with various morphologies or incorporation of particular substrate materials as per the literature [292]. In this context we attempt the incorporation of 1D MoO_3 on various substrates such as porous silicon which may be beneficial in the sensing performance since such hybrid structure already known for enhancement in the gas sensing [258,260]. Porous silicon (porosified silicon) has gained attention among the researchers because it possesses outstanding properties which are highly tunable. These features, unlike solid silicon, have opened opportunities in many fields, starting with electronics but now including microscopes, optoelectronics, optics, acoustics, energy conversion, diagnostics, nutrition, medical and gas sensing applications [293].

In this work chapter, we discuss about synthesis, micro-structural along with elemental characterization and gas sensing studies of 1D α-MoO_3 nanorods. For that, vacuum thermal deposition was used to deposit a specified orientation of α-MoO_3 nanorods onto a glass slide/porous silicon substrate, followed by thermal annealing. In addition, we show the detection and sensing approach for ammonia at ambient temperature and carbon dioxide at different working temperatures, as well as the detailed analysis of the parameters that influence

the performance of the built sensors. For the detection of carbon dioxide gas, we explore the utilization of a porous silicon/MoO_3 nanohybrid system. In the next part, we'll go into more depth about how we detect ammonia and carbon dioxide.

7.2 Ammonia sensing using α-MoO_3 nanorods on a glass substrate

7.2.1 Materials and Methods

α-MoO_3 nanorod powder was prepared using a hydrothermal procedure and then utilized as a raw material for vacuum deposition of α-MoO_3 nanorods over a glass substrate using the physical thermal evaporation deposition under vacuum. By regularly stirring for 45 minutes, sodium molybdate-dehydrate (Sigma Aldrich, >99 %) and hydrochloric acid (37 %; Merk) were dissolved in distilled water in a 1:5 molar ratio. It was then transferred to a Teflon-lined Parr bomb reactor for 2 hours of thermal treatment in a hot air oven while the synthesis temperature was varied (150 to 200 ºC in steps of 10 ºC). To eliminate unreacted HCl, the obtained powder was filtered and washed several times in ethanol and distilled water until pH 7 was reached. The powder was then collected by centrifugation at 3500 rpm and overnight drying in a hot air oven at 60°C. It was then annealed in a muffle furnace at 350°C for one hour at a heating rate of 5°C/min to improve crystallinity. For thermal vacuum deposition, the synthesized powder was utilized as a precursor (Fig 6.6). A vacuum chamber with a base pressure of 1 x 10^{-9} Pa and 250°C temperature on the substrate was used for the deposition. Throughout the experiment, the rate of evaporation was set at 10 kÅ/s and continually monitored with the use of a crystal thickness monitor. The distance between the source and the substrate, which was set at 17 cm, was also fixed. The thickness of the deposited films was kept within a range of 150-200 nanometers. After 15 minutes of evaporation, the as-deposited films were subjected to an oxygen plasma treatment. To increase crystallinity, as-deposited films were annealed in a muffle furnace at varied temperatures (100°C to 400°C) at a continuous rate of heating 5°C/min in ambient air.

PANlytical X'pert PRO HRXRD was used to examine the crystalline structure of the synthesized and heat-treated samples (Cu-Kα; λ=1.584 nm). Grazing incidence diffraction at an angle of 0.50º was used to study deposited and annealed film samples. Morphology of all samples was investigated using Carl Zeiss and Hitachi SU-8020 Field-emission scanning electron microscopes with operating voltages ranging from 1 to 5 kV. The vibrational properties of the film samples were analyzed using a Raman spectrometer equipped with a

laser source of wavelength 780 nm (Thermo Scientific). Transmission electron microscopy (TEM, FEI Titan G2 80-300) was used to acquire TEM images and the corresponding selective area diffraction patterns (SAED). The α-MoO_3 nanorods were carefully removed off the glass substrate using a blade and deposited on a copper mesh for TEM characterizations. For X-ray photoelectron spectroscopy (XPS) characterization, a K-alpha Thermo Scientific X-ray Photoelectron Spectrometer (Al Kα; 1486.68 eV) was employed. Throughout the XPS spectrum acquisition, the chamber was kept at a pressure of 10^{-3} Pa. Sensor samples were 1x1 cm^2 in size and stored at ambient atmosphere (25 ºC and 35% RH) for 25 days before being fed into the XPS machine. The binding energy scale was calibrated by determining the location of the standard Ag $3d_{5/2}$ binding energy peak on standard Ag foils. The surfaces of the sensors were etched at a rate of 1.19 nm/s using Argon plasma at a power of 2000 eV using a 30° angle ion gun to a thickness of 5 nm. In this study, we didn't make use of the adventitious C 1s for referencing. The core-level spectra of molybdenum 3d and oxygen 1s levels were recorded over fifteen minutes and eighteen seconds. Analyses were carried out utilizing Avantege, a computer application. The binding energy correction factor was calculated as 0.04 eV by examining XPS data from many specimens. To conduct electrical characterization, the silver electrodes patterns were painted on the α-MoO_3 films with a diameter of 1 x 10^{-3} m and a spacing of 10 x 10^{-3} m (Fig:2.17). The Keithley 2450 measuring unit was used for the electrical characterization.

Gas sensing studies on the fabricated sensors were conducted utilizing a custom-built gas sensing system, as detailed by Jayababu et al. [281,286], with a glass chamber with a heater, thermocouple, and probes for measuring the temperature inside (Fig: 2.17).

Since the sensing material is an n-type semiconducting material, the sensing response is computed as in Equation (1)[8],

$$S = \frac{R_a}{R_g} \quad , \qquad \text{…….. (3.1)}$$

where the resistance to the air of the sensor is denoted by R_a, and the resistance to the target analyte is represented by R_g.

To determine the voltage, drop across the virtual resistor caused by a change in sensor resistance, a voltage meter was used. The schematic diagram depicts this circuit as a test circuit (Fig. 6.17). This circuit is tested with a 5 V input voltage provided to it, and the output voltage measured at the virtual resistor. The circuit produced equation below was used to calculate the sensor's resistance fluctuation. [285,294],

$$R_a \text{ or } R_g = ({}^{V_{in}}/_{V_{out}} - 1) \times R_{virtual} \quad \ldots\ldots\ldots\ldots\ldots (3.2)$$

The sensors were examined at 28 °C with a steady humidity level of 35% RH to produce the most accurate findings. The time required for sensors to achieve 90% of their maximum observed sensitivity once the flow of gas was utilized to determine the response time. The time it took for the sensitivity of the sensor to decline by 90% from its maximum value afterward when the flow of gas was turned off was then calculated to find the recovery time. The electrical resistance of the manufactured sensors in gas flow and air atmospheres was measured using digitally operated Keithley 2100 SMU and Keithley J136 source meters.

7.2.2 Results and discussions

Hydrothermally synthesized samples were analyzed structurally using XRD to determine the effect of the reaction temperature, which varied between 150°C to 200°C (Fig 7.1a). The samples were all orthorhombic in phase, as per the ICDD data sheet (File no: 00-001-0706). It was discovered that increasing the synthesis temperature enhanced crystallinity, with peak position in (0 2 0), (0 4 0), as well as (0 6 0) directions. This was confirmation of the specific alignment of the crystal in the (0 k 0) direction because of temperature alteration during the synthesis.

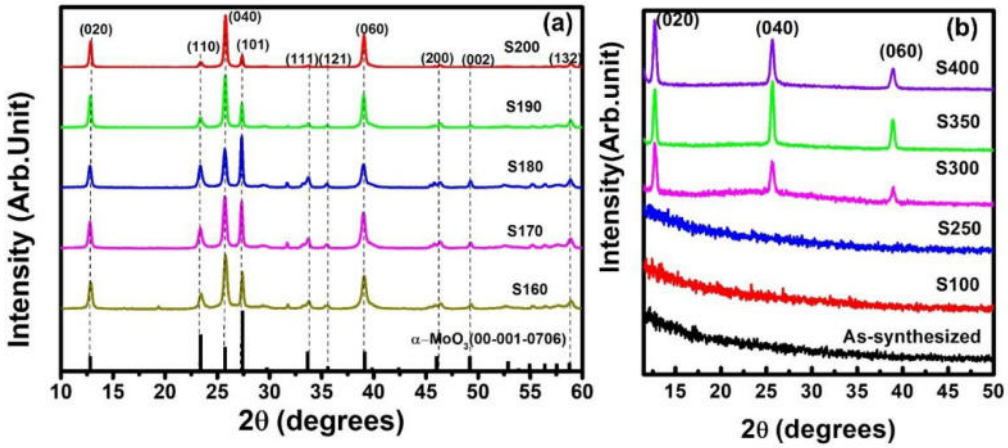

Figure 7.1: (a) XRD plot of hydrothermally synthesized MoO_3 nanorods powder varying synthesis temperature from 160 ºC to 200 ºC and (b) α-MoO_3 nanorods on glass substrate followed by thermally annealing at 100 ºC to 400 ºC post-deposition.

The as deposited MoO_3 samples on the glass substrate were amorphous when they were first deposited (Fig7.1b). This could be owing to the MoO_3 being deposited without any alignment on the glass substrate, or to a lack of subsequent crystallization temperature. The XRD experiments show that there is a temperature at which the crystallization of MoO_3 begins.

The crystallization threshold temperature for the current investigation was found as 300 ºC. Particles become crystalline orthorhombic α-MoO_3 on the glass substrate when the annealing temperature was increased above the threshold temperature (ICDD card no. 00-005-0508), having peaks along with directions (020), (040), and (060). It was clear that the annealing temperature is critical for crystallization and precise alignment along the (0 k 0) plane on the glass substrate. There was no evidence of mixed phases of MoO_3 in the films that were deposited. By using Bragg's law, the average inter-planar separation for both samples were determined as 6.91 Å.

The SEM images of the hydrothermally synthesized nanorod powder at different synthesis temperatures from 160 to 200 ºC are presented in Figure:7.2. The best nanorod morphologies which were uniform observed for the MoO_3 synthesized at 180 ºC.

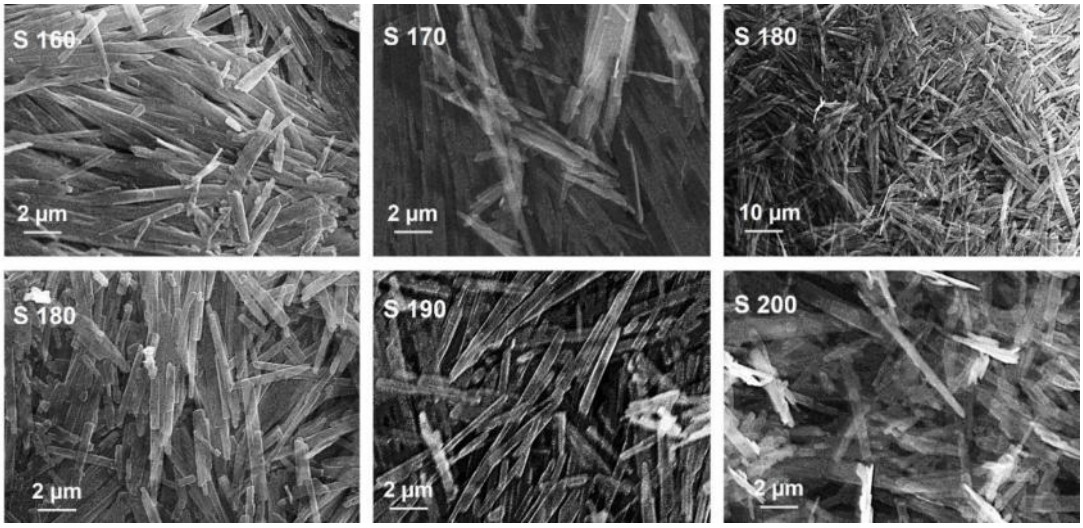

Figure 7.2 SEM images of the Hydrothermally synthesized MoO_3 nanorods powders by varying the synthesis temperature from 160 ºC to 200 ºC.

SEM images of sensors annealed at 350 ° C(S350) and 400 ° C (S400) revealed the nanorod structure (Fig:7.3 a-c). Sample S350 (Fig:7.3 e) had nanorods that were properly aligned on the glass substrate, but not when the annealing temperature increased by 50 °C (S400) Fig:7.3 f. SEM images of unannealed and annealed materials at temperatures less than 300 ºC, on the other hand, exhibited no visible nanorod structures. As a result, it was estimated that the formation of nanorods commences at a temperature between 300 and 350 ºC. There was no evidence of nanorod shape in the as-synthesized samples, which were simply continuous films (Fig:7.3d). The nanorod shape was visible in both the S350 and S400 (Fig:7.3 e and f) annealed samples. In sample S350, nanorods were found nearly perpendicular to the substrate, but in sample S400, they were found horizontally across the substrate. According to studies, when annealing temperatures increase from 350 to 400 ° C, nanorods become elongated and thinner [42,43]. S400 nanorods had an average length of roughly 3 microns, approximately five times the S350 nanorods (600 nm). Nanorods have formed on the glass substrate surface because of

annealing. [44,45]. When its annealing temperature is raised, the nanorods have a greater chance of recrystallizing, which leads to an increase in the internal dimension of the nanorods. The surface area to volume ratio of the S400 sample increases due to the increased linear dimensions. The SAED pattern (Fig. 7.3i) obtained from the TEM study of the S400 sample was in good correlation with the associated XRD pattern, allowing us to get a deeper understanding of the atomic structure of the α-MoO_3 nanorods. The presence of diffraction spots corresponding to the planes of the molybdenum trioxide which were not observed in the XRD may from the ultra-thin film below the nanorods acting as the base for the growth of 1D structure. The concentric ring like pattern confirms the polycrystalline nature of the deposited MoO_3.

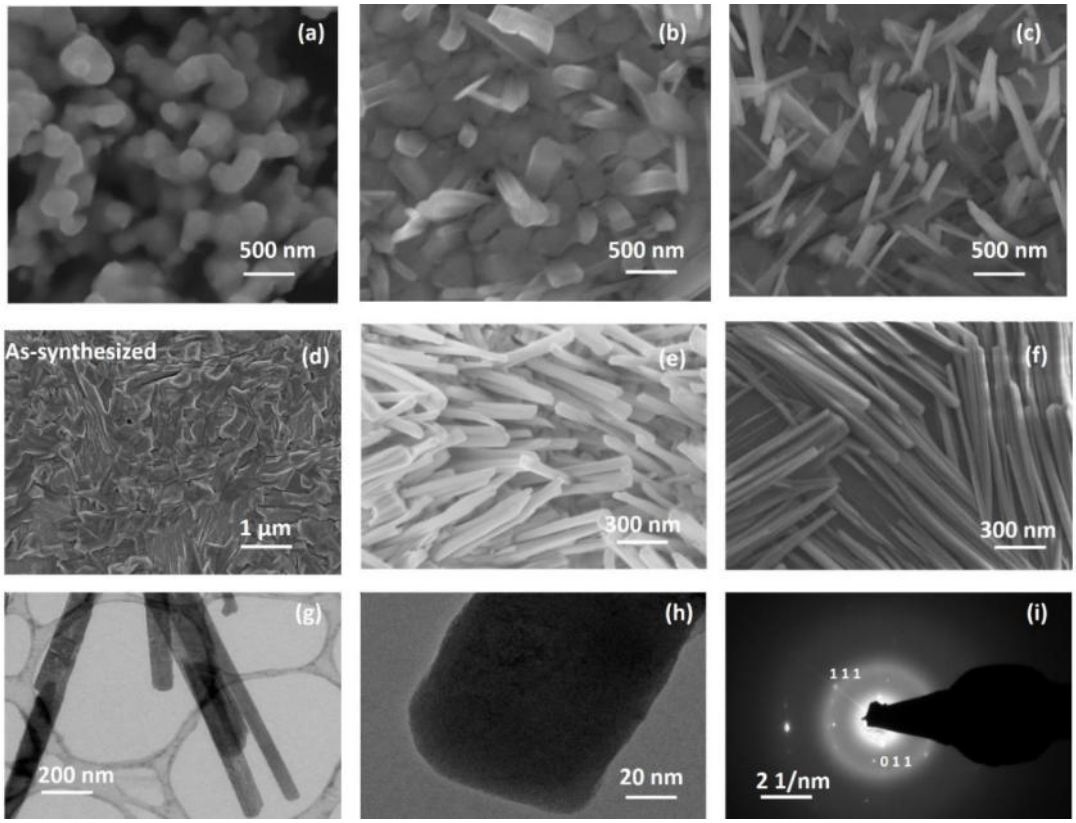

Figure 7.3 SEM images of annealed samples at (a) 300, (b) 350 and (c) 400 °C. FESEM images of (c) as-synthesized film, annealed films at (d) 350 and (e) 400 °C. HRTEM images (g-h) and SAED pattern of the annealed film at 400 °C.

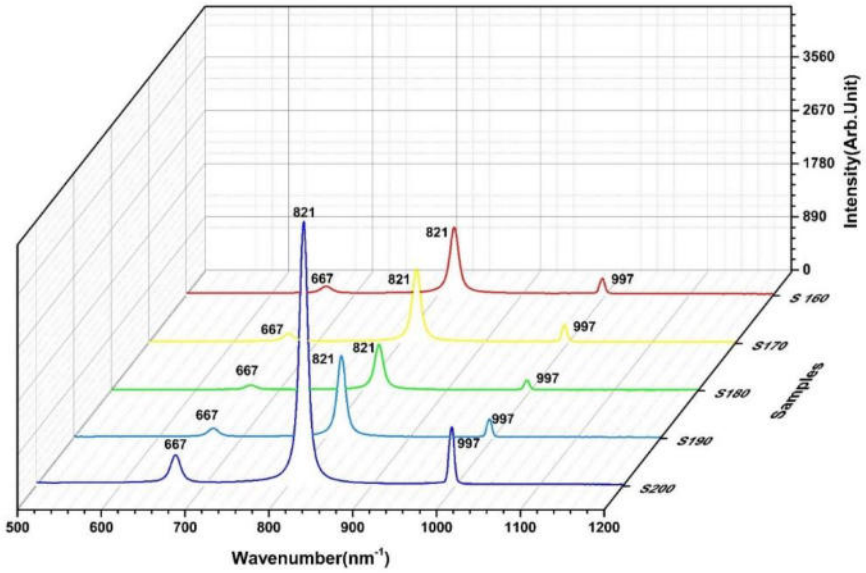

Figure 7.4 Raman spectrum of the MoO_3 nano rod powder synthesized for different temperatures from 160 to 200 ^oC.

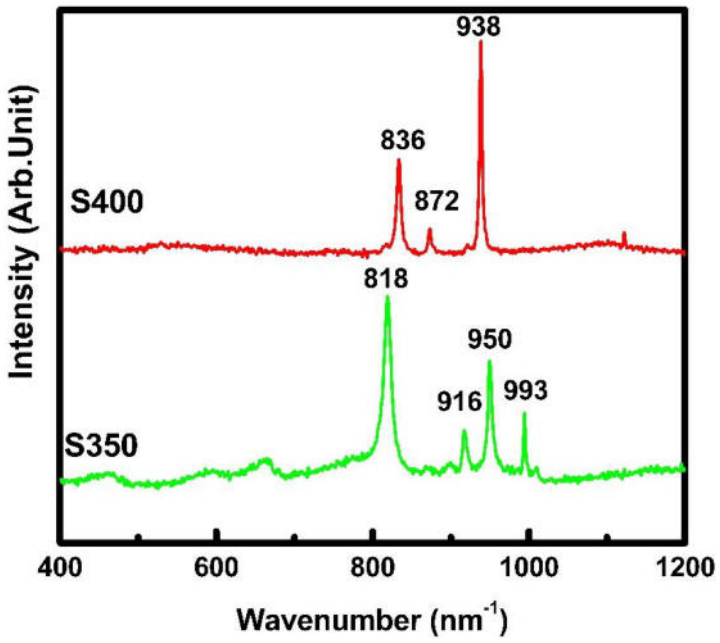

Figure 7.5: Raman spectroscopy of S350 and S400

To determine the structural changes that occur during annealing, Raman spectroscopy was employed (Fig:7.4 and 7.5). In the case of all the powder samples the peaks were at 667, 821, and 997 cm^{-1} associated with the orthorhombic MoO_3 phase (Fig. 7.4). In the case of sample S350, the Raman peaks observed at 818 cm^{-1}, 916 cm^{-1}, 950 cm^{-1},

as well as 993 cm^{-1} were all associated with the orthorhombic phase of the molybdenum trioxide phase(α-MoO_3) (Fig: 7.5) [9]. It is made up of a series of MoO_6 corner-shared octahedrons, each containing one unshared oxygen ion, two shared octahedrons, and three shared edges. Octahedral corner-sharing oxygen is responsible for the Raman spectrum at 815 cm^{-1}, which represents the oxygen stretching mode (Mo_2-O) (MoO_6)[9]. In the S400 sample, the annealing crystallization and bond length distortion induced this change in peak locations. The absence of 916 cm^{-1} as well as 950 cm^{-1} peaks in S400, and the creation of the new spectrum at 938 cm^{-1}, might both be attributable to the ordered transition of the MoO_6 octahedrons inside the MoO_3 lattice into one vibrational mode. It is also possible that the appearance of new stretching vibrations at 836 cm^{-1} is connected to a change in the atomic spacing between Mo_2-O bonds.

To get the high-resolution XPS spectra shown here, the sensor surface was etched with argon. High-resolution XPS spectra of the sensor's molybdenum (3d) state (S350/S400) were identified at 232.7 eV/232.5 eV as well as 235.8 eV/235.6 eV, which matched with the $3d_{5/2}$ and $3d_{3/2}$ levels were in line with earlier literature (Fig: 7.6 a and c) [288,295]. Additionally, two different oxygen peaks were identified in the magnified spectra of O (1s) after the deconvolution for both the sensors S350 and S400 (Fig: 7.6b and d). The presence of such asymmetric peaks suggests that oxygen species such as adsorbed ones inside lattice and associated with the -OH groups are existing at the film surface.[42]. The peak around 530.6 eV /530.33 eV (S350/S400) was revealed to correlate to O^{2-} ions in the α-MoO_3 matrix, whereas the peak at 532.1/532.4 eV belonged to the oxygen-deficient area inside the α-MoO_3 matrix.[296]. After the subtraction of the Shirley background, the molybdenum and oxygen atomic percentages calculated from the XPS readings were 10.8% and 89.1%, respectively.

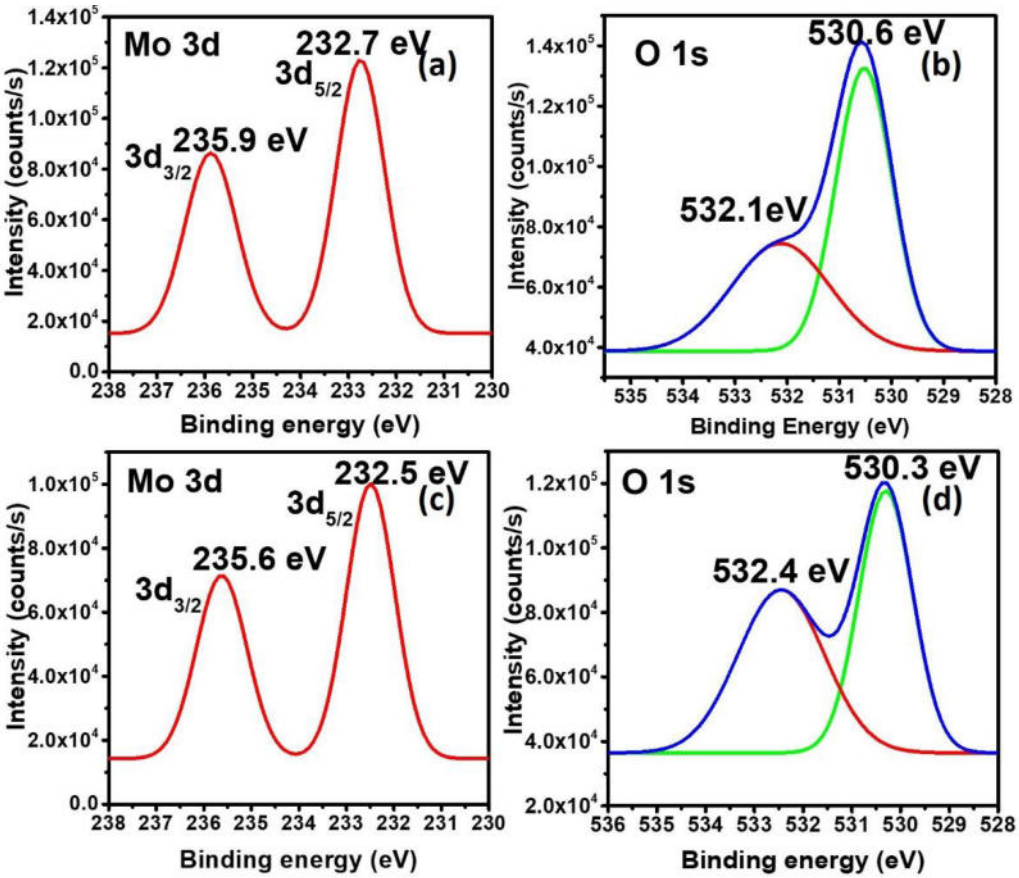

Figure 7.6 XPS spectra of molybdenum (Mo 3d) and oxygen (1s) from S350 (a and b) and S400 (c and d) films at high resolution.

Gas selectivity investigations on the sensors S350 (Fig:7.7 a) and S400 (Fig:7.7 b) were carried out at an ambient room temperature (28 ^{o}C) and relative humidity (35%, RH) for a range of different species (ammonia, ethanol, methanol, n-butanol, 2-methoxy ethanol, isopropanol, toluene, acetone, and xylene) at a fixed concentration of 200 ppm. Fabricated sensors S350 and S400 exhibited high sensitivity values 911 and 3139, respectively towards ammonia, which were larger than the sensitivity towards other target gases. Additional gas sensing investigations using ammonia as the target gas were conducted based on the findings for a full evaluation of the sensors' ideal working parameters.

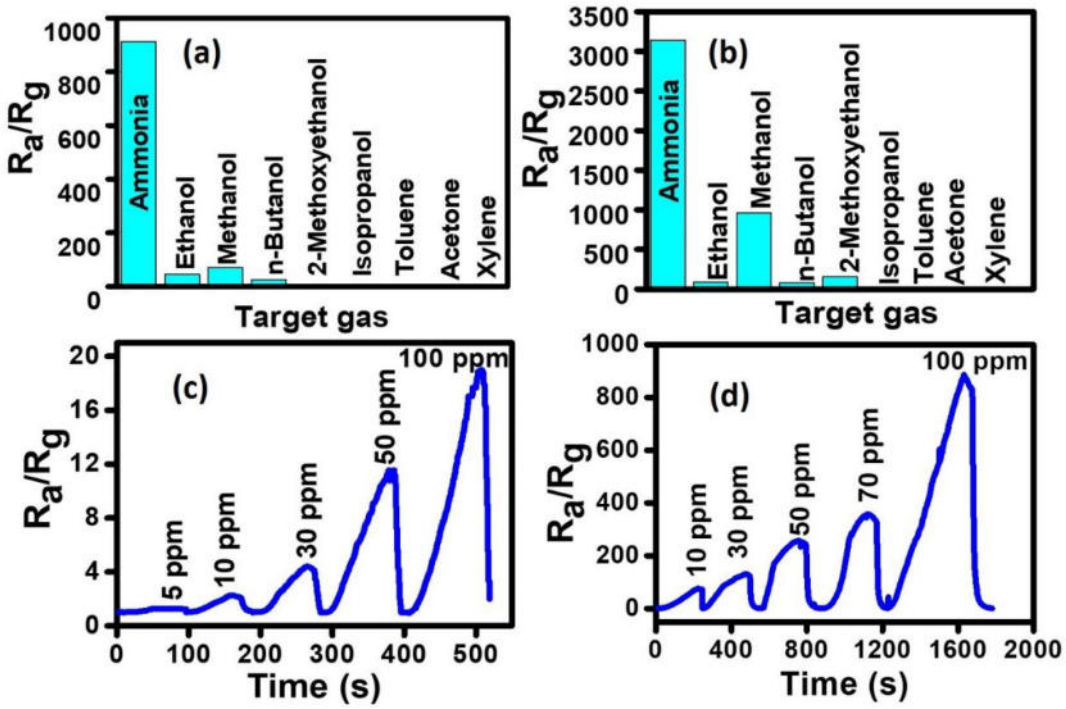

Figure 7.7 S350 (a) and S400 (b) selectivity investigations for several target gases are depicted schematically. The dynamic response curve of the S350 (c) and S400 (d) sensors at ambient temperature with increasing ammonia gas concentration. The x-axes in diagrams (c) and (d) represent the uninterrupted time frame used to introduce various quantities of ammonia gas into the sensors.

To identify the optimal operating conditions and lowest detection limit, dynamic response tests of sensors S350 (Fig:7.7c) and S400 (Fig:7.7d) were conducted at room temperature (28 ^{o}C) for varying concentrations of ammonia gas (1 ppm to 100 ppm). For 100 ppm of NH_3 at 28 ^{o}C, the S400 sensor showed the lower limit of detection (Fig. 7.8) and the highest sensitivity response (S = 886). (Table 7.1). This might be due to an increase in the surface area caused by thermal annealing during linear dimension expansion. The concentration ammonia under 5 ppm did not change the S350 sensor resistance (Fig:7.7c).

Table 7.1: Ammonia gas sensors: a review of the literature

Material	Operation temp (°C)	S	R_a	R_g	Concentration	Ref.
MoO_3	RT	**15**	**229 s**	**73 s**	**1 ppm**	**Present work**
V_2O_5	RT	2.05 Hz/ppm	2 s	9 s	9 ppm	[297]
SnO_2@PANI	RT	35.4	-	-	100 ppm	[298]
Ta_2O_5	RT	74.4	495 s	>1.5 hr	1000 ppm	[299]
ZnO	RT	52%	49 s	59 s	50 ppm	[300]
Graphene	RT	2.8%	-	-	10 ppm	[301]
h-MoO_3	200	36%	230 s	267 s	5 ppm	[185]
FGO	RT	12.2%	60 s	80 s	100 ppm	[302]
Ag- TiO_2	RT	25.1	150 s	600 s	80 ppm	[303]
P/Ag@polyaniline	RT	15	-	-	100 ppm	[304]
Sn−TiO_2@rGO/CNT	RT	85%	99 s	66 s	250 ppm	[305]
n-MoS_2/p- CuO	RT	47%	17 s	26 s	100 ppm	[306]
c-TiO_2/PANI	RT	6.3	-	-	250 ppm	[307]

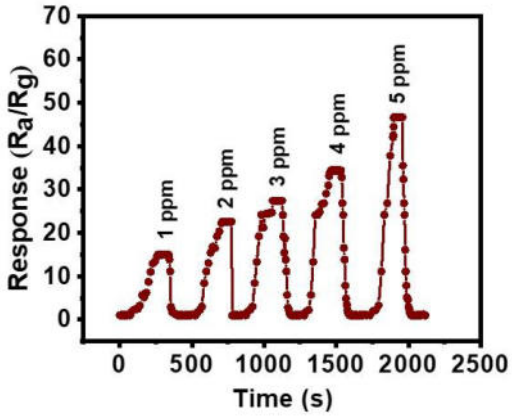

Figure 7.8: Studies of the S400 sensor's dynamic sensitivity at reduced ammonia gas concentrations

The reproducibility of the built sensors was evaluated over several cycles at an ammonia concentration of 100 ppm (Fig:7.9a-b). Even after several cycles of ammonia exposure, neither sensor demonstrated any discernible change in sensing response, indicating its suitability for commercial production sensors. One year following fabrication, stability studies revealed that the sensors were exceptionally stable, with sensitivity decreasing by about 1% following 30 days of continuous assessments (Fig:7.9c-d).

The calculation of response and recovery times was done in the manner depicted in the graph (Fig:7.10 a and b). The S350 sensor exhibited the quickest reaction time of 37 s and the quickest recovery time of 17 s at an ammonia concentration of 5-ppm (Fig:7.10c and d). The response and recovery times for the S400 sensor were abnormally long, even though it had a faster sensing response than compared to the S350 sensor (Fig:7.10 c and d). This might be due to the S400 sensors having a lower nanorod density than the sensor S350 (Fig:7.3). In all testing conditions, the response time of both the sensors was delayed than recovery times. This was mostly owing to the rapid removal of the target analyte from the chamber using the associated vacuum pump during the experiment.

As ammonia gas concentration increases, the sensor's reaction changes. This is seen in Figure 7.10. During the whole experiment, the sensor response increased as ammonia concentration increased. The enhanced adsorption might be ascribed to the greater number of gas molecules accessible. [180]. However, when comparing the S400 sensor to the S350 sensor, the improvement in sensing response obtained for the S400 sensor was substantially larger (Fig 7.10). A possible explanation for this is the increase in effective surface area, which itself is accompanied by linear expansion, that occurs during the annealing, as well as the development of deformities and re-ordering in the crystalline that was seen during the Raman study of the material. Increased availability of particle surface and adsorption sites within the lattice results in increased sensing response because of a higher supply of atoms and active sites within the lattice.

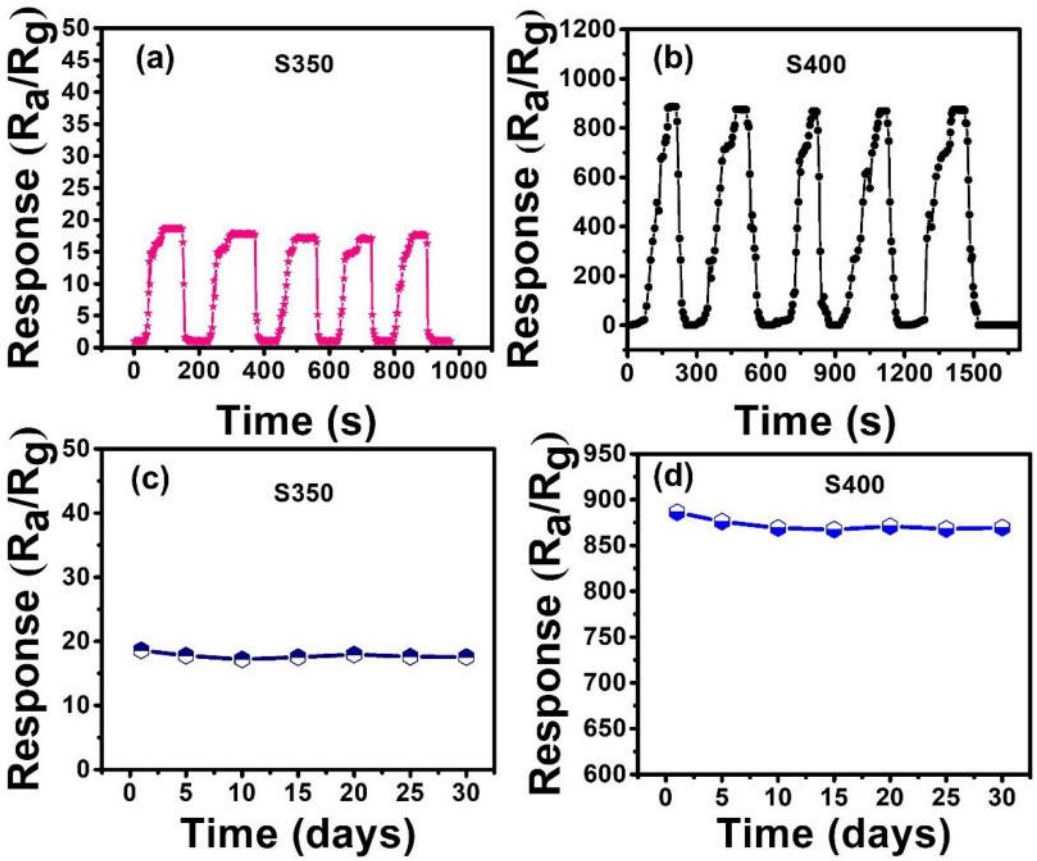

Figure 7.9: Repeatability and stability studies of (a and c) S350 and (b and d) S400 sensors at 100 ppm of ammonia concentration done at room temperature.

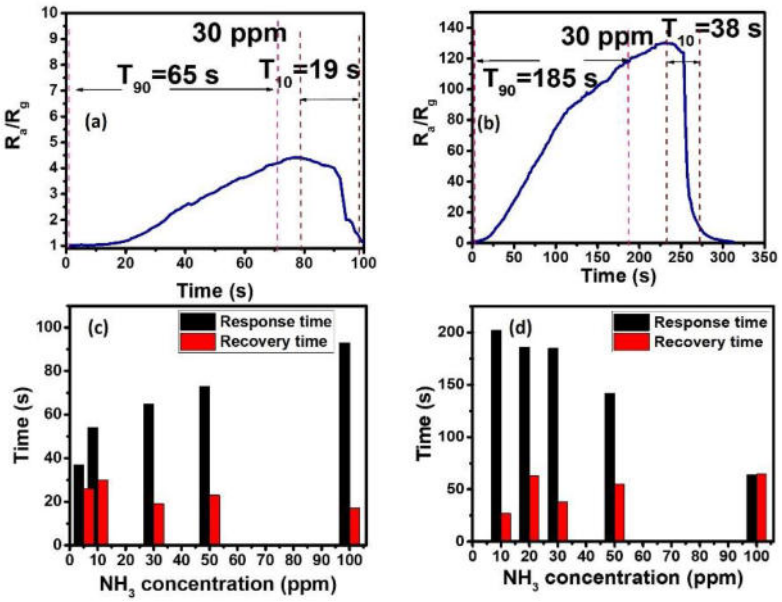

Figure 7.10 Sensor S350 (a and c) and S400 (b and d) response and recovery times determined at room temperature by altering ammonia gas concentration

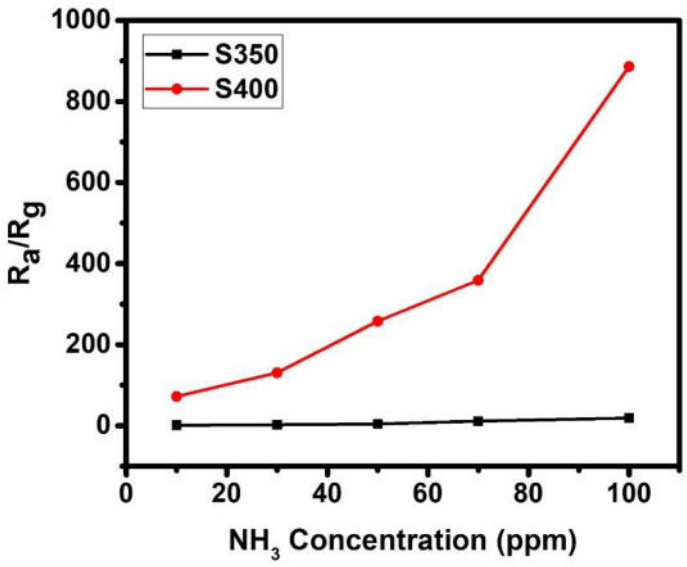

Figure:7.11: Sensing response of the S350 and S400 sensors as the function of NH_3 concentration

For the sensing mechanism of α-MoO_3 nanorods, the depletion layer modulation model [308] can be employed to describe the sensing process. A structural defect generated by Mo^{6+} ions in the MoO_6 octahedron, which acts as a high-affinity adsorbing site for gas molecules, is believed to be responsible for the sensing behavior in the α-MoO_3 nanorods, according to this model. When an oxygen ion is withdrawn out of a MoO_6 octahedron, the oxygen acts as adsorbed oxygen in the standard mechanism [42,309]. As a result of the adsorbed O_2 molecules capturing free electrons at the surface, a free charge carrier shortfall (electron depletion leading the depletion region to enlarge) occurs, resulting in increased resistance. When NH_3 gas is supplied to the surface, it combines with the adsorbed oxygen to generate N_2 and H_2O, which allow electrons that had been trapped in the conduction band to be released back into the conduction band[310–312]. During ammonia sensing, this results in a shortening of the bandgap as well as an enhancement in conduction at the surface of the α-MoO_3 molecule (Fig. 7.12). The equations that govern the sensing process can be expressed in the following manner:

$$2MoO_3 + 2e^- \rightarrow 2(MoO_3)O^- \quad \ldots\ldots (7.3)$$

$$2NH_{3(adsorbed)} + 4(MoO_3)O^- \rightarrow 4MoO_3 + N_2 + 6H_2O + 3e^-_{(to\ MoO_3)} \ldots\ldots (7.4)$$

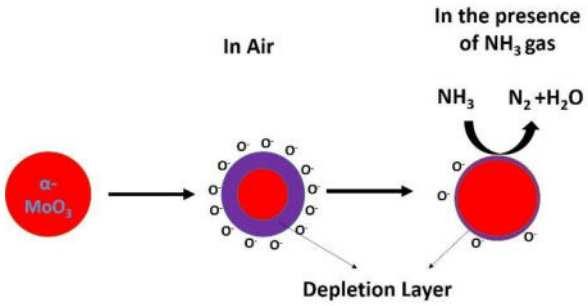

Figure 7.12: Schematic diagram of the sensing mechanism of α-MoO_3 nanorods for ammonia gas

The S400's enhanced sensing response is due to structural changes generated by the arrangement of the MoO_6 octahedrons inside the MoO_3 lattice, as well as variations in atomic spacing caused by annealing, as discovered by Raman analysis. These modifications may result in the formation of more flaws in the lattice, increasing the number of adsorption sites and so improving the sensing response to ammonia gas exposure.

7.3 CO_2 gas sensing using pSi/MoO_3 nanohybrid sensors

7.3.1 Materials and methods

In accordance with previously published procedures, the pSi substrate was created by electrochemical etching on a p-type c-Si substrate [211]. In summary, a (100) oriented p-type silicon wafer (14-22 Ω. cm) was immersed in a 1:1 (volume ratio) solution of 48 % concentrated hydrofluoric acid (HF; Fermont) and 99% dimethylformamide (Fermont) for 10 minutes at a current of 6 mA cm^{-1}.In order to build the sensors, a vacuum thermal evaporation deposition technique was used to create an orthorhombic MoO_3 nanocrystalline layer on either porous silicon (pSi) or crystalline silicon (c-Si) substrates (Fig. 7.13). Hydrothermally synthesized MoO3 nanorods were employed as a precursor in depositing a 100 nm layer on the substrates at a substrate temperature of 250 °C. At the end of the process, the hybrid nanostructures were annealed thermally at 350 ° C in the involvement of ambient air.

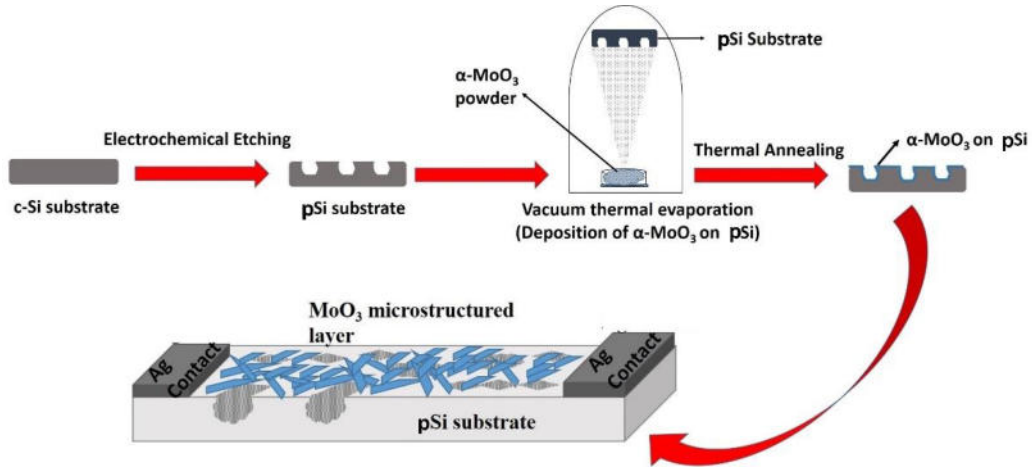

Figure 7.13 The fabrication of a pSi/MoO_3 sensor is illustrated schematically.

For the gas sensing measurements, silver dots were coated onto α-MoO_3 as probes with a separation of below 1.5 mm using silver paint, which was applied with a brush. After that, the samples were dried at 80 ° C for 2 hours to have the sensor. When measuring the structural characteristics of the synthesized hybrid structures in the 2θ-range of 10 to 80 degrees, we used an X-ray diffraction (XRD) instrument, which was equipped with a Bruker D2 Phaser diffractometer with Cu Kα as the radiation source and λ= 1.54nm. In order to evaluate the surface morphology of the sensors, a Hitachi SU-8020 microscope for field emission scanning electron microscopy (FESEM) was used. High-resolution transmission electron microscope (TEM) pictures as well as selected area diffraction patterns (SAED) of the coatings were captured using a transmission electron microscope (TEM, FEI-Titan G2 80-300). In this investigation, XPS measurements were utilized to identify the state of chemical bonding and the elemental makeup of the samples. The measurements were carried out using an X-ray photoelectron spectrometer from Thermo Scientific. An internal base pressure of 10^{-8} m.bar (with X-ray turned on) was maintained within the chamber during the acquisition using a combination of two turbomolecular pumps, one mechanical pump, and one sublimation pump. The excitation source was Al Kα, which operated at a voltage of 1486.68 eV. With a total acquisition period of 12 minutes and 17 seconds, the core levels spectra of Molybdenum 3d, oxygen 1s, carbon 1s, and valence states were recorded. Sequential spectral acquisition was used to obtain the data. The samples examined were 1x1 cm in size and were produced using the thermal evaporation technique. They were then held for 15 days at room temperature (25 ^{o}C) and 35% RH before being fed into the spectrometer. The core-level peak location of Ag $3d_{5/2}$ from the manufacturer's sputter cleaned standardized Ag foils was used to calibrate the binding energy level. The surfaces of the samples were etched with argon to a depth of 5 nm at a rate of 1.19 nm/s utilizing ion gun set at a 300-degree angle and a 2000-eV energy. During the XPS examination, a flood gun system with a low-energy electron/argon ion micro-

focused beam is utilized to neutralize charge on the sample surface. The C 1s peak of the adventitious carbon (Ad.C) layer is commonly used for charge referencing. When Garczynski et al. questioned whether or not the binding energy of the C1s peak was constant for all samples, conducting or non-conducting, they concluded that the C1s peak charge reference was flawed.[313–315]. The peak location of C 1s in relation to Ad.C changes considerably according to the substrate, ranging between 284.08 and 286.74 eV. C1s binding energy and sample work function remain constant for conducting samples, showing that Ad.C layer electronic levels are aligned to vacuum levels rather than Fermi levels [315]. It was decided not to utilize the Ad.C layer's C 1s charge reference because of the uncertainty in assuming the binding energy peak location and the practical challenges in getting the work function of our samples. We computed the error in the core level binding energy location to be 0.04 eV by analyzing XPS data from several materials. An SMU source meter (Keithley 2450 SMU, Fig. 6.18) linked to a PC was used to record the resistance as a function of time during the sensing measurements.

7.3.2 Results and discussions

Figure 7.14 illustrates the XRD pattern of the pSi/MoO_3 sensor. The XRD peaks observed in the pattern (at 2θ: 12.85°, 25.74°, and 39.05°) correspond to the standard ICDD data [00-001-0706] for orthorhombic MoO_3 phases with orientation in the (0 k 0) plane, where k = 2, 4, and 6, and the result is consistent with our previous observations [316,317]. The presence of the XRD peaks in the prescribed direction identifies the existence of an orthorhombic MoO3 packed double layer crystal structure on the substrate. Later, it was noted that the structure of the crystal is ideal for the physical adsorption, de-intercalation of molecules and ions between its layers, which increases the likelihood of faster electron transit when gas is adsorbed into the crystal. The Scherrer formula was used to compute the average crystallite size, which came out to 69 nm. In the (400) plane, the steep peak at 69.32° indicates a silicon substrate direction [318].

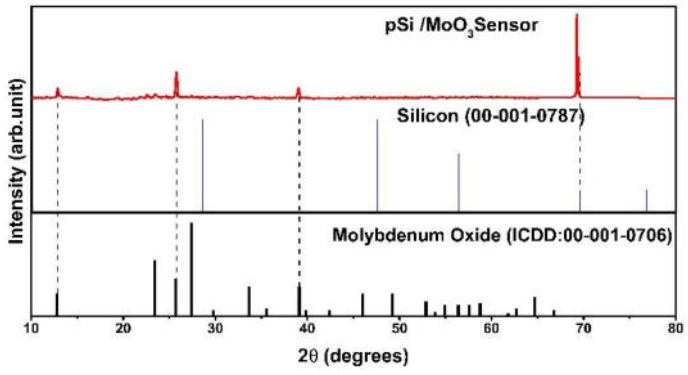

Figure 7.14 XRD analysis of the pSi/MoO_3 sensor

The FESEM images acquired for the pSi/MoO_3 sensor at different magnification are shown in Figure 7.15: a-c. MoO_3 nanorod thin films with a thickness of 100 nm were deposited above the symmetrical pores of the pSi substrate with diameters ranging from 328 to 945nm. HRTEM was utilized to obtain more surface data at a higher resolution. MoO_3 was removed from the pSi substrate and put on the Cu grid for TEM analysis. It is clear from the TEM images and SAED patterns (Fig. 7.15: d-f) that the formed MoO_3 film has a nanorod-like shape and strong crystallinity. Linear dimensions ranged from 256 nm to 451 nm for nanorods with 29-76 nm diameters **(**Fig.7.15: d-e**).** In addition, the SAED pattern (Fig.7.15f) validates the unique orientation of the MoO_3 planes seen during the XRD examination (Fig.7.14)**.**An appropriate nucleation site for the formation of nanosized MoO_3 rods that cover the whole surface is provided by the pSi substrate's large interior surface area and roughness [319].

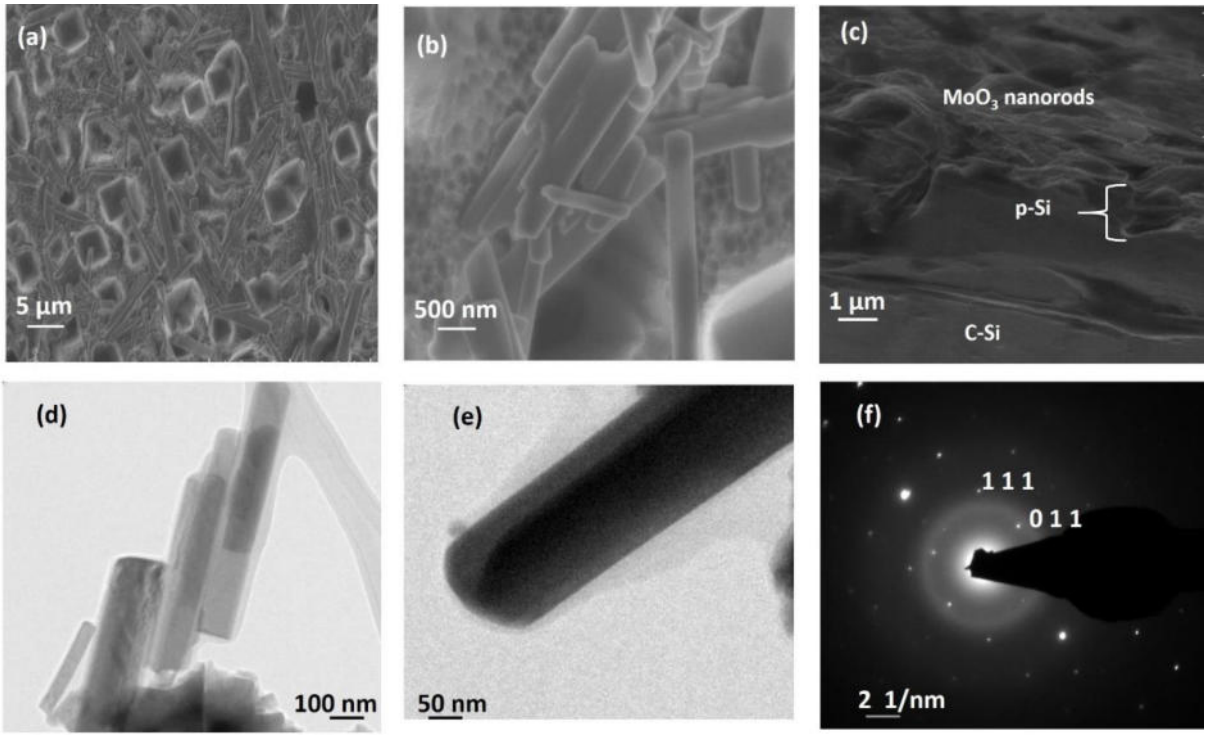

Figure 7.15 FESEM images of the pSi/MoO_3 hybrid structure with different magnifications (a and b) and cross-section images (c). HRTEM pictures of MoO_3 films (d and e) with nanorod shape and obtained SAED pattern (f).

Figure 7.16a depicts the XPS spectrum corresponding to the Mo 3d doublet of MoO_3 nanorods placed on a pSi substrate. With a baseline adjustment using the Shirley background, the peaks seen at 232.74 $\pm$0.04 eV and 235.9 $\pm$0.04 eV correspond to the molybdenum (Mo) $3d_{5/2}$ and $3d_{3/2}$ states, respectively [320]. The Mo^{6+} oxidation state of completely oxidized MoO_3 is responsible for the formation of these peaks [321]. There was a 3.2 eV difference in the binding energy between the $3d_{5/2}$ and $3d_{3/2}$ peaks, which confirmed the oxidation state of

Mo^{6+} [42]. Figure 7.16b shows the XPS spectra for oxygen's 1s energy state. The single strong signal at 530.56 eV can be assigned to 1s oxidation state, which is induced by the presence of an oxide layer on the surface of the sample [296]. A chemisorption process between the disassociated hydrogen and the terminal oxygen results in the production of oxygen in the surface hydroxyl group (OH^-) which causes the formation of this oxide layer [42]. The XPS spectra revealed two characteristic peaks of the 2p states of silicon (Fig 7.16c) linked with the SiO_2 signal, which were in good accord with the literature [322]. XPS report revealed that molybdenum and oxygen atoms make up 21.2 % and 78.79 % of the atoms in molybdenum and oxygen, respectively.

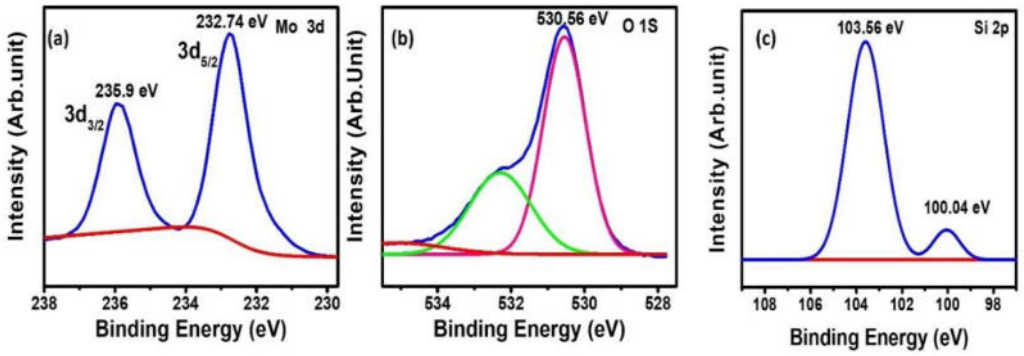

Figure 7.16 (a) Mo 3d, (b) O 1s, and (c) Si 2p: XPS core-level spectra of pSi/MoO_3.

To learn more about gas detecting properties, sensors were built on both pSi and c-Si substrates. Three different working temperatures (150 °C, 200 ºC, and 250 ºC) and target gas concentrations (50 ppm, 100 ppm, and 150 ppm) were used to test CO_2 sensing responses. When oxidizing CO_2 gas was introduced, the sensors' resistance increased, which is expected for an n-type semiconducting semiconductor (MoO_3)[245,323–325]. Equation (7.5) was used to obtain the percentage of sensing response (% S) [128]:

$$\%S = \frac{[R_g - R_a]}{R_a} \times 100\ \% \qquad (7.5)$$

where Ra denoted the resistance recorded during CO_2-containing ambient air and Rg denoted the resistance recorded in the presence of higher CO_2 gas concentrations. The sensor's response time is defined as the time needed to reach 90% of its maximum resistance, whereas the sensor's recovery time is described as the time needed to return 90% of the sensor's initial resistance after achieving 90% of its maximum resistance.

As shown in Fig. 7.17, measurements of the dynamic response of the sensors c-Si/MoO_3 and pSi/MoO_3 were taken when the working temperature was varied from 100°C to 250°C as well as the CO_2 concentrations varied from 50 ppm to 150 ppm while the relative humidity was maintained at 38 %. We discovered that the sensing response for both the c-Si/MoO3 and the pSi/MoO_3 sensors began to respond at a threshold temperature of 150 °C,

beneath which the sensor response was insignificant. The sensing response of both sensors rises proportionately to the increment in the working temperature and CO_2 concentration, which is similar to previous findings in the literature [133,198,211,326]. The response of the c-Si/MoO_3 sensor (Fig. 7.17(b)-(c)) was weak and noisy in comparison to the pSi/MoO_3 sensors (Fig. 7.17(d)-(f)), owing to the lesser availability of active sites on the c-Si/MoO_3 sensor due to its flat smooth surface. Due to this, the c-Si/MoO_3 surface may not be capable of adsorbing CO_2 molecules, resulting in lower sensing responses.When it comes to the pSi/MoO_3 sensor, the sensing response increases with temperature and concentration because of the large number of reaction sites available for adsorption. Although the pSi/MoO_3 sensor's response at 250 °C was exceptional to that at lower working temperatures, it was found to be less than satisfactory at temperatures higher than that.

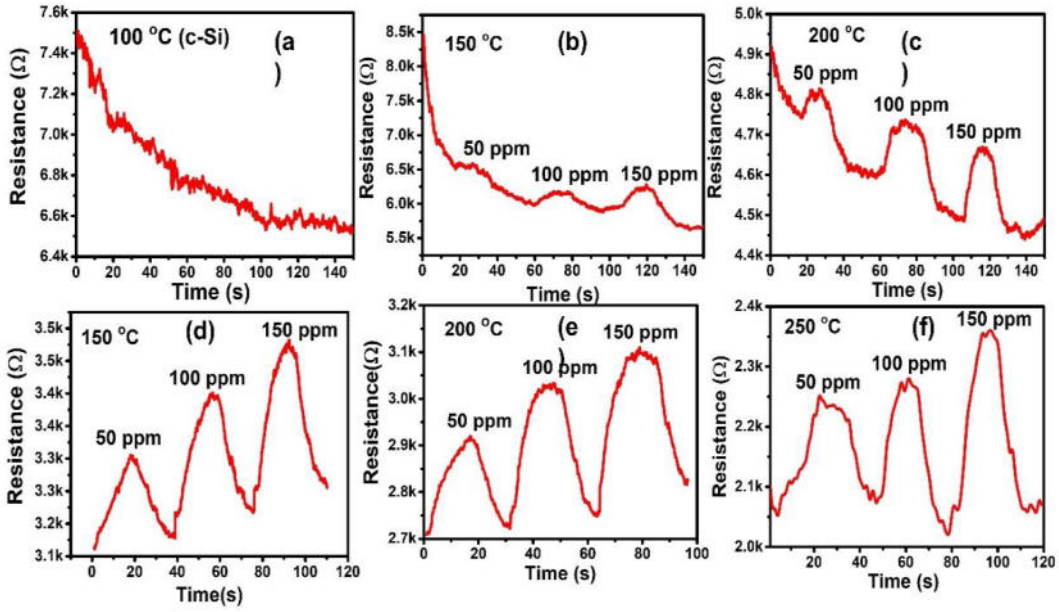

Figure 7.17 Dynamic response: C-Si/MoO_3 sensor working at (a) 100 ºC, (b) 150 ºC, and (c). pSi/MoO_3 sensor at (d) 150 °C, (e) 200 °C, and (f) 250 °C.

When used in industrial settings, sensors' repeatability is crucial. Tests of repeatability were carried out for various cycles varying temperature ranged from 150 to 250 ºC and CO_2 gas levels (50 ppm to 150 ppm). The repeatability graphs for the pSi/MoO_3 sensor are shown in Fig. 7.18**.** The sensors' responses were pretty constant over a number of cycles for the three different temperatures and CO_2 concentrations. As with the dynamic response tests, the pSi/MoO_3 sensor displayed an excellent performance at 250 °C for all three different CO2 gas concentrations (50 , 100, and 150 ppm).

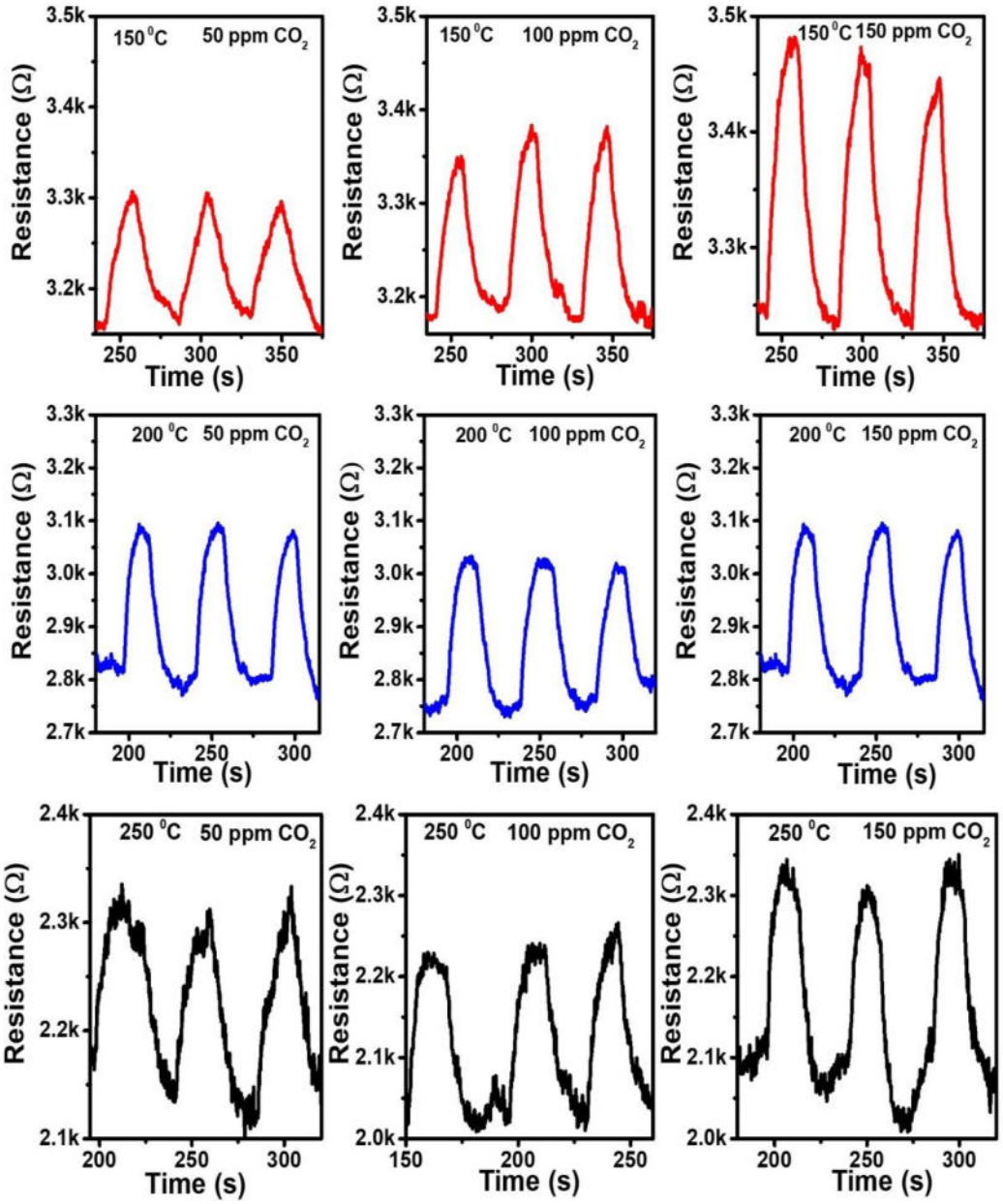

Figure 7.18 pSi/MoO_3 sensor repeatability tests at 150 °C, 200 °C, and 250 °C for three distinct target gas concentrations of 50 ppm, 100 ppm, and 150 ppm.

Figure 7.19 (a) and (b) show how CO_2 concentrations affect the c-Si/MoO_3 and pSi/MoO_3 sensors' sensing response. When operating at 250 °C and 150 ppm CO_2 concentration, the pSi/MoO_3 hybrid sensor showed a maximum sensing response (%S) of 15%. When the working temperature rises, the sensing response increases as well. This is consistent with prior observations [211]. It was noticed during the study that the response to concentration gradually improved. As a result, resistance increases, and sensing response becomes stronger. The gradual improvement in response with concentration was observed throughout the trial. The c-Si/MoO_3 sensor had sensing responses only at 150 and 200 °C, but they were significantly lower than the pSi/MoO_3 sensor's sensing responses at same temperatures (Fig.7.18). The lack

of detection for the c-Si/MoO_3 sensors at 250 °C might be due to the CO_2 molecule's quick adsorption and desorption on the sensor's surface, which results in no measurable changes in the sensor's resistance.

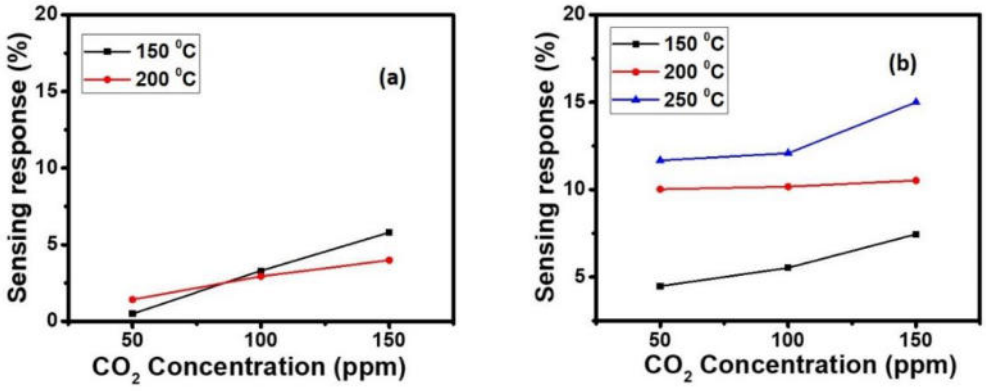

Figure 7.19 Sensor response (%S) variations with CO_2 concentration for (a) c-Si/MoO_3 and (b) pSi/MoO_3 sensors.

The response and recovery times of the prepared sensor are calculated schematically in Fig. 7.20 (a). A systematic investigation was done to evaluate the sensors' ideal functioning conditions using changes in target gas concentration as well as operating temperature. Figure 7.20 (b)-(d) shows the response and recovery times for the pSi/MoO_3 sensors at different operating temperatures and CO_2 gas concentrations. We observed that the response and recovery times for all three temperatures (150°C, 200°C, and 250°C), as well as CO_2 (50 ppm, 100 ppm, and 150 ppm) concentrations studied, were exceedingly fast. For the rise in temperature (150 to 250 °C) and concentrations (50 to 150 ppm), the response time varied between 14 and 15 seconds, and the recovery time varied between 15 and 20 seconds. The response time and recovery time were between 14 and 18 seconds when the operating temperature was elevated to 200 °C. With response and recovery periods of 8 and 15 seconds, respectively, the pSi/MoO_3 sensor working at 250 °C for a CO_2 concentration of 100 ppm exhibited the quickest response and recovery times. For a 200 °C working temperature and 150 ppm CO_2 concentration, the corresponding response and recovery times for the c-Si/MoO_3 sensor were 10 s and 9 s, respectively. Aside from that, the delayed recovery time of pSi/MoO_3 shown here relative to c-Si/MoO_3 might be due to the adsorbed target gas desorption from the porous structure taking longer[211]. Our research is the first to describe a pSi/MoO_3 nanohybrid-based CO_2 sensor with such a fast response and sensitivity, as shown in Table 7.2. The rapid reaction and great sensitivity were due to the distributions of submicron and nano-sized heterogeneous formations on the porous substrate. As a result, more CO_2 molecules can reach the reaction site more quickly with the aid of these structures. Because of this, the adsorption rate of gas is increased[211].

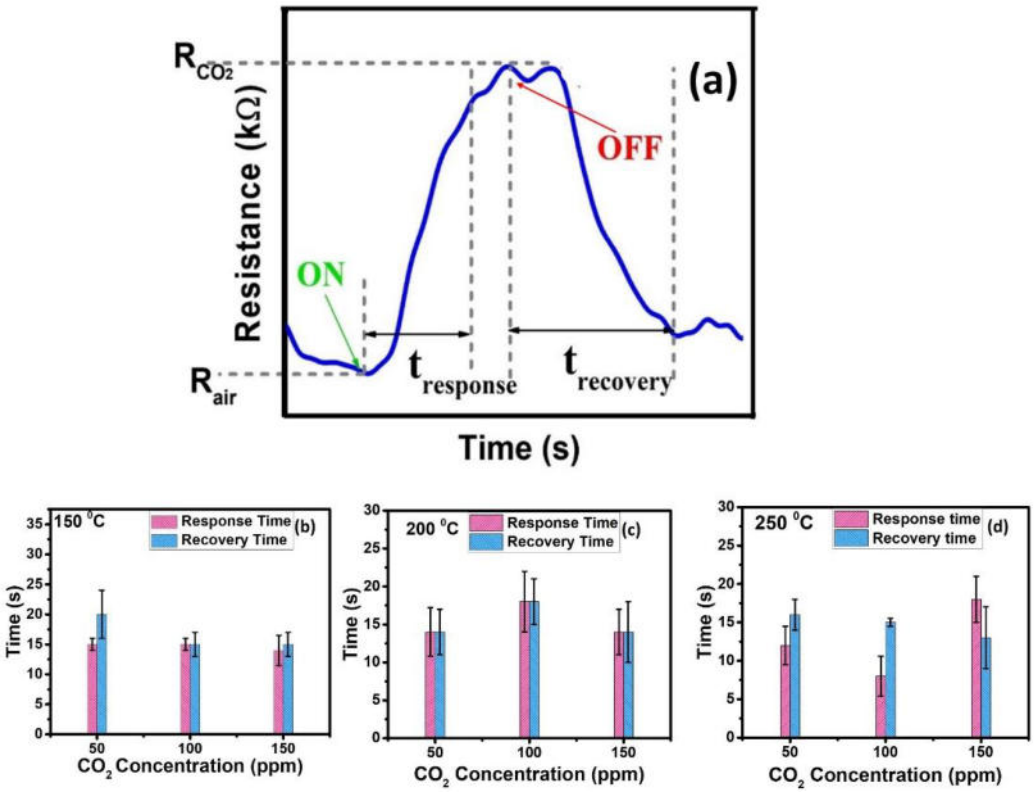

Figure 7.20 (a) The calculation of response time and recovery time is represented schematically in this diagram. Response and recovery times of a pSi/MoO_3 sensor as a function of CO_2 concentration for working temperatures (b) 150 °C, (c) 200 °C, and (d) 250 °C.

7.3.3Sensing mechanism

The sensing process for oxidizing gases in MOS, such as ZnO or SnO_2, is based on the variation in electrical resistance generated by the adsorption of the target gas on the surface of the active region, which is a well-known phenomena.The presence of adsorbed oxygen molecules is usually being associated with a change in resistance. The electrons originating from oxygen vacancy (VO) sites accumulate on the MOS surface as a result of the increase in operating temperature and combine with the adsorbed oxygen to create O^{2-} and/or O^{-} species in a metastable temperature-dependent adsorption-desorption process (equations 7.6-7.9) [327,328].

Table 7.2: A literature review on CO_2 gas sensors.

Sensor Material	Operating temp (°C)	S	R_a	R_g	CO_2 Conc.	Reference
pSi/MoO_3	250	12.08%	8 s	15 s	100 ppm	Present work 2020
S-polyether ether ketone	RT	47.00%	4.17 min	27.02 min	5000 ppm	[329]
Ca- ZnO	350	55.00%	111s	128s	50 ppm	[213]
Li_3PO_4 with MoO_3-doped Li_2CO_3	500	1.6	16 s	22 s	300 ppm	[210]
ZnO	350	64%	75 s	108 s	400 ppm	[330]
La_2O_3	250	64%	80s	50 s	400 ppm	[331]
CeO_2	250	35%	-	-	800 ppm	[326]
$Yb_{1-x}Ca_xFeO_3$ ($0 \leq x \leq 0.3$)	340	1.315	12 s	7 s	5000 ppm	[332]
Cal/Al co-doped zinc oxide	300	1.6	30s	2 min	1%	[212]
SnO_2	240	1.24	350	4	2000 ppm	[333]
$Li_4Ti_5O_{12}$	500	1.95	5 s	16 s	100 ppm	[334]
CN_x/pSi	RT	1.90	232 s	50 s	8 mbar	[130]
CuO/$CuFe_2O_4$	250	1.28	55 mins	8 mins	5000 ppm	[133]
Fe-Hydroxyapatite (Fe-HAp)	155	-	25 s	20 s	23000 ppm	[335]
$La_{0.8}Sr_{0.2}FeO_3$	380	1.25	11 mins	5 mins	2000 ppm	[134]
$LaFeO_3$	300	2.19	4 s	8 s	2000 ppm	[208]
In_2Te_3	RT	50%	15 s	-	1000 ppm	[336]
$CoAl_2O_4$	450	0.08	50 s	45 s	100 ppm	[337]
Hydroxyapatite (HAp)	165	31.1	20 s	15 s	1000 ppm	[338]

$$O_{2(gas)} \leftrightarrow O_{2(ads)} \quad (7.6)$$

$$O_{2(ads)} + e^- \leftrightarrow {O_2}^-_{(ads)} \ (< 100\ ℃) \quad (7.7)$$

$$O_2{}^-{}_{(ads)} + e^- \leftrightarrow 2O^-{}_{(ads)}\ (100 - 300\ ℃) \quad (7.8)$$

$$O^-{}_{(ads)} + e^- \leftrightarrow O^{2-}{}_{(ads)}\ (> 300\ ℃) \quad (7.9)$$

Then, those oxygen ionized species react with the target gas, resulting in a modification of the electrical resistance of the MOS film. Typically, the electrical resistance of n-type semiconductors decreases when exposed to a reducing gas environment such as CO [39] or H_2 [181], but the electrical resistance rises when exposed to an oxidizing gas atmosphere such as NO_2 [42] or CO_2 [245,323,324]. When CO_2 interacts with those oxygen species, electrons are transferred to CO_2 molecules, resulting in metastable $(CO_3)^{2-}$ complexes on MOS's surface [339–341]. The production of $(CO_3)^{2-}$ complexes decreases the conductivity of the MOS layer due to a drop in the free electron density [245,342] or causes a bandgap widening [340,341] due to the formation of a Schottky potential barrier, i.e., a depletion layer on the MOS surface [343,344], as seen for adsorbed CO_2 on other MOS. As a result, the drop in MOS conductivity is proportional to the amount of CO_2 present in the environment. Finally, when the CO_2 source is switched off, the $(CO_3)^{2-}$ complexes decompose into CO_2, and the trapped electrons are released into the MOS layer, decreasing the resistance of the MOS layer to its starting value.

Although it is similar to other MOS, the sensing process for MoO_3 is slightly different. For example, as seen in Fig. 7.21(a), orthorhombic MoO_3 has a double layer structure consisting of connected MoO_6 distorted octahedra that develop in a parallel fashion to the direction of [010] growth [309]. With increasing temperature, one oxygen ion in these double layers is removed to the surface, while a switch from corner-sharing to edge-sharing octahedron or face-sharing octahedron rearrangement occurs (Fig. 7.21(b) and 7.21(c)). In the typical mechanism [42,309], the removed oxygen takes on the role of the adsorbed oxygen. An increase in the operating temperature causes oxygen to be released from the surface of the MoO_3 sensor. This causes an increase in the electron density, which reduces the resistivity of the sensor material. When exposed to electrophilic CO_2 gas, the free electrons from the -MoO_3 layer are trapped as the target gas flows over the substrate. Fig. 7.21(d) shows how electrons are exchanged from ionized oxygen species on the surface of α-MoO_3 to CO_2 adsorbed on the surface, which become metastable $(CO_3)^{2-}$ complexes. This increases the resistance of the α-MoO_3. As per the equations (7.10) to (7.13) [42,340,341], the trapped electrons react with the CO_2 in the following ways:

$$Mo_xO_{3x} \xrightarrow{\Delta} Mo_xO_{3x-1} + V_O^{\cdot} + e^- + \frac{1}{2}O_2 \quad (7.10)$$

$$Mo_xO_{3x-1} + V_O^{\cdot} + e^- + \frac{1}{2}O_2 \xrightarrow{\Delta} Mo_xO_{3x-1} + V_O^{\cdot\cdot} + 2e^- + \frac{1}{2}O_{2\,(ads)} \quad (7.11)$$

(oxygen removal from MoO_3 crystal lattice)

$$Mo_xO_{3x-1} + V_O^{\cdot\cdot} + 2e^- + \frac{1}{2}O_2 + CO_{2(gas)} + 2e^- \leftrightarrow Mo_xO_{3x-1} + \frac{1}{2}O_2^{2-} + CO_{2\,(ads)}$$

(3.11)

(CO_2 adsorption)

$$Mo_xO_{3x-1} + \frac{1}{2}O_2^{2-} + CO_{2(ads)} \xleftrightarrow{e^- exchange} Mo_xO_{3x-1} + \frac{1}{2}O_2^- + CO_{2\,(ads)}^- \qquad (7.12)$$

$$Mo_xO_{3x-1} + \frac{1}{2}O_2^- + CO_{2\,(ads)}^- \xleftrightarrow{e^- exchange} Mo_xO_{3x-1} + (CO_3)_{(ads)}^{2-} \qquad (7.13)$$

Once the CO_2 flow is stopped, the CO_2 molecules begin to be desorbed, reversing the chemical reaction, and lowering the resistivity of MoO_3.

Thermally generated electrons contribute significantly to the reduction in resistivity. The free electron density in α-MoO_3 grows as the working temperature rises, while the initial resistance falls, resulting in a larger gap between R_a and R_g prior to the emergence of the target gas (CO_2). In this way, it is possible to explain why the sensing response at 250 °C was so much stronger than at 100 °C and 150 °C in the current investigation. Another factor in the lowering of resistivity originates from electrons created by thermal processes. At high temperatures, the free electron density in α-MoO_3 rises, resulting in a larger gap between Ra and Rg, before the introduction of the target gas (CO_2) [327].

An improvement in the surface area induced by the uniform distribution of the nanocrystalline α-MoO_3 layer is responsible for this study's higher sensitivities and low detection limits. In comparison to continuous thin-film sensors, the interactions of metal oxide MoO_3 with CO_2 at the intersecting points on micro- and nanostructured surfaces might have a significant influence on the sensor's resistance [328]. An increase in electrical resistance in nanostructured MoO_3 is a sign that it has a greater ability to interact with CO_2.

7.4 Summary

In this study, synthesis of orthorhombic MoO_3 nanorods were synthesized as powder and thin film different substrate materials by the means of hydrothermal method and vacuum thermal evaporation technique. The structural microstructural characterizations were carried out using, XRD, Raman, FESEM, and TEM, which confirm the formation of orthorhombic MOO_3 with nanorod morphology. The elemental characterization was carried out using XPS from which the oxidation states for corresponding elements i.e., molybdenum and oxygen was identified. Then ammonia gas sensors were constructed via vacuum thermal evaporation of α-MoO_3 nanorods over glass substrates, followed by an annealing procedure in ambient air, to detect the presence of ammonia gas. The gas sensing evaluation of the prepared sensors

revealed an outstanding sensitivity to ammonia gas at room temperature (28 ºC) for the specimen annealed at 400 ºC (S400). During testing, it was discovered that the sensors were responsive to ammonia concentrations as low as 1 ppm, reproducible, and exceptionally stable after a year of operation, with just a 1 % drop in sensing response. The existence of additional physisorption sites formed by thermal annealing, as indicated by FESEM and Raman spectroscopic characterizations of the sensor (S400), may be responsible for the improved sensing performance of the sensor (S400). The stable α-MoO_3 sensor reported in this study has the smallest limit of detection and the largest sensing response, making it a promising candidate for large-scale NH_3 sensing in practical production.

In addition to that, porous silicon/molybdenum trioxide hybrid structure, which was synthesized by simple physical vapor deposition of the MoO_3 over an electrochemically generated silicon substrate, was successful in detecting CO_2 gas at a relatively low concentration (50 ppm) and working temperature (150 ºC). In agreement with the XRD results, the high-resolution TEM and FESEM pictures demonstrate the development of the precisely oriented MoO_3 crystallites on the substrate with nanorod shape. Additionally, the compositional analysis performed using XPS confirms the homogeneous deposition of orthorhombic MoO_3 layer on the silicon substrate and confirms the formation of a hybrid structure on the sensor surface. The effect of the pSi substrate, operating temperature, and target gas concentration on sensor performance was investigated. The pSi/MoO_3 sensor operating at 250 ºC exhibited nearly four times the sensitivity (15% at 150 ppm) of the c-Si/MoO_3 sensor (3.9% at 200 ºC and 150 ppm) and a much quicker response time (8s at 100 ppm) than the latter (10 s at 200 ºC and 150 ppm). The high sensitivity and low detection limit of the pSi/MoO_3 sensor were deduced from the increase in specific surface area caused by the uniform distribution of the MoO_3 nanorods over the pSi substrate. As a result of the enhanced interaction and the establishment of a new potential barrier, a favorable condition for CO_2 detection is formed. The findings of this study suggest that it is possible to manufacture CO_2 sensors on a wide scale utilizing a porous silicon/molybdenum trioxide hybrid structure at a low cost and with improved efficiency; nevertheless, further research and optimization in the field are necessary.

8. Mo_2CT_x MXENE SYNTHESIZED FROM Mo-In-C NON-MAX PHASE FOR GAS SENSING AND HYDROGEN EVOLUTION REACTION APPLICATION

8.1 Introduction

MXenes are a new family of 2D materials with a wide range of uses, including energy storage, biomedical applications, catalysis, gas sensing, and other fields [250]. They have the generic formula $M_{n+1}X_nT_x$, where M may be any early transition metal, X can be carbon or nitrogen or both, and T_x can be any functional group added during the etching process from a parent MAX phase, where A = group III or IV elements[67,71]. The gas sensing capabilities of MXene are among the least researched aspects of the material since they are still in their early phases of development. According to Lee et al., ammonia sensing utilizing hybrid fibers of $Ti_3C_2T_x$ MXene/graphene with only a response of 6.6% at a concentration of 50 ppm at room temperature, with lengthier response and recovery time in the range of several minutes, has been demonstrated at room temperature [251]. Naqvi et al. employ DFT first-principle calculations to explain the adsorption capability of M_2NT_x (M=Ti, V) MXenes for a variety of air pollutants.[125] In addition, Yuvan et al. demonstrated the detection of flexible sensors employing the 3D MXene system for detecting volatile organic compounds at lower concentrations [252]. As a sensing material, the great majority have utilized titanium-derived $Ti_3C_2T_x$ MXenes.[253–256]. There have also been attempts to use different MXenes in gas sensing applications for other VOCs and pollution gases, including Sc_2CO_2 and V_2CT_x [123,126]. In spite of the fact that Ti-based MXenes have been extensively used, Mo-based Mo_2CT_x Mo_2CT_x MXenes offer greater conductivity as well as stronger chemical activity as relative to Ti-based MXenes, that could accelerate gas adsorption and, therefore, increase the sensing performance of the material.[83,107]. For example, Guo et al. reported on the selective sensing of toluene out of a variety of volatile organic compounds (VOCs) including such benzene, acetone, ethanol, and others, utilizing Mo_2CT_x as a detection method [124]. In spite of this, Zhou et al. used a complex nitrogen-doped $Ti_3C_2T_x$ MXene/polyethyleneimine combination with prolonged response and recovery (8.8-9 minutes), which may make it insufficient for real-time monitoring [257]. There is a demand for small, low-power consuming, ultrasensitive CO_2 gas detectors with quick response recovery for use in commercial applications.

The release of increased amounts of carbon dioxide into the atmosphere is the primary driver of global warming, which results in climate change and the occurrence of related natural disasters [345]. The primary source of these emissions is the combustion of fossil fuels, which is supplemented by industrial emissions.[129]. Detection and monitoring

of low concentrations of CO_2 are critical in a wide range of sectors, including agriculture, environmental monitoring, food processing, and biological applications[194,196,332,346]. One of the primary worries of the new world, as global corporations implement unique techniques to bypass green standards, is the low concentration discharges of CO_2 from industries, that should be regulated in real-time for a prolonged period of time [347]. In addition, the use of CO_2 gas detection in current medical diagnostics is critical[348]. Another requirement for large-scale agricultural production is that the greenhouse's CO_2 levels need controlled and regulated to ensure photosynthesis [128]. There is a pressing demand for CO_2 gas detectors with a good signal-to-noise ratio in all these applications.

On the other hand, Clean, sustainable, and carbon-free fuel is one of the main issues facing science and technology in the 21st century. For its carbon-free, high-efficiency, and environmentally friendly energy generation, hydrogen is seen as the fuel of the future [349]. When compared to other techniques of hydrogen fuel synthesis, such as coal gasification, steam methane reforming, and so on, electrocatalytic hydrogen evolution by means of water splitting is regarded to be the cleanest [350,351]. One main disadvantage of water splitting is the poor efficiency with which it produces hydrogen (H_2). To overcome this, scientists are in a search of highly efficient and robust catalysts capable of lowering the overpotential close to zero volts and thereby accelerating the cathodic hydrogen evolution reaction (HER)[352,353]. Noble metals such as platinum, rhodium, ruthenium, etc., or their composites are widely used because of their ability to lower the overpotential near zero along with the outstanding electrocatalytic HER efficiency[354]. Due to various limitations such as the high cost and scarcity of noble metal catalysts together with the low efficiency from the alternate catalysts, only 4% of H_2 is produced from water splitting [355,356] For the large-scale clean production of H_2 more economically, non-noble metal catalysts with low cost, stability, and higher efficiency are needed[91].

In this chapter we are going to discuss about the synthesis and characterization of Mo-In-C non-MAX phase and Mo_2CT_x MXenes by varying the synthesis parameters and extending their application for gas sensing and electrochemical hydrogen evolution reactions.

8.2 Materials and Methods

8.2.1 MXene Synthesis:

Mo_2CT_x was synthesized from Mo-In-C non-MAX phase synthesized via HF free etching method reported elsewhere [357]. For the preparation of Mo-In-C non-MAX phase, Mo_2C bulk powder (99.5%; Sigma Aldrich) and indium powder (In, 99.9%; Sigma Aldrich) mixed

in the molecular weight ratio of 1:5 using a mortar and pestle for 40 minutes until a uniform mixture is obtained. The obtained mixture was immediately passed to a tubular furnace equipped with constant Argon flow for the calcination in an inert atmosphere at different synthesis temperatures from 850 (M850), 1000 (M1000) to 1100 ºC (M1100) for a reaction time of 2 hours. Then, obtained solid substance was immersed in concentrated hydrochloric acid (37%; Sigma Aldrich) to remove the unreacted indium particles. After the removal of HCl and unreacted In, the obtained powder was etched under ultraviolet light in phosphoric acid for a time of 24 hours for etching out the In from the Mo-In-C MAX phase. Then the solution was washed several times using distilled water until pH ~ 6 to remove the phosphoric acid. After the above process, the obtained slurry was exfoliated using an ultrasonic bath for obtaining layered Mo_2CT_x MXene with -O terminated groups. The obtained MXenes were named as MX850, MX1000, and MX1100 respectively.

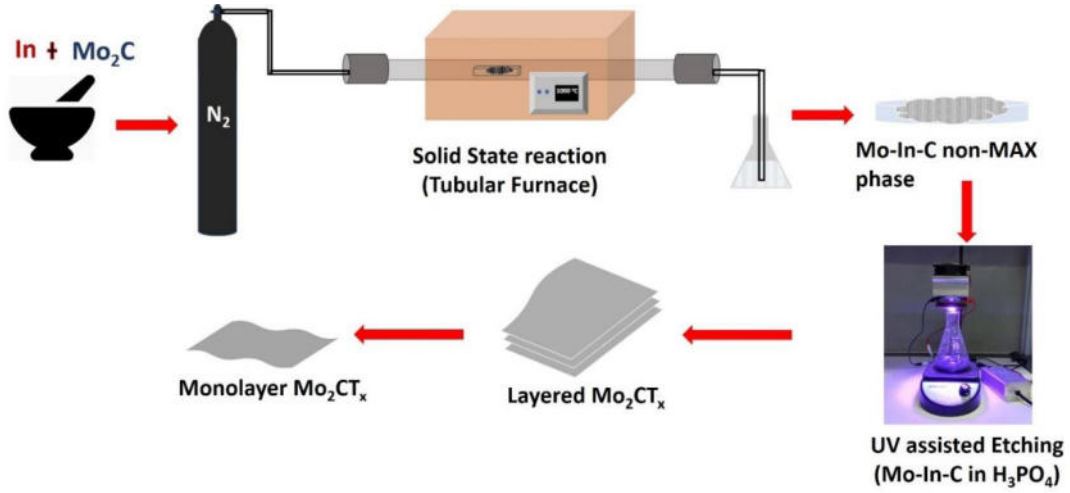

Figure 8.1 The preparation of 2D Mo_2C MXene out of Mo-In-C non-MAX phase is illustrated in this diagram.

8.2.2 Gas sensor fabrication

As part of the sensor's construction, we mixed the Mo_2CT_x powder with drops of distilled water to get the desired mud-like consistency and deposited it to either the porous or crystalline silicon substrates (University wafer; 14–22 cm resistivity). A hot plate at 50 °C was used to dry the substrates after deposition. The porous silicon substrate was made using a method described by our group elsewhere [358]. Briefly, p-type silicon wafers were electrochemically etched using concentrated hydrogen fluoride (48%; Fermont) over 10 minutes at a constant current of 6 $mAcm^{-1}$.

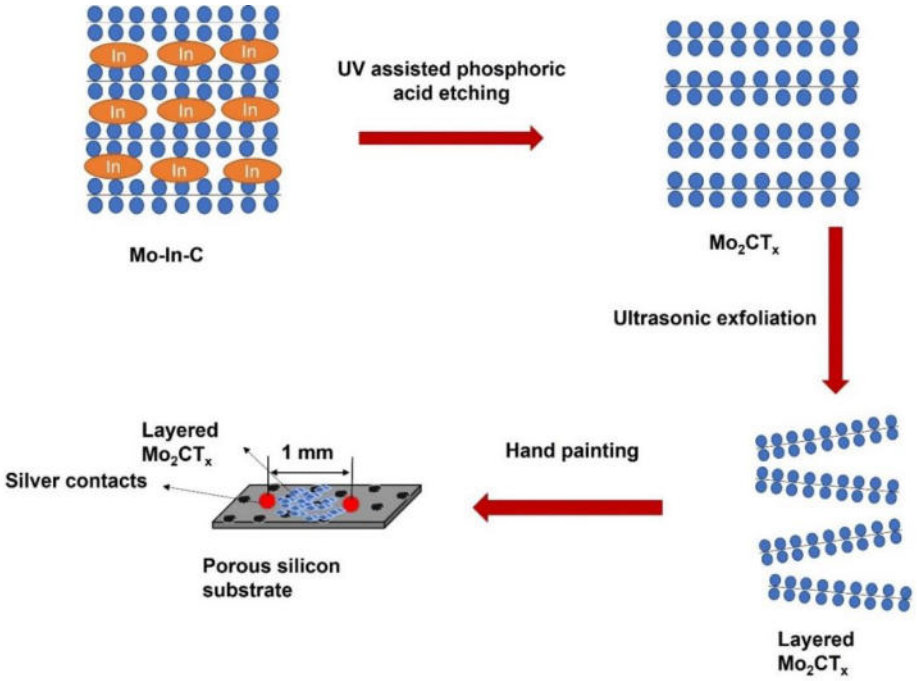

Figure 8.2 Pictorial representation of the production of Mo_2CT_x MXene and the fabrication of the sensor.

8.2.3 Preparation of electrocatalyst (working electrode) for electrochemical hydrogen evolution:

Obtained 4 sets of samples were used for the fabrication of electrocatalyst electrodes on nickel foam (Fig:8.3). For that, a slurry was prepared using 5mg of Mo_2CT_x MXene powder in 25 µL of Isopropyl alcohol (Sigma Aldrich;98%) and 25 µL of Nafion (Sigma Aldrich;1100W) binder mixed by ultrasonication for 1 hour to get a thick uniform slurry. The obtained slurry was uniformly deposited over 1x1 cm^2 nickel foam and dried in the hot air oven overnight at 60 ^oC used as the working electrode. For the cleaning of the nickel foam, 2M HCl followed by distilled water and ethanol and dried in hot air oven at 60 ^oC over night before deposition of the material.

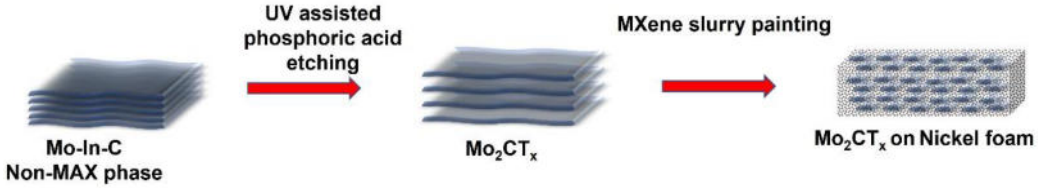

Figure 8.3 Schematic representation of the electrode preparation for the hydrogen evolution.

In this study, the structure of Mo-In-C and Mo_2CT_x was determined by utilizing an X-ray diffractometer (XRD) with a Co K_α source (λ = 1.78901 Å) using a PANalytical Empyrean X-ray diffractometer with a scan rate of 5 degrees per minute. Escalab 250Xi

Thermo Scientific X-ray Photoelectron spectrophotometer (XPS) with Al K source (λ = 1486.68 eV) was used to perform the elemental characterizations of the samples. Utilizing a Hitachi SU-8020 field emission scanning microscope with an integrated elemental analyzer, the morphology and EDS (energy dispersive x-ray spectroscopy) of the samples were determined. High-resolution transmission electron microscopy (HRTEM) using FEI-Titan G2 80-300 HRTEM was used to determine the crystal structure and morphology of the samples that were collected from the samples. A Keithley 2450 source measuring unit was used to conduct the electrical measurements. A thermo-resistance attached to the sensing setup was used to regulate the operating temperature of the produced sensors, and a conventional type-J thermocouple attached to the computer was used to monitor it. Finally, the electrochemical characterizations such as linear sweep voltammetry (LSV) and electrochemical impedance spectroscopy (EIS) were carried out utilizing Biologic SP300 potentiostat.

8.3 Results and discussions

8.3.1 Crystal Structure and Surface Morphology of Mo-In-C non-MAX phase and Mo_2CT_x MXene

The variation in the structure of the synthesized Mo-In-C non-MAX phases and corresponding MXene samples was analyzed by studying the XRD plots corresponding to each as shown in Figure 8.4. The XRD plot of the Mo-In-C non-MAX phase synthesized at different temperature is as shown in the Figure 3a. The major peaks for all the three samples were corresponding to indium (In) (ICDD:00-001-1042), Mo (00-001-1208) and orthorhombic Mo_2C (00-031-0871; a = 4.72 Å, b = 6.00 Å, c = 5.19 Å). It was observed that samples M850 and M1000 were mostly identical with all the peaks matching to each other with peak corresponding to Mo_2C at 46.38° from the plane (1 0 2). Whereas in the case of M1100 the intensity of the peak at 38.65° from the plane (1 1 1) which corresponds to the In dominates. This may be due to the involvement of the high temperature for the solid-state reaction causing the improved infusing of indium to the stoichiometry of the Mo_2C producing the non-MAX phase.

MXene samples' peaks (Figure: 4) were all same with major peaks at 40.13, 44.27, 46.19, 61.26, and 72.94°, which corresponds to the reflections from the crystal plane (0 0 2), (1 0 1), (1 0 2), and (1 1 0) of the hexagonal Mo_2C MXene (ICDD card no: 00-035-0787; a = b = 2.99 Å, c = 4.72 Å). For the samples, MX850, MX1000 and MX1100 made from the Mo-In-C non-MAX phases synthesized at 1000 and 1100 °C exhibited a peak at 47.34° corresponding to cubic molybdenum (ICDD card no:00-042-1120), which may be because of high temperature involved reaction causing the breakdown of Mo_2C crystal. Interestingly, the Mo peak was absent in the MX1000 even if synthesized at 1000 °C. This may be because of

the recrystallization of Mo_2C happening during this period or absence of the breakdown of the Mo_2C.

According to the results of the study, the structural alterations in Mo-In-C and Mo_2CT_x might be attributed to the lattice rearrangement that happened during the synthesis of MXene by UV aided phosphoric acid etching. The crystallite sizes of non-MAX Mo-In-C and Mo_2CT_x were estimated using a modified Scherrer's formula, and they were found to be 49.12±1.3 nm and 38.27±0.39 nm, respectively, according to the results. [359]

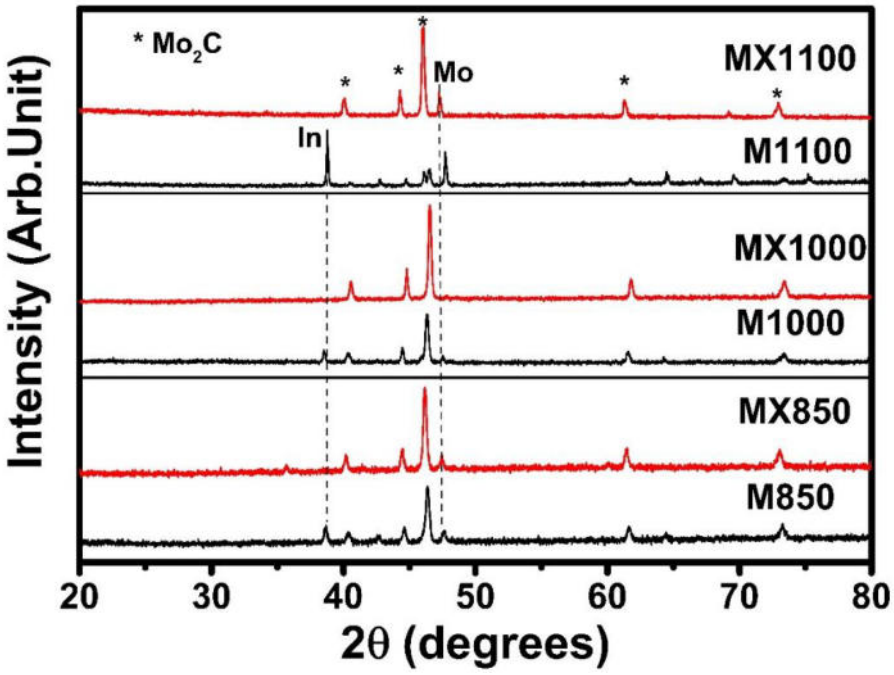

Figure 8.4 Structural characterization using XRD of different Mo-In-C non-MAX phases synthesized by varying reaction temperatures from 850 to 1100 °C and corresponding Mo_2CT_x MXenes.

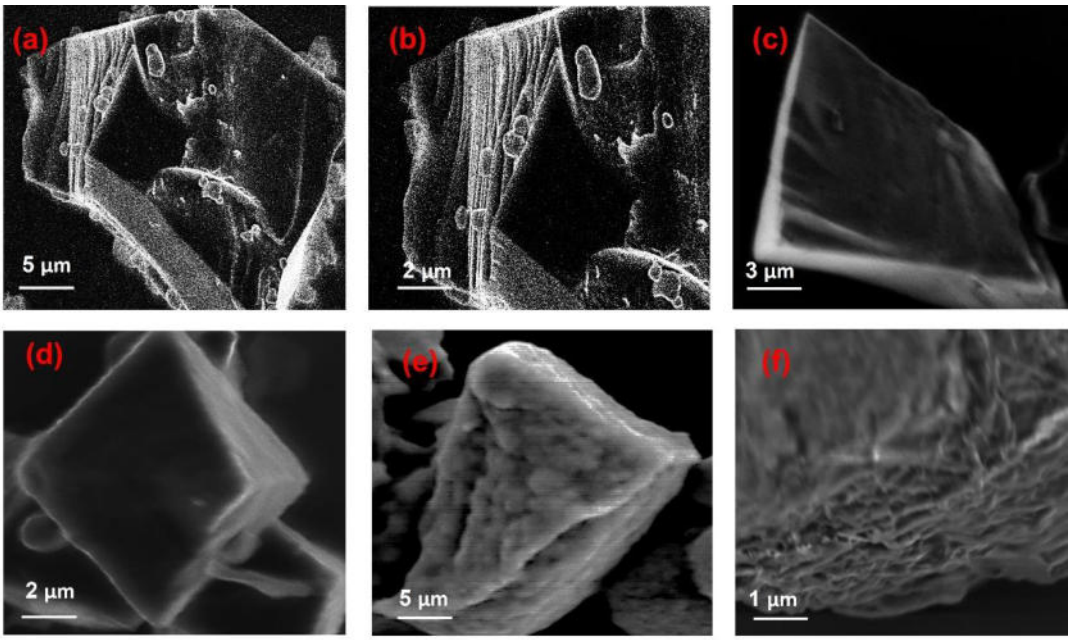

Figure 8.5 FESEM images of (a-b) MX850, (c-d) MX1000 and (e-f) MX1100 MXenes.

Morphology of the synthesized MXenes were analyzed using the FESEM characterization, which is illustrated as shown in Figure 5. The layered morphology of the 2D MXene was visible for the samples MX850 and MX1100 (Fig:8.5a-b, and 8.5 c-d). Whereas in the case of M1000 layers were not clearly visible from the FESEM images (Fig:5c-d). This could be the result of the lack of exfoliation or proper reaction at this temperature causing separation of the layers. The interplanar spacing of Mo_2CT_x (Fig:8.6b) increased little relative to its precursor Mo-In-C non-MAX (Fig:8.6a) when analyzed using HRTEM images. As a result of the phosphoric acid etching under UV light and ultrasonic exfoliation of the Mo_2CT_x MXene, the interplanar spacing has increased, perhaps due to the intercalation of the functional group (-O)[360]. This layered morphology increases the surface area which may enhance the HER performance or gas sensing performance due to the availabilities of more active sites.

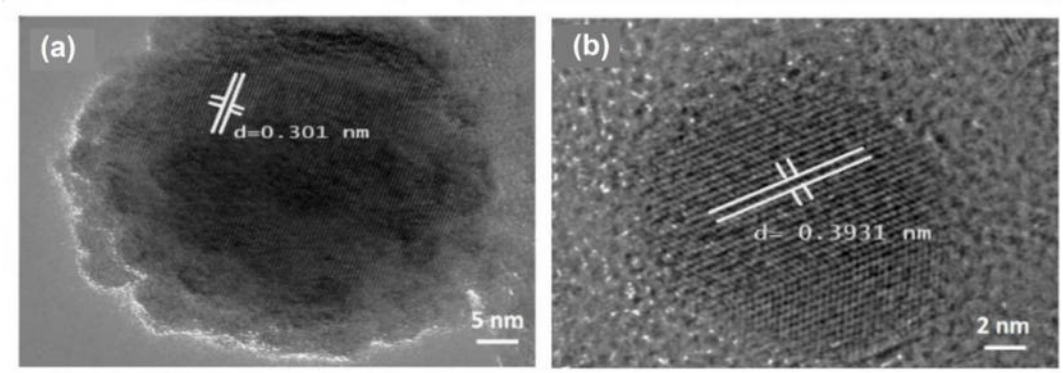

Figure 8.6 TEM images of (a)Mo-In-C and (b) Mo_2CT_x, respectively.

Samples were put on an Al substrate to record the EDS spectra, and as a result, an Al -K peak was identified in the EDS spectra (Fig:8.7). The empirical formula $Mo_6In_2C_7$ was derived from the relevant EDS data and applied to the as-synthesized non-MAX phase, which contained Mo, C, and In. A thorough examination on EDS spectrum of phosphoric acid etched Mo_2CT_x samples verified that In had been eliminated from the stoichiometry of $Mo_6In_2C_7$. The presence of an oxygen signal in the EDS spectrum of Mo_2CT_x indicates that the phosphoric acid etching process resulted in the intercalation of the -O functional group [228].

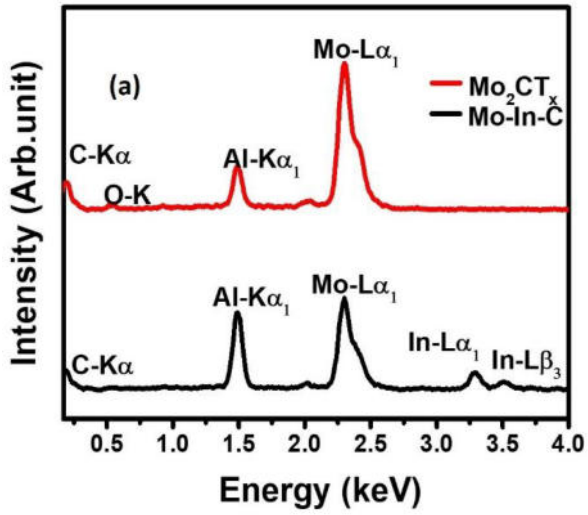

Figure 8.7 EDX spectra of Mo-In-C (M1100) and Mo_2CTx (MX1100).

The XPS survey spectra show the elemental composition Mo-In-C non-MAX phase and Mo_2CT_x MXene (Fig:8.8a). The core-level spectrum of Mo 3d related to Mo_2CT_x is shown as (Fig:8.8b) with doublet peaks of Mo $3d_{3/2}$ and Mo $3d_{5/2}$ at 235.92 and 232.89 eV, respectively. These peaks can be related to 3 main components with 235.92 and 235.68 corresponding to Mo^{6+} (Mo_xO_y), 232.89 eV agreeing with Mo^{4+} (Mo-X) sub-stoichiometric molybdenum carbide or molybdenum oxycarbide, and 231.65 eV equivalent to the Mo^{2+} (Mo-C) oxidation states of molybdenum [361,362]. In the core level spectrum of the C 1s (Fig:8.8c), the deconvolution resulted in 5 signals at 282.98, 283.78, 284.67, 285.57, and 286.67 eV, which correspond to typical Mo_2CT_x bonding Mo-C, C-C, C=O, and C-OH, respectively[228,363]. Whereas for the deconvoluted core level spectrum of O 1s (Fig:8.8d) there were 3 signals at 530.67, 531.95, and 532.97 related to the Mo-O (molybdenum oxide), C-OH, and M-OH, respectively[255]. Thus, the XPS characterization along with XRD results confirm the formation of the Mo_2CT_x MXene from the Mo-In-C non-MAX phase by the selective etching of In and the presence of -O in the stoichiometry by the means of UV-assisted phosphoric acid etching and exfoliation.

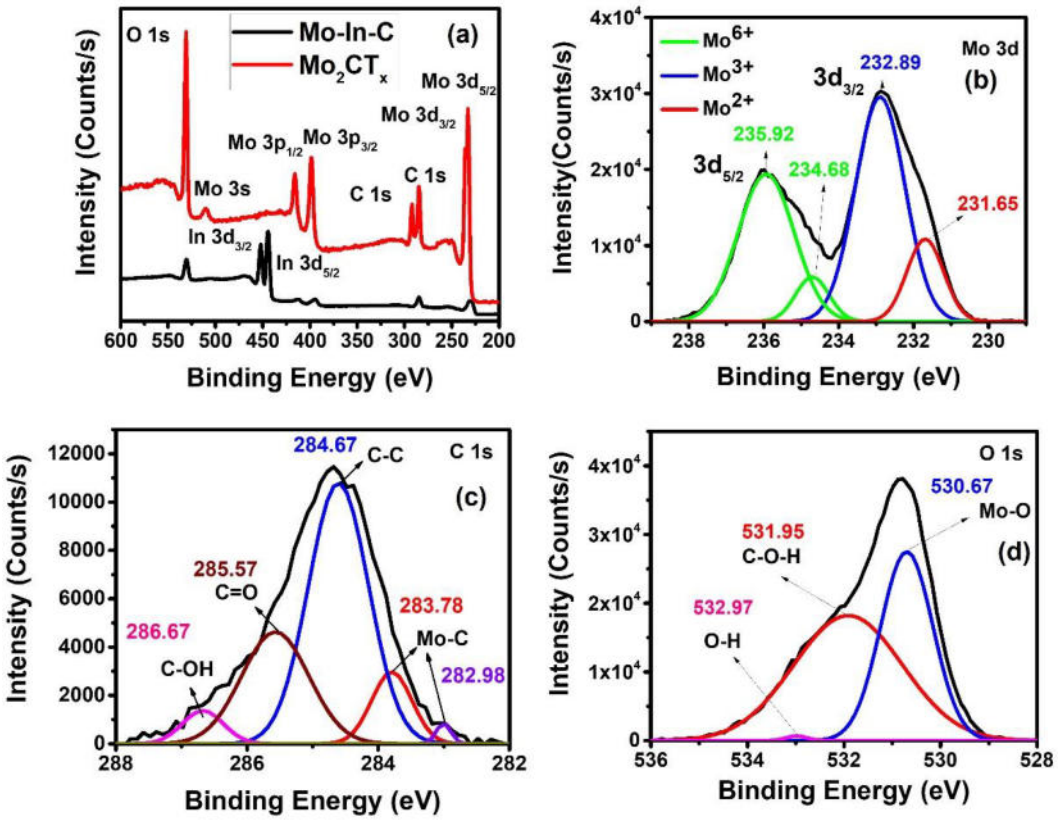

Figure 8.8 XPS survey spectrum of the as-synthesized Mo-In-C non-MAX phase (at 1100°C) and Mo_2CT_x MXene (a) and high-resolution spectrum of the Mo 3d, C1s, and O1s of the Mo_2CT_x MXene.

8.3.2 Mo_2CT_x MXene for carbon dioxide gas sensing

Following deposition of the Mo_2CT_x MXene layer on porous silicon substrate, the morphology of pSi/Mo_2CT_x was studied by FESEM characterisation (Fig:8.9). Before the deposition, the surface morphology of the porous silicon substrates was examined, and FESEM pictures revealed homogeneous pores with a pore size range of 350-950 nm. (Fig:8.9a-b). Surface and cross-section photos clearly show the homogeneous deposition of multilayered Mo_2CT_x MXene on porous silicon(Fig: 8.9c-f). There was a continuous film of Mo_2CT_x MXenes covering both the surface and the pores of the porous silicon substrates (Fig:8.9c,d, and f). The cross-section images were used to estimate the thin film thickness over the substrate and it is 1.096 ±0.34 μm on average. It was possible to see the Mo_2CT_x MXene's layered shape in the high-resolution FESEM pictures (Fig:8g-h), and the EDS elemental mappings confirmed the existence of Mo, C, and O in the atomic percentages of 51.57, 26.44, and 21.97% (Fig:8i-l).

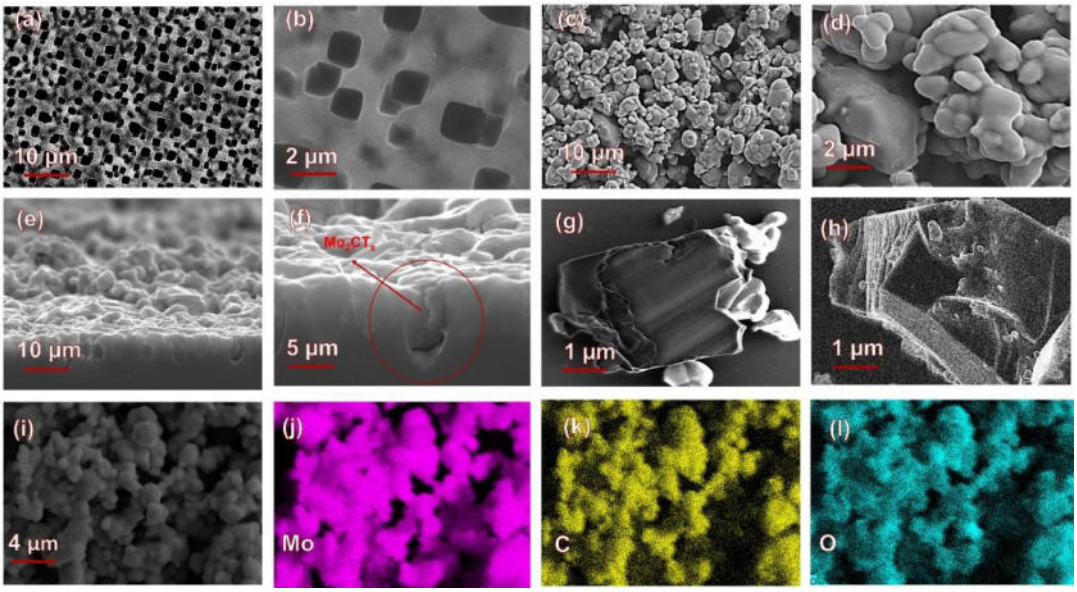

Figure 8.9 FESEM images of the porous silicon substrate (a and b), pSi/Mo_2CT_x sensor surface (c and d) cross-section images of the sensor (e and f), and high-resolution images of the layered Mo_2CT_x Mxenes. EDS mapping images of the Mo_2CT_x on pSi (i-l).

The effect of the substrate material on the sensing performance was investigated systematically by comparing the sensitivity of the fabricated sensors on cSi, pSi, and glass by varying concentrations of CO_2 gas (50ppm, 100 ppm, and 150 ppm) and working temperature from room temperature (30) to 250 °C. For the sensing measurements the percentage sensitivity ($\%S$) was calculated using the formula (Equation 8.1) [211,358]:

$$\%S = \frac{(R_g - R_a)}{R_a} \times 100 \qquad (8.1),$$

where R_a is the resistance in the ambient air and R_g is the resistance in the presence of the CO_2 gas. Sensing responses of the fabricated sensors are displayed in Fig:8.10. At room temperature, the sensor fabricated on a glass substrate (Fig:8.10a) showed the highest percentage response of 2.31% for 150 ppm of CO_2, which is the highest among other fabricated sensors of this study and the previous reports to the best of our knowledge (Table 8.1). In addition to that detection of 50 ppm of CO_2 at 30 °C was achieved with a percentage sensitivity of 1.14%, which is also the highest compared to the previous reports on MXene based CO_2 sensors working at low temperatures (Table 8.1). A gradual increase in the sensing response with the increase in the working temperature from 30 to 200 °C for pSi/Mo_2CT_x, cSi/Mo_2CT_x, and glass/Mo_2CT_x sensors for all three concentrations (50, 100, and 150 ppm) of CO_2. Similar to our previous report [358], pSi/Mo_2CT_x sensors showed a higher sensing response compared to cSi/Mo_2CT_x and glass/Mo_2CT_x sensors (Fig:8) at higher working temperatures (other than room temperature) and all CO_2 concentrations. The highest percentage sensitivity of 25% was detected for the pSi/Mo_2CT_x sensor working at 250 °C and 150 ppm of CO_2 gas (Fig:8c). In the case of cSi/Mo_2CT_x it was only 13% at the same condition and 9.5% for glass/Mo_2CT_x at

the same conditions(Fig:8a-b). Even though the sensitivity of cSi/Mo_2CT_x was almost half of the pSi/Mo_2CT_x, it was still higher than the cSi/MoO_3 sensor (S=8%) reported elsewhere by our group[358]. Also, we observed that after 200 ^oC the sensitivity of the cSi/Mo_2CT_x sensor was reaching saturation with no increase for all the 3 concentrations of CO_2 gas, unlike the pSi/Mo_2CT_x sensor. In the case of glass/Mo_2CT_x it decreases from 15.4% at 200 ^oC to 9.5% at 250 ^oC for a CO_2 concentration of 150 ppm which also indicates the presence of a saturating working temperature for the sensor. This indicates the porous nature of the substrate plays a critical role in the sensing mechanism as explained further. It was also observed that the resistance of the sensors kept increasing positively on the exposure of CO_2 gas in all cases similar to the previous reports on MXene based sensors [124,251,347], which is explained below in the mechanism part.

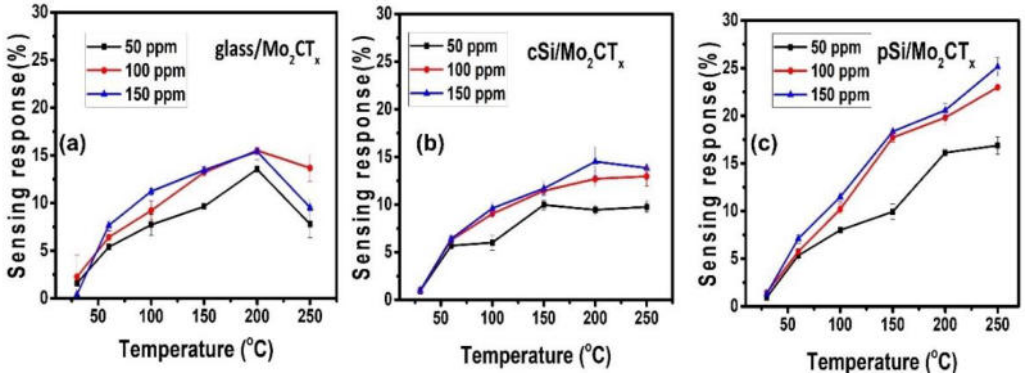

Figure 8.10 Working temperature v/s percentage sensitivity for **glass**/Mo_2CT_x (a), cSi/Mo_2CT_x (b) and pSi/Mo_2CT_x (c) sensors for different CO_2 concentrations.

After analyzing the pSi/Mo_2C at different concentrations and temperatures, the same device was further evaluated at dry (30%, RH) and wet conditions (66%, RH)(Fig:8.10 and 11) to study the effect of humidity. It was observed that there was an increase in the sensitivity with the increase in the humidity (66%, RH) i.e., the percentage sensitivity at 250 ^oC and 150 ppm of CO_2 increased to 32% (Fig:8.11b) from 25%. Similar observations were obtained during the experiments with other working temperatures and CO_2 gas concentrations (Fig:8.11). Thus it was observed that humidity plays a vital role in the sensing performance of the fabricated sensor which is explained in detail later.

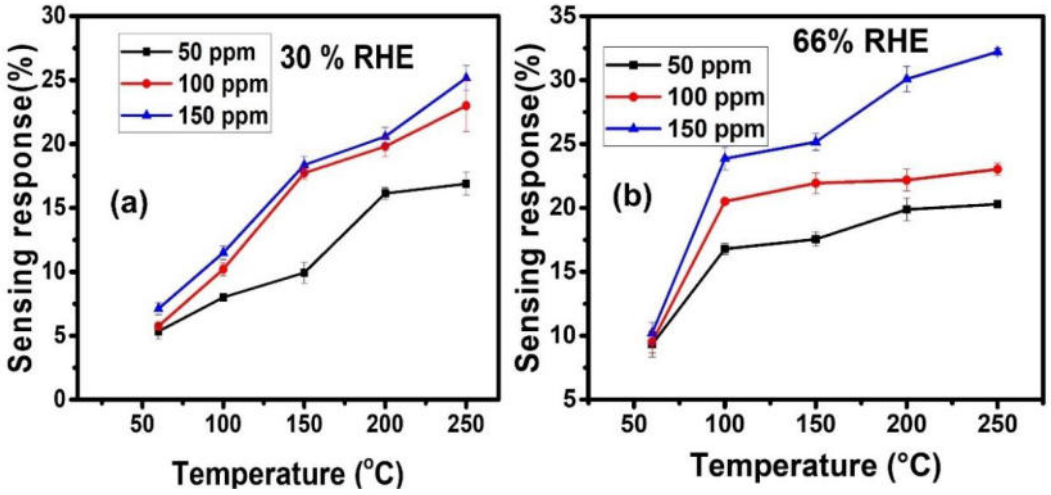

Figure 8.11 The variation in the sensing response with 30% (a) and 66% (b) of humidity for the pSi/Mo_2CT_x sensor.

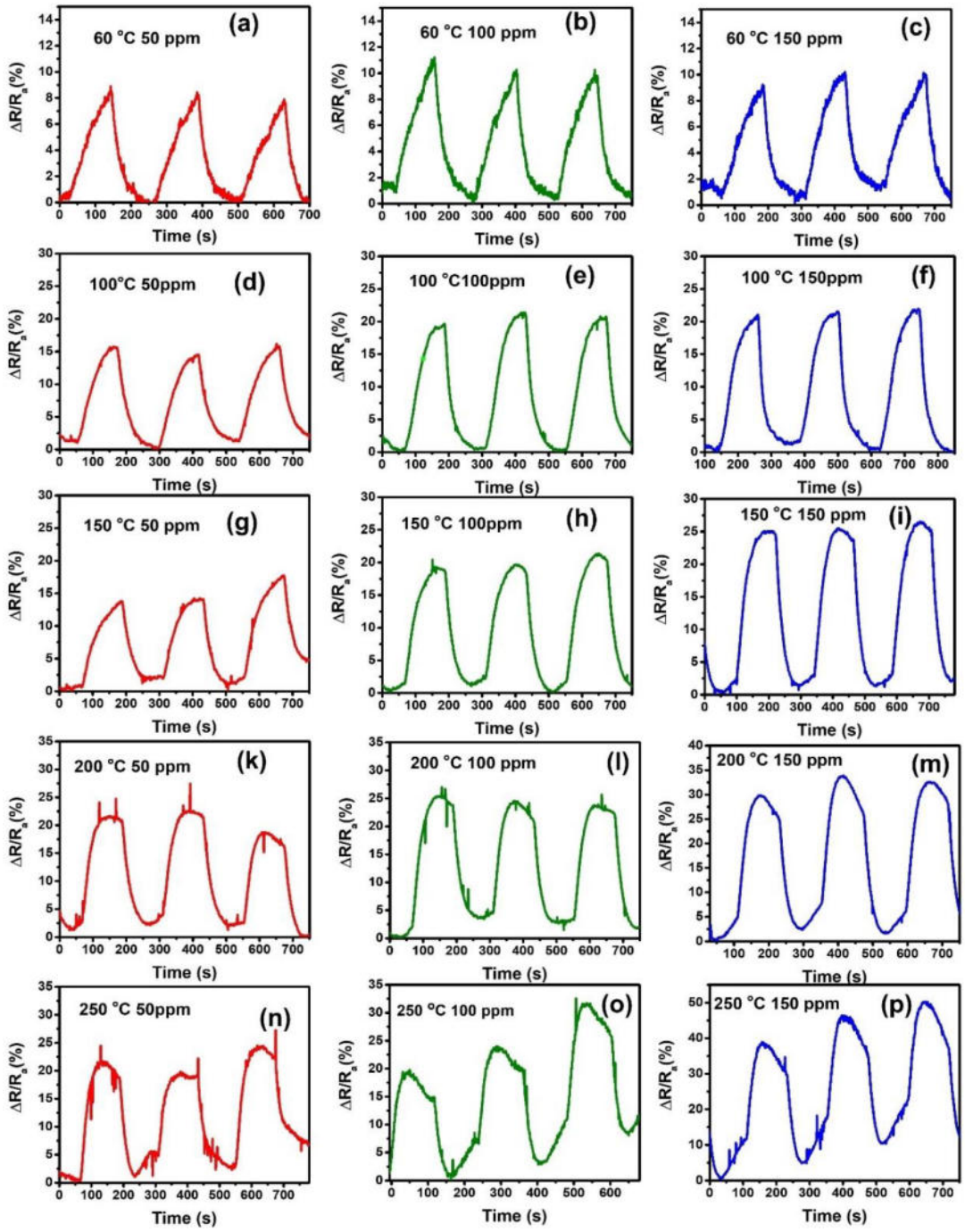

Figure 8.12 Dynamic response studies of pSi/Mo_2CT_x sensor at 66% humidity for different working temperatures (60, 100, 150, 200, and 250 °C) and CO_2 (50, 100, and 150 ppm) concentrations.

All the three fabricated sensors glass/Mo_2CT_x, pSi/Mo_2CT_x, and cSi/Mo_2CT_x sensors exhibited quick response and recovery times compared to other reported MXene based CO_2 gas sensors (Table 8.1). Even at a low room temperature of 30 °C, the pSi/Mo_2CT_x sensor showed a fast response and recovery times of 32 s and 45 s, respectively (Fig:8.13) for 50 ppm of CO_2 gas. With the increase in working temperature, we observed a quicker response and

recovery time for both sensors. In the higher humidity conditions (66%), the response and recovery times were a little slower with values of 66.57 s and 113.43 s, respectively for a pSi/Mo_2CT_x sensor working at 60 °C and 50 ppm of CO_2 (Fig:8.14). Among all the observations we made, the fastest response and recovery times of 27 s and 32 s were observed for the pSi/Mo_2CT_x sensor working at 250 °C and 150 ppm of CO_2 (Fig:8.13i), which is the lowest reported value for an MXene based CO_2 gas sensor. For a commercial application, low power consuming, highly sensitive sensors with fast response and recovery times are essential. In addition to that, miniaturization of the sensor devices is also desirable for low-cost production, where porous materials with higher surface areas can serve the purpose. For that, our fabricated pSi/Mo_2CT_x sensor can work at room temperature (30 °C) consuming low power with lower limits of detection (50 ppm) along with the fast response and recovery times compared to existing CO_2 sensors working at low temperatures (Table 8.1). Although there are reports on the room temperature CO_2 sensing based on the MXenes, the response and recovery times were too long in the order of several minutes and sensing responses were too low, which makes them difficult for real-time applications .

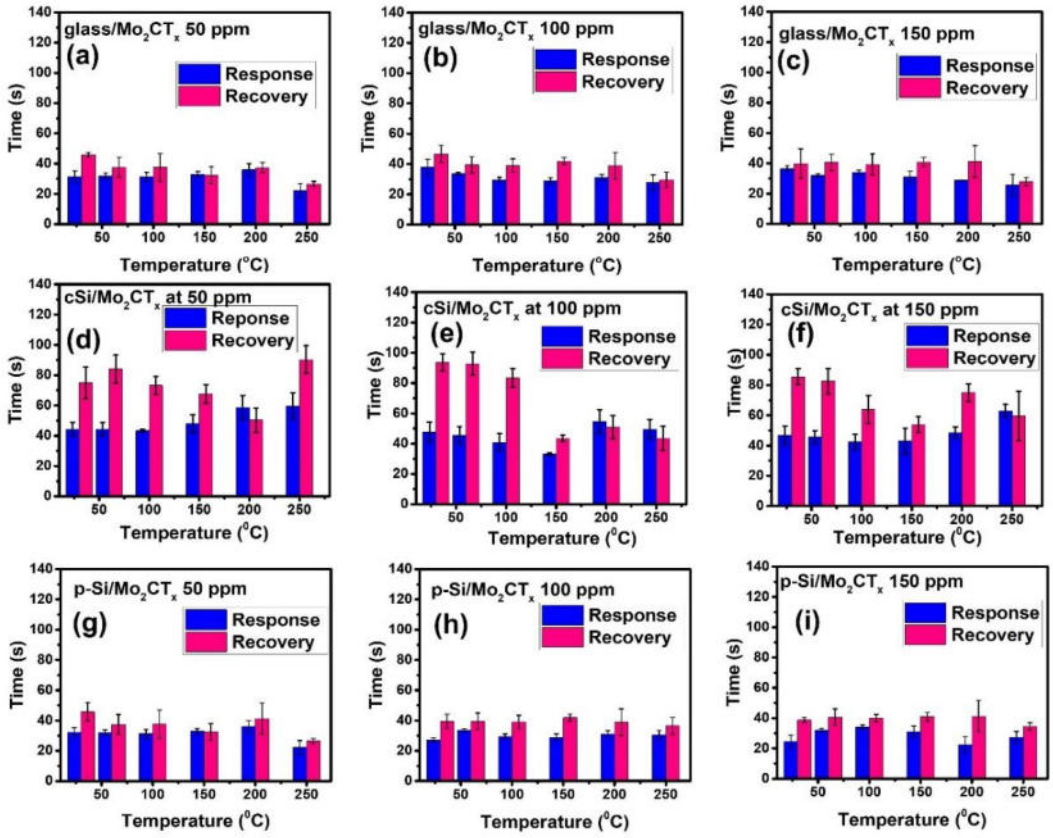

Figure 8.13 Response and recovery times for the SiO_2/Mo_2CT_x, cSi/Mo_2CT_x, and pSi/Mo_2CT_x sensors at different working temperatures and CO_2 concentrations.

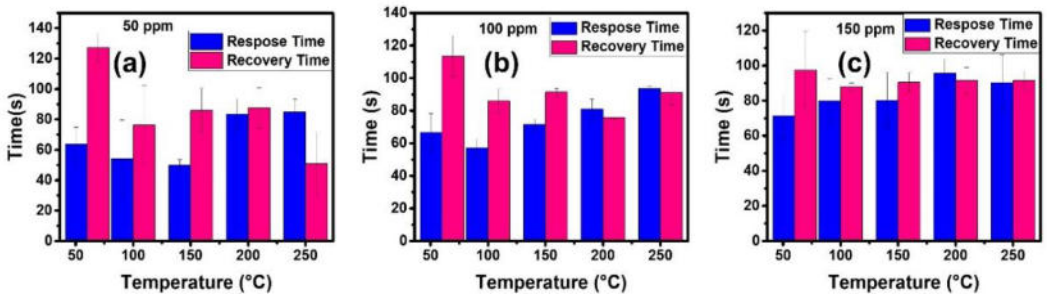

Figure 8.14 Response and recovery times calculated for pSi/Mo_2CT_x sensors at 66% humidity for different working temperatures (60, 100, 150, 200, and 250 ^oC) and CO_2 (50, 100, and 150 ppm) concentrations.

The repeatability studies of the fabricated pSi/Mo_2CT_x, cSi/Mo_2CT_x, and glass/Mo_2CT_x sensors were carried out by measuring the percentage sensitivity for repeated sensing cycles by varying the working temperature and the CO_2 concentrations as shown in (Figures 8.12,8.15-8.18). All the three sensors were mostly stable for repeated cycles with the response curves identical to each other for all the different variations in the concentrations and working temperature. There was a gradual increase in the sensing response with the increase in the working temperature as well as with the CO_2 concentrations. The percentage sensitivity was almost constant for repeated experimental cycles even at lower working temperatures (30 ^oC) and low CO_2 concentrations as low as 50 ppm (Fig:8.15a). This indicates that fabricated sensors were highly repeatable over a range of temperature as well as concentrations.

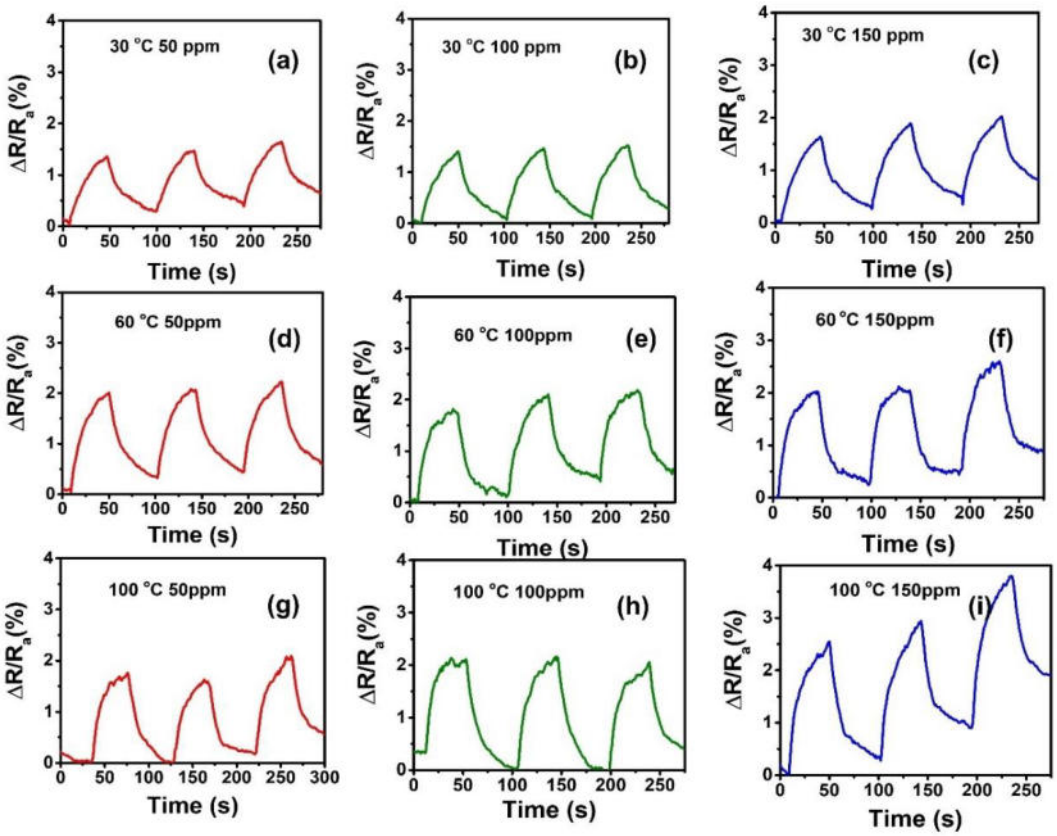

Figure 8.15 The low-temperature dynamic response studies of the fabricated pSi//Mo_2CT_x sensors for different working temperatures (30,60, and 100) and different CO_2 concentrations (50, 100, and 150 ppm)

The stability of the fabricated pSi/Mo_2CT_x sensor was studied by performing the sensing characterization at 60 °C and 150 ppm of CO_2 gas for 65 days after fabrication and comparing the percentage sensitivity (Fig:8.20). It was observed that the percentage sensitivity decreased ~2% after 65 days of stable operation which confirms the high stability of the fabricated pSi/Mo_2CT_x sensor.

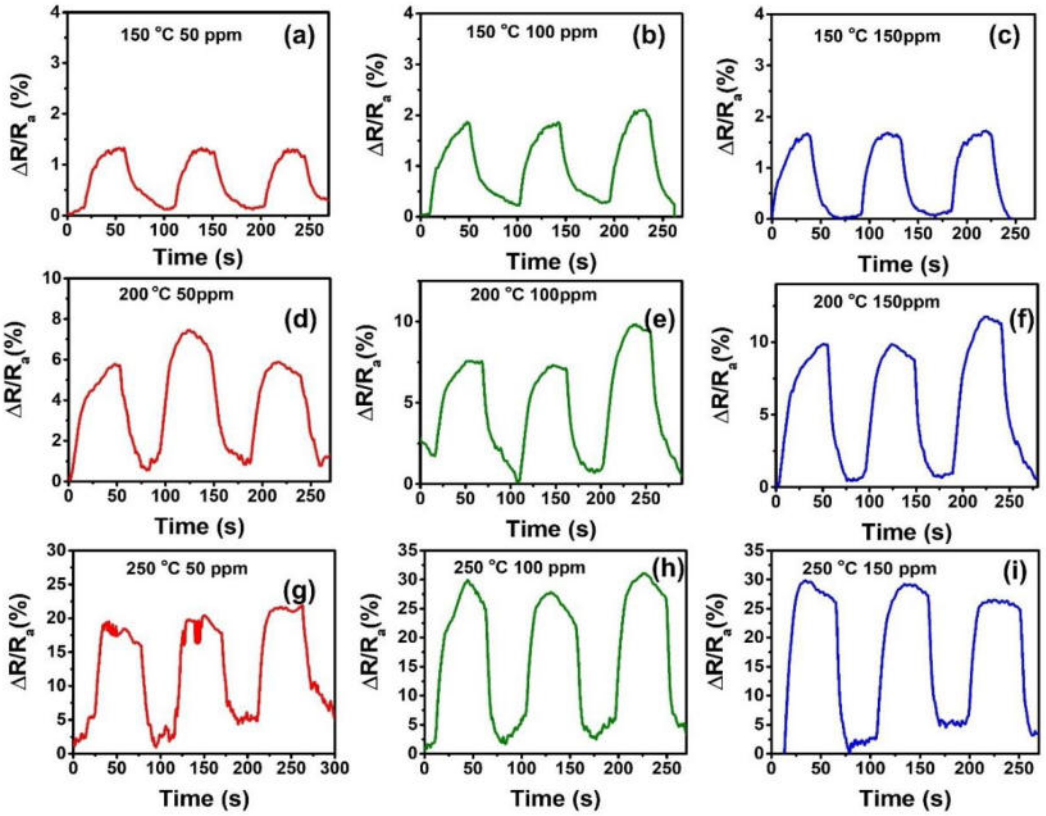

Figure 8.16 The high-temperature dynamic response studies of the fabricated pSi//Mo_2CT_x sensors for different working temperatures (150, 200, and 250 °C) and different CO_2 concentrations (50, 100, and 150 ppm)

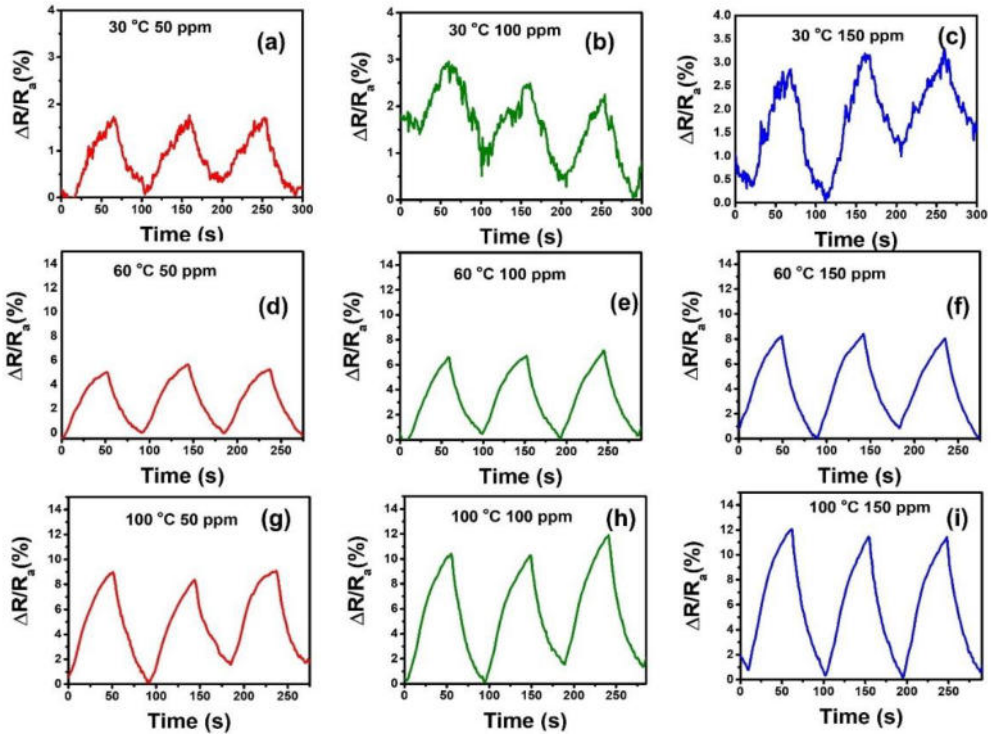

Figure 8.17 Low-temperature dynamic response studies of glass/Mo_2CT_x sensor for different working temperatures (30, 60, and 100 °C) and CO_2 (50, 100, and 150 ppm) concentrations.

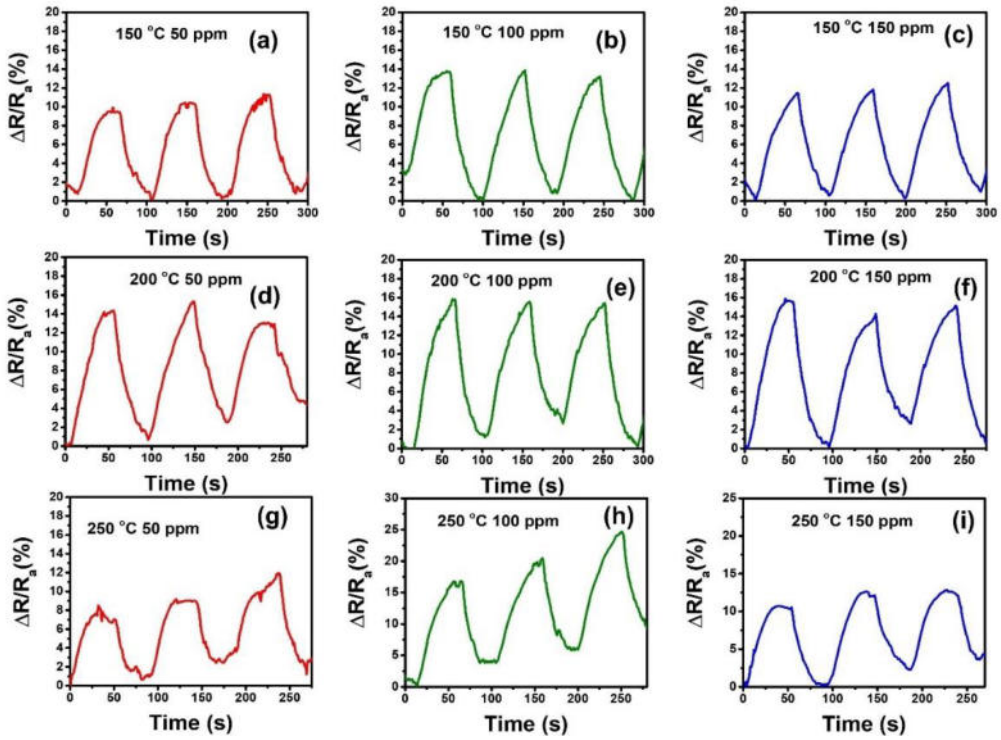

Figure 8.18 High-temperature dynamic response studies of glass/Mo_2CT_x sensor for different working temperatures (150, 200, and 250 °C) and CO_2 (50, 100, and 150 ppm) concentrations.

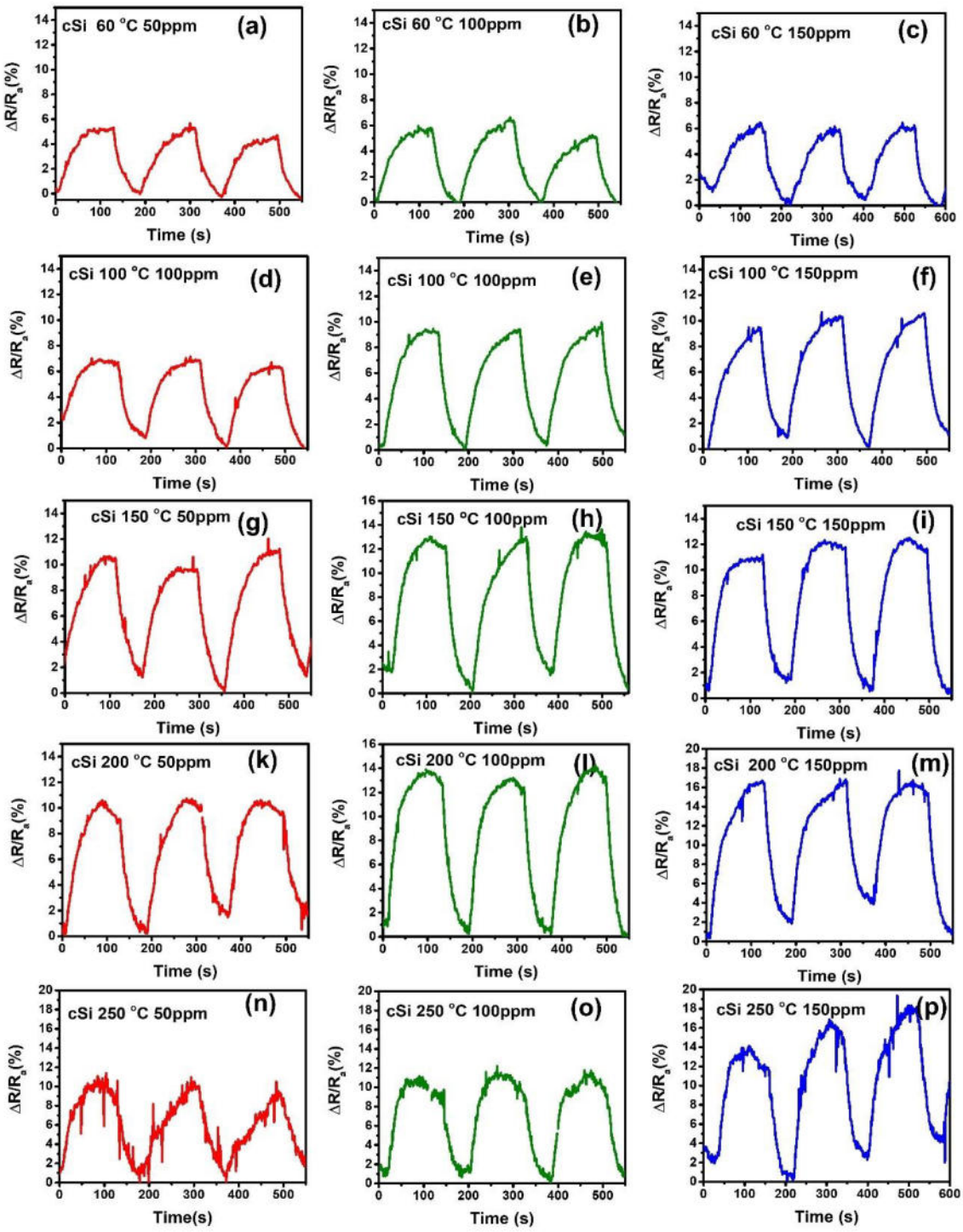

Figure 8.19 Dynamic response studies of cSi/Mo_2CT_x sensor for different working temperatures (60, 100, 150, 200, and 250 °C) and CO_2 (50, 100, and 150 ppm) concentrations.

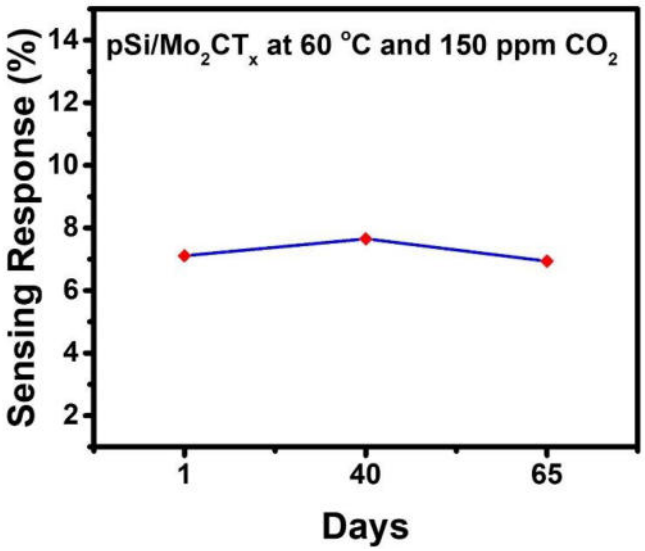

Figure 8.20 Stability curve for the fabricated pSi//Mo_2CT_x sensors working at 60 ºC and 150 ppm of CO_2 gas for 65 days.

Table 8.2 Comparison of CO_2 sensing performance with similar materials

Sensing material	**Sensing response (%)**	**The detection limit (ppm)**	**Response and recovery time**	**Working temperature (º C)**	**Reference**
pSi/Mo_2CT_x	1.14	50	30 and 45 s	30	
glass/Mo_2CT_x	2.3	150	28 and 40 s	30	This work
Si/SiO_2/rGO/N-MXene/PEI	~1	8	8.8 and 9 mins	20	[257]
Si/SiO_2/$Ti_3C_2T_x$	0.53	Not Reported	Not reported	RT	[256]
SiO_2/$Ti_3C_2T_x$	0.1	10000	Not reported	RT	[255]
SiO_2/Sulfonated polyether ether ketone	47	5000	4.17 and 27.02 mins	RT	[329]
PAA-amino CNT	-	1000	3.07 and 2.95 mins	RT	[364]
SnO_2/rGO	0.07	5	-	RT	[365]
$BaTiO_3$–CuO	-	500	2 mins	RT	[366]

TiO_2–PANI	53	1000	9.2 and 5.7 mins	RT	[367]
ZnO/CuO	9.7	1000	1-4 mins	RT	[368]

The sensing mechanism of the fabricated pSi/Mo_2CT_x, cSi/ Mo_2CT_x, glass/Mo_2CT_x sensors can be explained as the semiconducting behavior similar to the previous reports on MXene based gas sensors towards oxidizing gases [252,369]. The semiconducting behavior of the Mo_2CT_x MXene can be related to the presence of oxygen funtionalization on the surface [370]. A positive change in the resistance was observed throughout the experiment on the exposure of oxidizing electrophilic CO_2 gas on the sensor surface. This response is similar to the previous reports on MXene sensors, which is caused by a decrease in the density of charge carriers on the surface of the sensor when CO_2 gas molecules are adsorbed during exposure [255]. This phenomenon can be explained briefly as the reaction of the -O species (which are attached to the stoichiometric Mo_2CT_x MXene as a consequence of the UV-assisted phosphoric acid etching), and CO_2 molecule producing a metastable $(CO_3)^{2-}$ ion with the expense of thermal energy (Equation 8.2), causing an electron scarcity on the surface of the sensor during the exposure of the gas [358,369]. The proposed reactions are reversible once the gas flow is turned off, i.e., we observed a decrease in resistance to their initial values.

$$Mo_2C_{1-x}O_{1-y} + \ddot{V_{O_y}} + 2e^- + CO_2 \overset{\Delta T}{\rightleftharpoons} Mo_2C_{1-x}O_{2x} + (CO_3)^{2-} \quad (8.2)$$

The increase in the sensing response with the temperature can also be related to the semiconducting behavior of the fabricated sensor[127,333,346,369]. With the increase in the temperature, the initial resistance values decreased considerably due to the thermally generated electrons. This increment in electron density causes an increase in the relative difference between R_a and R_g. Therefore, we observed an increased sensitivity at higher operating temperatures compared to lower ones. On the other hand, a higher sensing response in the high humid condition can be explained as the acceleration of the reaction rate due to the increased water content trapped inside the hydrophilic layered Mo_2CT_x MXene (Figure 8.21) [371]. When a water molecule is attached to the hydrophilic surface of the pSi/cSi/Mo_2CT_x sensor in a high humid condition, it reacts with CO_2 thereby decreasing the initial resistance due to the presence of additional hydroxyl groups, which serve as the electron donors[372]. The increase in the sensing response of the sensor fabricated on the pSi substrate compared to the cSi and glass was due to the increase in the surface to volume ratio and availability of more adsorption sites due to the deposition of the layered Mo_2CT_x on the pores. However, some contradictory

results were found at 30 °C. The highest room temperature sensitivity was found for the glass/Mo_2CT_x sensor when compared to the other sensors. This peculiar sensing behavior can be explained by the absence of charge carriers transferred from the surface of either cSi or pSi substrates to the MXene layer at room temperature. In the case of glass, there are no charge carriers on its surface at all the temperatures, which resulted in a lower sensing response compared to pSi when the temperature is above 60 °C at high temperatures (above 60 °C), which may contribute to the sensing response by reducing the electrical resistance of MXene layer. Moreover, at room temperature in the case of porous silicon, other gases present in the atmosphere can block the active sites inside its pores, which leads to a decrease in the sensing response. But in the case of glass and cSi substrates, their surfaces are flat and there is less chance of blocking by the ambient gases which results in a higher sensing response at room temperature compared to pSi.

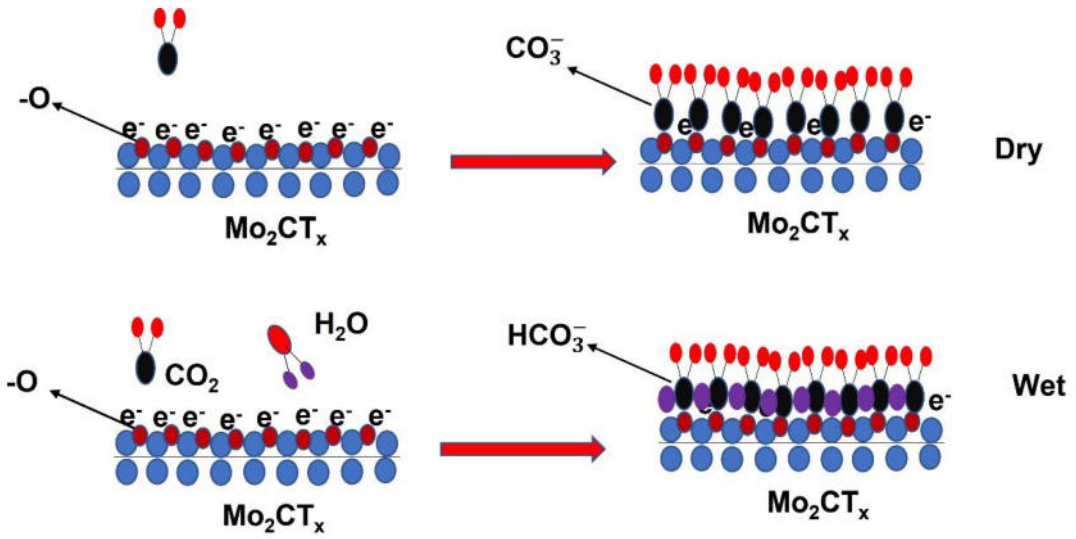

Figure 8.21 Schematic representation of the sensing mechanism at dry and wet conditions.

8.3.3 Mo_2CT_X MXene for electrochemical hydrogen evolution reaction application

The HER performance of the fabricated Mo_2CT_x electrodes was carried out in 0.5 M H_2SO_4 electrolyte. The influence of synthesis temperature of the non-MAX phase during the Mo_2CT_x on the HER performance was evaluated by performing LSV. The polarization curve for the corresponding electrodes is represented as in Figure 22a. The LSV measurements were performed at a scan rate of 5 mV/s in a stabilized system after running 20 cycles of CV. The bare nickel foam showed an overpotential of -585 mV at 10 $mA.cm^{-2}$ which confirmed the activity of the MXene material on it is solely responsible for the improved HER performance. The lowest overpotential was observed for the sample MX850, with a value of -

138 mV at a current density of 10 mA.cm^{-2}, which is the lowest reported for Mo_2CT_x MXene to the best of our knowledge [239]. For other MXene samples, the overpotentials were -350, and -240 mV for the samples MX1000, and MX1100, respectively at a current density of 10 mA.cm^{-2}. With the increase in the synthesis temperature up to 1100 ^oC the overpotential was observed increasing as shown in Fig: 8.22a. The lowest overpotential of MX850 may be due to the flaky layered morphology causing higher surface area and due to the increased conductivity.

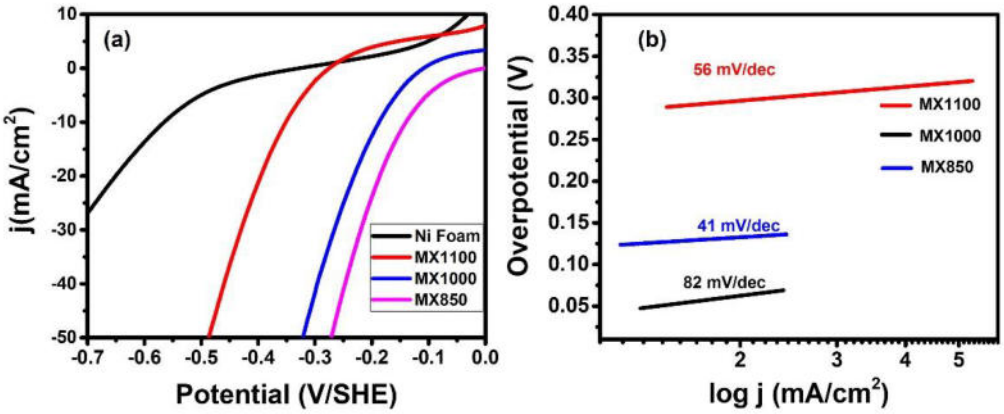

Figure 8.22 Polarization curve (a) of the fabricated Mo_2CT_x MXene synthesized from Mo-In-C non-MAX phase at different temperatures from 850 to 1100 ^oC along with the bare nickel foam and (b) corresponding Tafel slopes.

The kinetics of the HER was studied by analyzing the Tafel slopes (Fig:8.22a) drawn by fitting the polarization curves using the Tafel equation $\boldsymbol{\eta = b\ \log j + a}$, where b is the Tafel slope $\boldsymbol{\eta}$ is the overpotential, $\boldsymbol{j}$ is the current density and a is the overpotential at unit current density[373].By comparing the value of Tafel plots it's very easy to understand about the mechanism happening during the HER. Generally, HER may be happening through three steps in both acidic and basic medium, which are the Volmer reaction (Equation 8.3), the Heyrovsky reaction (Equation 8.4) followed by the Tafel reaction (Equation 8.5).

$$\boldsymbol{H^+ + e^- + M \leftrightarrows MH_{ads}\ (118.4\ mV.dec^{-1})} \quad \textbf{(8.3)}$$

$$\boldsymbol{MH_{ads} + H^+ + e^- \leftrightarrows M + H_2\ (39.4\ mV.dec^{-1})} \quad \textbf{(8.4)}$$

$$\boldsymbol{2MH_{ads} \leftrightarrows 2M + H_2\ (29.6\ mV.dec^{-1})} \quad \textbf{(8.5)}$$

where M is the electrode surface.

When HER process is limited by the Volmer-Heyrovsky mechanism, the Tafel slopes are equal to 39.4 and 118.3 mV.dec^{-1} [160]. The Tafel slope for the sample MX1000, MX1100 and MX850 were 82, 56 and 41 mV.dec^{-1}, respectively. This indicated that all the samples were performing HER through the Volmer-Heyrovsky mechanism. The excellent HER kinetics and improved conductivity of MX850 can be due consequence of the layered morphology and increased conductivity.

To understand the kinetics and surface interaction of the fabricated MXene electrodes, electrochemical impedance spectroscopy was performed, and Nyquist plots we drawn as shown in the Fig: 8.23. The charge transfer resistance (R_{ct}) was calculate by fitting the curves with corresponding equivalent circuits, which are matching with the modified Randles cell (Fig:8.23 {inset}) for all the 4 electrode with semicircles in the Nyquist plots [374]. The lowest R_{ct} was observed for sample MX850 with 10.38 ohms and the highest for MX1000 with 12.54 ohms. These were the smallest reported values for Mo_2CT_x MXene to the best of our knowledge. This can be correlated to the higher conductivity and improved chemical properties of Mo_2CT_x which resulted in the enhanced electron kinetics in electrolyte which is like what we observed in the polarization curve and the Tafel plot because of the increase in the reaction temperature during the formation of Mo-In-C non-MAX phase.

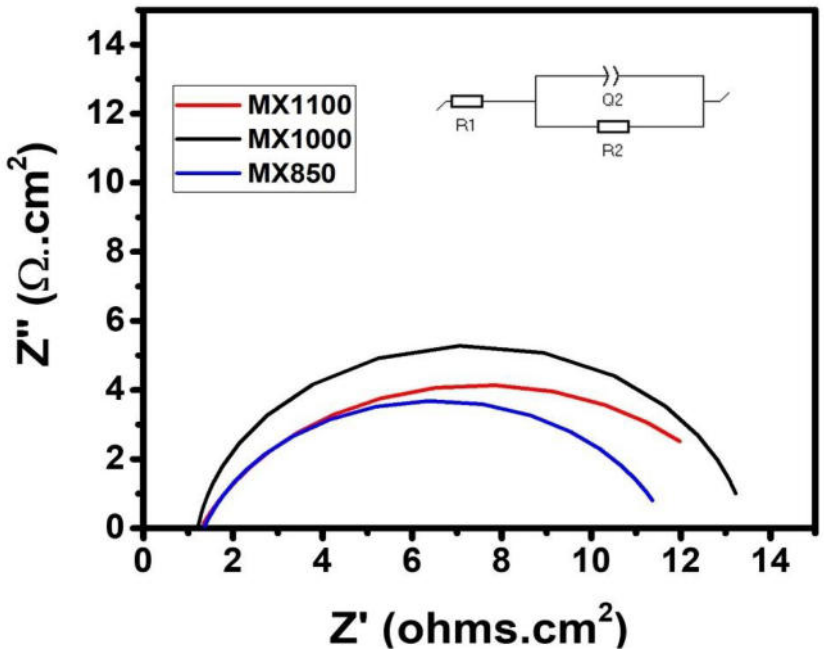

Figure 8.23 Nyquist plot of the fabricated MXene electrode measured in the frequency range 0.1 to 100 kHz and the equivalent circuit is indexed in the inset which resembles a simplified Randles cell.

8.4 Summary

In summary, we synthesized we Mo_2CT_x MXenes from Mo-In-C non-MAX phase by the means of solid-state reaction varying the synthesis temperature followed by UV assisted phosphoric acid etching and exfoliation. The microstructural characterization using the XRD and FESEM confirmed the formation of layered Mo_2CT_x MXene by etching out indium from the parent non-MAX phase. The elemental characterization using XPS, and EDS along with

the TEM also confirms the formation of the MXene. Then we fabricated Mo_2CT_x MXene sensors supported on different substrates (glass, crystalline, or porous silicon) for the detection of CO_2 at room temperature. The gas sensing studies were carried out by varying working temperature from 30 to 250 ^oC and CO_2 concentrations from 50 to 150 ppm. Compared with crystalline silicon sensors, sensors made on porous silicon and glass exhibit excellent room temperature sensing response and fast response and recovery time under 50 ppm CO_2 gas. On the other hand, the highest percentage sensitivity of 25% was exhibited by the sensor fabricated on porous silicon working at 250 ^oC for 150 ppm of CO_2 gas compared to crystalline silicon and glass substrate. In addition, the fabricated porous silicon/Mo_2CT_x sensor demonstrated fast response and recovery times of 30 and 45 s respectively working at 30 ^oC and 50 ppm of CO_2 which are the fastest reported values at room temperature. In addition to that, the percentage sensitivity was found to increase with the humidity accompanied by a delayed response and recovery. Dynamic response studies carried out for different working temperatures and CO_2 concentrations along with the stability tests confirmed the repeatability and stability of the fabricated sensor. This work is an attempt to fabricate a low cost highly stable, fast responding, and recovering CO_2 gas sensors working at room temperature using Mo_2CT_x MXene for commercial application.

In addition to that electrochemical hydrogen evolution reaction (HER) application of the synthesized Mo_2CT_x MXenes as working electrodes were performed using a three-electrode electrochemical cell with Ag/AgCl as the reference electrode and platinum as the counter electrode in 0.5M H_2SO_4 acidic electrolyte. The lowest overpotential was observed for the MXene synthesized from non-MAX phase at 850 ^oC with a value of -138 mV at 10 mA/cm^2 current density and the corresponding Tafel slope was 41 mV. The series resistance calculated using the equivalent circuit (modified Randle's) form the Nyquist plot was 10.38 ohms which is the lowest in the case of Mo_2CT_x MXene.

9. Conclusion

This thesis was an attempt to portray the gas sensing and hydrogen evolution application of molybdenum based 1D and 2D nanostructures with the help of systematic study of the synthesis and characterization strategies involved. The major conclusions obtained during this study is depicted as follows.

To detect the presence of ammonia gas, gas sensors were produced in this work using vacuum thermal evaporation of α-MoO_3 nanorods on glass substrates, followed by an annealing technique in ambient air. The gas sensing assessment of the produced sensors demonstrated that the specimen annealed at 400 ° C had exceptional sensitivity towards ammonia gas at room temperature (28 ºC). In the process of the testing, it was determined that the sensors remained responding to ammonia levels as low as 1ppm, highly repeatable, and remarkably stable after one year of working, with just a 1% decline in the sensing response. According to the results of FESEM as well as Raman spectroscopic studies of the sensors, the presence of extra physisorption sites produced by thermal annealing may be the reason for the increased device properties of the sensor annealed at 400 ºC. The stable α-MoO_3 sensor disclosed in this work has the narrowest limit of detection and the highest sensing response, making it a potential choice for big NH_3 sensing in practical manufacturing.

Additionally, a porous silicon/molybdenum trioxide hybrid structure, that was produced via simple thermal evaporation of the MoO_3 over an electrochemically produced silicon substrate, proved effective in sensing CO_2 gas at a low concentration level (50 ppm) and working temperature (150 ºC). TEM and FESEM images with high resolution show the formation of properly aligned MoO_3 crystallites on a nanorod-shaped substrate, which is consistent with the XRD data. The compositional study done using XPS also verifies the uniform deposition of orthorhombic MoO_3 layers on the porous silicon substrate as well as the creation of a hybrid structure on the substrate surface, which is consistent with the previous findings. The sensor performance was examined in relation to the pSi substrate, working temperature, as well as target gas concentration. At 250 ºC, the pSi/MoO_3 sensor demonstrated approximately fourfold the sensitivity (15 % at 150 ppm) of the c-Si/MoO_3 sensor (3.9 % at 200 ºC and 150 ppm) and a much faster response time (8s at 100 ppm) compared to the c-Si sensor (10 s at 200 ºC and 150 ppm). Due to the homogeneous distribution of MoO_3 nanorods on pSi substrate, the increased specific surface area of pSi/MoO_3 sensor was observed, leading to a higher response and limit of detection for the sensor. A favorable environment for CO_2 detection is created as a result of the increased interaction and the formation of a new depletion layer. However, more research and improvement in the field are required to confirm that it is viable to construct CO_2 sensors on a large scale using a porous silicon/molybdenum trioxide hybrid system at a minimal cost and with better efficiency.

After that for the first time, Mo_2CT_x MXene was prepared and characterized using Mo-In-C non-MAX phase using a solid-state process followed by UV aided phosphoric acid etch and ultrasonic exfoliation. When the samples were subjected to EDX and XPS examination, it was found that In was then selectively etched out from Mo-In-C MAX stoichiometry, resulting in the production of Mo_2CT_x MXene. The production of Mo-In-C as well as Mo_2CTx phases, and their related layered morphologies and crystallite sizes, were shown by microstructural study utilizing XRD, FESEM, and TEM. With the change in the period of exfoliation, 2D MXene morphologies such as multilayered or monolayered 2D MXene were seen for the produced MXene. Mo_2CT_x is synthesized from non-MAX phases using an ecofriendly process, which has the potential to be used in electrochemical and gas sensing applications.

Then, we developed Mo_2CT_x MXene sensors that were supported on a variety of substrates (glass, crystalline, and porous silicon) and used to detect CO_2 at room temperature. The gas sensing experiments were carried out at temperatures ranging from 30 to 250 degrees Celsius and CO_2 concentrations ranging from 50 to 150 parts per million (ppm). When compared to crystalline silicon sensors, sensors built of porous silicon and glass demonstrate superior room temperature sensing response as well as rapid reaction and recovery time when exposed to CO_2 gas concentrations of 50 ppm. In contrast, the sensor manufactured on porous silicon and operating at 250 degrees Celsius for 150 ppm of CO_2 gas had the maximum percentage sensitivity of 25% when compared to the sensors fabricated on crystalline silicon and glass substrate. Furthermore, the built porous silicon/Mo_2CT_x sensor displayed quick response and recovery times of 30 and 45 s, respectively, when operated at 30 °C and 50 ppm of CO_2, which are the fastest recorded values at ambient temperature to date. Aside from that, it was shown that humidity causes the percentage sensitivity to rise, which is followed by a delay in reaction and recovery time. The repeatability and stability of the constructed sensor were proven by dynamic response experiments carried out at various operating temperatures and CO_2 concentrations, as well as through stability testing. For commercial applications, this study is an effort to build a low-cost, highly stable, rapid responsive, and recovering CO_2 gas sensor based on Mo_2CT_x MXene that operates at room temperature.

Finally, electrochemical hydrogen evolution reaction (HER) application of the produced Mo_2CT_x MXenes as working electrodes was carried out in a three-electrode electrochemical cell with Ag/AgCl as the reference electrode and platinum as the counter electrode in 0.5M H_2SO_4 acidic electrolyte. The MXene synthesized from non-MAX phase at 850 ^oC exhibited the lowest overpotential, with a value of -138 mV at 10 mA/cm^2 current density and a Tafel slope of -41 mV. With the equivalent circuit (modified Randle's) from the Nyquist plot, we were able to compute the series resistance, which was 10.38 ohms, which was the lowest value found in the case of Mo_2CT_x MXene. Further investigations are needed

for the optimization of the HER performance and fabrication of real device gas sensors, which opens a wide door towards the possibility of future work.

The works explained in the chapters 7 and 8 are published in the journals Thin solid films (2021), Vacuum (2021), Ceramics International (2021) and Microporous and Mesoporous Materials (2022) , as follows:

1. T. Thomas, N. Jayababu, J. Shruthi, A. Mathew, A. Cerdán-Pasarán, J.A. Hernández-Magallanes, K.C. Sanal, R. R, Room temperature ammonia sensing of α-MoO_3 nanorods grown on glass substrates, Thin Solid Films. 722 (2021) 138575. https://doi.org/10.1016/j.tsf.2021.138575.
2. T. Thomas, Y. Kumar, J.A. Ramos Ramón, V. Agarwal, S. Sepúlveda Guzmán, R. R, S. Pushpan, S.L. Loredo, K.C. Sanal, Porous silicon/α-MoO_3 nanohybrid based fast and highly sensitive CO_2 gas sensors, Vacuum. 184 (2021). https://doi.org/10.1016/j.vacuum.2020.109983.
3. T. Thomas, S. Pushpan, J.A. Aguilar Martínez, A. Torres Castro, N. Pineda Aguilar, A. Álvarez-Méndez, K.C. Sanal, UV-assisted safe etching route for the synthesis of Mo2CTx MXene from Mo–In–C non-MAX phase, Ceram. Int. 47 (2021) 35384–35387. https://doi.org/10.1016/j.ceramint.2021.08.342.
4. T. Thomas, J.A. Ramos Ramon, V. Agarwal, A.Á. Méndez, J.A.A. Martinez, Y. Kumar, K.C. Sanal, Highly stable, fast responsive Mo_2CT_x MXene sensors for room temperature carbon dioxide detection, Microporous Mesoporous Mater. 336 (2022) 111872. https://doi.org/10.1016/j.micromeso.2022.111872.

Reference

[1] G. Cao, Nanostructures and Nanomaterials (Synthesis, Properties and Applications) ‖ Introduction, published by imperial college press and distributed by world scientific publishing co., 2004. https://doi.org/10.1142/9781860945960_0001.

[2] N.K. Bakirhan, B. Uslu, S.A. Ozkan, Sensitive and Selective Assay of Antimicrobials on Nanostructured Materials by Electrochemical Techniques, Elsevier Inc., 2017. https://doi.org/10.1016/B978-0-323-46152-8.00003-2.

[3] S. Smita, S.K. Gupta, A. Bartonova, M. Dusinska, A.C. Gutleb, Q. Rahman, Nanoparticles in the environment: Assessment using the causal diagram approach, Environ. Heal. A Glob. Access Sci. Source. 11 (2012) S13. https://doi.org/10.1186/1476-069X-11-S1-S13.

[4] G. Ramalingam, P. Kathirgamanathan, G. Ravi, T. Elangovan, B. Arjun kumar, N. Manivannan, K. Kasinathan, Quantum Confinement Effect of 2D Nanomaterials, Quantum Dots - Fundam. Appl. (2020). https://doi.org/10.5772/intechopen.90140.

[5] L.E. Brus, Electron–electron and electron-hole interactions in small semiconductor crystallites: The size dependence of the lowest excited electronic state, J. Chem. Phys. 80 (1984) 4403–4409. https://doi.org/10.1063/1.447218.

[6] L. Bányai, S.W. Koch, Semiconductor Quantum Dots, WORLD SCIENTIFIC, 1993. https://doi.org/10.1142/2019.

[7] P.N. Sudha, K. Sangeetha, K. Vijayalakshmi, A. Barhoum, Chapter 12 - Nanomaterials history, classification, unique properties, production and market, Elsevier Inc., 2021. https://doi.org/10.1016/B978-0-323-51254-1/00012-9.

[8] A.M. Smith, S. Nie, Semiconductor Nanocrystals: Structure, Properties, and Band Gap Engineering, Acc. Chem. Res. 43 (2010) 190–200. https://doi.org/10.1021/ar9001069.

[9] I. Navas, R. Vinodkumar, K.J. Lethy, A.P. Detty, V. Ganesan, V. Sathe, V.P. Mahadevan Pillai, Growth and characterization of molybdenum oxide nanorods by RF magnetron sputtering and subsequent annealing, J. Phys. D. Appl. Phys. 42 (2009). https://doi.org/10.1088/0022-3727/42/17/175305.

[10] Patricia I. Dolez, Nanoengineering, 2015.

[11] H. Zhang, Introduction: 2D Materials Chemistry, Chem. Rev. 118 (2018) 6089–6090. https://doi.org/10.1021/acs.chemrev.8b00278.

[12] G. Cao, Y. Wang, Characterization and Properties of Nanomaterials, Nanostructures Nanomater. (2011) 433–508. https://doi.org/10.1142/9789814340571_0008.

[13] H. Zhang, Ultrathin Two-Dimensional Nanomaterials, ACS Nano. 9 (2015) 9451–9469. https://doi.org/10.1021/acsnano.5b05040.

[14] C. Tan, X. Cao, X.J. Wu, Q. He, J. Yang, X. Zhang, J. Chen, W. Zhao, S. Han, G.H. Nam, M. Sindoro, H. Zhang, Recent Advances in Ultrathin Two-Dimensional Nanomaterials, Chem. Rev. 117 (2017) 6225–6331. https://doi.org/10.1021/acs.chemrev.6b00558.

[15] J.J. Ramsden, Nanotechnology, Elsevier, 2011. https://doi.org/10.1016/C2009-0-20342-4.

[16] Y.X. Gan, A.H. Jayatissa, Z. Yu, X. Chen, M. Li, Hydrothermal Synthesis of Nanomaterials, J. Nanomater. 2020 (2020) 1–3. https://doi.org/10.1155/2020/8917013.

[17] N. Miyata, T. Suzuki, R. Ohyama, Physical properties of evaporated molybdenum oxide films, Thin Solid Films. 281–282 (1996) 218–222. https://doi.org/10.1016/0040-6090(96)08617-8.

[18] T. Siciliano, A. Tepore, E. Filippo, G. Micocci, M. Tepore, Characteristics of molybdenum trioxide nanobelts prepared by thermal evaporation technique, Mater. Chem. Phys. 114 (2009) 687–691. https://doi.org/10.1016/j.matchemphys.2008.10.018.

[19] S. Yang, W. Chen, W. Jin, J. Zhou, H. Zhang, G.S. Zakharova, Y. Liu, High sensitivity and good selectivity of ultralong MoO_3 nanobelts for trimethylamine gas, Sensors Actuators B. Chem. 226 (2015) 478–485. https://doi.org/10.1016/j.snb.2015.12.005.

[20] R. Jamal, F. Xu, W. Shao, T. Abdiryim, The study on the application of solid-state method for synthesizing the polyaniline/noble metal (Au or Pt) hybrid materials, Nanoscale Res. Lett. 8 (2013) 117. https://doi.org/10.1186/1556-276X-8-117.

[21] C.N.R.R. and G.V.S. Rao, Trensition Metal Oxides, 1974.

[22] C. N. R. Rao, Transition metal oxides1, Annu. Rev. Phys. Chem. 40 (1989) 291–326. https://doi.org/10.1146/annurev.pc.40.100189.001451.

[23] I.A. de Castro, R.S. Datta, J.Z. Ou, A. Castellanos-Gomez, S. Sriram, T. Daeneke, K. Kalantar-zadeh, Molybdenum Oxides – From Fundamentals to Functionality, Adv. Mater. 29 (2017) 1701619. https://doi.org/10.1002/adma.201701619.

[24] A. Khademi, R. Azimirad, A.A. Zavarian, A.Z. Moshfegh, Growth and field emission study of molybdenum oxide nanostars, J. Phys. Chem. C. 113 (2009) 19298–19304. https://doi.org/10.1021/jp9056237.

[25] P. Justin, G. Ranga Rao, Methanol oxidation on MoO_3 promoted Pt/C electrocatalyst, Int. J. Hydrogen Energy. 36 (2011) 5875–5884. https://doi.org/10.1016/j.ijhydene.2011.01.122.

[26] I. Shakir, M. Shahid, H.W. Yang, D.J. Kang, Structural and electrochemical characterization of α-MoO_3 nanorod-based electrochemical energy storage devices,

Electrochim. Acta. 56 (2010) 376–380.
https://doi.org/10.1016/j.electacta.2010.09.028.

[27] Y. Jin, H. Wang, J. Li, X. Yue, Y. Han, P.K. Shen, Y. Cui, Porous MoO_2 Nanosheets as Non-noble Bifunctional Electrocatalysts for Overall Water Splitting, Adv. Mater. 28 (2016) 3785–3790. https://doi.org/10.1002/adma.201506314.

[28] D. Xiang, C. Han, J. Zhang, W. Chen, Gap States Assisted MoO_3 Nanobelt Photodetector with Wide Spectrum Response, Sci. Rep. 4 (2015) 1–6. https://doi.org/10.1038/srep04891.

[29] S. Yang, Z. Wang, Y. Hu, X. Luo, J. Lei, D. Zhou, L. Fei, Y. Wang, H. Gu, Highly responsive room-temperature hydrogen sensing of α-MoO_3 nanoribbon membranes, ACS Appl. Mater. Interfaces. 7 (2015) 9247–9253. https://doi.org/10.1021/acsami.5b01858.

[30] L. Zhang, Z. Liu, L. Jin, B. Zhang, H. Zhang, M. Zhu, W. Yang, Self-assembly gridding α-MoO_3 nanobelts for highly toxic H2S gas sensors, Sensors Actuators, B Chem. 237 (2016) 350–357. https://doi.org/10.1016/j.snb.2016.06.104.

[31] S. Alizadeh, S.A. Hassanzadeh-Tabrizi, MoO_3 fibers and belts: Molten salt synthesis, characterization and optical properties, Ceram. Int. 41 (2015) 10839–10843. https://doi.org/10.1016/j.ceramint.2015.05.024.

[32] P. Song, Q. Wang, J. Li, Z. Yang, Morphology-controllable synthesis, characterization and sensing properties of single-crystal molybdenum trioxide, Sensors Actuators B Chem. 181 (2013) 620–628. https://doi.org/10.1016/j.snb.2013.02.070.

[33] N. Floquet, O. Bertrand, J.J. Heizmann, Structural and morphological studies of the growth of MoO_3 scales during high-temperature oxidation of molybdenum, Oxid. Met. 37 (1992) 253–280. https://doi.org/10.1007/BF00665191.

[34] R. Coquet, D.J. Willock, The (010) surface of α-MoO_3, a DFT + U study, Phys. Chem. Chem. Phys. 7 (2005) 3819. https://doi.org/10.1039/b511044k.

[35] W. Li, F. Cheng, Z. Tao, J. Chen, Vapor-transportation preparation and reversible lithium intercalation/deintercalation of α-MoO_3 microrods, J. Phys. Chem. B. 110 (2006) 119–124. https://doi.org/10.1021/jp0553784.

[36] K. Inzani, T. Grande, F. Vullum-Bruer, S.M. Selbach, A van der Waals Density Functional Study of MoO_3 and Its Oxygen Vacancies, J. Phys. Chem. C. 120 (2016) 8959–8968. https://doi.org/10.1021/acs.jpcc.6b00585.

[37] A. Chithambararaj, N.S. Sanjini, S. Velmathi, A. Chandra Bose, Preparation of h-MoO3 and α-MoO_3 nanocrystals: Comparative study on photocatalytic degradation of methylene blue under visible light irradiation, Phys. Chem. Chem. Phys. 15 (2013) 14761–14769. https://doi.org/10.1039/c3cp51796a.

[38] H. Ren, S. Sun, J. Cui, X. Li, Synthesis, Functional Modifications, and Diversified Applications of Molybdenum Oxides Micro-/Nanocrystals: A Review, Cryst. Growth Des. 18 (2018) 6326–6369. https://doi.org/10.1021/acs.cgd.8b00894.

[39] E. Comini, L. Yubao, Y. Brando, G. Sberveglieri, Gas sensing properties of MoO_3 nanorods to CO and CH_3OH, Chem. Phys. Lett. 407 (2005) 368–371. https://doi.org/10.1016/j.cplett.2005.03.116.

[40] J.Z. Ou, J.L. Campbell, D. Yao, W. Wlodarski, K. Kalantar-Zadeh, In situ Raman spectroscopy of H_2 gas interaction with layered MoO_3, J. Phys. Chem. C. 115 (2011) 10757–10763. https://doi.org/10.1021/jp202123a.

[41] A.K. Prasad, P.I. Gouma, D.J. Kubinski, J.H. Visser, R.E. Soltis, P.J. Schmitz, Reactively sputtered MoO_3 films for ammonia sensing, Thin Solid Films. 436 (2003) 46–51. https://doi.org/10.1016/S0040-6090(03)00524-8.

[42] A.A. Mane, A. V. Moholkar, Orthorhombic MoO_3 nanobelts based NO_2 gas sensor, Appl. Surf. Sci. 405 (2017) 427–440. https://doi.org/10.1016/j.apsusc.2017.02.055.

[43] Shahab-ud-Din, M.Z. Ahmad, K. Qureshi, I.A. Bhatti, M. Zahid, J. Nisar, M. Iqbal, M. Abbas, Hydrothermal synthesis of molybdenum trioxide, characterization and photocatalytic activity, Mater. Res. Bull. 100 (2018) 120–130. https://doi.org/10.1016/j.materresbull.2017.11.044.

[44] S. Shen, X. Zhang, X. Cheng, Y. Xu, S. Gao, H. Zhao, X. Zhou, L. Huo, Oxygen-Vacancy-Enriched Porous α-MoO_3 Nanosheets for Trimethylamine Sensing, ACS Appl. Nano Mater. 2 (2019) 8016–8026. https://doi.org/10.1021/acsanm.9b02072.

[45] Q. Fu, J. Chen, C. Shi, D. Ma, Room-temperature sol-gel derived molybdenum oxide thin films for efficient and stable solution-processed organic light-emitting diodes, ACS Appl. Mater. Interfaces. 5 (2013) 6024–6029. https://doi.org/10.1021/am4007319.

[46] A. Ashok, S.N. Vijayaraghavan, S. V. Nair, M. Shanmugam, Molybdenum trioxide thin film recombination barrier layers for dye sensitized solar cells, RSC Adv. 7 (2017) 48853–48860. https://doi.org/10.1039/c7ra08988k.

[47] X. Liao, A.R. Jeong, R.G. Wilks, S. Wiesner, M. Rusu, R. Félix, T. Xiao, C. Hartmann, M. Bär, Tunability of MoO_3 Thin-Film Properties Due to Annealing in Situ Monitored by Hard X-ray Photoemission, ACS Omega. 4 (2019) 10985–10990. https://doi.org/10.1021/acsomega.9b01027.

[48] H. Ma, H. Fang, W. Wu, C. Zheng, L. Wu, H. Wang, A highly transparent humidity sensor with fast response speed based on α-MoO_3 thin films, RSC Adv. 10 (2020) 25467–25474. https://doi.org/10.1039/d0ra03958f.

[49] S.A. Khalate, R.S. Kate, H.M. Pathan, R.J. Deokate, Structural and electrochemical properties of spray deposited molybdenum trioxide (α-MoO_3) thin films, J. Solid

State Electrochem. 21 (2017) 2737–2746. https://doi.org/10.1007/s10008-017-3540-4.

[50] K. He, S. He, W. Yang, Q. Tian, Ag nanoparticles-decorated α-MoO_3 nanorods for remarkable and rapid triethylamine-sensing response boosted by pulse-heating technique, J. Alloys Compd. 808 (2019) 1–9. https://doi.org/10.1016/j.jallcom.2019.151704.

[51] R. Nadimicherla, H.Y. Li, K. Tian, X. Guo, SnO_2 doped MoO_3 nanofibers and their carbon monoxide gas sensing performances, Solid State Ionics. 300 (2017) 128–134. https://doi.org/10.1016/j.ssi.2016.12.022.

[52] A. Hermawan, N.L.W. Septiani, A. Taufik, B. Yuliarto, Suyatman, S. Yin, Advanced Strategies to Improve Performances of Molybdenum-Based Gas Sensors, Springer Singapore, 2021. https://doi.org/10.1007/s40820-021-00724-1.

[53] R. Malik, N. Joshi, V.K. Tomer, Advances in the designs and mechanisms of MoO_3 nanostructures for gas sensors: A holistic review, Mater. Adv. 2 (2021) 4190–4227. https://doi.org/10.1039/d1ma00374g.

[54] S. He, W. Li, L. Feng, W. Yang, Rational interaction between the aimed gas and oxide surfaces enabling high-performance sensor: The case of acidic α-MoO_3 nanorods for selective detection of triethylamine, J. Alloys Compd. 783 (2019) 574–582. https://doi.org/10.1016/j.jallcom.2018.12.349.

[55] H.Y. Li, L. Huang, X.X. Wang, C.S. Lee, J.W. Yoon, J. Zhou, X. Guo, J.H. Lee, Molybdenum trioxide nanopaper as a dual gas sensor for detecting trimethylamine and hydrogen sulfide, RSC Adv. 7 (2017) 3680–3685. https://doi.org/10.1039/C6RA26280E.

[56] C. V. Ramana, A. Mauger, C.M. Julien, Growth, characterization and performance of bulk and nanoengineered molybdenum oxides for electrochemical energy storage and conversion, Prog. Cryst. Growth Charact. Mater. 67 (2021) 100533. https://doi.org/10.1016/j.pcrysgrow.2021.100533.

[57] Y. Ou, Y. Zhou, Y. Guo, X. Zhu, B. Liu, C. Gao, Room-temperature high-performance ammonia gas sensing based on rGO nanosheets/MoO_3 nanoribbons nanocomposites film, FlatChem. 32 (2022) 100333. https://doi.org/10.1016/j.flatc.2021.100333.

[58] H. Hu, C. Deng, J. Xu, K. Zhang, M. Sun, Metastable h-MoO3 and stable α-MoO_3 microstructures: controllable synthesis, growth mechanism and their enhanced photocatalytic activity, J. Exp. Nanosci. 10 (2015) 1336–1346. https://doi.org/10.1080/17458080.2015.1012654.

[59] A.A. Mane, A. V. Moholkar, Palladium (Pd) sensitized molybdenum trioxide (MoO3) nanobelts for nitrogen dioxide (NO2) gas detection, Solid. State. Electron.

139 (2018) 21–30. https://doi.org/10.1016/j.sse.2017.09.011.

[60] S. Yang, Y. Liu, T. Chen, W. Jin, T. Yang, M. Cao, S. Liu, J. Zhou, G.S. Zakharova, W. Chen, Zn doped MoO_3 nanobelts and the enhanced gas sensing properties to ethanol, Appl. Surf. Sci. 393 (2017) 377–384. https://doi.org/10.1016/j.apsusc.2016.10.021.

[61] X.W. Lou, H.C. Zeng, Complex α-MoO3 nanostructures with external bonding capacity for self-assembly, J. Am. Chem. Soc. 125 (2003) 2697–2704. https://doi.org/10.1021/ja029086h.

[62] H. Yin, Y. Kuwahara, K. Mori, H. Cheng, M. Wen, H. Yamashita, High-surface-area plasmonic MoO_3-: X: Rational synthesis and enhanced ammonia borane dehydrogenation activity, J. Mater. Chem. A. 5 (2017) 8946–8953. https://doi.org/10.1039/c7ta01217a.

[63] M.J. Allen, V.C. Tung, R.B. Kaner, Honeycomb carbon: A review of graphene, Chem. Rev. 110 (2010) 132–145. https://doi.org/10.1021/cr900070d.

[64] Y. Shao, J. Wang, H. Wu, J. Liu, I.A. Aksay, Y. Lin, Graphene based electrochemical sensors and biosensors: A review, Electroanalysis. 22 (2010) 1027–1036. https://doi.org/10.1002/elan.200900571.

[65] M. Xu, T. Liang, M. Shi, H. Chen, Graphene-Like Two-Dimensional Materials, Chem. Rev. 113 (2013) 3766–3798. https://doi.org/10.1021/cr300263a.

[66] G.R. Bhimanapati, Z. Lin, V. Meunier, Y. Jung, J. Cha, S. Das, D. Xiao, Y. Son, M.S. Strano, V.R. Cooper, L. Liang, S.G. Louie, E. Ringe, W. Zhou, S.S. Kim, R.R. Naik, B.G. Sumpter, H. Terrones, F. Xia, Y. Wang, J. Zhu, D. Akinwande, N. Alem, J.A. Schuller, R.E. Schaak, M. Terrones, J.A. Robinson, Recent Advances in Two-Dimensional Materials beyond Graphene, ACS Nano. 9 (2015) 11509–11539. https://doi.org/10.1021/acsnano.5b05556.

[67] M. Naguib, M. Kurtoglu, V. Presser, J. Lu, J. Niu, M. Heon, L. Hultman, Y. Gogotsi, M.W. Barsoum, Two-dimensional nanocrystals produced by exfoliation of Ti_3AlC_2, Adv. Mater. 23 (2011) 4248–4253. https://doi.org/10.1002/adma.201102306.

[68] M. Naguib, V. Presser, D. Tallman, J. Lu, L. Hultman, Y. Gogotsi, M.W. Barsoum, On the topotactic transformation of Ti_2AlC into a Ti-C-O-F cubic phase by heating in molten lithium fluoride in air, J. Am. Ceram. Soc. 94 (2011) 4556–4561. https://doi.org/10.1111/j.1551-2916.2011.04896.x.

[69] M. Naguib, O. Mashtalir, J. Carle, V. Presser, J. Lu, L. Hultman, Y. Gogotsi, M.W. Barsoum, Two-Dimensional Transition Metal Carbides, ACS Nano. 6 (2012) 1322–1331. https://doi.org/10.1021/nn204153h.

[70] X. Zhang, J. Xu, H. Wang, J. Zhang, H. Yan, B. Pan, J. Zhou, Y. Xie, Ultrathin nanosheets of MAX phases with enhanced thermal and mechanical properties in

polymeric compositions: $Ti_3Si_{0.75}Al_{0.25}C_2$, Angew. Chemie - Int. Ed. 52 (2013) 4361–4365. https://doi.org/10.1002/anie.201300285.

[71] M. Naguib, V.N. Mochalin, M.W. Barsoum, Y. Gogotsi, 25th Anniversary Article : MXenes : A New Family of Two-Dimensional Materials, (2013) 992–1005. https://doi.org/10.1002/adma.201304138.

[72] Y. Xie, M. Naguib, V.N. Mochalin, M.W. Barsoum, Y. Gogotsi, X. Yu, K.-W. Nam, X.-Q. Yang, A.I. Kolesnikov, P.R.C. Kent, Role of Surface Structure on Li-Ion Energy Storage Capacity of Two-Dimensional Transition-Metal Carbides, J. Am. Chem. Soc. 136 (2014) 6385–6394. https://doi.org/10.1021/ja501520b.

[73] X. Liang, A. Garsuch, L.F. Nazar, Sulfur cathodes based on conductive MXene nanosheets for high-performance lithium-sulfur batteries, Angew. Chemie - Int. Ed. 54 (2015) 3907–3911. https://doi.org/10.1002/anie.201410174.

[74] X. Liang, Y. Rangom, C.Y. Kwok, Q. Pang, L.F. Nazar, Interwoven MXene Nanosheet/Carbon-Nanotube Composites as Li–S Cathode Hosts, Adv. Mater. 29 (2017) 1–7. https://doi.org/10.1002/adma.201603040.

[75] M.A. Hope, A.C. Forse, K.J. Griffith, M.R. Lukatskaya, M. Ghidiu, Y. Gogotsi, C.P. Grey, NMR reveals the surface functionalisation of Ti3C2 MXene, Phys. Chem. Chem. Phys. 18 (2016) 5099–5102. https://doi.org/10.1039/c6cp00330c.

[76] X. Wang, S. Kajiyama, H. Iinuma, E. Hosono, S. Oro, I. Moriguchi, M. Okubo, A. Yamada, Pseudocapacitance of MXene nanosheets for high-power sodium-ion hybrid capacitors, Nat. Commun. 6 (2015) 1–6. https://doi.org/10.1038/ncomms7544.

[77] H. Tang, Q. Hu, M. Zheng, Y. Chi, X. Qin, H. Pang, Q. Xu, MXene–2D layered electrode materials for energy storage, Prog. Nat. Sci. Mater. Int. 28 (2018) 133–147. https://doi.org/10.1016/j.pnsc.2018.03.003.

[78] J. Liu, W. Peng, Y. Li, F. Zhang, X. Fan, 2D MXene-Based Materials for Electrocatalysis, Trans. Tianjin Univ. 26 (2020) 149–171. https://doi.org/10.1007/s12209-020-00235-x.

[79] Q. Jiang, Y. Lei, H. Liang, K. Xi, C. Xia, H.N. Alshareef, Review of MXene electrochemical microsupercapacitors, Energy Storage Mater. 27 (2020) 78–95. https://doi.org/10.1016/j.ensm.2020.01.018.

[80] Y. Liu, J. Yu, D. Guo, Z. Li, Y. Su, $Ti_3C_2T_x$ MXene/graphene nanocomposites: Synthesis and application in electrochemical energy storage, J. Alloys Compd. 815 (2020) 152403. https://doi.org/10.1016/j.jallcom.2019.152403.

[81] S.K. Hwang, S.M. Kang, M. Rethinasabapathy, C. Roh, Y.S. Huh, MXene: An emerging two-dimensional layered material for removal of radioactive pollutants, Chem. Eng. J. 397 (2020) 125428. https://doi.org/10.1016/j.cej.2020.125428.

[82] Y.A.J. Al-Hamadani, B.M. Jun, M. Yoon, N. Taheri-Qazvini, S.A. Snyder, M. Jang,

J. Heo, Y. Yoon, Applications of MXene-based membranes in water purification: A review, Chemosphere. 254 (2020) 126821. https://doi.org/10.1016/j.chemosphere.2020.126821.

[83] S.Y. Cho, J.Y. Kim, O. Kwon, J. Kim, H.T. Jung, Molybdenum carbide chemical sensors with ultrahigh signal-to-noise ratios and ambient stability, J. Mater. Chem. A. 6 (2018) 23408–23416. https://doi.org/10.1039/C8TA07168C.

[84] R. Bhardwaj, A. Hazra, MXene-based gas sensors, J. Mater. Chem. C. 9 (2021) 15735–15754. https://doi.org/10.1039/d1tc04085e.

[85] B. Xu, C. Zhi, P. Shi, Latest advances in MXene biosensors, J. Phys. Mater. 3 (2020) 031001. https://doi.org/10.1088/2515-7639/ab8f78.

[86] K. Zhu, J. Chen, W. Wang, J. Liao, J. Dong, M.O.L. Chee, N. Wang, P. Dong, P.M. Ajayan, S. Gao, J. Shen, M. Ye, Etching-Doping Sedimentation Equilibrium Strategy: Accelerating Kinetics on Hollow Rh-Doped CoFe-Layered Double Hydroxides for Water Splitting, Adv. Funct. Mater. 30 (2020) 1–10. https://doi.org/10.1002/adfm.202003556.

[87] T. Zhou, W. Xu, N. Zhang, Z. Du, C. Zhong, W. Yan, H. Ju, W. Chu, H. Jiang, C. Wu, Y. Xie, Ultrathin Cobalt Oxide Layers as Electrocatalysts for High-Performance Flexible Zn–Air Batteries, Adv. Mater. 31 (2019) 1–8. https://doi.org/10.1002/adma.201807468.

[88] Y. Yang, S. Bremner, C. Menictas, M. Kay, Battery energy storage system size determination in renewable energy systems: A review, Renew. Sustain. Energy Rev. 91 (2018) 109–125. https://doi.org/10.1016/j.rser.2018.03.047.

[89] N. Mahmud, A. Zahedi, Review of control strategies for voltage regulation of the smart distribution network with high penetration of renewable distributed generation, Renew. Sustain. Energy Rev. 64 (2016) 582–595. https://doi.org/10.1016/j.rser.2016.06.030.

[90] A. Djire, X. Wang, C. Xiao, O.C. Nwamba, M. V. Mirkin, N.R. Neale, Basal Plane Hydrogen Evolution Activity from Mixed Metal Nitride MXenes Measured by Scanning Electrochemical Microscopy, Adv. Funct. Mater. 2001136 (2020) 1–12. https://doi.org/10.1002/adfm.202001136.

[91] P.C.K. Vesborg, B. Seger, I. Chorkendorff, Recent development in hydrogen evolution reaction catalysts and their practical implementation, J. Phys. Chem. Lett. 6 (2015) 951–957. https://doi.org/10.1021/acs.jpclett.5b00306.

[92] A. Djire, X. Wang, C. Xiao, O.C. Nwamba, M. V. Mirkin, N.R. Neale, Basal Plane Hydrogen Evolution Activity from Mixed Metal Nitride MXenes Measured by Scanning Electrochemical Microscopy, Adv. Funct. Mater. 2001136 (2020) 1–12. https://doi.org/10.1002/adfm.202001136.

[93] R. Xiao, C. Zhao, Z. Zou, Z. Chen, L. Tian, H. Xu, H. Tang, Q. Liu, Z. Lin, X. Yang, In situ fabrication of 1D CdS nanorod/2D Ti_3C_2 MXene nanosheet Schottky heterojunction toward enhanced photocatalytic hydrogen evolution, Appl. Catal. B Environ. 268 (2020) 118382. https://doi.org/10.1016/j.apcatb.2019.118382.

[94] S. Wang, S. Chen, L. Ma, J.A. Zapien, Recent progress in cobalt-based carbon materials as oxygen electrocatalysts for zinc-air battery applications, Mater. Today Energy. 20 (2021) 100659. https://doi.org/10.1016/j.mtener.2021.100659.

[95] T. Zhu, S. Liu, B. Huang, Q. Shao, M. Wang, F. Li, X. Tan, Y. Pi, S.C. Weng, B. Huang, Z. Hu, J. Wu, Y. Qian, X. Huang, High-performance diluted nickel nanoclusters decorating ruthenium nanowires for pH-universal overall water splitting, Energy Environ. Sci. 14 (2021) 3194–3202. https://doi.org/10.1039/d0ee04028b.

[96] Z. Wang, X. Yao, Y. Kang, L. Miao, D. Xia, L. Gan, Structurally Ordered Low-Pt Intermetallic Electrocatalysts toward Durably High Oxygen Reduction Reaction Activity, Adv. Funct. Mater. 29 (2019) 1–9. https://doi.org/10.1002/adfm.201902987.

[97] Y. Wen, T. Yang, C. Cheng, X. Zhao, E. Liu, J. Yang, Engineering Ru(IV) charge density in $Ru@RuO_2$ core-shell electrocatalyst via tensile strain for efficient oxygen evolution in acidic media, Chinese J. Catal. 41 (2020) 1161–1167. https://doi.org/10.1016/S1872-2067(20)63543-4.

[98] X. Zhang, B. Shao, Z. Sun, Z. Gao, Y. Qin, C. Zhang, F. Cui, X. Yang, Platinum Nanoparticle-Deposited $Ti_3C_2T_x$ MXene for Hydrogen Evolution Reaction, Ind. Eng. Chem. Res. 59 (2020) 1822–1828. https://doi.org/10.1021/acs.iecr.9b05046.

[99] Y. Dong, H. Shi, Z.S. Wu, Recent Advances and Promise of MXene-Based Nanostructures for High-Performance Metal Ion Batteries, Adv. Funct. Mater. 30 (2020) 1–24. https://doi.org/10.1002/adfm.202000706.

[100] J. Xie, J. Qi, F. Lei, Y. Xie, Modulation of electronic structures in two-dimensional electrocatalysts for the hydrogen evolution reaction, Chem. Commun. 56 (2020) 11910–11930. https://doi.org/10.1039/d0cc05272h.

[101] J. Zhao, Z. Tu, S.H. Chan, Carbon corrosion mechanism and mitigation strategies in a proton exchange membrane fuel cell (PEMFC): A review, J. Power Sources. 488 (2021) 229434. https://doi.org/10.1016/j.jpowsour.2020.229434.

[102] S.G. Peera, C. Liu, J. Shim, A.K. Sahu, T.G. Lee, M. Selvaraj, R. Koutavarapu, MXene ($Ti_3C_2T_x$) supported electrocatalysts for methanol and ethanol electrooxidation: A review, Ceram. Int. 47 (2021) 28106–28121. https://doi.org/10.1016/j.ceramint.2021.07.075.

[103] K. Li, M. Liang, H. Wang, X. Wang, Y. Huang, J. Coelho, S. Pinilla, Y. Zhang, F. Qi, V. Nicolosi, Y. Xu, 3D MXene Architectures for Efficient Energy Storage and Conversion, Adv. Funct. Mater. 30 (2020) 1–22.

https://doi.org/10.1002/adfm.202000842.

[104] D. Kan, D. Wang, X. Zhang, R. Lian, J. Xu, G. Chen, Y. Wei, Rational design of bifunctional ORR/OER catalysts based on Pt/Pd-doped Nb_2CT_2 MXene by first-principles calculations, J. Mater. Chem. A. 8 (2020) 3097–3108. https://doi.org/10.1039/c9ta12255a.

[105] Z. Li, Y. Cui, Z. Wu, C. Milligan, L. Zhou, G. Mitchell, B. Xu, E. Shi, J.T. Miller, F.H. Ribeiro, Y. Wu, Reactive metal-support interactions at moderate temperature in two-dimensional niobium-carbide-supported platinum catalysts, Nat. Catal. 1 (2018) 349–355. https://doi.org/10.1038/s41929-018-0067-8.

[106] T.Y. Ma, J.L. Cao, M. Jaroniec, S.Z. Qiao, Interacting carbon nitride and titanium carbide nanosheets for high-performance oxygen evolution, Angew. Chemie - Int. Ed. 55 (2016) 1138–1142. https://doi.org/10.1002/anie.201509758.

[107] Z.W. Seh, K.D. Fredrickson, B. Anasori, J. Kibsgaard, A.L. Strickler, M.R. Lukatskaya, Y. Gogotsi, T.F. Jaramillo, A. Vojvodic, Two-Dimensional Molybdenum Carbide (MXene) as an Efficient Electrocatalyst for Hydrogen Evolution, ACS Energy Lett. 1 (2016) 589–594. https://doi.org/10.1021/acsenergylett.6b00247.

[108] A.D. Handoko, K.D. Fredrickson, B. Anasori, K.W. Convey, L.R. Johnson, Y. Gogotsi, A. Vojvodic, Z.W. Seh, Tuning the Basal Plane Functionalization of Two-Dimensional Metal Carbides (MXenes) to Control Hydrogen Evolution Activity, ACS Appl. Energy Mater. 1 (2018) 173–180. https://doi.org/10.1021/acsaem.7b00054.

[109] D.A. Kuznetsov, Z. Chen, P. V. Kumar, A. Tsoukalou, A. Kierzkowska, P.M. Abdala, O. V. Safonova, A. Fedorov, C.R. Müller, Single Site Cobalt Substitution in 2D Molybdenum Carbide (MXene) Enhances Catalytic Activity in the Hydrogen Evolution Reaction, J. Am. Chem. Soc. 141 (2019) 17809–17816. https://doi.org/10.1021/jacs.9b08897.

[110] J. Zhang, Y. Zhao, X. Guo, C. Chen, C.L. Dong, R.S. Liu, C.P. Han, Y. Li, Y. Gogotsi, G. Wang, Single platinum atoms immobilized on an MXene as an efficient catalyst for the hydrogen evolution reaction, Nat. Catal. 1 (2018) 985–992. https://doi.org/10.1038/s41929-018-0195-1.

[111] C. Wan, Y.N. Regmi, B.M. Leonard, Multiple phases of molybdenum carbide as electrocatalysts for the hydrogen evolution reaction, Angew. Chemie - Int. Ed. 53 (2014) 6407–6410. https://doi.org/10.1002/anie.201402998.

[112] J. Greeley, T.F. Jaramillo, J. Bonde, I. Chorkendorff, J.K. Nørskov, Computational high-throughput screening of electrocatalytic materials for hydrogen evolution, Nat. Mater. 5 (2006) 909–913. https://doi.org/10.1038/nmat1752.

[113] B. Ding, W.J. Ong, J. Jiang, X. Chen, N. Li, Uncovering the electrochemical mechanisms for hydrogen evolution reaction of heteroatom doped M_2C MXene (M = Ti, Mo), Appl. Surf. Sci. 500 (2020) 143987. https://doi.org/10.1016/j.apsusc.2019.143987.

[114] T. Li, L. Yao, Q. Liu, J. Gu, R. Luo, J. Li, X. Yan, W. Wang, P. Liu, B. Chen, W. Zhang, W. Abbas, R. Naz, D. Zhang, Fluorine-Free Synthesis of High-Purity $Ti_3C_2T_x$ (T=OH, O) via Alkali Treatment, Angew. Chemie - Int. Ed. 57 (2018) 6115–6119. https://doi.org/10.1002/anie.201800887.

[115] X. Xie, Y. Xue, L. Li, S. Chen, Y. Nie, W. Ding, Z. Wei, Surface Al leached Ti_3AlC_2 as a substitute for carbon for use as a catalyst support in a harsh corrosive electrochemical system, Nanoscale. 6 (2014) 11035–11040. https://doi.org/10.1039/c4nr02080d.

[116] F. Han, S. Luo, L. Xie, J. Zhu, W. Wei, X. Chen, F. Liu, W. Chen, J. Zhao, L. Dong, K. Yu, X. Zeng, F. Rao, L. Wang, Y. Huang, Boosting the Yield of MXene 2D Sheets via a Facile Hydrothermal-Assisted Intercalation, ACS Appl. Mater. Interfaces. 11 (2019) 8443–8452. https://doi.org/10.1021/acsami.8b22339.

[117] M. Khazaei, M. Arai, T. Sasaki, M. Estili, Y. Sakka, The effect of the interlayer element on the exfoliation of layered Mo_2AC (A = Al, Si, P, Ga, Ge, As or In) MAX phases into two-dimensional Mo_2C nanosheets, Sci. Technol. Adv. Mater. 15 (2014) 014208. https://doi.org/10.1088/1468-6996/15/1/014208.

[118] Q. Li, Y. Li, W. Zeng, Preparation and application of 2D MXene-based gas sensors: A review, Chemosensors. 9 (2021). https://doi.org/10.3390/chemosensors9080225.

[119] Y. Gogotsi, B. Anasori, The Rise of MXenes, ACS Nano. 13 (2019) 8491–8494. https://doi.org/10.1021/acsnano.9b06394.

[120] S. Mehdi Aghaei, A. Aasi, B. Panchapakesan, Experimental and Theoretical Advances in MXene-Based Gas Sensors, ACS Omega. 6 (2021) 2450–2461. https://doi.org/10.1021/acsomega.0c05766.

[121] X. Zhan, C. Si, J. Zhou, Z. Sun, MXene and MXene-based composites: Synthesis, properties and environment-related applications, Nanoscale Horizons. 5 (2020) 235–258. https://doi.org/10.1039/c9nh00571d.

[122] PDF hosted at the Radboud Repository of the Radboud University Nijmegen The version of the following full text has not yet been defined or was untraceable and may, (2017).

[123] S. Ma, D. Yuan, Z. Jiao, T. Wang, X. Dai, Monolayer Sc_2CO_2: A promising candidate as a SO_2 gas sensor or capturer, J. Phys. Chem. C. 121 (2017). https://doi.org/10.1021/acs.jpcc.7b07921.

[124] W. Guo, S.G. Surya, V. Babar, F. Ming, S. Sharma, H.N. Alshareef, U.

Schwingenschlögl, K.N. Salama, Selective Toluene Detection with Mo_2CT_x MXene at Room Temperature, ACS Appl. Mater. Interfaces. 12 (2020) 57218–57227. https://doi.org/10.1021/acsami.0c16302.

[125] S.R. Naqvi, V. Shukla, N.K. Jena, W. Luo, R. Ahuja, Exploring two-dimensional M_2NS_2 (M = Ti, V) MXenes based gas sensors for air pollutants, Appl. Mater. Today. 19 (2020) 100574. https://doi.org/10.1016/j.apmt.2020.100574.

[126] E. Lee, A. Vahidmohammadi, Y.S. Yoon, M. Beidaghi, D.J. Kim, Two-Dimensional Vanadium Carbide MXene for Gas Sensors with Ultrahigh Sensitivity Toward Nonpolar Gases, ACS Sensors. 4 (2019) 1603–1611. https://doi.org/10.1021/acssensors.9b00303.

[127] A.A. Yadav, A.C. Lokhande, J.H. Kim, C.D. Lokhande, Enhanced sensitivity and selectivity of CO_2 gas sensor based on modified La_2O_3 nanorods, J. Alloys Compd. 723 (2017) 880–886. https://doi.org/10.1016/j.jallcom.2017.06.223.

[128] Y. Lin, Z. Fan, Compositing strategies to enhance the performance of chemiresistive CO_2 gas sensors, Mater. Sci. Semicond. Process. 107 (2020) 104820. https://doi.org/10.1016/j.mssp.2019.104820.

[129] K.C. Hsu, T.H. Fang, Y.J. Hsiao, C.A. Chan, Highly response CO_2 gas sensor based on Au-La_2O_3 doped SnO_2 nanofibers, Mater. Lett. 261 (2020) 127144. https://doi.org/10.1016/j.matlet.2019.127144.

[130] N. Zouadi, S. Messaci, S. Sam, D. Bradai, N. Gabouze, CO_2 detection with CN_x thin films deposited on porous silicon, Mater. Sci. Semicond. Process. 29 (2015) 367–371. https://doi.org/10.1016/j.mssp.2014.07.023.

[131] M. Habib, S.S. Hussain, S. Riaz, S. Naseem, Preparation and Characterization of ZnO Nanowires and their Applications in CO_2 Gas Sensors, Elsevier Ltd., 2015. https://doi.org/10.1016/j.matpr.2015.11.116.

[132] W. Zhang, C. Xie, G. Zhang, J. Zhang, S. Zhang, D. Zeng, Porous $LaFeO_3/SnO_2$ nanocomposite film for CO_2 detection with high sensitivity, Mater. Chem. Phys. 186 (2017) 228–236. https://doi.org/10.1016/j.matchemphys.2016.10.048.

[133] A. Chapelle, F. Oudrhiri-Hassani, L. Presmanes, A. Barnabé, P. Tailhades, CO_2 sensing properties of semiconducting copper oxide and spinel ferrite nanocomposite thin film, Appl. Surf. Sci. 256 (2010) 4715–4719. https://doi.org/10.1016/j.apsusc.2010.02.079.

[134] K. Fan, H. Qin, L. Wang, L. Ju, J. Hu, CO_2 gas sensors based on $La_{1-x}Sr_xFeO_3$ nanocrystalline powders, Sensors Actuators, B Chem. 177 (2013) 265–269. https://doi.org/10.1016/j.snb.2012.11.004.

[135] Z. Yunusa, M.N. Hamidon, A. Kaiser, Z. Awang, Gas sensors: A review, Sensors and Transducers. 168 (2014) 61–75. https://doi.org/10.13074/jent.2015.12.153163.

[136] U. Yaqoob, M.I. Younis, Chemical Gas Sensors: Recent Developments, Challenges, and the Potential of Machine Learning—A Review, Sensors. 21 (2021) 2877. https://doi.org/10.3390/s21082877.

[137] P. Shankar, J. Rayappan, Gas sensing mechanism of metal oxides: The role of ambient atmosphere, type of semiconductor and gases-A review, ScienceJet. 4 (2015) 1–18.

[138] N.M. Vuong, D. Kim, H. Kim, Surface gas sensing kinetics of a WO_3 nanowire sensor: part 1—oxidizing gases, Sensors Actuators B Chem. 220 (2015) 932–941. https://doi.org/10.1016/j.snb.2015.06.031.

[139] N.M. Vuong, D. Kim, H. Kim, Surface gas sensing kinetics of a WO_3 nanowire sensor: Part 2—Reducing gases, Sensors Actuators B Chem. 224 (2016) 425–433. https://doi.org/10.1016/j.snb.2015.10.070.

[140] H. Wang, X. Sun, Z. Liu, Z. Lei, Creation of nanopores on graphene planes with MgO template for preparing high-performance supercapacitor electrodes, Nanoscale. 6 (2014) 6577–6584. https://doi.org/10.1039/c4nr00538d.

[141] Z. Wang, Y. Hu, W. Wang, X. Zhang, B. Wang, H. Tian, Y. Wang, J. Guan, H. Gu, Fast and highly-sensitive hydrogen sensing of Nb_2O_5 nanowires at room temperature, Int. J. Hydrogen Energy. 37 (2012) 4526–4532. https://doi.org/10.1016/j.ijhydene.2011.12.004.

[142] K. Xu, C. Fu, Z. Gao, F. Wei, Y. Ying, C. Xu, G. Fu, Nanomaterial-based gas sensors: A review, Instrum. Sci. Technol. 46 (2018) 115–145. https://doi.org/10.1080/10739149.2017.1340896.

[143] C. Wang, L. Yin, L. Zhang, D. Xiang, R. Gao, Metal Oxide Gas Sensors: Sensitivity and Influencing Factors, Sensors. 10 (2010) 2088–2106. https://doi.org/10.3390/s100302088.

[144] P.-J. Cao, M. Li, C.N. Rao, S. Han, W.-Y. Xu, M. Fang, X.-K. Liu, Y.-X. Zeng, W.-J. Liu, D.-L. Zhu, Y.-M. Lu, High Sensitivity NO_2 Gas Sensor Based on 3D WO_3 Microflowers Assembled by Numerous Nanoplates, J. Nanosci. Nanotechnol. 20 (2020) 1790–1798. https://doi.org/10.1166/jnn.2020.17175.

[145] M.-W. Ahn, K.-S. Park, J.-H. Heo, J.-G. Park, D.-W. Kim, K.J. Choi, J.-H. Lee, S.-H. Hong, Gas sensing properties of defect-controlled ZnO-nanowire gas sensor, Appl. Phys. Lett. 93 (2008) 263103. https://doi.org/10.1063/1.3046726.

[146] R. IONESCU, Low-level detection of ethanol and H_2S with temperature-modulated WO_3 nanoparticle gas sensors, Sensors Actuators B Chem. 104 (2005) 132–139. https://doi.org/10.1016/j.snb.2004.05.015.

[147] S. Lin, D. Li, J. Wu, X. Li, S.A. Akbar, A selective room temperature formaldehyde gas sensor using TiO2 nanotube arrays, Sensors Actuators B Chem. 156 (2011) 505–

509. https://doi.org/10.1016/j.snb.2011.02.046.

[148] Y.-J. Choi, I.-S. Hwang, J.-G. Park, K.J. Choi, J.-H. Park, J.-H. Lee, Novel fabrication of an SnO_2 nanowire gas sensor with high sensitivity, Nanotechnology. 19 (2008) 095508. https://doi.org/10.1088/0957-4484/19/9/095508.

[149] D.R. Miller, S.A. Akbar, P.A. Morris, Nanoscale metal oxide-based heterojunctions for gas sensing: A review, Sensors Actuators B Chem. 204 (2014) 250–272. https://doi.org/10.1016/j.snb.2014.07.074.

[150] Q. Sun, J. Wang, J. Hao, S. Zheng, P. Wan, T. Wang, H. Fang, Y. Wang, SnS_2 /SnS p–n heterojunctions with an accumulation layer for ultrasensitive room-temperature NO_2 detection, Nanoscale. 11 (2019) 13741–13749. https://doi.org/10.1039/C9NR02780G.

[151] U.T. Nakate, R. Ahmad, P. Patil, Y. Wang, K.S. Bhat, T. Mahmoudi, Y.T. Yu, E. Suh, Y.-B. Hahn, Improved selectivity and low concentration hydrogen gas sensor application of Pd sensitized heterojunction n-ZnO/p-NiO nanostructures, J. Alloys Compd. 797 (2019) 456–464. https://doi.org/10.1016/j.jallcom.2019.05.111.

[152] H.-F. Bao, T.-T. Yue, X.-X. Zhang, Z. Dong, Y. Yan, W. Feng, Enhanced Ethanol-Sensing Properties Based on Modified NiO–ZnO p–n Heterojunction Nanotubes, J. Nanosci. Nanotechnol. 20 (2020) 731–740. https://doi.org/10.1166/jnn.2020.16903.

[153] A.D. Brailsford, M. Yussouff, E.M. Logothetis, Theory of gas sensors, Sensors Actuators B. Chem. 13 (1993) 135–138. https://doi.org/10.1016/0925-4005(93)85344-A.

[154] H. Wang, J. Ma, J. Zhang, Y. Feng, M.T. Vijjapu, S. Yuvaraja, S.G. Surya, K.N. Salama, C. Dong, Y. Wang, Q. Kuang, Z.P. Tshabalala, D.E. Motaung, X. Liu, J. Yang, H. Fu, X. Yang, X. An, S. Zhou, B. Zi, Q. Liu, M. Urso, B. Zhang, A.A. Akande, A.K. Prasad, C.M. Hung, N. Van Duy, N.D. Hoa, K. Wu, C. Zhang, R. Kumar, M. Kumar, Y. Kim, J. Wu, Z. Wu, X. Yang, S.A. Vanalakar, J. Luo, H. Kan, M. Li, H.W. Jang, M.O. Orlandi, A. Mirzaei, H.W. Kim, S.S. Kim, A.S.M.I. Uddin, J. Wang, Y. Xia, C. Wongchoosuk, A. Nag, S. Mukhopadhyay, N. Saxena, P. Kumar, J.-S. Do, J.-H. Lee, S. Hong, Y. Jeong, G. Jung, W. Shin, J. Park, M. Bruzzi, C. Zhu, R.E. Gerald, J. Huang, Gas sensing materials roadmap, J. Phys. Condens. Matter. 33 (2021) 303001. https://doi.org/10.1088/1361-648X/abf477.

[155] D.R. Kauffman, A. Star, Carbon nanotube gas and vapor sensors, Angew. Chemie - Int. Ed. 47 (2008) 6550–6570. https://doi.org/10.1002/anie.200704488.

[156] N. Dubouis, A. Grimaud, The hydrogen evolution reaction: From material to interfacial descriptors, Chem. Sci. 10 (2019) 9165–9181. https://doi.org/10.1039/c9sc03831k.

[157] Y. Zheng, Y. Jiao, A. Vasileff, S. Qiao, The Hydrogen Evolution Reaction in

Alkaline Solution: From Theory, Single Crystal Models, to Practical Electrocatalysts, Angew. Chemie Int. Ed. 57 (2018) 7568–7579. https://doi.org/10.1002/anie.201710556.

[158] C. Hu, L. Zhang, J. Gong, Recent progress made in the mechanism comprehension and design of electrocatalysts for alkaline water splitting, Energy Environ. Sci. 12 (2019) 2620–2645. https://doi.org/10.1039/C9EE01202H.

[159] J. Janata, Physical Electrochemistry. Fundamentals, Techniques and Applications. By Eliezer Gileadi., Angew. Chemie Int. Ed. 50 (2011) 9538–9538. https://doi.org/10.1002/anie.201104618.

[160] A. Lasia, Hydrogen evolution reaction, in: Handb. Fuel Cells, John Wiley & Sons, Ltd, Chichester, UK, 2010. https://doi.org/10.1002/9780470974001.f204033.

[161] J.O. Bockris, E.C. Potter, The Mechanism of the Cathodic Hydrogen Evolution Reaction, J. Electrochem. Soc. 99 (1952) 169. https://doi.org/10.1149/1.2779692.

[162] B.E. Conway, B.V. Tilak, Interfacial processes involving electrocatalytic evolution and oxidation of H2, and the role of chemisorbed H, Electrochim. Acta. 47 (2002) 3571–3594. https://doi.org/10.1016/S0013-4686(02)00329-8.

[163] C. Costentin, S. Drouet, M. Robert, J.-M. Savéant, Turnover Numbers, Turnover Frequencies, and Overpotential in Molecular Catalysis of Electrochemical Reactions. Cyclic Voltammetry and Preparative-Scale Electrolysis, J. Am. Chem. Soc. 134 (2012) 11235–11242. https://doi.org/10.1021/ja303560c.

[164] A. Eftekhari, Electrocatalysts for hydrogen evolution reaction, Int. J. Hydrogen Energy. 42 (2017) 11053–11077. https://doi.org/10.1016/j.ijhydene.2017.02.125.

[165] J. Tymoczko, F. Calle-Vallejo, W. Schuhmann, A.S. Bandarenka, Making the hydrogen evolution reaction in polymer electrolyte membrane electrolysers even faster, Nat. Commun. 7 (2016) 10990. https://doi.org/10.1038/ncomms10990.

[166] S. Wirth, F. Harnisch, M. Weinmann, U. Schröder, Comparative study of IVB–VIB transition metal compound electrocatalysts for the hydrogen evolution reaction, Appl. Catal. B Environ. 126 (2012) 225–230. https://doi.org/10.1016/j.apcatb.2012.07.023.

[167] A. Abdellaoui, G. Lévêque, A. Donnadieu, A. Bath, B. Bouchikhi, Iteratively derived optical constants of MoO_3 polycrystalline thin films prepared by CVD, Thin Solid Films. 304 (1997) 39–44. https://doi.org/10.1016/S0040-6090(97)00092-8.

[168] T. Nagyné-Kovács, L. Studnicka, I.E. Lukács, K. László, P. Pasierb, I.M. Szilágyi, G. Pokol, Hydrothermal synthesis and gas sensing of monoclinic MoO_3 nanosheets, Nanomaterials. 10 (2020) 2–13. https://doi.org/10.3390/nano10050891.

[169] I. Shaheen, K.S. Ahmad, Modified sol gel synthesis of MoO_3 NPs using organic template: synthesis, characterization and electrochemical investigations, J. Sol-Gel Sci. Technol. 97 (2021) 178–190. https://doi.org/10.1007/s10971-020-05398-6.

[170] N. Zhao, H. Fan, M. Zhang, J. Ma, Z. Du, B. Yan, H. Li, X. Jiang, Simple electrodeposition of MoO_3 film on carbon cloth for high-performance aqueous symmetric supercapacitors, Chem. Eng. J. 390 (2020) 124477. https://doi.org/10.1016/j.cej.2020.124477.

[171] J.S. Chen, Y.L. Cheah, S. Madhavi, X.W. Lou, Fast synthesis of α-MoO_3 nanorods with controlled aspect ratios and their enhanced lithium storage capabilities, J. Phys. Chem. C. 114 (2010) 8675–8678. https://doi.org/10.1021/jp1017482.

[172] L. Khandare, S.S. Terdale, D.J. Late, Ultra-fast α-MoO_3 nanorod-based Humidity sensor, Adv. Device Mater. 2 (2016) 15–22. https://doi.org/10.1080/20550308.2016.1221605.

[173] S. Bai, C. Chen, Y. Tian, S. Chen, R. Luo, D. Li, A. Chen, C.C. Liu, Facile synthesis of α-MoO_3 nanorods with high sensitivity to CO and intrinsic sensing performance, Mater. Res. Bull. 64 (2015) 252–256. https://doi.org/10.1016/j.materresbull.2014.12.049.

[174] G.S. Zakharova, C. Täschner, V.L. Volkov, I. Hellmann, R. Klingeler, A. Leonhardt, B. Büchner, $MoO_{3-\delta}$ nanorods: Synthesis, characterization and magnetic properties, Solid State Sci. 9 (2007) 1028–1032. https://doi.org/10.1016/j.solidstatesciences.2007.07.022.

[175] J. Zhou, S.Z. Deng, N.S. Xu, J. Chen, J.C. She, Synthesis and field-emission properties of aligned MoO_3 nanowires, Appl. Phys. Lett. 83 (2003) 2653–2655. https://doi.org/10.1063/1.1613992.

[176] M.B. Rahmani, S.H. Keshmiri, J. Yu, A.Z. Sadek, L. Al-Mashat, A. Moafi, K. Latham, Y.X. Li, W. Wlodarski, K. Kalantar-zadeh, Gas sensing properties of thermally evaporated lamellar MoO_3, Sensors Actuators, B Chem. 145 (2010) 13–19. https://doi.org/10.1016/j.snb.2009.11.007.

[177] N.G. Prakash, M. Dhananjaya, A.L. Narayana, D.P. Shaik, P. Rosaiah, O.M. Hussain, High Performance One Dimensional α-MoO_3 Nanorods for Supercapacitor Applications, Elsevier Ltd and Techna Group S.r.l., 2018. https://doi.org/10.1016/j.ceramint.2018.03.032.

[178] J. Wang, Q. Zhou, S. Peng, L. Xu, W. Zeng, Volatile Organic Compounds Gas Sensors Based on Molybdenum Oxides: A Mini Review, Front. Chem. 8 (2020) 1–7. https://doi.org/10.3389/fchem.2020.00339.

[179] F. Rahman, A. Zavabeti, M.A. Rahman, A. Arash, A. Mazumder, S. Walia, S. Sriram, M. Bhaskaran, S. Balendhran, Dual Selective Gas Sensing Characteristics of 2D α-MoO_{3-x} via a Facile Transfer Process, ACS Appl. Mater. Interfaces. 11 (2019) 40189–40195. https://doi.org/10.1021/acsami.9b11311.

[180] L. Chen, D. Li, R. Luo, C.C. Liu, S. Chen, K. Zhang, S. Bai, Ultrasonic synthesis of

MoO_3 nanorods and their gas sensing properties, Sensors Actuators B Chem. 174 (2012) 51–58. https://doi.org/10.1016/j.snb.2012.08.015.

[181] S. Yang, Z. Wang, Y. Hu, X. Luo, J. Lei, D. Zhou, L. Fei, Y. Wang, H. Gu, Highly Responsive Room-Temperature Hydrogen Sensing of α-MoO_3 Nanoribbon Membranes, ACS Appl. Mater. Interfaces. 7 (2015) 9247–9253. https://doi.org/10.1021/acsami.5b01858.

[182] S. Yang, Y. Liu, W. Chen, W. Jin, J. Zhou, H. Zhang, G.S. Zakharova, Y. Liu, High sensitivity and good selectivity of ultralong MoO_3 nanobelts for trimethylamine gas, Sensors Actuators B. Chem. 226 (2015) 478–485. https://doi.org/10.1016/j.snb.2015.12.005.

[183] L. Wang, P. Gao, D. Bao, Y. Wang, Y. Chen, C. Chang, G. Li, P. Yang, Synthesis of crystalline/amorphous core/shell MoO_3 composites through a controlled dehydration route and their enhanced ethanol sensing properties, Cryst. Growth Des. 14 (2014) 569–575. https://doi.org/10.1021/cg401384t.

[184] L. Cai, P.M. Rao, X. Zheng, Morphology-Controlled Flame Synthesis of Single, Branched, and Flower-like r -MoO_3 Nanobelt Arrays, Nano Lett. 11 (2011) 872–877. https://doi.org/10.1021/nl104270u.

[185] S. Kumar, A. Singh, R. Singh, S. Singh, P. Kumar, R. Kumar, Facile h-MoO_3 synthesis for NH_3 gas sensing application at moderate operating temperature, Sensors Actuators, B Chem. 325 (2020) 128974. https://doi.org/10.1016/j.snb.2020.128974.

[186] S.S. Sunu, E. Prabhu, V. Jayaraman, K.I. Gnanasekar, T. Gnanasekaran, Gas sensing properties of PLD made MoO_3 films, Sensors Actuators, B Chem. 94 (2003) 189–196. https://doi.org/10.1016/S0925-4005(03)00342-3.

[187] C. Imawan, F. Solzbacher, H. Steffes, E. Obermeier, Gas-sensing characteristics of modified -MoO_3 thin films using Ti-overlayers for NH_3 gas sensors, Sensors Actuators, B Chem. 64 (2000) 193–197. https://doi.org/10.1016/S0925-4005(99)00506-7.

[188] E. Comini, G. Faglia, G. Sberveglieri, C. Cantalini, M. Passacantando, S. Santucci, Carbon monoxide response of molybdenum oxide thin films deposited by different techniques, Sensors Actuators B Chem. 68 (2000) 168–174.

[189] D. Mutschall, K. Holzner, E. Obermeier, Sputtered molybdenum oxide thin films for NH3 detection, Sensors Actuators, B Chem. 36 (1996) 320–324. https://doi.org/10.1016/S0925-4005(97)80089-5.

[190] S. Pollalis, Energy Infrastructure, Plan. Sustain. Cities. 243116 (2019) 143–180. https://doi.org/10.4324/9781315642352-9.

[191] L.H.U.W. Abeydeera, J.W. Mesthrige, T.I. Samarasinghalage, Global research on carbon emissions: A scientometric review, Sustain. 11 (2019) 1–25.

https://doi.org/10.3390/su11143972.

[192] D. Yan, M. Hu, S. Li, J. Liang, Y. Wu, S. Ma, Electrochemical deposition of ZnO nanostructures onto porous silicon and their enhanced gas sensing to NO_2 at room temperature, Electrochim. Acta. 115 (2014) 297–305. https://doi.org/10.1016/j.electacta.2013.10.007.

[193] J. Flávio da Silveira Petruci, P.R. Fortes, V. Kokoric, A. Wilk, I.M. Raimundo, A.A. Cardoso, B. Mizaikoff, Monitoring of hydrogen sulfide via substrate-integrated hollow waveguide mid-infrared sensors in real-time, Analyst. 139 (2014) 198–203. https://doi.org/10.1039/c3an01793a.

[194] Duk-Dong Lee, Dae-Sik Lee, Environmental gas sensors, IEEE Sens. J. 1 (2001) 214–224. https://doi.org/10.1109/JSEN.2001.954834.

[195] X. Han, M. Jin, S. Xie, Q. Kuang, Z. Jiang, Y. Jiang, Z. Xie, L. Zheng, Synthesis of Tin Dioxide Octahedral Nanoparticles with Exposed High-Energy {221} Facets and Enhanced Gas-Sensing Properties, Angew. Chemie. 121 (2009) 9344–9347. https://doi.org/10.1002/ange.200903926.

[196] C. Wang, L. Yin, L. Zhang, D. Xiang, R. Gao, Metal oxide gas sensors: Sensitivity and influencing factors, Sensors. 10 (2010) 2088–2106. https://doi.org/10.3390/s100302088.

[197] N. Rajesh, J.C. Kannan, T. Krishnakumar, A. Bonavita, S.G. Leonardi, G. Neri, Microwave irradiated Sn-substituted CdO nanostructures for enhanced CO_2 sensing, Ceram. Int. 41 (2015) 14766–14772. https://doi.org/10.1016/j.ceramint.2015.07.208.

[198] D. Mardare, N. Cornei, C. Mita, D. Florea, A. Stancu, V. Tiron, A. Manole, C. Adomnitei, Low temperature TiO_2 based gas sensors for CO_2, Ceram. Int. 42 (2016) 7353–7359. https://doi.org/10.1016/j.ceramint.2016.01.137.

[199] P.F. Cao, S.Y. Ma, X.L. Xu, B.J. Wang, O. Almamoun, T. Han, X.H. Xu, S.T. Pei, R. Zhang, J.L. Zhang, W.W. Liu, Preparation and characterization of a novel ethanol gas sensor based on $FeYO_3$ microspheres by using orange peels as bio-templates, Vacuum. 177 (2020). https://doi.org/10.1016/j.vacuum.2020.109359.

[200] B.J. Wang, S.Y. Ma, High response ethanol gas sensor based on orthorhombic and tetragonal SnO_2, Vacuum. 177 (2020) 109428. https://doi.org/10.1016/j.vacuum.2020.109428.

[201] Z. Li, Y. Liu, D. Guo, J. Guo, Y. Su, Room-temperature synthesis of CuO/reduced graphene oxide nanohybrids for high-performance NO_2 gas sensor, Sensors Actuators, B Chem. 271 (2018) 306–310. https://doi.org/10.1016/j.snb.2018.05.097.

[202] B. Mandal, A. Biswas, Aaryashree, D.S. Sharma, R. Bhardwaj, M. Das, M.A. Rahman, S. Kuriakose, M. Bhaskaran, S. Sriram, M. Than Htay, A.K. Das, S. Mukherjee, π-Conjugated Amine-ZnO Nanohybrids for the Selective Detection of

CO_2 Gas at Room Temperature, ACS Appl. Nano Mater. 1 (2018) 6912–6921. https://doi.org/10.1021/acsanm.8b01731.

[203] J.W. Kim, Y. Porte, K.Y. Ko, H. Kim, J.M. Myoung, Micropatternable Double-Faced ZnO Nanoflowers for Flexible Gas Sensor, ACS Appl. Mater. Interfaces. 9 (2017) 32876–32886. https://doi.org/10.1021/acsami.7b09251.

[204] J.M. Polfus, B. Yildiz, H.L. Tuller, R. Bredesen, Adsorption of CO_2 and Facile Carbonate Formation on $BaZrO_3$ Surfaces, J. Phys. Chem. C. 122 (2018) 307–314. https://doi.org/10.1021/acs.jpcc.7b08223.

[205] V.K. Tomer, K. Singh, H. Kaur, M. Shorie, P. Sabherwal, Rapid acetone detection using indium loaded WO_3/SnO_2 nanohybrid sensor, Sensors Actuators, B Chem. 253 (2017) 703–713. https://doi.org/10.1016/j.snb.2017.06.179.

[206] J. Wu, Y. Yang, H. Yu, X. Dong, T. Wang, Ultra-efficient room-temperature H_2S gas sensor based on $NiCo_2O_4$/r-GO nanocomposites, New J. Chem. 43 (2019) 10501–10508. https://doi.org/10.1039/c9nj01094g.

[207] A. Chapelle, I. El Younsi, S. Vitale, Y. Thimont, T. Nelis, L. Presmanes, A. Barnabé, P. Tailhades, Improved semiconducting CuO/$CuFe_2O_4$ nanostructured thin films for CO_2 gas sensing, Sensors Actuators, B Chem. 204 (2014) 407–413. https://doi.org/10.1016/j.snb.2014.07.088.

[208] X. Wang, H. Qin, L. Sun, J. Hu, CO_2 sensing properties and mechanism of nanocrystalline $LaFeO_3$ sensor, Sensors Actuators, B Chem. 188 (2013) 965–971. https://doi.org/10.1016/j.snb.2013.07.100.

[209] P.K. Kannan, R. Saraswathi, J.B.B. Rayappan, CO_2 gas sensing properties of DC reactive magnetron sputtered ZnO thin film, Ceram. Int. 40 (2014) 13115–13122. https://doi.org/10.1016/j.ceramint.2014.05.011.

[210] H. Wang, H. Chen, M. Zhang, J. Wang, J. Sun, Solid-state potentiometric CO_2 sensor combining Li_3PO_4 with MoO_3-doped Li_2CO_3 sensing electrode, Ionics (Kiel). 25 (2019) 3397–3406. https://doi.org/10.1007/s11581-019-02862-4.

[211] T.V.K. Karthik, L. Martinez, V. Agarwal, Porous silicon ZnO/SnO_2 structures for CO_2 detection, J. Alloys Compd. 731 (2018) 853–863. https://doi.org/10.1016/j.jallcom.2017.10.070.

[212] R. Dhahri, S.G. Leonardi, M. Hjiri, L. El Mir, A. Bonavita, N. Donato, D. Iannazzo, G. Neri, Sensors and Actuators B : Chemical Enhanced performance of novel calcium / aluminum co-doped zinc oxide for CO_2 sensors, Sensors Actuators B. Chem. 239 (2017) 36–44. https://doi.org/10.1016/j.snb.2016.07.155.

[213] A. Ghosh, C. Zhang, H. Zhang, S. Shi, CO_2 Sensing Behavior of Calcium-Doped ZnO Thin Film: A Study To Address the Cross-Sensitivity of CO_2 in H_2 and CO Environment, Langmuir. 35 (2019) 10267–10275.

https://doi.org/10.1021/acs.langmuir.9b00724.

[214] D. Wang, Y. Cheng, K. Wan, J. Yang, J. Xu, X. Wang, High efficiency xylene detection based on porous MoO_3 nanosheets, Vacuum. 179 (2020) 109487. https://doi.org/10.1016/j.vacuum.2020.109487.

[215] H. Yu, L. Li, X. Gao, Y. Zhang, F. Meng, T. Wang, G. Xiao, Y. Chen, C. Zhu, Synthesis and H2S gas sensing properties of cage-like α-MoO_3/ZnO composite, Sensors Actuators B Chem. 171–172 (2012) 679–685. https://doi.org/10.1016/j.snb.2012.05.054.

[216] S. Yang, Y. Liu, T. Chen, W. Jin, T. Yang, M. Cao, S. Liu, J. Zhou, G.S. Zakharova, W. Chen, Applied Surface Science Zn doped MoO_3 nanobelts and the enhanced gas sensing properties to ethanol, Appl. Surf. Sci. 393 (2017) 377–384. https://doi.org/10.1016/j.apsusc.2016.10.021.

[217] L. Sui, Y. Xu, X. Zhang, X. Cheng, S. Gao, H. Zhao, Sensors and Actuators B : Chemical hierarchical structure for highly selective triethylamine sensor, Sensors Actuators B. Chem. 208 (2015) 406–414. https://doi.org/10.1016/j.snb.2014.10.138.

[218] N. Naderi, M.R. Hashim, T.S.T. Amran, Enhanced physical properties of porous silicon for improved hydrogen gas sensing, Superlattices Microstruct. 51 (2012) 626–634. https://doi.org/10.1016/j.spmi.2012.03.010.

[219] V.A. Moshnikov, I. Gracheva, A.S. Lenshin, Y.M. Spivak, M.G. Anchkov, V. V. Kuznetsov, J.M. Olchowik, Porous silicon with embedded metal oxides for gas sensing applications, J. Non. Cryst. Solids. 358 (2012) 590–595. https://doi.org/10.1016/j.jnoncrysol.2011.10.017.

[220] L. Canham, Handbook of Porous Silicon, Handb. Porous Silicon. (2014) 1–1017. https://doi.org/10.1007/978-3-319-05744-6.

[221] J.-S. Li, Y. Wang, C.-H. Liu, S.-L. Li, Y.-G. Wang, L.-Z. Dong, Z.-H. Dai, Y.-F. Li, Y.-Q. Lan, Coupled molybdenum carbide and reduced graphene oxide electrocatalysts for efficient hydrogen evolution, Nat. Commun. 7 (2016) 11204. https://doi.org/10.1038/ncomms11204.

[222] M.D. Scanlon, X. Bian, H. Vrubel, V. Amstutz, K. Schenk, X. Hu, B. Liu, H.H. Girault, Low-cost industrially available molybdenum boride and carbide as “platinum-like” catalysts for the hydrogen evolution reaction in biphasic liquid systems, Phys. Chem. Chem. Phys. 15 (2013) 2847. https://doi.org/10.1039/c2cp44522k.

[223] J. Pang, R.G. Mendes, A. Bachmatiuk, L. Zhao, H.Q. Ta, T. Gemming, H. Liu, Z. Liu, M.H. Rummeli, Applications of 2D MXenes in energy conversion and storage systems, Chem. Soc. Rev. 48 (2019) 72–133. https://doi.org/10.1039/c8cs00324f.

[224] A. Rodriguez, M.S. Jaman, O. Acikgoz, B. Wang, J. Yu, P.G. Grützmacher, A.

Rosenkranz, M.Z. Baykara, The potential of $Ti_3C_2T_x$ nano-sheets (MXenes) for nanoscale solid lubrication revealed by friction force microscopy, Appl. Surf. Sci. 535 (2021) 147664. https://doi.org/10.1016/j.apsusc.2020.147664.

[225] D. Fang, D. Zhao, S. Zhang, Y. Huang, H. Dai, Y. Lin, Black phosphorus quantum dots functionalized MXenes as the enhanced dual-mode probe for exosomes sensing, Sensors Actuators, B Chem. 305 (2020) 127544. https://doi.org/10.1016/j.snb.2019.127544.

[226] X.H. Zha, J. Zhou, P. Eklund, X. Bai, S. Du, Q. Huang, Non-MAX phase precursors for MXenes, 2D Met. Carbides Nitrides Struct. Prop. Appl. (2019) 53–68. https://doi.org/10.1007/978-3-030-19026-2_4.

[227] S. Zhao, R. Nivetha, Y. Qiu, X. Guo, Two-dimensional hybrid nanomaterials derived from MXenes ($Ti_3C_2T_x$) as advanced energy storage and conversion applications., Chinese Chem. Lett. (2019). https://doi.org/10.1016/j.cclet.2019.11.045.

[228] J. Mei, G.A. Ayoko, C. Hu, J.M. Bell, Z. Sun, Two-dimensional fluorine-free mesoporous Mo2C MXene via UV-induced selective etching of Mo_2Ga_2C for energy storage, Sustain. Mater. Technol. 25 (2020) e00156. https://doi.org/10.1016/j.susmat.2020.e00156.

[229] S. Bai, M. Yang, J. Jiang, X. He, J. Zou, Z. Xiong, G. Liao, S. Liu, Recent advances of MXenes as electrocatalysts for hydrogen evolution reaction, Npj 2D Mater. Appl. 5 (2021). https://doi.org/10.1038/s41699-021-00259-4.

[230] A. Iqbal, P. Sambyal, C.M. Koo, 2D MXenes for Electromagnetic Shielding: A Review, Adv. Funct. Mater. 2000883 (2020) 1–25. https://doi.org/10.1002/adfm.202000883.

[231] J. Jimmy, B. Kandasubramanian, Mxene functionalized polymer composites: Synthesis and applications, Eur. Polym. J. 122 (2020) 109367. https://doi.org/10.1016/j.eurpolymj.2019.109367.

[232] V.H. Nguyen, R. Tabassian, S. Oh, S. Nam, M. Mahato, P. Thangasamy, A. Rajabi-Abhari, W.J. Hwang, A.K. Taseer, I.K. Oh, Stimuli-Responsive MXene-Based Actuators, Adv. Funct. Mater. 1909504 (2020) 1–27. https://doi.org/10.1002/adfm.201909504.

[233] Y.Z. Zhang, Y. Wang, Q. Jiang, J.K. El-Demellawi, H. Kim, H.N. Alshareef, MXene Printing and Patterned Coating for Device Applications, Adv. Mater. 32 (2020) 1–26. https://doi.org/10.1002/adma.201908486.

[234] Q. Song, F. Ye, L. Kong, Q. Shen, L. Han, L. Feng, G. Yu, Y. Pan, H. Li, Graphene and MXene Nanomaterials: Toward High-Performance Electromagnetic Wave Absorption in Gigahertz Band Range, Adv. Funct. Mater. 2000475 (2020) 1–30. https://doi.org/10.1002/adfm.202000475.

[235] B. Anasori, Y. Xie, M. Beidaghi, J. Lu, B.C. Hosler, L. Hultman, P.R.C. Kent, Y. Gogotsi, M.W. Barsoum, Two-Dimensional, Ordered, Double Transition Metals Carbides (MXenes), ACS Nano. 9 (2015) 9507–9516. https://doi.org/10.1021/acsnano.5b03591.

[236] M. Ghidiu, M. Naguib, C. Shi, O. Mashtalir, L.M. Pan, B. Zhang, J. Yang, Y. Gogotsi, S.J.L. Billinge, M.W. Barsoum, Synthesis and characterization of two-dimensional Nb_4C_3 (MXene), Chem. Commun. 50 (2014) 9517–9520. https://doi.org/10.1039/c4cc03366c.

[237] Z. Fu, N. Wang, D. Legut, C. Si, Q. Zhang, S. Du, T.C. Germann, J.S. Francisco, R. Zhang, Rational Design of Flexible Two-Dimensional MXenes with Multiple Functionalities, Chem. Rev. 119 (2019) 11980–12031. https://doi.org/10.1021/acs.chemrev.9b00348.

[238] Y. Yoon, M. Lee, S.K. Kim, G. Bae, W. Song, S. Myung, J. Lim, S.S. Lee, T. Zyung, K.S. An, A Strategy for Synthesis of Carbon Nitride Induced Chemically Doped 2D MXene for High-Performance Supercapacitor Electrodes, Adv. Energy Mater. 8 (2018) 1–11. https://doi.org/10.1002/aenm.201703173.

[239] Y. Tan, M. Yi, Z. Zhu, X. Zhang, K. Qin, J. Zhang, R. Zhu, Carbon-coated $MoSe_2/Mo_2CT_x$ (MXene) heterostructure for efficient hydrogen evolution, Mater. Sci. Eng. B Solid-State Mater. Adv. Technol. 271 (2021). https://doi.org/10.1016/j.mseb.2021.115239.

[240] Y.-Z. Wang, Y.-M. Ding, C.-H. Zhang, B.-W. Xue, N.-W. Li, L. Yu, Formation of hierarchical Co-decorated Mo_2C hollow spheres for enhanced hydrogen evolution, Rare Met. 40 (2021) 2785–2792. https://doi.org/10.1007/s12598-021-01765-6.

[241] S. Liu, Z. Lin, R. Wan, Y. Liu, Z. Liu, S. Zhang, X. Zhang, Z. Tang, X. Lu, Y. Tian, Cobalt phosphide supported by two-dimensional molybdenum carbide (MXene) for the hydrogen evolution reaction, oxygen evolution reaction, and overall water splitting, J. Mater. Chem. A. 9 (2021) 21259–21269. https://doi.org/10.1039/d1ta05648d.

[242] Y. Tang, C. Yang, M. Sheng, X. Yin, W. Que, J. Henzie, Y. Yamauchi, Phosphorus-doped molybdenum carbide/MXene hybrid architectures for upgraded hydrogen evolution reaction performance over a wide pH range, Chem. Eng. J. 423 (2021) 130183. https://doi.org/10.1016/j.cej.2021.130183.

[243] L. Zhang, Z. Liu, L. Jin, B. Zhang, H. Zhang, M. Zhu, W. Yang, Sensors and Actuators B : Chemical Self-assembly gridding -MoO_3 nanobelts for highly toxic H_2S gas sensors, Sensors Actuators B. Chem. 237 (2016) 350–357. https://doi.org/10.1016/j.snb.2016.06.104.

[244] T. Suzuki, A. Sackmann, A. Oprea, U. Weimar, N. Barsan, Rare-Earth Based

Chemoresistive CO_2 Sensors and Their Operando Investigations, Proceedings. 14 (2019) 17. https://doi.org/10.3390/proceedings2019014017.

[245] M.E. DMello, N.G. Sundaram, S.B. Kalidindi, Assembly of ZIF-67 Metal–Organic Framework over Tin Oxide Nanoparticles for Synergistic Chemiresistive CO_2 Gas Sensing, Chem. - A Eur. J. 24 (2018) 9220–9223. https://doi.org/10.1002/chem.201800847.

[246] S. Yang, Y. Liu, W. Chen, W. Jin, J. Zhou, H. Zhang, G.S. Zakharova, Sensors and Actuators B : Chemical High sensitivity and good selectivity of ultralong MoO_3 nanobelts for trimethylamine gas, Sensors Actuators B. Chem. 226 (2016) 478–485. https://doi.org/10.1016/j.snb.2015.12.005.

[247] S.Y. Cho, S.J. Kim, Y. Lee, J.S. Kim, W. Bin Jung, H.W. Yoo, J. Kim, H.T. Jung, Highly Enhanced Gas Adsorption Properties in Vertically Aligned MoS_2 Layers, ACS Nano. 9 (2015) 9314–9321. https://doi.org/10.1021/acsnano.5b04504.

[248] S.Y. Cho, Y. Lee, H.J. Koh, H. Jung, J.S. Kim, H.W. Yoo, J. Kim, H.T. Jung, Superior Chemical Sensing Performance of Black Phosphorus: Comparison with MoS2and Graphene, Adv. Mater. 28 (2016) 7020–7028. https://doi.org/10.1002/adma.201601167.

[249] M. Donarelli, L. Ottaviano, 2d materials for gas sensing applications: A review on graphene oxide, MoS_2, WS_2 and phosphorene, Sensors (Switzerland). 18 (2018). https://doi.org/10.3390/s18113638.

[250] M. Kurtoglu, M. Naguib, Y. Gogotsi, M.W. Barsoum, First principles study of two-dimensional early transition metal carbides, MRS Commun. 2 (2012) 133–137. https://doi.org/10.1557/mrc.2012.25.

[251] S.H. Lee, W. Eom, H. Shin, R.B. Ambade, J.H. Bang, H.W. Kim, T.H. Han, Room-Temperature, Highly Durable $Ti_3C_2T_x$ MXene/Graphene Hybrid Fibers for NH3 Gas Sensing, ACS Appl. Mater. Interfaces. 12 (2020) 10434–10442. https://doi.org/10.1021/acsami.9b21765.

[252] W. Yuan, K. Yang, H. Peng, F. Li, F. Yin, A flexible VOCs sensor based on a 3D Mxene framework with a high sensing performance, J. Mater. Chem. A. 6 (2018) 18116–18124. https://doi.org/10.1039/c8ta06928j.

[253] X. Sang, Y. Xie, M.W. Lin, M. Alhabeb, K.L. Van Aken, Y. Gogotsi, P.R.C. Kent, K. Xiao, R.R. Unocic, Atomic defects in monolayer titanium carbide ($Ti_3C_2T_x$) MXene, ACS Nano. 10 (2016) 9193–9200. https://doi.org/10.1021/acsnano.6b05240.

[254] S. Hajian, P. Khakbaz, M. Moshayedi, D. Maddipatla, B.B. Narakathu, V.S. Turkani, B.J. Bazuin, M. Pourfath, M.Z. Atashbar, Impact of Different Ratios of Fluorine, Oxygen, and Hydroxyl Surface Terminations on $Ti_3C_2T_x$ MXene as Ammonia Sensor: A First-Principles Study, Proc. IEEE Sensors. 2018-Octob (2018) 1–4.

https://doi.org/10.1109/ICSENS.2018.8589699.

[255] S.J. Kim, H.J. Koh, C.E. Ren, O. Kwon, K. Maleski, S.Y. Cho, B. Anasori, C.K. Kim, Y.K. Choi, J. Kim, Y. Gogotsi, H.T. Jung, Metallic $Ti_3C_2T_x$ MXene Gas Sensors with Ultrahigh Signal-to-Noise Ratio, ACS Nano. 12 (2018) 986–993. https://doi.org/10.1021/acsnano.7b07460.

[256] H.J. Koh, S.J. Kim, K. Maleski, S.Y. Cho, Y.J. Kim, C.W. Ahn, Y. Gogotsi, H.T. Jung, Enhanced Selectivity of MXene Gas Sensors through Metal Ion Intercalation: In Situ X-ray Diffraction Study, ACS Sensors. 4 (2019) 1365–1372. https://doi.org/10.1021/acssensors.9b00310.

[257] Y. Zhou, Y. Wang, Y. Wang, X. Li, Humidity-Enabled Ionic Conductive Trace Carbon Dioxide Sensing of Nitrogen-Doped $Ti_3C_2T_x$ MXene/Polyethyleneimine Composite Films Decorated with Reduced Graphene Oxide Nanosheets, Anal. Chem. 92 (2020) 16033–16042. https://doi.org/10.1021/acs.analchem.0c03664.

[258] P. Dwivedi, S. Das, S. Dhanekar, Wafer-Scale Synthesized MoS_2/Porous Silicon Nanostructures for Efficient and Selective Ethanol Sensing at Room Temperature, ACS Appl. Mater. Interfaces. 9 (2017) 21017–21024. https://doi.org/10.1021/acsami.7b05468.

[259] S. OZDEMIR, J. GOLE, The potential of porous silicon gas sensors, Curr. Opin. Solid State Mater. Sci. 11 (2007) 92–100. https://doi.org/10.1016/j.cossms.2008.06.003.

[260] N. Eom, H.-B. Cho, Y. Song, W. Lee, T. Sekino, Y.-H. Choa, Room-Temperature H_2 Gas Sensing Characterization of Graphene-Doped Porous Silicon via a Facile Solution Dropping Method, Sensors. 17 (2017) 2750. https://doi.org/10.3390/s17122750.

[261] A.A. Bunaciu, E. gabriela Udriştioiu, H.Y. Aboul-Enein, X-Ray Diffraction: Instrumentation and Applications, Crit. Rev. Anal. Chem. 45 (2015) 289–299. https://doi.org/10.1080/10408347.2014.949616.

[262] Paul Scherrer, Bestimmung der Grösse und der Inneren Struktur von Kolloidteilchen Mittels Röntgenstrahlen, Nachrichten von der Gesellschaft der Wissenschaften, Göttingen, Math. Klasse. 2 (1918) 98–100.

[263] A. Monshi, M.R. Foroughi, M.R. Monshi, Modified Scherrer Equation to Estimate More Accurately Nano-Crystallite Size Using XRD, World J. Nano Sci. Eng. 02 (2012) 154–160. https://doi.org/10.4236/wjnse.2012.23020.

[264] H.G.M. Edwards, Modern Raman spectroscopy—a practical approach.Ewen Smith and Geoffrey Dent. John Wiley and Sons Ltd, Chichester, 2005. Pp. 210. ISBN 0 471 49668 5 (cloth, hb); 0 471 49794 0 (pbk), 2005. https://doi.org/10.1002/jrs.1320.

[265] D.W. Shipp, F. Sinjab, I. Notingher, Raman spectroscopy: techniques and

applications in the life sciences, Adv. Opt. Photonics. 9 (2017) 315. https://doi.org/10.1364/aop.9.000315.

[266] B. Lewczuk, N. Szyryńska, Field-emission scanning electron microscope as a tool for large-area and large-volume ultrastructural studies, Animals. 11 (2021) 1–21. https://doi.org/10.3390/ani11123390.

[267] J.M. Huggett, H.F. Shaw, Field emission scanning electron microscopy — a high-resolution technique for the study of clay minerals in sediments, Clay Miner. 32 (1997) 197–203. https://doi.org/10.1180/claymin.1997.032.2.03.

[268] F. Krumeich, Introduction Into Transmission and Scanning Transmission, (2018).

[269] Suparti, Fundamentals of transmission electron microscopy, the technique with the best resolution in the world, Bogota. (2019) 0–6.

[270] F. Spanish, Técnicas de analisis y caracterización de materiales , Técnicas de análisis y caracTerización de MaTeriales Marisol Faraldos, (2016).

[271] W.F. Tivol, Selected Area Electron Diffraction and its Use in Structure Determination, Micros. Today. 18 (2010) 22–28. https://doi.org/10.1017/S1551929510000441.

[272] D.J. Smith, Chapter 14 - High Resolution Transmission Electron Microscopy, Handb. Microsc. Nanotechnol. (2005) 427–453.

[273] F.A. Stevie, C.L. Donley, Introduction to x-ray photoelectron spectroscopy, J. Vac. Sci. Technol. A. 38 (2020) 063204. https://doi.org/10.1116/6.0000412.

[274] A.V. Girão, G. Caputo, M.C. Ferro, Application of Scanning Electron Microscopy–Energy Dispersive X-Ray Spectroscopy (SEM-EDS), Compr. Anal. Chem. 75 (2017) 153–168. https://doi.org/10.1016/bs.coac.2016.10.002.

[275] K.J. Rountree, B.D. Mccarthy, E.S. Rountree, T.T. Eisenhart, J.L. Dempsey, A Practical Beginner ' s Guide to Cyclic Voltammetry, (2017). https://doi.org/10.1021/acs.jchemed.7b00361.

[276] L. Nadjo, J.M. Savéant, Linear sweep voltammetry: Kinetic control by charge transfer and/or secondary chemical reactions. I. Formal kinetics, J. Electroanal. Chem. 48 (1973) 113–145. https://doi.org/10.1016/S0022-0728(73)80300-6.

[277] F.S. Semaan, U.F. Fluminense, Voltammetry Complimentary Contributor Copy, 2016.

[278] M. Poloju, N. Jayababu, E. Manikandan, M. V. Ramana Reddy, Enhancement of the isopropanol gas sensing performance of SnO_2/ZnO core/shell nanocomposites, J. Mater. Chem. C. 5 (2017) 2662–2668. https://doi.org/10.1039/c6tc05095f.

[279] Z. Yunusa, M.N. Hamidon, A. Kaiser, Z. Awang, Gas Sensors- A Review, J. Environ. Nanotechnol. 4 (2015) 01–14. https://doi.org/10.13074/jent.2015.12.153163.

[280] T. Kida, A. Nishiyama, Z. Hua, K. Suematsu, M. Yuasa, K. Shimanoe, WO3

nanolamella gas sensor: Porosity control using SnO_2 nanoparticles for enhanced NO_2 sensing, Langmuir. 30 (2014) 2571–2579. https://doi.org/10.1021/la4049105.

[281] N. Jayababu, M. Poloju, M. V. Ramana Reddy, Facile synthesis of SnO_2-Fe_2O_3 core-shell nanostructures and their 2-methoxyethanol gas sensing characteristics, J. Alloys Compd. 780 (2019) 523–533. https://doi.org/10.1016/j.jallcom.2018.11.413.

[282] S. Elouali, L.G. Bloor, R. Binions, I.P. Parkin, C.J. Carmalt, J.A. Darr, Gas sensing with nano-indium oxides (In_2O_3) prepared via continuous hydrothermal flow synthesis, Langmuir. 28 (2012) 1879–1885. https://doi.org/10.1021/la203565h.

[283] S. Lin, D. Li, J. Wu, X. Li, S.A. Akbar, A selective room temperature formaldehyde gas sensor using TiO_2 nanotube arrays, Sensors Actuators, B Chem. 156 (2011) 505–509. https://doi.org/10.1016/j.snb.2011.02.046.

[284] Y. Li, J. Liang, Z. Tao, J. Chen, CuO particles and plates: Synthesis and gas-sensor application, Mater. Res. Bull. 43 (2008) 2380–2385. https://doi.org/10.1016/j.materresbull.2007.07.045.

[285] M. Poloju, N. Jayababu, M. V. Ramana Reddy, Improved gas sensing performance of Al doped ZnO/CuO nanocomposite based ammonia gas sensor, Mater. Sci. Eng. B Solid-State Mater. Adv. Technol. 227 (2018) 61–67. https://doi.org/10.1016/j.mseb.2017.10.012.

[286] N. Jayababu, M. Poloju, J. Shruthi, M.V.R. Reddy, Synthesis of ZnO/NiO nanocomposites for the rapid detection of ammonia at room temperature, Mater. Sci. Semicond. Process. 102 (2019) 104591. https://doi.org/10.1016/j.mssp.2019.104591.

[287] I. Navas, R. Vinodkumar, V.P. Mahadevan Pillai, Self-assembly and photoluminescence of molybdenum oxide nanoparticles, Appl. Phys. A Mater. Sci. Process. 103 (2011) 373–380. https://doi.org/10.1007/s00339-011-6345-9.

[288] Y. Nerthigan, A.K. Sharma, S. Pandey, K.H. Sharma, M. Shahnawaz Khan, D.R. Hang, H.F. Wu, Glucose oxidase assisted visual detection of glucose using oxygen deficient α-MoO_{3-x} nanoflakes, Microchim. Acta. 185 (2018) 3–10. https://doi.org/10.1007/s00604-017-2612-6.

[289] S.K.S. Patel, K. Dewangan, S.K. Srivastav, N.K. Verma, P. Jena, A.K. Singh, N.S. Gajbhiye, Synthesis of α-MoO_3 nanofibers for enhanced field-emission properties, Adv. Mater. Lett. 9 (2018) 585–589. https://doi.org/10.5185/amlett.2018.2022.

[290] X. Hou, J. Huang, M. Liu, X. Li, Z. Hu, Z. Feng, M. Zhang, J. Luo, Single-Crystal MoO_3 Micrometer and Millimeter Belts Prepared from Discarded Molybdenum Disilicide Heating Elements, Sci. Rep. 8 (2018) 2–9. https://doi.org/10.1038/s41598-018-34849-y.

[291] M. Yu, X. Cheng, Y. Zeng, Z. Wang, Y. Tong, X. Lu, S. Yang, Dual-Doped Molybdenum Trioxide Nanowires: A Bifunctional Anode for Fiber-Shaped

Asymmetric Supercapacitors and Microbial Fuel Cells, Angew. Chemie - Int. Ed. 55 (2016) 6762–6766. https://doi.org/10.1002/anie.201602631.

[292] S. Singh, N. Dogra, S. Sharma, A sensitive H2S sensor using MoS_2/WO_3 composite, Mater. Today Proc. 28 (2020) 8–10. https://doi.org/10.1016/j.matpr.2019.12.104.

[293] M. Ge, X. Fang, J. Rong, C. Zhou, Review of porous silicon preparation and its application for lithium-ion battery anodes, Nanotechnology. 24 (2013) 422001. https://doi.org/10.1088/0957-4484/24/42/422001.

[294] N. Jayababu, M. Poloju, J. Shruthi, M.V.R. Reddy, Ultrasensitive resistivity-based ethanol sensor based on the use of CeO_2-Fe_2O_3 core-shell microclusters, Microchim. Acta. 186 (2019) 712. https://doi.org/10.1007/s00604-019-3809-7.

[295] S.K.S. Patel, K. Dewangan, N.S. Gajbhiye, Synthesis and Room Temperature d0 Ferromagnetic Properties of α-MoO_3 Nanofibers, J. Mater. Sci. Technol. 31 (2015) 453–457. https://doi.org/10.1016/j.jmst.2014.08.013.

[296] E. Tan, P.G. Mather, A.C. Perrella, J.C. Read, R.A. Buhrman, Oxygen stoichiometry and instability in aluminum oxide tunnel barrier layers, Phys. Rev. B - Condens. Matter Mater. Phys. 71 (2005) 1–4. https://doi.org/10.1103/PhysRevB.71.161401.

[297] M. Berouaken, L. Talbi, C. Yaddadene, M. Maoudj, H. Menari, R. Alkama, Room temperature ammonia gas sensor based on - V_2O_5 nanoplatelets/Quartz crystal microbalance, Appl. Phys. A. (2020) 1–9. https://doi.org/10.1007/s00339-020-04129-6.

[298] A. Jia, B. Liu, H. Liu, Q. Li, Y. Yun, Interface Design of SnO_2@PANI Nanotube With Enhanced Sensing Performance for Ammonia Detection at Room Temperature, Front. Chem. 8 (2020) 1–9. https://doi.org/10.3389/fchem.2020.00383.

[299] B.-Y. Liu, W. Liu, New Room Temperature Ammonia Gas Sensor Synthesized by a Tantalum Pentoxide (Ta_2O_5) Dielectric and Catalytic Platinum (Pt) Metals, IEEE Trans. Electron Devices. 67 (2020) 2566–2572. https://doi.org/10.1109/TED.2020.2986795.

[300] E. Vinoth, N. Gopalakrishnan, Fabrication of interdigitated electrode (IDE) based ZnO sensors for room temperature ammonia detection, J. Alloys Compd. 824 (2020) 153900. https://doi.org/10.1016/j.jallcom.2020.153900.

[301] S. Huang, L.A. Panes-Ruiz, A. Croy, M. Löffler, V. Khavrus, V. Bezugly, G. Cuniberti, Highly Sensitive Room Temperature Ammonia Gas Sensor Using Pristine Graphene: The Role of Biocompatible Stabilizer, Carbon N. Y. 173 (2020) 262–270. https://doi.org/10.1016/j.carbon.2020.11.001.

[302] R. Kumar, A. Kumar, R. Singh, R. Kumar, D. Kumar, S. Kumar, M. Kumar, Toluic Acid Functionalized Graphene Oxide, Mater. Chem. Phys. (2019). https://doi.org/10.1016/j.matchemphys.2019.121922.

[303] H. Liu, W. Shen, X. Chen, A room temperature operated ammonia gas sensor based on Ag-decorated TiO_2 quantum dot clusters, RSC Adv. 9 (2019) 24519–24526. https://doi.org/10.1039/c9ra05439a.

[304] Z. Pang, Y. Zhu, X. Li, M. Chen, M. Ge, Room Temperature Ammonia Gas Sensor Based on Polyacrylonitrile/Silver@Polyaniline Nanofibers, IEEE Sens. J. 19 (2019) 11021–11026. https://doi.org/10.1109/JSEN.2019.2935232.

[305] Y. Seekaew, W. Pon-On, C. Wongchoosuk, Ultrahigh Selective Room-Temperature Ammonia Gas Sensor Based on Tin-Titanium Dioxide/reduced Graphene/Carbon Nanotube Nanocomposites by the Solvothermal Method, ACS Omega. 4 (2019) 16916–16924. https://doi.org/10.1021/acsomega.9b02185.

[306] S. Sharma, A. Kumar, N. Singh, D. Kaur, Excellent room temperature ammonia gas sensing properties of n-MoS_2/p-CuO heterojunction nanoworms, Sensors Actuators, B Chem. 275 (2018) 499–507. https://doi.org/10.1016/j.snb.2018.08.046.

[307] Z. Pang, Z. Yang, Y. Chen, J. Zhang, Q. Wang, F. Huang, Q. Wei, A room temperature ammonia gas sensor based on cellulose/TiO_2/PANI composite nanofibers, Colloids Surfaces A Physicochem. Eng. Asp. 494 (2016) 248–255. https://doi.org/10.1016/j.colsurfa.2016.01.024.

[308] S. Yang, Z. Wang, Y. Zou, X. Luo, X. Pan, X. Zhang, Y. Hu, K. Chen, Z. Huang, S. Wang, K. Zhang, H. Gu, Remarkably accelerated room-temperature hydrogen sensing of MoO_3 nanoribbon/graphene composites by suppressing the nanojunction effects, Sensors Actuators, B Chem. 248 (2017) 160–168. https://doi.org/10.1016/j.snb.2017.03.106.

[309] S.S. Sunu, E. Prabhu, V. Jayaraman, K.I. Gnanasekar, T.K. Seshagiri, T. Gnanasekaran, Electrical conductivity and gas sensing properties of MoO_3, Sensors Actuators, B Chem. 101 (2004) 161–174. https://doi.org/10.1016/j.snb.2004.02.048.

[310] H. Naderi, S. Hajati, M. Ghaedi, K. Dashtian, M.M. Sabzehmeidani, Sensitive, selective and rapid ammonia-sensing by gold nanoparticle-sensitized V_2O_5/$CuWO_4$ heterojunctions for exhaled breath analysis, Appl. Surf. Sci. 501 (2020) 144270. https://doi.org/10.1016/j.apsusc.2019.144270.

[311] S. Sharma, A. Kumar, N. Singh, D. Kaur, Excellent room temperature ammonia gas sensing properties of n-MoS_2/p-CuO heterojunction nanoworms, Sensors Actuators, B Chem. 275 (2018) 499–507. https://doi.org/10.1016/j.snb.2018.08.046.

[312] A. Sharma, P. Bhojane, A.K. Rana, Y. Kumar, P.M. Shirage, Mesoporous nickel cobalt hydroxide/oxide as an excellent room temperature ammonia sensor, Scr. Mater. 128 (2017) 65–68. https://doi.org/10.1016/j.scriptamat.2016.10.003.

[313] G. Greczynski, L. Hultman, X-ray photoelectron spectroscopy: Towards reliable binding energy referencing, Prog. Mater. Sci. 107 (2020) 100591.

https://doi.org/10.1016/j.pmatsci.2019.100591.

[314] G. Greczynski, B. Bakhit, L. Hultman, M. Odén, High Si content TiSiN films with superior oxidation resistance, Surf. Coatings Technol. 398 (2020) 126087. https://doi.org/10.1016/j.surfcoat.2020.126087.

[315] G. Greczynski, L. Hultman, Reliable determination of chemical state in x-ray photoelectron spectroscopy based on sample-work-function referencing to adventitious carbon: Resolving the myth of apparent constant binding energy of the C 1s peak, Appl. Surf. Sci. 451 (2018) 99–103. https://doi.org/10.1016/j.apsusc.2018.04.226.

[316] T. Thomas, A. Mathew, R. Reshmi, Influence of post annealing on the properties of α-MoO_3 nano rods grown on glass substrate by thermal evaporation, AIP Conf. Proc. 2115 (2019) 0–4. https://doi.org/10.1063/1.5112955.

[317] T. Thomas, A. Mathew, R. Reshmi, Vertically aligned α-MoO_3 nanorods on commercial glass substrate by vacuum thermal evaporation, Mater. Lett. 227 (2018) 29–32. https://doi.org/10.1016/j.matlet.2018.04.126.

[318] A.A. El-Gamal, S.M. Ibrahim, M. Amin, Impact of thermal oxidation on the structural and optical properties of porous silicon microcavity, Nanomater. Nanotechnol. 7 (2017) 1–7. https://doi.org/10.1177/1847980417735702.

[319] R. Dalvand, S. Mahmud, J. Rouhi, Direct growth of flower-like ZnO nanostructures on porous silicon substrate using a facile lowerature technique, Mater. Lett. 160 (2015) 444–447. https://doi.org/10.1016/j.matlet.2015.08.029.

[320] Z. Li, L. Gao, S. Zheng, SEM, XPS, and FTIR studies of MoO_3 dispersion on mesoporous silicate MCM-41 by calcination, Mater. Lett. 57 (2003) 4605–4610. https://doi.org/10.1016/S0167-577X(03)00369-0.

[321] Y.J. Chen, X.M. Gao, X.P. Di, Q.Y. Ouyang, P. Gao, L.H. Qi, C.Y. Li, C.L. Zhu, Porous iron molybdate nanorods: In situ Diffusion Synthesis and Low-Temperature H_2S Gas Sensing, ACS Appl. Mater. Interfaces. 5 (2013) 3267–3274. https://doi.org/10.1021/am400324g.

[322] M. Li, L. Zeng, Y. Chen, L. Zhuang, X. Wang, H. Shen, Realization of Colored Multicrystalline Silicon Solar Cells with SiO_2 /SiN_x:H Double Layer Antireflection Coatings, Int. J. Photoenergy. 2013 (2013) 1–8. https://doi.org/10.1155/2013/352473.

[323] S. Deepa, K. Prasanna Kumari, B. Thomas, Contribution of oxygen-vacancy defect-types in enhanced CO_2 sensing of nanoparticulate Zn-doped SnO_2 films, Ceram. Int. 43 (2017) 17128–17141. https://doi.org/10.1016/j.ceramint.2017.09.134.

[324] A. Ghosh, C. Zhang, S. Shi, H. Zhang, High temperature CO_2 sensing and its cross-sensitivity towards H_2 and CO gas using calcium doped ZnO thin film coated langasite SAW sensor, Sensors Actuators, B Chem. 301 (2019) 126958.

https://doi.org/10.1016/j.snb.2019.126958.

[325] B. Mandal, M. Das, M. Than, S. Mukherjee, Architecture tailoring of MoO_3 nanostructures for superior ethanol sensing performance, Mater. Res. Bull. 109 (2019) 281–290. https://doi.org/10.1016/j.materresbull.2018.09.041.

[326] A.A. Aboud, H. Al-Kelesh, W.M.A.E. Rouby, A.A. Farghali, A. Hamdedein, M.H. Khedr, CO_2 responses based on pure and doped CeO_2 nano-pellets, J. Mater. Res. Technol. 7 (2018) 14–20. https://doi.org/10.1016/j.jmrt.2017.03.003.

[327] P. Mitra, A.P. Chatterjee, H.S. Maiti, ZnO thin film sensor, Mater. Lett. 35 (1998) 33–38. https://doi.org/10.1016/S0167-577X(97)00215-2.

[328] S.L. Zhang, J.O. Lim, J.S. Huh, J.S. Noh, W. Lee, Two-step fabrication of ZnO nanosheets for high-performance VOCs gas sensor, Curr. Appl. Phys. 13 (2013) 1–6. https://doi.org/10.1016/j.cap.2012.12.021.

[329] S. Bag, K. Pal, Sulfonated poly (ether ether ketone) based carbon dioxide gas sensor: Impact of sulfonation degree on sensing behavior at different humid condition, Sensors Actuators, B Chem. 303 (2020) 127115. https://doi.org/10.1016/j.snb.2019.127115.

[330] Y.M. Hunge, A.A. Yadav, S.B. Kulkarni, V.L. Mathe, A multifunctional ZnO thin film based devises for photoelectrocatalytic degradation of terephthalic acid and CO_2 gas sensing applications, Sensors Actuators, B Chem. 274 (2018) 1–9. https://doi.org/10.1016/j.snb.2018.07.117.

[331] A.A. Yadav, A.C. Lokhande, J.H. Kim, C.D. Lokhande, Enhanced sensitivity and selectivity of CO_2 gas sensor based on modi fi ed La_2O_3 nanorods, J. Alloys Compd. 723 (2017) 880–886. https://doi.org/10.1016/j.jallcom.2017.06.223.

[332] P. ZHANG, H. QIN, H. ZHANG, W. LÜ, J. HU, CO_2 gas sensors based on $Yb_{1-x}Ca_xFeO_3$ nanocrystalline powders, J. Rare Earths. 35 (2017) 602–609. https://doi.org/10.1016/S1002-0721(17)60953-0.

[333] D. Wang, Y. Chen, Z. Liu, L. Li, C. Shi, H. Qin, J. Hu, CO_2-sensing properties and mechanism of nano-SnO_2 thick-film sensor, Sensors Actuators, B Chem. 227 (2016) 73–84. https://doi.org/10.1016/j.snb.2015.12.025.

[334] S. Joshi, S. Lanka, S.J. Ippolito, S.K. Bhargava, M. V. Sunkara, {111} faceted $Li_4Ti_5O_{12}$ octahedra as the reference electrode material in a nanostructured potentiometric CO_2 sensor, J. Mater. Chem. A. 4 (2016) 16418–16431. https://doi.org/10.1039/c6ta05013a.

[335] R.U. Mene, M.P. Mahabole, K.C. Mohite, R.S. Khairnar, Fe doped hydroxyapatite thick films modified via swift heavy ion irradiation for CO and CO_2 gas sensing application, J. Alloys Compd. 584 (2014) 487–493. https://doi.org/10.1016/j.jallcom.2013.09.111.

[336] P. Matheswaran, R. Sathyamoorthy, K. Asokan, Effect of 130 MeV Au ion irradiation on CO_2 gas sensing properties of In2Te3 thin films, Sensors Actuators, B Chem. 177 (2013) 8–13. https://doi.org/10.1016/j.snb.2012.10.115.

[337] C.R. Michel, CO and CO_2 gas sensing properties of mesoporous $CoAl_2O_4$, Sensors Actuators, B Chem. 147 (2010) 635–641. https://doi.org/10.1016/j.snb.2010.04.013.

[338] R. Mene, M. Mahabole, Hydroxyapatite Nanoceramic Thick Film: An Efficient CO_2 Gas Sensor., Open Appl. Phys. …. 3 (2010) 10–16. https://doi.org/https://doi.org/10.2174/1874183501003010010.

[339] J.A. Ramos-Ramón, N.K.R. Bogireddy, J.A. Giles Vieyra, T.V.K. Karthik, V. Agarwal, Nitrogen-Doped Carbon Dots Induced Enhancement in CO_2 Sensing Response From ZnO–Porous Silicon Hybrid Structure, Front. Chem. 8 (2020) 1–15. https://doi.org/10.3389/fchem.2020.00291.

[340] K. V. Sopiha, O.I. Malyi, C. Persson, P. Wu, Band gap modulation of $SrTiO_3$ upon CO_2 adsorption, Phys. Chem. Chem. Phys. 19 (2017) 16629–16637. https://doi.org/10.1039/C7CP01462G.

[341] U. Terranova, F. Viñes, N.H. de Leeuw, F. Illas, Mechanisms of carbon dioxide reduction on strontium titanate perovskites, J. Mater. Chem. A. 8 (2020) 9392–9398. https://doi.org/10.1039/D0TA01502D.

[342] J. Tamaki, M. Akiyama, C. Xu, N. Miura, N. Yamazoe, Conductivity Change of SnO 2 with CO_2 Adsorption, Chem. Lett. 19 (1990) 1243–1246. https://doi.org/10.1246/cl.1990.1243.

[343] M.E. Franke, T.J. Koplin, U. Simon, Metal and metal oxide nanoparticles in chemiresistors: Does the nanoscale matter?, Small. 2 (2006) 36–50. https://doi.org/10.1002/smll.200500261.

[344] Z. Li, H. Li, Z. Wu, M. Wang, J. Luo, H. Torun, P. Hu, C. Yang, M. Grundmann, X. Liu, Y. Fu, Advances in designs and mechanisms of semiconducting metal oxide nanostructures for high-precision gas sensors operated at room temperature, Mater. Horizons. 6 (2019) 470–506. https://doi.org/10.1039/C8MH01365A.

[345] J.P. Morán-Lázaro, O. Blanco, V.M. Rodríguez-Betancourtt, J. Reyes-Gómez, C.R. Michel, Enhanced CO_2-sensing response of nanostructured cobalt aluminate synthesized using a microwave-assisted colloidal method, Sensors Actuators B Chem. 226 (2016) 518–524. https://doi.org/10.1016/j.snb.2015.12.013.

[346] A.A. Mane, M.P. Suryawanshi, J.H. Kim, A. V. Moholkar, Fast response of sprayed vanadium pentoxide (V_2O_5) nanorods towards nitrogen dioxide (NO_2) gas detection, Appl. Surf. Sci. 403 (2017) 540–550. https://doi.org/10.1016/j.apsusc.2017.01.220.

[347] S. Sun, M. Wang, X. Chang, Y. Jiang, D. Zhang, D. Wang, Y. Zhang, Y. Lei, $W_{18}O_{49}/Ti_3C_2T_x$ Mxene nanocomposites for highly sensitive acetone gas sensor with

low detection limit, Sensors Actuators, B Chem. 304 (2020) 127274. https://doi.org/10.1016/j.snb.2019.127274.

[348] Y. Tang, J. Chen, H. Wu, J. Yu, J. Jia, W. Xu, Y. Fu, Q. He, H. Cao, J. Cheng, A highly fluorescent post-modified metal organic framework probe for selective, reversible and rapid carbon dioxide detection, Dye. Pigment. 172 (2020) 107798. https://doi.org/10.1016/j.dyepig.2019.107798.

[349] H. Wei, Q. Xi, X. Chen, D. Guo, F. Ding, Z. Yang, S. Wang, J. Li, S. Huang, Molybdenum Carbide Nanoparticles Coated into the Graphene Wrapping N-Doped Porous Carbon Microspheres for Highly Efficient Electrocatalytic Hydrogen Evolution Both in Acidic and Alkaline Media, Adv. Sci. 5 (2018) 1700733. https://doi.org/10.1002/advs.201700733.

[350] N.S. Lewis, D.G. Nocera, Powering the planet: Chemical challenges in solar energy utilization, Proc. Natl. Acad. Sci. 103 (2006) 15729–15735. https://doi.org/10.1073/pnas.0603395103.

[351] D.G. Nocera, The Artificial Leaf, Acc. Chem. Res. 45 (2012) 767–776. https://doi.org/10.1021/ar2003013.

[352] M. Cabán-Acevedo, M.L. Stone, J.R. Schmidt, J.G. Thomas, Q. Ding, H.C. Chang, M.L. Tsai, H. He, S. Jin, Efficient hydrogen evolution catalysis using ternary pyrite-type cobalt phosphosulphide, Nat. Mater. 14 (2015) 1245–1251. https://doi.org/10.1038/nmat4410.

[353] J. Zhang, Y. Zhao, X. Guo, C. Chen, C.L. Dong, R.S. Liu, C.P. Han, Y. Li, Y. Gogotsi, G. Wang, Single platinum atoms immobilized on an MXene as an efficient catalyst for the hydrogen evolution reaction, Nat. Catal. 1 (2018) 985–992. https://doi.org/10.1038/s41929-018-0195-1.

[354] Q. He, L. Wang, K. Yin, S. Luo, Vertically Aligned Ultrathin 1T-WS_2 Nanosheets Enhanced the Electrocatalytic Hydrogen Evolution, Nanoscale Res. Lett. 13 (2018) 1–9. https://doi.org/10.1186/s11671-018-2570-x.

[355] J. Ren, H. Zong, Y. Sun, S. Gong, Y. Feng, Z. Wang, L. Hu, K. Yu, K. Yu, 2D organ-like molybdenum carbide (MXene) coupled with MoS_2 nanoflowers enhances the catalytic activity in the hydrogen evolution reaction, CrystEngComm. 22 (2020) 1395–1403. https://doi.org/10.1039/c9ce01777a.

[356] Z. Lv, W. Ma, M. Wang, J. Dang, K. Jian, D. Liu, D. Huang, Co-Constructing Interfaces of Multiheterostructure on MXene ($Ti_3C_2T_x$)-Modified 3D Self-Supporting Electrode for Ultraefficient Electrocatalytic HER in Alkaline Media, Adv. Funct. Mater. 31 (2021) 1–8. https://doi.org/10.1002/adfm.202102576.

[357] T. Thomas, S. Pushpan, J.A. Aguilar Martínez, A. Torres Castro, N. Pineda Aguilar, A. Álvarez-Méndez, K.C. Sanal, UV-assisted safe etching route for the synthesis of

Mo_2CT_x MXene from Mo–In–C non-MAX phase, Ceram. Int. 47 (2021) 35384–35387. https://doi.org/10.1016/j.ceramint.2021.08.342.

[358] T. Thomas, Y. Kumar, J.A. Ramos Ramón, V. Agarwal, S. Sepúlveda Guzmán, R. R, S. Pushpan, S.L. Loredo, K.C. Sanal, Porous silicon/α-MoO_3 nanohybrid based fast and highly sensitive CO_2 gas sensors, Vacuum. 184 (2021). https://doi.org/10.1016/j.vacuum.2020.109983.

[359] M. Mastragostino, F. Soavi, C. Arbizzani, Electrochemical Supercapacitors, Adv. Lithium-Ion Batter. (2002) 481–505. https://doi.org/10.1007/0-306-47508-1_17.

[360] J. Tang, X. Huang, T. Qiu, X. Peng, T. Wu, L. Wang, B. Luo, L. Wang, Interlayer Space Engineering of MXenes for Electrochemical Energy Storage Applications, Chem. - A Eur. J. 27 (2021) 1921–1940. https://doi.org/10.1002/chem.202002283.

[361] D.A. Kuznetsov, Z. Chen, P.M. Abdala, O. V. Safonova, A. Fedorov, C.R. Müller, Single-Atom-Substituted Mo_2C Tx:Fe-Layered Carbide for Selective Oxygen Reduction to Hydrogen Peroxide: Tracking the Evolution of the MXene Phase, J. Am. Chem. Soc. 143 (2021) 5771–5778. https://doi.org/10.1021/jacs.1c00504.

[362] A. Hermawan, B. Zhang, A. Taufik, Y. Asakura, T. Hasegawa, J. Zhu, P. Shi, S. Yin, CuO Nanoparticles/$Ti_3C_2T_x$ MXene Hybrid Nanocomposites for Detection of Toluene Gas, ACS Appl. Nano Mater. 3 (2020) 4755–4766. https://doi.org/10.1021/acsanm.0c00749.

[363] S. Chung, J.M. Moon, J. Choi, H. Hwang, Y.B. Shim, Magnetic force assisted electrochemical sensor for the detection of thrombin with aptamer-antibody sandwich formation, Biosens. Bioelectron. 117 (2018) 480–486. https://doi.org/10.1016/j.bios.2018.06.068.

[364] B.N. Shivananju, S. Yamdagni, R. Fazuldeen, A.K. Sarin Kumar, G.M. Hegde, M.M. Varma, S. Asokan, CO_2 sensing at room temperature using carbon nanotubes coated core fiber Bragg grating, Rev. Sci. Instrum. 84 (2013). https://doi.org/10.1063/1.4810016.

[365] Z.Y. Lee, H.F. Bin Hawari, G.W. Bin Djaswadi, K. Kamarudin, A highly sensitive room temperature CO_2 gas sensor based on SnO_2-rgo hybrid composite, Materials (Basel). 14 (2021) 1–16. https://doi.org/10.3390/ma14030522.

[366] J. Herrán, O. Fernández-González, I. Castro-Hurtado, T. Romero, G. G[a] Mandayo, E. Castaño, Photoactivated solid-state gas sensor for carbon dioxide detection at room temperature, Sensors Actuators B Chem. 149 (2010) 368–372. https://doi.org/10.1016/j.snb.2010.06.050.

[367] R.K. Sonker, S.R. Sabhajeet, B.C. Yadav, TiO_2–PANI nanocomposite thin film prepared by spin coating technique working as room temperature CO_2 gas sensing, J. Mater. Sci. Mater. Electron. 27 (2016) 11726–11732. https://doi.org/10.1007/s10854-

016-5310-y.

[368] S. Keerthana, K. Rathnakannan, Hierarchical ZnO/CuO nanostructures for room temperature detection of carbon dioxide, J. Alloys Compd. 897 (2022) 162988. https://doi.org/10.1016/j.jallcom.2021.162988.

[369] E. Lee, A. Vahidmohammadi, B.C. Prorok, Y.S. Yoon, M. Beidaghi, D.J. Kim, Room Temperature Gas Sensing of Two-Dimensional Titanium Carbide (MXene), ACS Appl. Mater. Interfaces. 9 (2017) 37184–37190. https://doi.org/10.1021/acsami.7b11055.

[370] Z. Yang, A. Liu, C. Wang, F. Liu, J. He, S. Li, J. Wang, R. You, X. Yan, P. Sun, Y. Duan, G. Lu, Improvement of gas and humidity sensing properties of organ-like mxene by alkaline treatment, ACS Sensors. 4 (2019) 1261–1269. https://doi.org/10.1021/acssensors.9b00127.

[371] H. Farahani, R. Wagiran, M. Hamidon, Humidity Sensors Principle, Mechanism, and Fabrication Technologies: A Comprehensive Review, Sensors. 14 (2014) 7881–7939. https://doi.org/10.3390/s140507881.

[372] D.S. Vlachos, P.D. Skafidas, J.N. Avaritsiotis, The effect of humidity on tin-oxide thick-film gas sensors in the presence of reducing and combustible gases, Sensors Actuators B Chem. 25 (1995) 491–494. https://doi.org/10.1016/0925-4005(95)85105-4.

[373] L. Huang, L. Ai, M. Wang, J. Jiang, S. Wang, Hierarchical MoS 2 nanosheets integrated Ti_3C_2 MXenes for electrocatalytic hydrogen evolution, Int. J. Hydrogen Energy. 44 (2019) 965–976. https://doi.org/10.1016/j.ijhydene.2018.11.084.

[374] J. Aguedo, L. Lorencova, M. Barath, P. Farkas, J. Tkac, Electrochemical Impedance Spectroscopy on 2D Nanomaterial MXene Modified Interfaces: Application as a Characterization and Transducing Tool, Chemosensors. 8 (2020) 127. https://doi.org/10.3390/chemosensors8040127.